



A University of Sussex PhD thesis

Available online via Sussex Research Online:

<http://sro.sussex.ac.uk/>

This thesis is protected by copyright which belongs to the author.

This thesis cannot be reproduced or quoted extensively from without first obtaining permission in writing from the Author

The content must not be changed in any way or sold commercially in any format or medium without the formal permission of the Author

When referring to this work, full bibliographic details including the author, title, awarding institution and date of the thesis must be given

Please visit Sussex Research Online for more information and further details

The Synthesis, Catalytic Investigation, and Theoretical Rationalisation of Unsymmetrical Pincer Palladacycles

Gavin William Roffe

Submitted towards fulfilment of the requirement for the degree of Doctor of
Philosophy



School of Life Sciences
University of Sussex
United Kingdom

March 2016

Declaration

I hereby declare that this thesis has not been and will not be, submitted in whole or in part to another University for the award of any other degree.

Gavin William Roffe

Abstract

This thesis presents the synthesis of a number of unsymmetrical SCN, N'CN, PCN and PCS pincer palladacycles. A new synthetic route has been designed towards unsymmetrical pincer ligands, involving a key Suzuki-Miyaura coupling, yielding the characteristic biaryl ligand backbone presented.

New unsymmetrical SCN pincer ligands, containing a pyridine and a thioether ligand were synthesised. A number of substituents were used on the thioether ligand arm, with various steric demand and electron donating characteristics. These unsymmetrical ligands underwent C-H bond activation with palladium (II) salts, yielding the corresponding palladacycles.

In order to investigate the effect of changing the sulphur donor atom, the thioether ligand arm was replaced by amines in the synthesis of N'CN pincer palladacycles, and phosphinites in the synthesis of PCN pincer palladacycles. Also changing the pyridine donor arm to a thioether was investigated, yielding a PCS pincer palladacycle.

The palladacycles were tested in a number of catalytic applications: Suzuki-Miyaura coupling of sterically demanding and electronically deactivated aryl bromides; cross coupling of arylboronic acids and vinyl epoxides; and catalytic aldol condensations; revealing differences between the SCN, N'CN and PCN pincer palladacycles.

In order to investigate the differences in catalytic activity, density functional theory was employed. A palladacycle formation pathway containing a key C-H bond activation step was investigated for an SCN pincer palladacycle, revealing differences in energy barriers of the C-H bond activation step depending on whether

the thioether or the pyridine arm coordinates to the PdCl_2 first.

Next, the activation pathway of the palladacycles in the Suzuki-Miyaura coupling reaction was studied, identifying key transmetallation and reductive elimination steps. Differences in the overall thermodynamics and kinetics provide explanations for differences in catalytic activity. The results show that slower release of the catalytically active $\text{Pd}(0)$ species yield a better precatalyst in the Suzuki-Miyaura coupling reaction, due to the lower propensity to form catalytically inactive palladium black.

Overall this thesis provides a novel synthetic route to a family of unsymmetrical pincer palladacycles; their testing in catalytic activity in several applications, revealing differences in catalytic activity; and a theoretical study into key mechanisms, C-H bond activation, and catalyst activation in the Suzuki-Miyaura coupling reaction, which provide a rationalisation to the varying catalytic activities of the unsymmetrical pincer palladacycles.

Acknowledgements

I would like to extend my gratitude to everyone at the University of Sussex who made this thesis possible. I would like to thank the School of Life Sciences for providing the funding for my PhD studies.

I would particularly like to thank my supervisors Dr John Spencer and Dr Hazel Cox for their unwavering support throughout my studies. Both were always on hand to provide extremely friendly and supportive advice regarding my academic direction and personal development. I would also like to thank Prof. Tony McCaffery for his helpful discussions in preparing for various presentations throughout my studies.

I would like to acknowledge the use of the EPSRC UK National Service for Computational Chemistry Software (NSCCS) at Imperial College London in carrying out this work. The EPSRC National Mass Spectrometry facility at Swansea University, and the EPSRC NCS UK National Crystallography Service of the University of Southampton are acknowledged for carrying out HRMS measurements and X-ray crystallographic measurements. My thanks also go out to those at Sussex for various technical support, especially Dr Alaa Abdul-Sada, Dr Iain Day, and Chris Dadswell for their MS, NMR and GC assistance, respectively.

I would like to thank past and present members of the Spencer and Cox groups: Adam Close, Rhiannon Jones, Supojanee Sansook (Poj), Melvyn Ansell, Raysa Khan, Bradley Springett, Andrew King, Adam Baskerville, Msugh Targema, Sarote Boonseng (Pop), Rob Ziolk and Luke Rhodes for helping me to develop my experimental and computational skills, providing excellent friendship, and stimulating new ideas and pathways.

I would like to express my gratitude to Rhiannon and Msugh who directly contributed to my studies of pincer palladacycles. My special thanks go to Sarote Boonseng (Pop) for our enjoyable and fruitful collaboration.

To all of my friends at Sussex, I would like to thank you for all your support and for making my PhD an enjoyable experience.

Finally, I would like to thank my family, especially Mum, Dad, Nan, Grandad and Ollie for their love, support and encouragement.

Contents

1	Introduction	3
1.1	Palladacycle history	3
1.2	Classification of palladacycles	5
1.2.1	CY palladacycles	5
1.2.2	Symmetrical YCY pincer palladacycles	6
1.2.3	Unsymmetrical YCY' pincer palladacycles	7
1.2.4	Pyridine containing palladacycles	9
1.3	Hemilability	10
1.4	Applications of palladacycles	11
1.5	Pincer ligands with other metals	19
1.6	Microwave assisted organic synthesis	21
1.7	Thesis overview	23
2	Theoretical details and a computational method validation study	25
2.1	Density functional theory (DFT)	25
2.1.1	Introduction	25
2.1.2	Exchange correlation functionals	27
2.2	Using density functional theory to study non-covalent interactions . .	32
2.3	Basis sets	33
2.3.1	Introduction	33
2.3.2	Gaussian functions	34
2.3.3	Minimal basis set	34

2.3.4	Double and triple ζ , split-valence basis sets	34
2.3.5	Polarisation and diffuse functions	35
2.3.6	Basis sets used in this thesis for atoms other than palladium .	35
2.3.7	Effective core potentials for palladium	36
2.4	Solvation effects in DFT	36
2.5	Atoms in Molecules	37
2.5.1	Introduction	37
2.5.2	Use of AIM to investigate the strength and nature of bonding	41
2.6	Method validation results	42
2.6.1	Introduction	42
2.6.2	Quatfit analysis	43
2.6.3	Bonded distances	45
2.6.4	Interatomic distances	46
2.6.5	Analysis	48
2.7	Computational Details	49
3	An SCN pincer palladacycle: a DFT pathway and a synthetic route	51
3.1	Introduction	52
3.1.1	SCN pincer palladacycles	52
3.1.2	Efforts towards synthesising the SCN ligand and palladacycle presented in this thesis	53
3.1.3	Cationic palladacycles, and salt metathesis	56
3.1.4	C-H bond activation	57
3.2	Results and Discussion	61
3.2.1	New ligand synthesis with late stage diversification	61
3.2.2	Suzuki-Miyaura coupling optimisation	62
3.2.3	Conversion of benzyl alcohol 5 to a benzyl bromide for nucleo- philic displacement	64
3.2.4	Benzylic bromide nucleophilic substitution with thiol nucleophiles	65
3.2.5	C-H bond activation of ligand 1a	65

3.2.6	Unsymmetrical SCN pincer palladacycle formation reaction pathway	68
3.2.7	Pathway towards 2a with either N- or S-coordinating to Pd first	69
3.2.8	Comparison to previously studied PdSCS and PdNCN palladacycles	80
3.2.9	Solvation effects	83
3.2.10	Summary	86
3.2.11	Comparison of theoretically determined and experimental solid state geometry of 2a	86
3.3	Conclusions	88
3.4	Experimental details	88
3.4.1	General Details	88
3.4.2	Instrumentation	89
3.4.3	Experimental Procedures	89
4	Expanding the scope: A family of SCN pincer palladacycles	93
4.1	Introduction	93
4.1.1	Steric and electronic ligand effects	94
4.1.2	Suzuki-Miyaura catalysis	96
4.1.3	Suzuki-Miyaura coupling mechanistic insight	98
4.1.4	Comparison of catalyst activation to previous DFT studies . .	102
4.2	Experimental results	107
4.2.1	SCN ligand library synthesis	107
4.2.2	SCN pincer palladacycle synthesis	109
4.2.3	Suzuki-Miyaura coupling catalysis	112
4.3	Theoretical results	119
4.3.1	Catalyst activation pathway	121
4.3.2	Bader charge analysis	130
4.4	Rationalisation of the catalysis results	133
4.5	Conclusion	136

4.6	Experimental details	137
4.6.1	Experimental procedures	137
5	Beyond sulphur: N'CN unsymmetrical pincer palladacycles	149
5.1	Introduction	150
5.1.1	N'CN pincer palladacycles	150
5.1.2	Reductive amination	151
5.2	Results and discussion	152
5.2.1	N'CN ligand synthesis	152
5.2.2	C-H bond activation	155
5.2.3	Suzuki-Miyaura catalysis	160
5.2.4	Suzuki-Miyaura catalyst activation pathway	162
5.3	Conclusion	168
5.4	Experimental details	170
6	Unsymmetrical phosphorus containing palladacycles, and Pd(II) catalysis	177
6.1	Introduction	178
6.1.1	Phosphorus containing palladium catalysis	178
6.1.2	Phosphorus containing palladacycles	181
6.2	Results and discussion	182
6.2.1	Phosphorus containing palladacycle synthesis	182
6.2.2	Catalytic investigation	191
6.2.3	Suzuki-Miyaura coupling rationalisation	204
6.3	Conclusion	211
6.4	Experimental Details	213
6.4.1	General procedure for aldol condensation	219
6.4.2	General procedure for vinyl epoxide coupling	220
6.4.3	General Procedure for Suzuki-Miyaura catalysis	221

7	Pincer palladacycle catalytic activity: an analysis and comparison	224
7.1	Suzuki-Miyaura catalysis	224
8	Concluding remarks, and future directions	229
8.1	Concluding remarks	229
8.2	Future directions	231

List of Figures

1.1	Original Cope and Siekman palladacycles.	4
1.2	Abbreviation of Cope and Siekman palladacycles.	4
1.3	N,N-dimethylbenzylamine palladacycles by Cope and Friedrich. . . .	4
1.4	Further examples of palladacycles.	4
1.5	First pincer palladacycle by Shaw and Moulton.	5
1.6	CY and YCY palladacycle classification for donor ligands.	5
1.7	Cisoid or transoid dimeric palladacycles.	5
1.8	Monomeric, cationic, and anionic palladacycles.	6
1.9	Symmetrical SCS pincer palladacycles.	6
1.10	Symmetrical NCN pincer palladacycles.	6
1.11	Symmetrical PCP pincer palladacycles.	6
1.12	Symmetrical SeCSe pincer palladacycles.	6
1.13	Synthesis of an unsymmetrical PCS ligand from 1,3-bis(bromomethyl)benzene by Szabó and co-workers.	8
1.14	Unsymmetrical pincer palladacycles.	9
1.15	Unsymmetrical pincer palladacycles synthesised <i>via trans</i> -chloropalladation by Dupont and co-workers.	9
1.16	Pyridine containing palladacycles.	10
1.17	Catalytic C-H bond activation <i>via</i> palladacycles by Spencer <i>et al.</i> . . .	17
1.18	Ir containing symmetrical phosphorus pincers.	19
1.19	Milstein and co-workers' ruthenium containing pincer complexes. . . .	19
1.20	Metal pincer complexes of Ni, Sn and Pt.	20

1.21	Bimetallic pincer ruthenium palladium complexes by Klein Gebbink and co-workers.	20
1.22	Trianionic symmetrical NCN pincer complexes with hafnium, chromium and uranium.	21
1.23	Temperature gradients in a vessel heated by traditional heating (left), and microwave irradiation (right), taken from Kappe and co-workers.	21
2.1	Topology of the electron density for cyclopropane.	38
2.2	Symmetrical palladacycles, PdSCS by van Koten and co-workers, and PdNCN by Lu and co-workers, studied for method validation purposes.	42
2.3	Classification of DFT functionals with respect to Jacob's ladder.	43
3.1	Unsymmetrical SCN palladacycle as an intermediate in the synthesis of Narwedine by Holton and co-workers.	52
3.2	SNC pincer palladacycle by Spencer <i>et al.</i> with a benzodiazepine backbone.	52
3.3	SNC pincer palladacycle by Singh and co-workers.	52
3.4	SNC pincer palladacycle by Grévy and co-workers.	53
3.5	SCN pincer palladacycles by Odinet and co-workers.	53
3.6	Water bound SCN pincer palladacycle X-ray crystal structure from Baltus.	55
3.7	Dimeric SCN pincer palladacycle X-ray crystal structure from Baltus.	55
3.8	Desired SCN palladacycle (R=SMe) from Baltus synthesis, but unobtainable.	56
3.9	Examples of cationic palladacycles by, Herrmann and co-workers (left), Thirupathi and co-workers (middle), and Szabó and co-workers (right).	56
3.10	LiCl metathesis of acetate bound palladacycle by Spencer <i>et al.</i>	57
3.11	Buchwald's catalyst tested in Suzuki-Miyaura coupling optimisation.	64
3.12	C-H bond activation position. C-H bond to be palladated shown in red, and chelating groups for regioselective palladation shown in blue.	66

3.13 Twinned crystal structure of 2a	67
3.14 Separated crystal structures of 2a . Left is structure A, right is structure B.	67
3.15 Odinets and co-workers SCN pincer palladacycles.	68
3.16 Examples of unsymmetrical palladacycles synthesised by chloropalladation by Dupont and co-workers.	68
3.17 Symmetrical pincer palladacycle comparison with unsymmetrical ligand and palladacycle.	69
3.18 Int 2 structures with N-H and S-H stabilising bonds, highlighted in red.	78
3.19 TS 2-3 for the <i>S-coordinates</i> pathway, with the cleaving N-H bond shown in red.	79
3.20 TS 2-3 for the <i>N-coordinates</i> pathway, with the cleaving S-H bond shown in red.	79
3.21 A model unsymmetrical PdSCN palladacycle.	80
3.22 Gibbs free and solvent corrected energetic profile for the formation reaction pathway to 2a	86
4.1 SCN pincer ligand, 1a , with a methyl thioether substituent.	94
4.2 Selenium palladacycles by Szabó and co-workers, with ligand electronic fine tuning on Se donor group (middle), and the ligand backbone (right).	95
4.3 Substituent effects on IrPCP pincer complexes by Krogh-Jespersen <i>et al.</i>	95
4.4 Adding additional steric bulk to symmetrical NCN pincer platinum complexes by van Koten.	95
4.5 Herrmann-Beller palladacycle.	97
4.6 Buchwald and co-workers' palladacycle precatalysts.	97
4.7 Sulphur based nucleophiles studied in this thesis.	107
4.8 Unsymmetrical SCN pincer ligands.	108
4.9 Experimentally synthesised unsymmetrical SCN pincer palladacycles.	109
4.10 Crystal structure of 2b	110
4.11 Crystal structure of 2c	111

4.12	Crystal structure of 2f	111
4.13	Literature palladacycles compared in Table 4.4.	114
4.14	Reaction time optimisation for Suzuki-Miyaura coupling reaction using 2a , average of two runs.	115
4.15	Suzuki-Miyaura coupling reactions of sterically hindered substrates undertaken using 2a	116
4.16	Symmetric PdSCS pincer palladacycle.	116
4.17	Literature sterically hindered Suzuki coupling palladacycle examples. .	118
4.18	Suzuki-Miyaura coupling of 8d and 9b with various palladacycle catalysts.	119
4.19	Gibbs free energies (ΔG_s) for SCN pincer palladacycle catalyst activation pathway.	127
4.20	Zhang and Li transmetallation pathway.	129
4.21	Harvey and co-workers transmetallation pathway.	129
5.1	Symmetrical NCN pincer palladacycle by van Koten and co-workers. .	150
5.2	Symmetrical bis(oxazole) palladacycle by Reiser and co-workers (left), bis(thizole) palladacycle by Xiao and co-workers (centre), and unsymmetrical oxazole palladacycle by Song and co-workers (right).	150
5.3	Products from palladacycle formation of van Koten and co-workers. Kinetic product (a), R=H, i) Pd(OAc) ₂ , MeOH, NEt ₃ , ii) LiCl, iii) py (pyridine). Thermodynamic product (b), R=SiMe ₃ , i) Li ₂ [PdCl ₄]. . .	151
5.4	Pd ₂ (dmba) ₂ Cl ₂ palladacycle used in transcyclopalladation.	155
5.5	NCN pincer palladacycles synthesised by Song and co-workers (left and centre), and Richards and Folley (right).	156
5.6	Likely active catalyst in <i>ortho</i> selective bromination by Bedford <i>et al.</i>	157
5.7	Attempted <i>ortho</i> bromination of 14c	157
5.8	N'CN pincer palladacycles.	158
5.9	X-ray crystal structure of 15a	159
5.10	X-ray crystal structure of 15b	159

5.11	X-ray crystal structure of 15c	160
5.12	Suzuki-Miyaura coupling testing with N'CN pincer palladacycles. . .	161
5.13	Key steps in the catalyst activation pathway of N'CN pincer palladacycles for the Suzuki-Miyaura coupling reactions.	163
5.14	Bridging structure of Int 7a for 15a	164
5.15	Singly coordinated structure of Int 7b for 15a	164
5.16	Gibbs free energies, ΔG_S for the catalyst activation pathway of N'CN pincer palladacycles (pathway a).	166
6.1	Phosphorus containing palladium complexes and ligands.	178
6.2	Phosphorus containing palladacycles utilised in Suzuki-Miyaura catalysis.	178
6.3	Traditional π back-donation orbital diagram for M-P bond.	181
6.4	PCN pincer palladacycle examples by SanMartin, Wendt, Punji and Dupont and co-workers.	182
6.5	Other phosphorus containing pincer palladacycles by Szabó, Bedford, Wendt and co-workers.	182
6.6	Proposed product from reaction shown in Scheme 6.8.	184
6.7	X-ray crystal structure of 17a	184
6.8	X-ray crystal structure of 17b	186
6.9	X-ray crystal structure of PCS palladacycle, 21	187
6.10	Other SCN and N'CN palladacycles tested in the aldol condensation reaction.	193
6.11	Crude ^1H NMR of the non-aromatic region of the aldol condensation reaction performed using 15c achieving a <i>trans/cis</i> ratio of 58/42. . .	195
6.12	Active catalytic species in catalytic aldol condensation by Szabó and co-workers.	197
6.13	Symmetrical PdSeCSe palladacycle by Szabó and co-workers.	199
6.14	Crude ^1H NMR of linear/branched mixture of 23 performed using 15c in 60/40 linear/branched ratio.	202

List of Schemes

1.1	Symmetrical SeCSe pincer palladacycle synthesis demonstrated by Yao <i>et al.</i>	7
1.2	Hemilability investigation by Wendt and co-workers.	11
1.3	Cross coupling reactions performed using palladacycles.	12
1.4	Aldol condensation investigation by symmetrical, SCS and PCP, and unsymmetrical PCS pincer palladacycles by Szabó and co-workers. . .	13
1.5	Tandem stannylation and allylation by Szabó and co-workers.	14
1.6	Catalytic allylation of aldehydes using a SePdSe pincer palladacycle by Yao and Sheets.	14
1.7	Enantioselective catalytic allylation reaction catalysed by a BINOL-based palladacycle by Bedford and co-workers.	15
1.8	Investigation into possible mechanisms for allyltin allylation by Le Floch and co-workers.	16
1.9	Michael addition by Richards and co-workers.	16
1.10	Pincer palladacycle catalysed vinyl epoxide coupling with phenyl boronic acid by Szabó and co-workers.	18
1.11	Proposed catalytic cycle for vinyl expode coupling to phenylboronic acid by Szabó and co-workers.	18
1.12	Palladacycle catalysed ring opening of oxabicyclic alkenes with organozinc halides by Hou and co-workers.	19

3.1	Biaryl synthesis by Baltus. a) Pinacol, MgSO ₄ , THF, rt, 1 h. b) HSR, THF, MW 150 °C, 20 min. c) 2-Bromopyridine, Na ₂ CO ₃ , Pd(PPh ₃) ₄ , toluene, EtOH, H ₂ O, MW 130 °C, 10 min.	54
3.2	C-H activation of unsymmetrical SCN ligand by Baltus.	54
3.3	Salt metathesis of cationic palladacycles by Szabó and coworkers. . .	56
3.4	Proposed mechanistic pathway for C-H bond activation with pivalic acid by Fagnou and Lafrance.	58
3.5	Various C-H bond activation mechanisms suggested by Echaverren and co-workers.	59
3.6	Model formation pathway to symmetrical pincer palladacycles.	59
3.7	Symmetrical palladacycle unassisted formation pathway.	60
3.8	SCN palladacycle retrosynthesis.	62
3.9	SCN Suzuki-Miyaura coupling between 3 and 4 , to 5	63
3.10	Bromination of 5 using $\geq 48\%$ HBr in H ₂ O.	64
3.11	Nucleophilic displacement of 6 with sodium thiomethoxide.	65
3.12	C-H bond activation of 1a with salt metathesis to 2a	66
3.13	Model formation reaction of 1a to 2a by C-H bond activation with PdCl ₂	69
3.14	Model formation pathway to 2a , <i>S-coordinates</i> , with SMe coordinating to PdCl ₂ first.	70
3.15	Model formation pathway to 2a , <i>N-coordinates</i> , with 2-pyridyl coordinating to PdCl ₂ first.	71
3.16	Model formation pathway to (III), <i>S-coordinates</i> first.	81
3.17	Model formation pathway to III , <i>N-coordinates</i> first.	81
3.18	Solvent dependent C-H bond activation by Macgregor and co-workers. .	83
4.1	Full reaction scheme to 1a . a) Pd(PPh ₃) ₄ , K ₃ PO ₄ , Tol, EtOH, H ₂ O. b) HBr. c) NaSMe, EtOH.	94
4.2	General Suzuki-Miyaura coupling.	96

4.3	Generation of Pd(0) from a palladacycle precatalyst, by Louie and Hartwig.	98
4.4	Bedford <i>et al.</i> 's investigation into generation of Pd(0) from a PC palladacycle.	99
4.5	Generation of Pd(0) from palladacycles by Spencer <i>et al.</i>	100
4.6	Generation of Pd(0) by Odinet and co-workers.	101
4.7	Reductive elimination of Pd(0) proposed by Fairlamb and co-workers.	101
4.8	Transmetallation mechanisms by Maseras and co-workers.	103
4.9	Transmetallation step by Hong and co-workers.	104
4.10	Morokuma and co-workers reductive elimination.	106
4.11	Nucleophilic displacement of 6 by a range of sulphur based nucleophiles.	108
4.12	C-H bond activation of SCN pincer ligands.	109
4.13	Catalyst loading investigation for Suzuki-Miyaura coupling using 2a	113
4.14	Catalyst reaction time optimisation using 2a , an average of two separate runs.	115
4.15	Key steps in the catalyst activation pathway.	122
4.16	Ligand decooordination leading to reductive elimination.	123
4.17	N-decoordination transition state.	123
4.18	Full catalyst activation pathway for SCN pincer palladacycles in the generation of Pd(0). For R \neq Me barrier not calculated for TS 5-6 , denoted by the dashed arrow.	125
4.19	Proposed role of Pd(0) in catalysis by de Vries <i>et al.</i>	135
4.20	Proposed catalyst deactivation by Dupont and co-workers.	136
5.1	General reductive amination.	151
5.2	Reductive amination using Ti(OiPr) ₄	152
5.3	N'CN pincer palladacycle retrosynthesis.	152
5.4	N'CN Suzuki-Miyaura coupling between 11 and 4	152
5.5	Synthesis of 14a	153

5.6	Nucleophilic displacement of bromide by amine nucleophiles, where X is a range of amine donor groups.	154
5.7	Palladacycle formation <i>via</i> oxidative addition by van Koten and co-workers.	157
5.8	Attempted Suzuki-Miyaura coupling of an aryl chloride using N'CN pincer palladacycles.	162
5.9	Pathway a for the Suzuki-Miyaura catalyst activation pathway for unsymmetrical N'CN pincer palladacycles.	165
5.10	Possible reductive elimination pathway for 15a,c in the Suzuki-Miyaura reaction.	168
6.1	Tandem stannylation and allylation by Szabó and co-workers.	179
6.2	Tandem coupling between vinyl oxirane and an aldehyde by Szabó and co-workers.	179
6.3	Metal organic framework encapsulated PCP pincer palladacycle in a transfer hydrogenation catalyst application by Wade and co-workers.	180
6.4	Allylation using less toxic allylborates by Szabó and co-workers.	180
6.5	Asymmetric allylation of sulfonimines by Szabó and co-workers.	181
6.6	Retrosynthetic pathway towards PCN pincer palladacycle.	183
6.7	Mixed phosphine and phosphinite PCP pincer palladacycle synthesis by Eberhard <i>et al.</i>	183
6.8	Attempted synthesis of PCN pincer ligand.	183
6.9	Synthesis of PCN pincer palladacycle.	184
6.10	Phenol intermediate synthesis.	185
6.11	Synthesis of 5-,5- membered ring PCN pincer palladacycle.	185
6.12	Suzuki-Miyaura coupling leading to an intermediate in the synthesis of a PCS pincer palladacycle.	186
6.13	PCS pincer palladacycle synthesis.	187
6.14	Aldol condensation investigation by symmetrical, SCS and PCP, and unsymmetrical PCS pincer palladacycles by Szabó and co-workers.	191

6.15	Proposed catalytic cyclic of aldol condensation.	192
6.16	Catalytic aldol condensation using phosphorus containing palladacycles.	193
6.17	Methylisocyanoacetate insertion into Pd-C bond of a silica immobilised symmetrical SCS pincer palladacycle by van Koten and co-workers. . .	197
6.18	Vinyl epoxide coupling to phenylboronic acid catalysed by palladium catalysts.	199
6.19	Proposed mechanism for the coupling of vinyl epoxide and phenyl- boronic acid by Szabó and co-workers.	203
6.20	Suzuki-Miyaura coupling reaction tested using PCN and PCS pincer palladacycles.	203
6.21	Key steps in the Suzuki-Miyaura coupling catalyst activation pathway for PCN pincer palladacycles.	205
6.22	Key steps in the Suzuki-Miyaura coupling catalyst activation pathway for the PCS pincer palladacycle.	206
6.23	Ligand decoordination step post reductive elimination for 17b palla- dacycle.	208
6.24	Suzuki-Miyaura catalyst activation pathway for 17b	209
7.1	Suzuki-Miyaura coupling reaction used to compare SCN, N'CN, PCN and PCS pincer palladacycles.	225
8.1	Sulfonimine and isocyanoacetate condensation by Szabó and co-workers.	232
8.2	Tandem stannylation and allylation by Szabó and co-workers. . . .	233
8.3	Experimental hemilability probe of unsymmetrical pincer palladacycles by Wendt and co-workers.	233
8.4	Potential route to a chiral unsymmetrical N'CN pincer palladacycle. .	234

List of Tables

1.1	Selection of loss tangent, $\tan \delta$, values for various solvents, at 2.45 GHz and 20°C.	22
2.1	Quatfit analysis for PdNCN and PdSCS structures, to compare cartesian coordinates of experimentally determined and theoretically calculated structures, all numbers quoted in Å.	44
2.2	MSE_{AV} and MUE_{AV} values for bonded distances in PdNCN and PdSCS symmetrical pincer palladacycles.	47
2.3	MSE_{AV} and MUE_{AV} values for interatomic distances in PdNCN and PdSCS symmetrical pincer palladacycles.	47
3.1	Optimisation of Suzuki-Miyaura coupling shown in Scheme 3.9. . . .	63
3.2	Zero-point corrected (ΔE_0), and Gibbs free (ΔG) energies for <i>S-coordinates</i> and <i>N-coordinates</i> formation pathways to 2a	72
3.3	AIM parameters for the <i>S-coordinates</i> pathway in the formation reaction pathway of 2a (Scheme 3.14). All values given in a.u.	74
3.4	AIM parameters for the <i>N-coordinates</i> pathway in the formation reaction pathway of 2a . All values given in a.u.	75
3.5	Bader charges for the formation reaction pathway of 2a . All charges are given in a.u.	77
3.6	C-H bond activation energy barrier comparison between various symmetrical and unsymmetrical pincer palladacycles.	82

3.7	Energy of Int 1 comparison between various symmetrical and unsymmetrical pincer palladacycles	82
3.8	Solvent corrected ΔE_{0S} and ΔG_S energies for each pathway to 2a	84
3.9	Int 1 coordination energy of 1a to PdCl_2 comparison with (ΔX_S) and without (ΔX) MeCN solvent (where $X = E_0$ or G).	84
3.10	TS 1-2 C-H bond activation energy barrier comparison with and without MeCN solvent.	85
3.11	Overall formation energy with and without MeCN solvent.	85
3.12	Experimental and theoretical Pd-L bond distance comparison for 2a	87
3.13	Experimental and theoretical bond angle and dihedral comparison for 2a around the palladium centre.	88
4.1	SCN ligand synthesis yields.	109
4.2	SCN pincer palladacycle synthesis yields.	110
4.3	SCN pincer palladacycle X-ray crystal structure Pd-L bond lengths.	112
4.4	Catalyst loading investigation for Suzuki-Miyaura coupling using 2a GC conversions.	113
4.5	Suzuki-Miyaura coupling reactions of sterically hindered substrates undertaken using 2a	117
4.6	Suzuki-Miyaura coupling of 8d and 9b with SCN pincer palladacycles, symmetrical SCS palladacycle and the Herrmann-Beller palladacycle.	120
4.7	Gibbs free energies, ΔG_S , the energies including a solvent correction, for the catalyst activation pathway of SCN pincer palladacycles.	126
4.8	Gibbs free activation energy barriers (ΔG_S^\ddagger) for key steps for the SCN pincer palladacycle catalyst activation pathways.	128
4.9	Bader charge analysis of S atom in the catalyst activation pathway of SCN pincer palladacycles.	131
4.10	Bader charge analysis of Pd atom in the catalyst activation pathway of SCN pincer palladacycles.	132

4.11	SCN pincer palladacycle catalysis results, compared to overall catalyst activation pathway energy.	134
5.1	Optimisation of the Suzuki-Miyaura coupling to form biaryl ligand 12 .	153
5.2	N'CN pincer ligand synthesis yields.	154
5.3	Optimisation of palladation of 14c	156
5.4	Literature yields for palladation of NCN ligands.	156
5.5	N'CN pincer palladacycle X-ray crystal structure Pd-L bond lengths.	160
5.6	Suzuki-Miyaura coupling test using N'CN and NCN pincer palladacycles, and the Herrmann-Beller palladacycle.	161
5.7	Gibbs free energies, ΔG_S for the catalyst activation pathway of N'CN pincer palladacycles (pathway a).	166
5.8	Gibbs free activation energy barriers (ΔG_S^\ddagger) for key steps for the N'CN pincer palladacycle catalyst activation pathways.	167
5.9	Bader charges for N'CN pincer palladacycles.	169
6.1	Phosphorus containing pincer palladacycle X-ray crystal structure Pd-L bond lengths.	188
6.2	SCN pincer palladacycle X-ray crystal structure Pd-L bond lengths. .	188
6.3	N'CN pincer palladacycle X-ray crystal structure Pd-L bond lengths.	189
6.4	Pd-N _{pyr} experimental and theoretical bond lengths.	190
6.5	Novel palladacycle aldol condensation catalysis results, crude ¹ H NMR ratios, with reactions performed in duplicate.	194
6.6	Literature and known compound aldol condensation catalysis results, crude ¹ H NMR ratios, with reactions performed in duplicate.	195
6.7	Pd-L bond $\rho(\mathbf{r})$ values (a.u.) for palladacycles tested in the catalytic aldol condensation.	198
6.8	Vinyl epoxide coupling to phenylboronic acid pincer palladacycle results.	200
6.9	Vinyl epoxide coupling with phenylboronic acid other palladium catalyst results.	201

6.10	PCN and PCS pincer palladacycle Suzuki-Miyaura coupling testing. .	204
6.11	Suzuki-Miyaura coupling reactions performed using 17a to obtain % yield and analytical data.	207
6.12	Solvent corrected gibbs free energies (ΔG_S) for the Suzuki-Miyaura coupling reaction catalyst activation pathway for PCN and PCS pincer palladacycles.	210
6.13	Key energetic parameters in the Suzuki-Miyaura coupling catalyst activation pathway for PCN and PCS pincer palladacycles.	210
6.14	Bond strength $\rho(\mathbf{r})$ values for Pd-P, Pd-N _{amine} and Pd-S bonds in PCN, PCS, N'CN and SCN pincer palladacycles.	212
7.1	Summary of Suzuki-Miyaura catalysis reaction results for that shown in Scheme 7.1 for SCN, N'CN, PCN and PCS pincer palladacycles. .	226
7.2	GC conversion for reaction shown in Scheme 7.1, overall reaction energies (ΔG_s), and transmetallation barriers (ΔG_S^{iTM}) for SCN, N'CN, PCN and PCS pincer palladacycles.	228

Abbreviations

AcOH	Acetic acid
AIM	Atoms in Molecules
DCE	Dichloroethane
DCM	Dichloromethane
DFT	Density functional theory
DMAP	Dimethylaminopyridine
DMF	Dimethylformamide
EtOAc	Ethyl acetate
EtOH	Ethanol
GC	Gas-chromatography
GGA	Generalised gradient approximation
HF	Hartree-Fock theory
HRMS	High resolution mass spectrometry
IR	Infrared spectroscopy
LCAO	Linear combination of atomic orbitals
LDA	Local density approximation
LSDA	Local spin density approximation
MeCN	Acetonitrile
MSE	Mean signed error
MUE	Mean unsigned error
mGGA	Meta generalised gradient approximation
MP2	Møller-Plesset perturbation theory, 2nd order
MW	Microwave

NMR	Nuclear magnetic resonance spectroscopy
PCM	Polarisable continuum model
RMS	Route mean square error
SMD	Solvation model based on density
rt	Room temperature
TBAB	Tert-butyl ammonium bromide
THF	Tetrahydrofuran
TLC	Thin layer chromatography
Tol	Toluene

Chapter 1

Introduction

This chapter provides an introduction to symmetrical and unsymmetrical pincer palladacycles, the concept of hemilability, and the various applications of palladacycles in catalysis. The chapter also discusses the importance of pincer ligands with other metals, and details on microwave assisted organic synthesis. All of these details will be addressed in various chapters throughout this thesis. A thesis overview will also be provided.

1.1 Palladacycle history

The first examples of palladacycles were demonstrated by Cope and Siekman in 1965,¹ with the structures depicted in Figure 1.1. The presence of the Pd-C bond was confirmed by reaction with LiAlD_4 and detection of the resultant deuterated ligand by mass spectrometry. These palladacycles are dimeric, to maintain the four coordinate square planar palladium geometry, and can be abbreviated as shown in Figure 1.2.

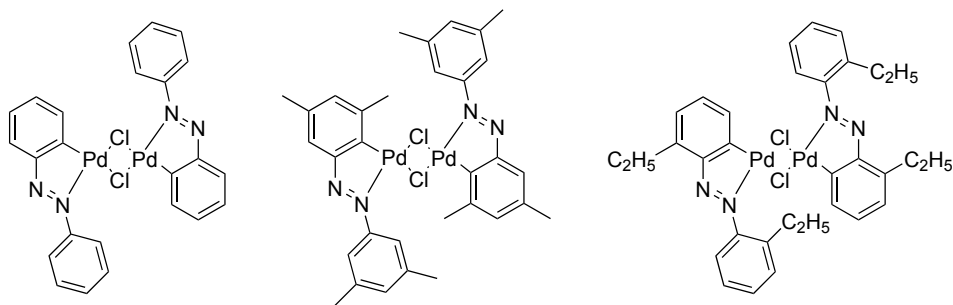


Figure 1.1 Original Cope and Siekman palladacycles.

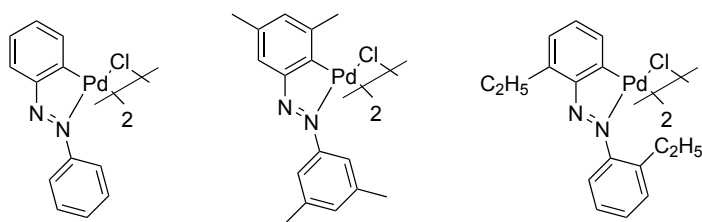


Figure 1.2 Abbreviation of Cope and Siekman palladacycles.

The scope of the new Pd-C bond was expanded by Cope and Friedrich from azo compounds to amines, forming N,N-dimethylbenzylamine palladacycles such as that presented in Figure 1.3.²

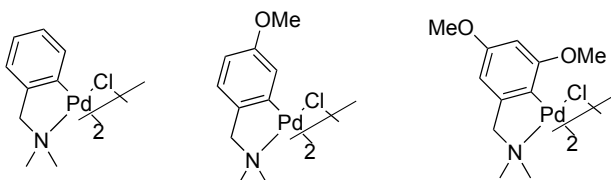


Figure 1.3 N,N-dimethylbenzylamine palladacycles by Cope and Friedrich.

A wide variety of palladacycles have henceforth been reported, including examples with more than one carbon atom bound to the same palladium atom (left, Figure 1.4),³ with aliphatic Pd-C bonds (centre, Figure 1.4),⁴ and the elaborate 9-membered palladacycle formed by phenylacetylene insertion into the Pd-C bond of Cope and Friedrich's N,N-dimethylbenzylamine palladacycle (right, Figure 1.4).⁵

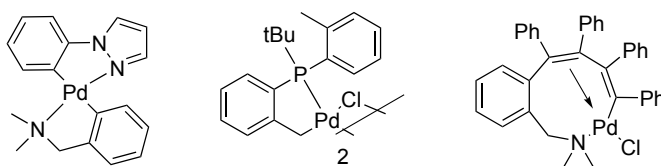


Figure 1.4 Further examples of palladacycles.

Another major development in the field of palladacycle chemistry was the first pincer palladacycle by Shaw and Moulton (Figure 1.5),⁶ whereby two donor atoms coordinate to the palladium in a chelating motif, forming a remarkably stable compound up to 240 °C in air without degradation.

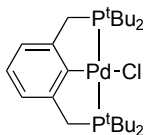


Figure 1.5 First pincer palladacycle by Shaw and Moulton.

1.2 Classification of palladacycles

Palladacycles normally are formed from either donors of the CY type (with C representing the metalated carbon, and Y the donor atom), or donors of the YCY type (Figure 1.6). For the CY ligands, to maintain a 16 electron palladium centre, dimers are formed, and two different isomers are possible, the cisoid, or the transoid configuration (Figure 1.7).

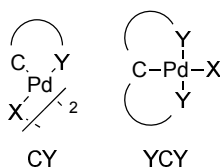


Figure 1.6 CY and YCY palladacycle classification for donor ligands.

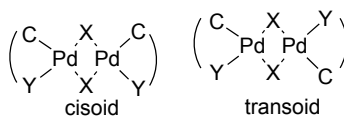


Figure 1.7 Cisoid or transoid dimeric palladacycles.

1.2.1 CY palladacycles

There are a plethora of examples of the CY type (Figure 1.6), ranging from the first palladacycle by Cope and Siekman,¹ and can exist as monomeric palladacycles with coordinating groups such as pyridine, or as cationic, or anionic palladacycles (Figure 1.8).⁷

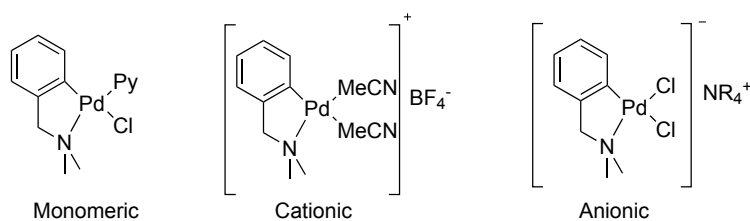


Figure 1.8 Monomeric, cationic, and anionic palladacycles.

1.2.2 Symmetrical YCY pincer palladacycles

YCY pincer palladacycles are now widely reported, with SCS examples such as in Figure 1.9,⁸ NCN examples such as in Figure 1.10,⁹ PCP examples such as in Figure 1.11¹⁰ and also SeCSe examples in Figure 1.12.¹¹

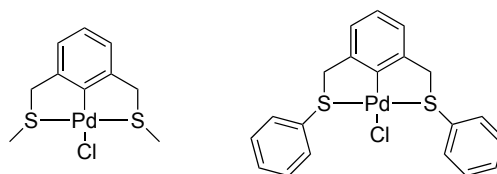


Figure 1.9 Symmetrical SCS pincer palladacycles.

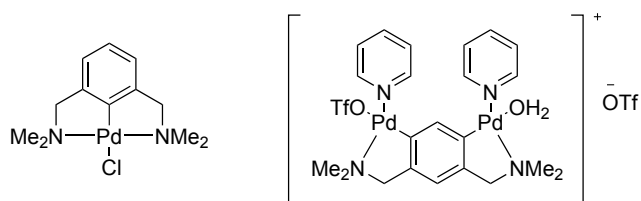


Figure 1.10 Symmetrical NCN pincer palladacycles.

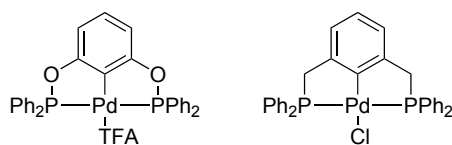


Figure 1.11 Symmetrical PCP pincer palladacycles.

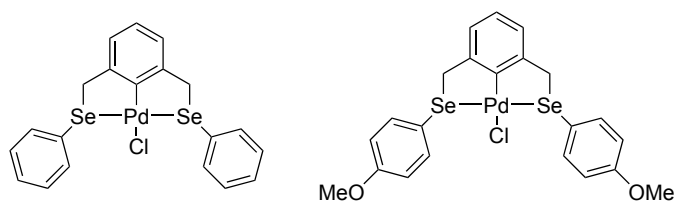
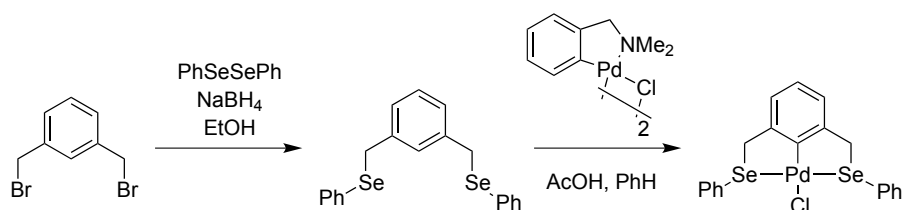


Figure 1.12 Symmetrical SeCSe pincer palladacycles.

The majority of pincer palladacycles are symmetrical, due to their ease of synthesis. For example, a simple route to the palladacycles discussed above is from 1,3-bis(bromomethyl)benzene, which readily undergoes nucleophilic displacement by nucleophilic donor atoms, such as in Scheme 1.1, followed by transcyclopalladation shown by Yao *et al.*¹²



Scheme 1.1 Symmetrical SeCSe pincer palladacycle synthesis demonstrated by Yao *et al.*

1.2.3 Unsymmetrical YCY' pincer palladacycles

Unsymmetrical pincer palladacycles, YCY' where Y and Y' groups are not equal, are much less commonly studied mainly due to their more difficult synthesis, as compared to the 1,3-bis(bromomethyl)benzene route shown in Scheme 1.1. For example, Szabó and co-workers synthesised unsymmetrical PCS pincer palladacycles from the same 1,3-bis(bromomethyl)benzene starting material, however the synthesis was not chemoselective, resulting in mixtures of intermediates, and an overall yield of 38 %.¹³

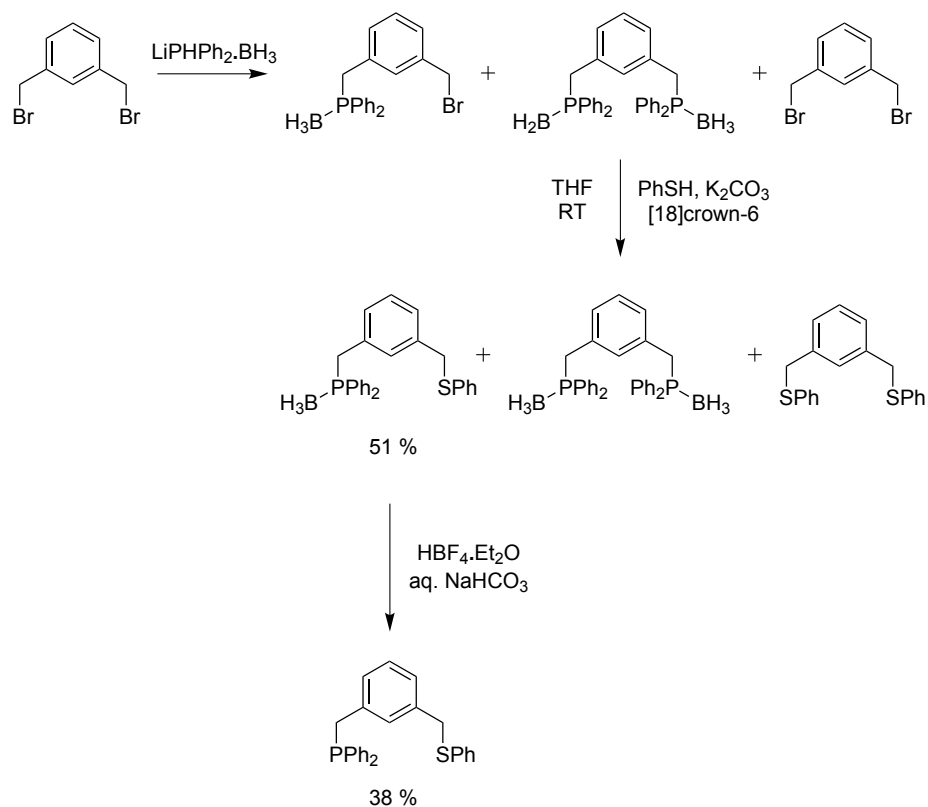


Figure 1.13 Synthesis of an unsymmetrical PCS ligand from 1,3-bis(bromomethyl)benzene by Szabó and co-workers.

The number of unsymmetrical pincer palladacycles is increasing, with many based on the same ligand architecture as the example shown in Figure 1.13. Wendt and co-workers¹⁴ synthesised an unsymmetrical PCN pincer palladacycle from 3-methylbenzoate to circumvent the issue of chemoselectivity when starting from 1,3-bis(bromomethyl)benzene (left, Figure 1.14). The Wendt example is an unsymmetrical pincer palladacycle with different donor atoms, however other unsymmetrical pincer palladacycles include unsymmetrical N'CN examples, where despite both being nitrogen donor atoms, they are in different chemical environments. For example, work by Song and co-workers¹⁵ provided an unsymmetrical N'CN pincer palladacycle (centre, Figure 1.14) from benzene-1,3-dicarboxaldehyde followed by mono bromination to yield the unsymmetrical ligand backbone. Another example reported includes a NCS pincer palladacycle (right, Figure 1.14) synthesised from 3-bromobenzaldehyde by Odinet and co-workers.¹⁶ These show the variety of methods used to desymmetrise palladacycles based on the same design as that synthesised

from 1,3-bis(bromomethyl)benzene.

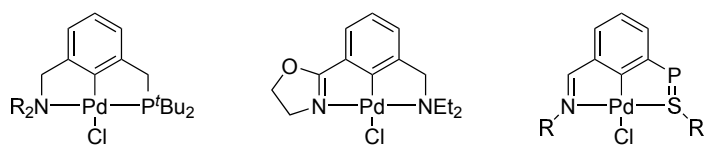


Figure 1.14 Unsymmetrical pincer palladacycles.

Another interesting route to unsymmetrical pincer palladacycles was reported by Dupont and co-workers,¹⁷ yielding palladacycles with very different backbones to that shown previously, resulting from *trans*-chloropalladation of alkynes. This also provided an example of a palladacycle with a pyridine donor ligand to palladium.

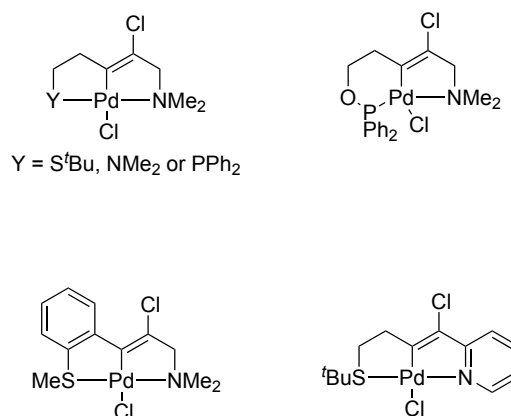


Figure 1.15 Unsymmetrical pincer palladacycles synthesised *via trans*-chloropalladation by Dupont and co-workers.

1.2.4 Pyridine containing palladacycles

A number of pyridine based palladacycles have been reported, including by Callear *et al.* based on 2-(thiophen-2-yl)pyridine (top left, Figure 1.16);¹⁸ other examples synthesised by chloropalladation have been reported by Dupont and co-workers (top centre and right, Figure 1.16);¹⁹ an example bound to a polyoxometalate by Thorimbert and co-workers (bottom left, Figure 1.16);²⁰ and other examples by Solan and co-workers (bottom centre, Figure 1.16)²¹ and Cárdenas *et al.* (bottom right, Figure 1.16).²²

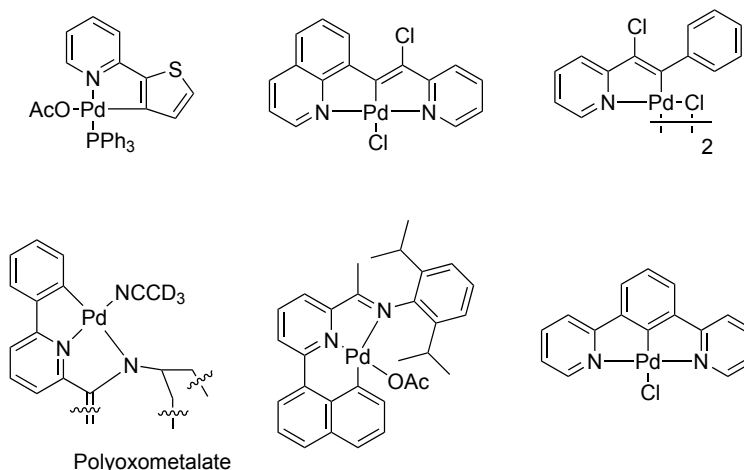
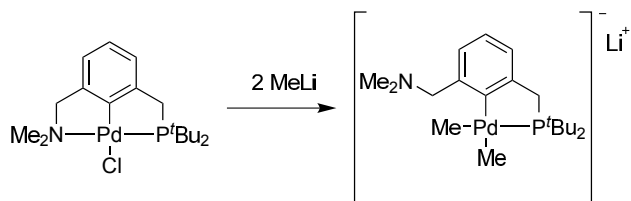


Figure 1.16 Pyridine containing palladacycles.

1.3 Hemilability

An advantage of unsymmetrical palladacycles is the opportunity to fine tune the steric and electronic properties of the donor atoms. For example, it is possible to modify the properties using a number of options, including substituents on the donor atoms, giving the ability to alter the hard/soft properties of the Lewis base; the ability to alter ring sizes to change the steric properties at the palladium centre, with mixed ring sizes; and also alter the donor atom substituents to vary the steric properties of the palladacycle.²³

The potential for hemilability^{24–26} has been widely discussed as an advantage for the design of new unsymmetrical pincer palladacycles. Hemilability is the combining of different physical and chemical properties of donor ligands possible in unsymmetrical, or hybrid, pincer ligands, resulting in preferential decoordination of one of the ligand arms. This has been discussed on numerous occasions for unsymmetrical pincer palladacycles: an excellent example by Wendt and co-workers investigated the potential hemilability of phosphorus and nitrogen donor ligands, by exposing the palladacycle to weak and strong nucleophiles, showing that a strong nucleophile (MeLi) can substitute the amine donor arm, whilst leaving the phosphorus donor arm still coordinated, demonstrating the different palladium donor atom interactions (Scheme 1.2).¹⁴



Scheme 1.2 Hemilability investigation by Wendt and co-workers.

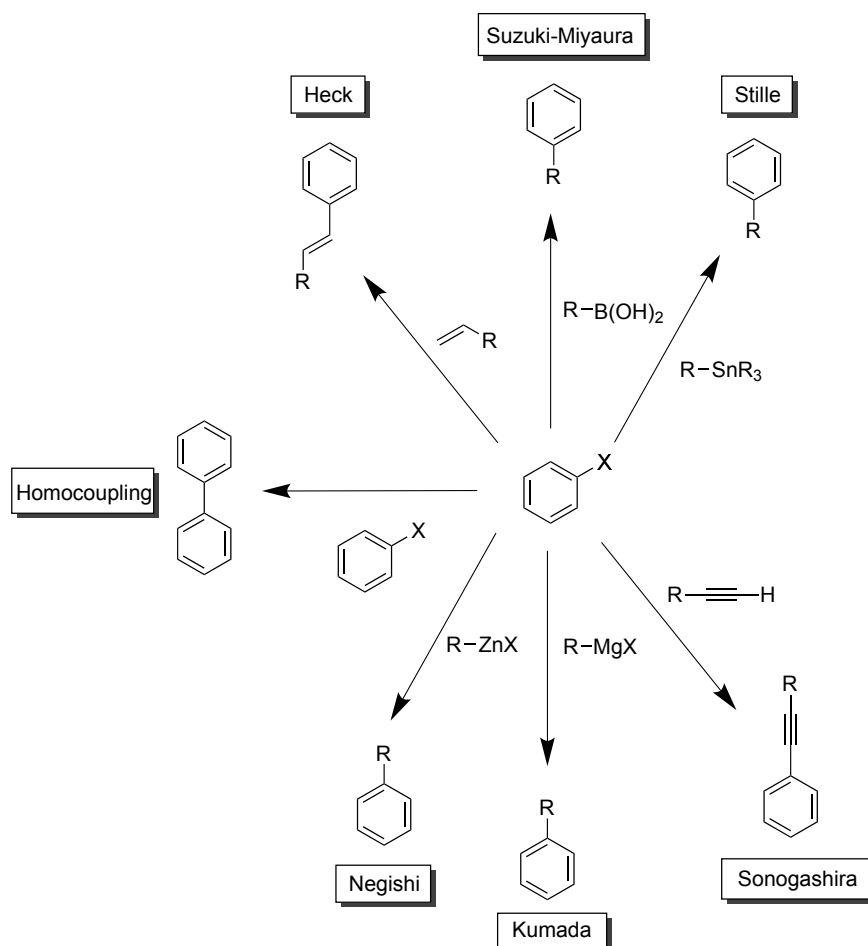
Catalytic investigations using a CNS pincer palladacycle discuss the likely hemilabile effect of thioether ligand decooordination to generate catalytic sites by Grévy and co-workers;²⁷ the potential hemilabile effect of Pd-C bonds were also investigated for a NC pincer palladacycle by Sarker and co-workers²⁸ evidenced by interconversion of two isomers resulting in enantiomeric structures, suggesting the hemilability of the Pd-C bond. Hemilability has also been investigated for a variety of other pincer complexes, including unsymmetrical platinum pincer PCN complexes, where it was found by Milstein and co-workers²⁹ that amine arm lengths, either forming 5 or 6 membered rings have significant hemilabile effects, and similarly for PNS ruthenium complexes by the same group.³⁰

Clearly the potential for hemilability, and different propensity for palladium donor atom decooordination provide the desire to synthesise a range of unsymmetrical pincer ligands to attempt to exploit this effect in catalysis.

1.4 Applications of palladacycles

Palladacycles have found application in a plethora of cases, ranging from common C-C, C-N or C-X bond formation, C-H bond activation processes, to exploiting luminescence properties.³¹ Since the first reported use of palladacycles in catalytic C-C bond coupling in the Suzuki-Miyaura³² (discussed in more detail in Section 4.1.2) and Heck reactions,³³ by Herrmann, Beller and co-workers, the application of palladacycles in other bond formation reactions have been studied. In addition to the numerous examples of application of palladacycles in the Suzuki-Miyaura coupling between boronic acids and organic halides,^{15,27,34–42} and the Heck coupling between alkenes and organic halides;^{12,43–47} examples include the coupling of organic

halides in the Sonogashira coupling with terminal alkynes,^{47–50} the Stille coupling with organotin reagents,^{50–52} the Kumada coupling with Grignard reagents,⁵¹ the Negishi coupling with organic zinc,⁵³ and the homocoupling of organic halides.^{50,54} A general summary of coupling reactions performed using a number of palladacycles is provided in Scheme 1.3.

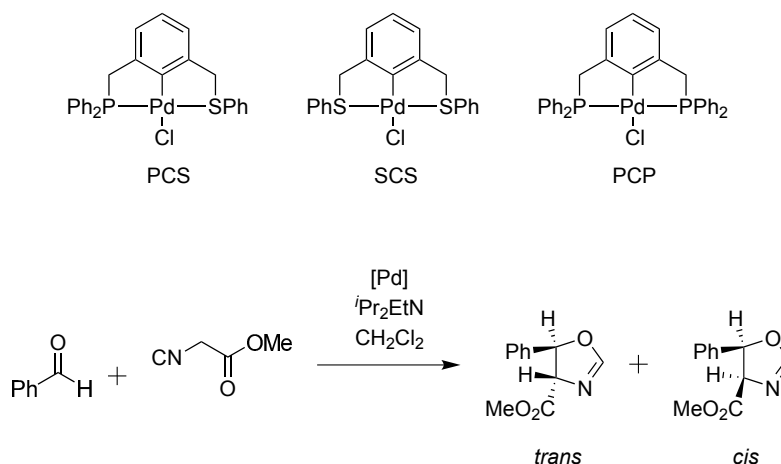


Scheme 1.3 Cross coupling reactions performed using palladacycles.

The Pd(II)/Pd(0) coupling reactions discussed above result in the degradation of the palladacycle backbone and formation of Pd(0) species, resulting in the inability for enantioselective processes. Examples discussed below occur via a Pd(II)/Pd(II) mechanism with retention of the palladacycle structure, allowing the possibility of enantioselective transformations.

Palladacycles also have received application in other types of C-C bond formation, for example in aldol and Michael reactions.^{7,55–58} A particularly interesting example

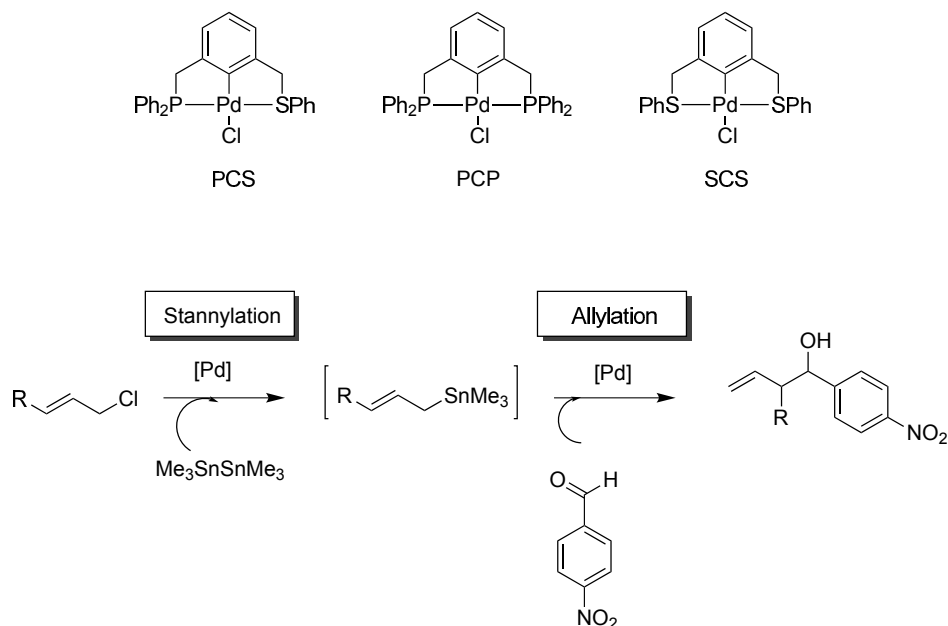
of aldol condensations was reported by Szabó and co-workers¹³ which generated interesting results exhibiting differences between symmetrical and unsymmetrical pincer palladacycles. The aldol condensation studied is shown in Scheme 1.4 with the palladium SCS, PCP or PCS pincer catalysts. It was found that the turnover frequency (TOF) was highest for the PCS palladacycle (75) compared to the SCS (46) and the PCP (17), however different *cis* to *trans* ratios were found for each catalyst, with the PCS and SCS examples achieving approximately $\approx 60\%$ *trans*, whereas the PCP example gave 82% of the *trans* product. It was found that the PCS and SCS acted as precatalysts in this reaction, whereas the PCP example was the real catalyst. This was attributed to the weaker Pd-S bond, allowing Pd-S bond decoordination, an example of hemilability, followed by coordination of the isocyanide, resulting in the faster reaction (higher TOF) as the reaction proceeds *via* a different mechanism. This provides interesting evidence that combining the different ligand effects in the same molecule is a desirable strategy. The same aldol condensation has been studied using a dendritic bound symmetrical NCN pincer palladacycle,⁵⁹ and other examples of aldol condensations also been studied using palladacycles.^{58,60–62}



Scheme 1.4 Aldol condensation investigation by symmetrical, SCS and PCP, and unsymmetrical PCS pincer palladacycles by Szabó and co-workers.

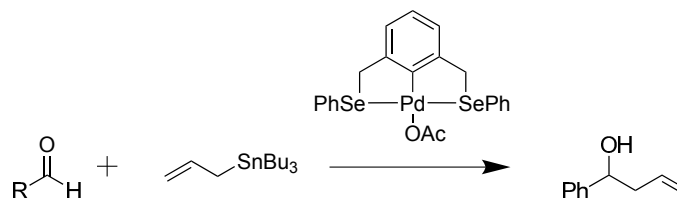
In the same paper by Szabó and co-workers,¹³ the palladacycles were tested in the tandem catalytic approach of stannylation of allyl chlorides, followed by allylation of aldehydes or imines. This is exemplified in Scheme 1.5 and differences were found between the symmetrical and unsymmetrical pincer palladacycles. The symmetrical

PCP pincer was inefficient in the stannylation reaction, whereas performed well in the allylation reaction, though the PCS example performed well in both reactions, taking advantage of the π -acceptor characteristics of the P atom, and the σ -donation capability of the S ligand.

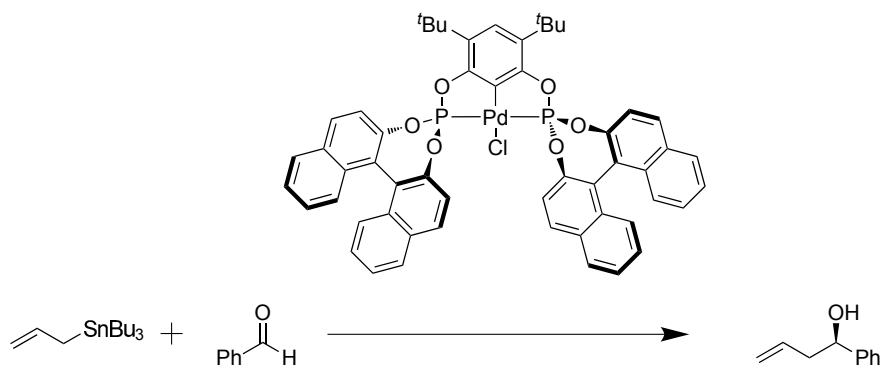


Scheme 1.5 Tandem stannylation and allylation by Szabó and co-workers.

Included in the tandem catalysis by Szabó and co-workers (Scheme 1.5)¹³ is the interesting allylation of aldehydes and imines.⁵⁵ This reaction is another important C-C bond coupling reaction. Other examples of allylation of aldehydes and imines were performed by other groups include those by Yao and Sheets, using a SePdSe palladacycle (Scheme 1.6);⁶³ and enantioselective versions using a chiral BINOL-based palladacycle by Bedford and co-workers (Scheme 1.7).⁶⁴

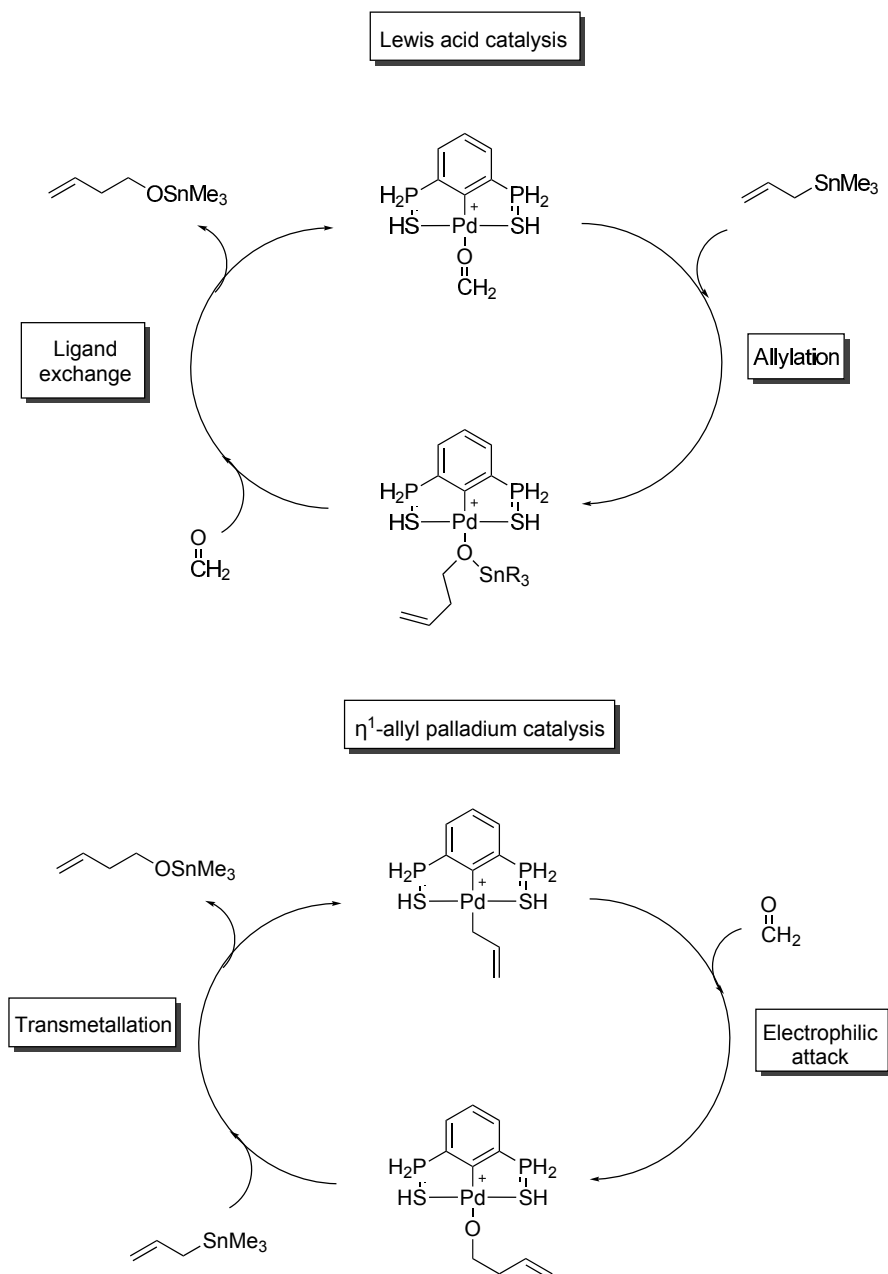


Scheme 1.6 Catalytic allylation of aldehydes using a SePdSe pincer palladacycle by Yao and Sheets.



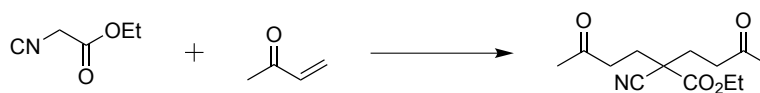
Scheme 1.7 Enantioselective catalytic allylation reaction catalysed by a BINOL-based palladacycle by Bedford and co-workers.

An interesting mechanistic investigation has been performed by Le Floch and co-workers using DFT into potential mechanisms for palladacycle catalysis where they act as a Lewis acid, and by η^1 -allyl palladium allyl complexes for palladacycle catalysed allylation reactions (Scheme 1.8), revealing that the Lewis-acid catalysis pathway is favoured ($\Delta G^\ddagger = 15.6 \text{ kJ mol}^{-1}$) over the allyl palladium pathway ($\Delta G^\ddagger = 22.6 \text{ kJ mol}^{-1}$). The B3PW91 functional was used with a 6-31+G(d) basis set for all atoms other than palladium, and the SDD effective core potential for palladium.⁶⁵



Scheme 1.8 Investigation into possible mechanisms for allyltin allylation by Le Floch and co-workers.

Michael additions catalysed by a palladacycle were reported by Richards and co-workers for the reaction between α -cyanocarboxylates and methyl vinyl ketone, with the palladacycle acting as a Lewis acid catalyst (Scheme 1.9),⁶⁰ and examples have been reported by a number of other groups.^{66–68}



Scheme 1.9 Michael addition by Richards and co-workers.

Another application of palladacycles are to undertake catalytic C-H bond activation, via *in situ* generated palladacycles, along with oxidising iodonium salts. The direct coupling of an aryl group with a C-H bond to form C-C bonds is a desirable route, as the use of other reagents such as boronic acids are not required, as in the case of the Suzuki-Miyaura coupling reaction.³¹

An example of this is shown in Figure 1.17 using $\text{Pd}(\text{OAc})_2$ to catalytically arylate benzodiazepine based systems, forming *in situ* generated palladacycles bound to the nitrogen of the imine functional group.⁶⁹ This work has further been expanded to synthesise a range of these arylated examples.⁷⁰

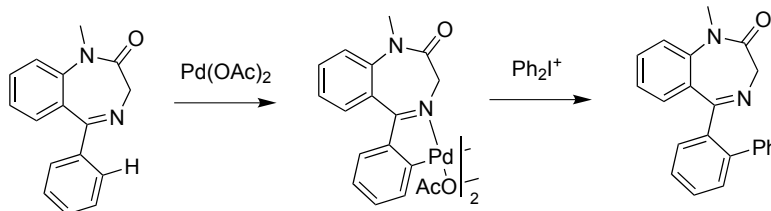
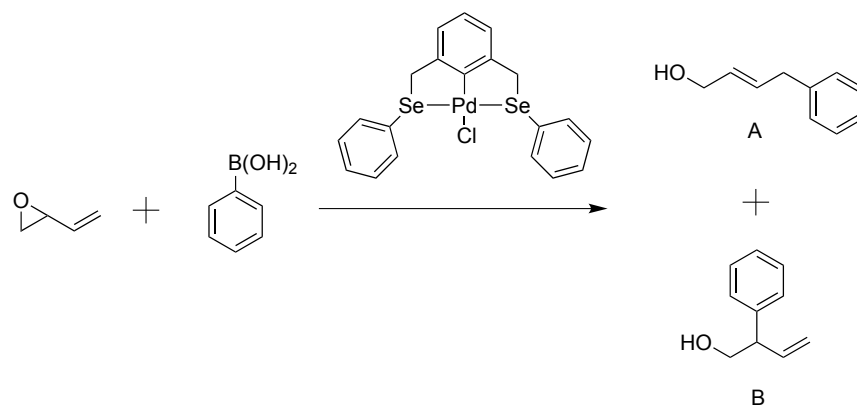
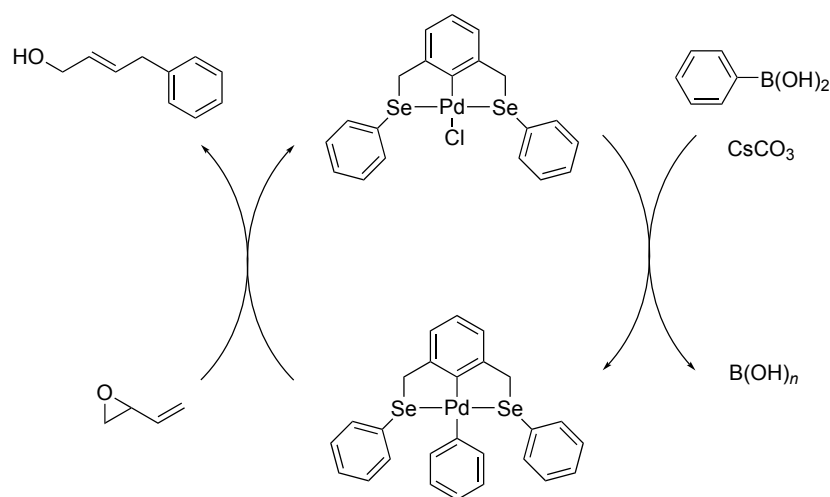


Figure 1.17 Catalytic C-H bond activation *via* palladacycles by Spencer *et al.*

A further application of pincer palladacycles in catalysis is in the catalytic cross coupling of vinyl epoxides and aziridines with boronic acids by Szabó and co-workers.⁷¹ These redox free reactions occur with palladium remaining in the +2 oxidation state. An example of a coupling reaction with a symmetrical SeCSe pincer palladacycle is shown (Scheme 1.10) and it was found however the ratio of products A to B gave product A in a substantial majority (11:1). This was significantly different than when $[\text{Pd}_2(\text{dba})_3]$ was used as the catalyst (A:B 7:3). A catalytic cycle was proposed (Scheme 1.11) suggesting that the palladium retains its structure and remains in the +2 oxidation state.

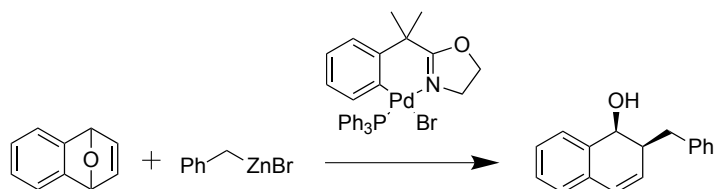


Scheme 1.10 Pincer palladacycle catalysed vinyl epoxide coupling with phenyl boronic acid by Szabó and co-workers.



Scheme 1.11 Proposed catalytic cycle for vinyl epoxide coupling to phenylboronic acid by Szabó and co-workers.

Another example of palladacycle catalysis where the palladacycle retains its ligated structure, rather than being reduced to Pd(0), was reported by Hou and co-workers in their catalytic ring opening study of oxabicyclic alkenes with organozinc halides.⁷² The reaction performed is shown in Scheme 1.12, and was found to proceed in 95 % yield. The reaction was monitored using ³¹P NMR to provide evidence of retaining the palladacycle structure.



Scheme 1.12 Palladacycle catalysed ring opening of oxabicyclic alkenes with organozinc halides by Hou and co-workers.

1.5 Pincer ligands with other metals

The use of pincer ligands has been discussed with palladium, however pincer ligands are also widely used with a number of other metals.⁷³ Many symmetrical examples are reported (with either N or C central donor atoms), including Ir PNP pincers by Milstein and co-workers (left, Figure 1.18),⁷⁴ and Li and co-workers (centre, Figure 1.18),⁷⁵ and Ir PCP pincers by Krogh-Jespersen *et al.* (right, Figure 1.18).⁷⁶

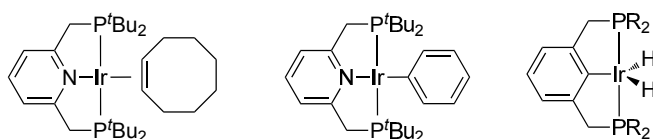


Figure 1.18 Ir containing symmetrical phosphorus pincers.

Ruthenium pincer complexes have also been reported, with examples by Milstein and co-workers, such as the unsymmetrical PNS pincer (left, Figure 1.19),³⁰ and PNN' pincers (centre and right, Figure 1.19).⁷⁷

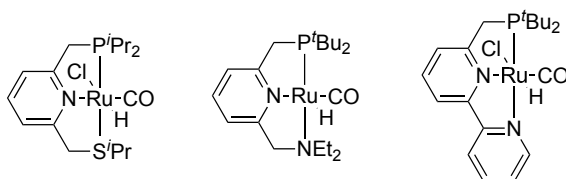


Figure 1.19 Milstein and co-workers' ruthenium containing pincer complexes.

A number of other metals have been used, including symmetrical NCN pincers by van Koten and co-workers, with Ni (left, Figure 1.20);⁷⁸ and Sn (centre, Figure 1.20);⁷⁹ unsymmetrical PCN platinum pincers have also been reported by Milstein and co-workers (right, Figure 1.20).⁸⁰

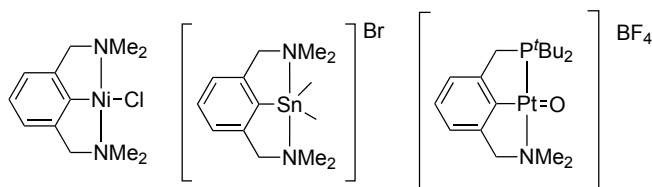


Figure 1.20 Metal pincer complexes of Ni, Sn and Pt.

Another interesting case of using other metals is in dimetallic pincer complexes, with a pincer palladacycle bound to a ruthenium atom by Klein-Gebbink and co-workers. Both unsymmetrical,⁸¹ and symmetrical pincer palladacycles (Figure 1.21) are reported.⁸² These bimetallic complexes are synthesised by treating the unsymmetrical pincer palladacycles with $[\text{Ru}(\text{C}_5\text{H}_5)(\text{MeCN})_3]\text{PF}_6$ or $[\text{Ru}(\text{C}_5\text{Me}_5)(\text{MeCN})_3]\text{BF}_4$ in dichloromethane. It was found that the symmetrical examples were effective catalysts for the coupling between *trans*-phenylvinylboronic acid and vinyl epoxide.⁸²

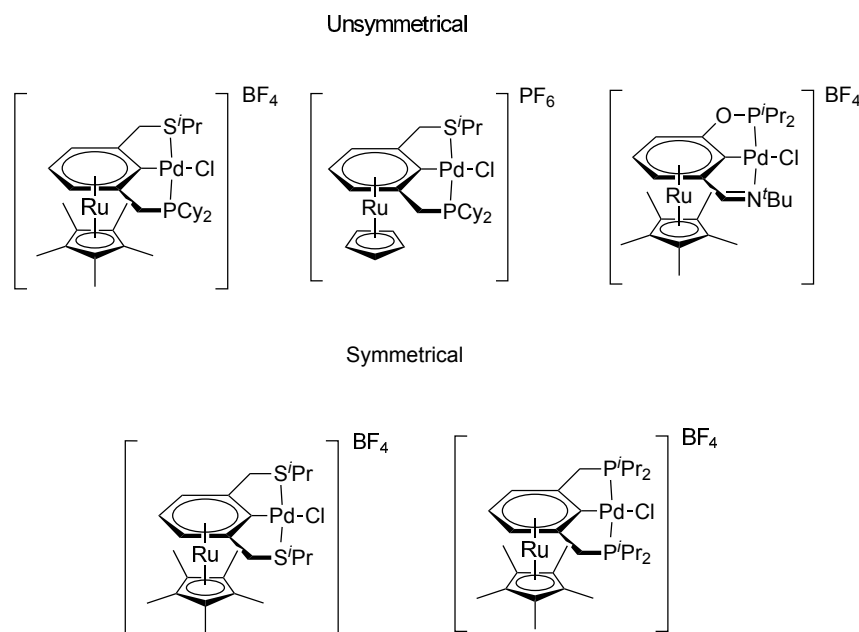


Figure 1.21 Bimetallic pincer ruthenium palladium complexes by Klein Gebbink and co-workers.

Another family of pincer ligands are the trianionic ligands, and these have been recently reviewed by Veige and O'Reilly,⁸³ with reports included by Veige and co-workers on symmetrical trianionic NCN pincer ligand coordinated to hafnium (left, Figure 1.22),⁸⁴ chromium (centre, Figure 1.22),⁸⁵ and a uranium example by Gambarotta and co-workers (right, Figure 1.22).⁸⁶

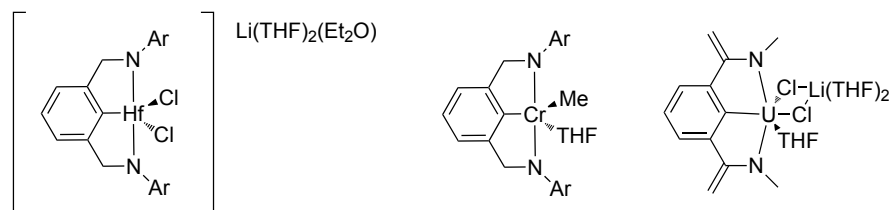


Figure 1.22 Trianionic symmetrical NCN pincer complexes with hafnium, chromium and uranium.

1.6 Microwave assisted organic synthesis

The use of microwave radiation in organic synthesis originated in the 1980s,^{87,88} and it was found to drastically reduce reaction times and provide fewer side reactions. The use of microwaves in organic chemistry is now widespread, with numerous reviews covering the thousands of reported examples.^{89–91}

One of the main advantages of using microwave irradiation is that a uniform temperature is achieved during the reaction, eliminating hot spots which can cause side reactions. This is exemplified in Figure 1.23 by Kappe and co-workers,⁹² where traditional heating heats the walls of the vessel, and the centre of the vessel is only heated by convection currents and efficient stirring, causing a temperature gradient; whereas microwave irradiation causes a more constant temperature, by heating the whole solution.⁹³

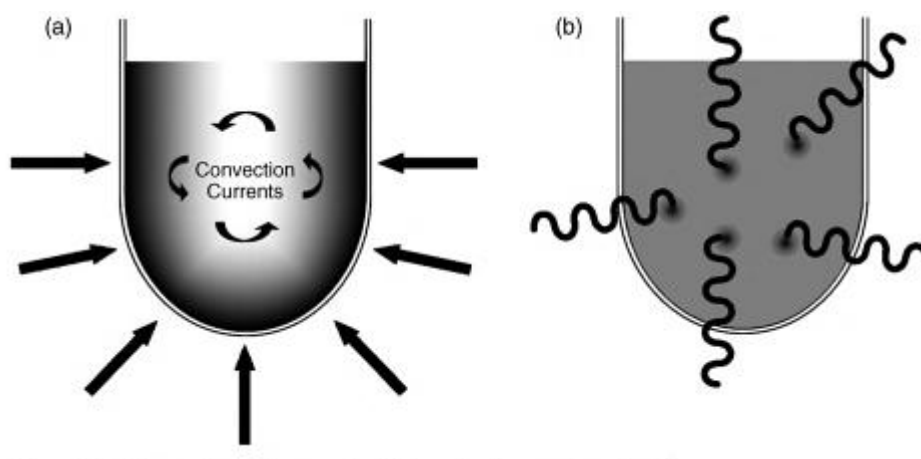


Figure 1.23 Temperature gradients in a vessel heated by traditional heating (left), and microwave irradiation (right), taken from Kappe and co-workers.

The explanation for this difference in temperature gradient is due to the mode of

heating: in the traditional heating method, the heating of the solution occurs via conduction from the vessel walls, causing a higher temperature at the vessel wall, as compared to the centre. In microwave irradiation, the heating occurs via radiation with a frequency of approximately 2.45 GHz⁹⁰ which causes molecules with dipole moments to rotate *via* the dipolar polarisation mechanism. Ions in the solution are heated *via* the conduction mechanism by moving with the applied electric field.^{94,95} The motion caused by these two modes cause the solution to heat, generating the energy for chemical reactions. Therefore for effective microwave heating, polar molecules and/or ions are required as the solvent or solute to heat the reaction.

The ability of solvents or solutes to efficiently heat the reaction at specific temperatures is measured by its loss tangent, $\tan \delta$. A large value of $\tan \delta$ suggests lots of microwave energy is transferred to the molecules, providing effective microwave heating, as evident in highly polar solvents such as ethanol or DMSO, whereas smaller $\tan \delta$ values for non-polar solvents suggest poor solvents for microwave heating, such as hexane or toluene. The microwave vessels made of glass also have very small $\tan \delta$ meaning all of the microwave energy is used to heat the solution, rather than the reaction vessel, minimising temperature gradients. A number of $\tan \delta$ values at 2.45 GHz and at 20 °C is provided in Table 1.1.⁹⁰

Table 1.1 Selection of loss tangent, $\tan \delta$, values for various solvents, at 2.45 GHz and 20 °C.

Solvent	$\tan \delta$
Ethylene glycol	1.350
Ethanol	0.941
DMSO	0.825
Methanol	0.659
Acetic acid	0.174
DMF	0.161
Water	0.123
Chloroform	0.091
Acetonitrile	0.062
THF	0.047
DCM	0.042
Toluene	0.040
Hexane	0.020

1.7 Thesis overview

Due to the increasing interest in unsymmetrical pincer ligands in the formation of palladacycles and involving metals other than palladium, this thesis presents a new synthetic route towards unsymmetrical SCN, N'CN, PCN and PCS pincer ligands, with late stage diversification allowing facile library generation. These unsymmetrical pincer ligands provide the potential for hemilability, combining the different Lewis basicities of sulphur, nitrogen and phosphorus with palladium. These pincer ligands were selected to undergo C-H bond activation to synthesise the family of unsymmetrical pincer palladacycles.

Due to the plethora of examples reported for application of palladacycles in C-C bond coupling reactions, this allows a useful benchmark to study their catalytic activity compared to similar reported examples. Therefore the palladacycles are tested in the Suzuki-Miyaura coupling reaction, revealing differences in their catalytic activity. The underlying chemical and physical properties of these ligands and palladacycles are investigated using density functional theory in order to rationalise the varying catalytic activity.

The ligands and palladacycles synthesised may find additional applications in some of the areas discussed in this chapter such as other catalytic applications, or formation of bimetallic complexes. The ligands could also be used for ligation to different metal centres to take advantage of different catalytic applications.

Chapter 2 provides theoretical details of the density functional theory calculations presented in this thesis, along with a method validation study to determine an appropriate computational methodology. This work has been published in Dalton Transactions.⁹⁶ A new synthetic route to an SCN pincer palladacycle and a density functional theory investigation into a possible formation reaction pathway is presented in Chapter 3. This work has been published in Royal Society Open Science.⁹⁷ This synthesis is expanded to a family of SCN pincer palladacycles, along with a catalytic investigation in the Suzuki-Miyaura reaction, and a density functional theory investigation into the catalyst activation pathway is presented in Chapter 4.

A manuscript is in preparation of this work. Chapter 5 studies a modified synthetic route to N'CN unsymmetrical pincer palladacycles and the Suzuki-Miyaura coupling and catalyst activation pathway is studied. This manuscript is also in preparation. In Chapter 6 the studies are expanded to PCN and PCS pincer palladacycles. Finally Chapter 7 provides an analysis and comparison of the SCN, N'CN, PCN and PCS pincer palladacycles in catalysis, and the rationalisation of their catalytic activity provided by the density functional theory calculations.

Chapter 2

Theoretical details and a computational method validation study

This chapter describes the theoretical background to the computational results presented in this thesis, including density functional theory (DFT), basis sets, and Atoms in Molecules analysis. Several DFT computational methodologies are tested, and analysis undertaken to ascertain the optimum methodology for the accurate prediction of experimental X-ray crystal structures for symmetrical pincer palladacycles. This is undertaken by studying the cartesian coordinates of experimental and calculated structures obtained for a number of computational methodologies by using the Quatfit program, and by comparing all bonded, and interatomic distances. This analysis has been published in Dalton Transactions.⁹⁶

2.1 Density functional theory (DFT)

2.1.1 Introduction

Density functional theory is a computational methodology which can be used to investigate a number of properties of molecules, such as geometries, energies, electron

density, and spectral data such as IR/Raman and NMR. Compared to traditional wavefunction based methods, such as Hartree-Fock theory (HF) and Möller-Plesset perturbation theory (MP2), DFT provides the opportunity to accurately predict the properties mentioned above at much lower computational cost.

The theory behind DFT, devised by Hohenberg and Kohn,⁹⁸ is that there is a one-to-one relation between the ground state energy of a molecule and its electron density, ρ , a physical observable (as compared to the wavefunction used in wavefunction based methods, which is not a physical observable). The energy as a functional of the electron density (2.1) contains several terms: the kinetic energy ($T[\rho]$); the potential energy between the nuclei and electrons ($E_{ne}[\rho]$); and the electron-electron repulsion ($E_{ee}[\rho]$).^{99,100}

$$E[\rho] = T[\rho] + E_{ne}[\rho] + E_{ee}[\rho] \quad (2.1)$$

The electron-electron repulsion ($E_{ee}[\rho]$) is composed of classical coulomb repulsion ($J[\rho]$) and the exchange term ($K[\rho]$), giving (2.2). The exchange term arises due to the non-classical antisymmetry principle. The problem with this formalism is that, although exact in principle, the kinetic energy, $T[\rho]$, is poorly treated using a simple analytical formula, yielding unsatisfactory results.

$$E[\rho] = T[\rho] + E_{ne}[\rho] + J[\rho] + K[\rho] \quad (2.2)$$

Developments by Kohn and Sham,¹⁰¹ altered the way this troublesome kinetic energy was treated. They hypothesised that the kinetic energy could be split into two different terms, one of which could be solved by introducing one-electron orbitals, termed $T_s[\rho]$, and the remaining unknown part included along with the exchange term $K[\rho]$ in the exchange correlation term, $E_{XC}[\rho]$, represented in (2.3).¹⁰²

$$E_{XC}[\rho] = (T[\rho] - T_s[\rho]) + (E_{ee}[\rho] - J[\rho]) \quad (2.3)$$

Up until this point, unlike in wavefunction based methods, orbitals were not used

in DFT, however to calculate $T_S[\rho]$ Kohn and Sham proposed the use of orbitals to solve this term exactly, giving (2.4).

$$\rho(r) = \sum_{i=1}^N |\psi_i(r)|^2 \quad (2.4)$$

The inclusion of these Kohn-Sham orbitals gives rise to the Kohn-Sham equation (2.5),⁹⁹ with $V_{XC}[\rho]$ the exchange-correlation potential, which is the functional derivative of the exchange-correlation energy. In this equation everything other than $V_{XC}(r_1)$ can be evaluated, which remains unknown.

$$\left\{ -\frac{\hbar^2}{2m_e} \nabla_1^2 - \sum_{j=1}^N \frac{Z_j e^2}{4\pi\epsilon_0 r_{j1}} + \int \frac{\rho(r_2) e^2}{4\pi\epsilon_0 r_{12}} dr_2 + V_{XC}(r_1) \right\} \psi_i(r_1) = \epsilon_i \psi_i(r_1) \quad (2.5)$$

The exchange correlation term is composed of the non-classical exchange energy; the dynamic correlation energies arising from electron-electron interactions; and kinetic energy not included when calculating assuming non-interacting electrons.^{100,103}

The choice of density functional method used (how $V_{XC}(r_1)$ is treated) is imperative to get the most accurate results for a particular type of system. However, as there is no systematic way to improve the quality of exchange correlation density functionals, method validation is crucial to check the validity of the results obtained from the chosen method.

2.1.2 Exchange correlation functionals

Local, and spin, density approximation

The Local Density Approximation (LDA), the simplest form of the exchange correlation functional, is derived from a uniform homogeneous electron gas, and does not take into account electron spin. The approximation is that the electron density is evenly distributed throughout space, which is not ideal as electron density is more likely to be found around nuclei.

The LDA method uses the E_X^{LDA} exchange functional, which can be written as

(2.6),¹⁰⁴ dependent only on the electron density, ρ , with C a constant, (2.7) and is termed slater exchange. This LDA exchange functional forms the basis of many other density functionals, albeit with the addition of extra terms.

$$E_X^{LDA}[\rho] = -C_X \int \rho^{4/3}(r) dr \quad (2.6)$$

$$C_X = \frac{3}{4} \left(\frac{3}{\pi} \right)^{1/3} \quad (2.7)$$

Increasing in complexity is the local spin density approximation (LSDA) which includes the electron spin, allowing the calculation of systems with unpaired electrons.¹⁰⁰ The exchange term is expressed in (2.8) and takes into account the spin of the electrons (α and β).

$$E_X^{LSDA}[\rho] = -2^{1/3} C_X \int (\rho_\alpha^{4/3}(r) + \rho_\beta^{4/3}(r)) dr \quad (2.8)$$

The correlation functional for LDA and LSDA was obtained from numerical quantum Monte-Carlo simulations of the homogeneous electron gas by Ceperly and Alder in 1980.¹⁰² In Gaussian 09, when LSDA is specified, the Vosko, Wilk and Nusiar LSDA correlation functional is employed (based on the Ceperly and Alder simulations), combined with slater exchange, forming the S-VWN functional, with LSDA exchange and correlation, again dependent only on ρ . The issue with LSDA is that it typically overestimates the exchange energy by $\approx 10\%$.¹⁰⁵ It also overestimates binding energies and overly favours high spin state structures.¹⁰⁴ The general form of the LSDA correlation functional is shown in 2.9 which depends only on the density of the electrons, ρ .¹⁰⁶

$$E_C^{LSDA}[\rho] = \int d^3r \rho(r) \epsilon_C(\rho_\alpha(r), \rho_\beta(r)) \quad (2.9)$$

Generalised gradient approximation

LSDA only depends on the electron density (ρ), and although giving satisfactory results, to correct for the overestimation of the exchange energy, the gradient of the electron density can be incorporated, in the generalised gradient corrected functionals (GGA). These functionals are a significant improvement on the homogeneous uniform gas method. The inclusion of the gradient of the electron density takes into account that electron density is not going to be homogeneous.

The general form of the exchange term of the generalised gradient approximation (GGA) functionals is shown in (2.10)¹⁰² and it can be seen that the exchange functional now depends on both the electron density, ρ , and the gradient of the electron density, $\nabla\rho$ for each of the α and β electrons.

$$E_X^{GGA}[\rho_\alpha, \rho_\beta] = \int f(\rho_\alpha, \rho_\beta, \nabla\rho_\alpha, \nabla\rho_\beta) dr \quad (2.10)$$

The form of the correlation term of a generalised gradient functional as proposed by Perdew in 1986¹⁰⁶ is shown in 2.11, clearly showing the inclusion of an extra term which encompasses the gradient of the electron density, $\nabla\rho$.

$$E_C^{P86}[\rho] = \int d^3r \rho \epsilon_C(\rho_\alpha, \rho_\beta) + \int \frac{d^3r d^{-1} e^{-\Phi} C(\rho) |\nabla\rho|^2}{\rho^{4/3}} \quad (2.11)$$

The range of density functional methods depend on the combination of functionals for the separate exchange and correlation portions.¹⁰⁰

An example of a GGA functional tested in this method validation study includes BP86,¹⁰⁷ which combines the gradient-corrected exchange correlation functional (E_X) B88, and P86 gradient-corrected correlation energy functional (E_C), forming the BP86 functional implemented within Gaussian 09.¹⁰⁸

The B88 exchange functional developed by Becke,¹⁰⁵ is shown in (2.12) where $\beta = 0.0042$ a.u., σ represents the α or β electrons, and x_α is represented in (2.13), introducing the gradient of the electron density, $\nabla\rho$. It adds corrections to the LSDA exchange functional, therefore building on the already determined LSDA functional.

$$E_X^{B88} = E_X^{LDA} - \beta \sum_a \rho_\sigma^{4/3} \frac{x_\sigma^2}{1 + 6\beta \sinh^{-1} x_\sigma} d^3r \quad (2.12)$$

$$x_\sigma = \frac{|\nabla \rho_\sigma|}{\rho_\sigma^{4/3}} \quad (2.13)$$

Many GGA exchange and correlation functionals have been developed, however they all include the key $\nabla \rho$ term to take into account the gradient of the electron density.

Meta generalised gradient approximation

In a further improvement on the GGA functionals, the second derivative of the electron density can be used, the Laplacian of the electron density (discussed fully in Section 2.5), however, due to computational difficulties the kinetic energy density is used, which varies with the energy density in the same way.¹⁰⁹ Examples of meta GGA (m-GGA) functionals discussed in this work include TPSS¹¹⁰ and M06L.¹¹¹

Hybrid functionals

Hybrid functionals include an extra layer of complexity, in the aim to improve the results obtained from DFT. In HF theory the exchange term, K is evaluated exactly for a non-interacting electron system. The theory behind hybrid functionals is the adiabatic connection, which can be represented as in (2.14) where λ is the degree of interaction between electrons. At $\lambda = 0$ this is the ideal non-interacting case, where there is no contribution to the correlation of the exchange functional, and the only contribution is the non-interacting exchange functional. As λ moves smoothly towards 1, you increase the degree of electron correlation. At $\lambda = 1$ the electrons are fully correlated in the exchange functional.

$$E_X = \int_0^1 \langle \psi(\lambda) | V_X | \psi(\lambda) \rangle d\lambda \quad (2.14)$$

If at $\lambda = 0$ the exchange correlation functional consists only of an exchange

contribution, and in HF the exchange term K is exact, this term can then be calculated using the Kohn-Sham orbitals and included as exact HF exchange. This is especially useful as the majority contribution to the exchange correlation functional is the exchange term.¹⁰² However correlation is vital for chemical accuracy.

The advantage of adding the HF exchange term is that it is exact for non-interacting electrons, however it does not include the correlation effects, when $\lambda > 0$. Therefore, combined use of exact HF and DFT exchange retains the correlation effects from the DFT exchange functionals, however includes the exact HF exchange for non-interacting electrons.¹⁰⁰

In this case, an exchange term from HF can be added, providing a new form for the exchange correlation functional (2.15), with different values of constants, c to form the new functional, to connect the non-interacting electrons ($\lambda = 0$) and fully interacting electrons ($\lambda = 1$).¹¹²

$$E_{hybrid}^{XC} = c_{HF}E_{HF}^X + c_{DFT}E_{DFT}^{XC} \quad (2.15)$$

The HF exchange can be added to GGA functionals, to make a GGA-hybrid functional such as B3LYP^{107,113} discussed in this work, or to mGGA functionals to make the ω B97XD,¹¹⁴ and M06¹¹⁵ mGGA-hybrid functionals discussed in this work.

The mostly widely used functional is B3LYP and is used in approximately 80 % of publications up to 2009.¹⁰⁴ It combines LSDA, Becke GGA and HF exchange terms, with LSDA and LYP correlation. The General form of B3LYP is shown in (2.16) where $a = 0.20$, $b = 0.72$, and $c = 0.81$ and are fitted semiempirically. Therefore the B3LYP functional consists of 20 % HF exchange, with 80 % Becke's GGA DFT exchange and 100 % Lee, Yang and Parr's DFT correlation (consisting of 19 % LSDA and 81 % GGA correlation).

$$E_{XC}^{B3LYP} = (1 - a)E_X^{LSDA} + aE_X^{HF} + b\Delta E_X^B + (1 - c)E_C^{LSDA} + cE_C^{LYP} \quad (2.16)$$

2.2 Using density functional theory to study non-covalent interactions

A draw back for density functional theory, is that it has often been shown to struggle when modelling non-covalent interactions, especially the difficult to model dispersion forces.^{116–121}

Post HF methods including MP2, MP4 and CCSD(T) are capable of accurately modelling non-covalent interactions, and as they include the non-dynamic electron correlation, can accurately model long range non-covalent interactions,^{120,121} however they are computationally expensive, in comparison to modern DFT methods.

The ω B97XD functional has been designed in order to more accurately model non-covalent interactions, without the additional expense of post-HF methods. This functional provides the opportunity for DFT to more accurately model non-covalent interactions, with the addition of an empirical dispersion correction to correct for the attractive dispersion forces.¹¹⁴

The functional is a hybrid, analogous to B3LYP discussed. However, this functional includes 100 % HF exchange at long range, whilst using a smaller percentage of HF exchange at short distance (22 % for ω B97XD). At long range the exchange functional dominates, and therefore addition of exact HF exchange is advantageous. At short range the correlation term has greater importance, resulting in the smaller HF exchange. The X term in ω B97XD denotes the variable HF exchange at short and long distance, and the ω term denotes the separation between short and long range exchange, and in ω B97XD is $0.2 a_0^{-1}$.¹¹⁴

In order to address the issue with long range dispersion interactions, an empirical dispersion term is added, denoted by D in the functional. The dispersion force is an attractive force, responsible for interactions such as $\pi - \pi$ stacking,¹²² and is calculated as shown in 2.17.¹¹⁴ This dispersion correction for two atoms (i and j), depends on the number of atoms (N_{at}), the interatomic distance (R_{ij}), a dispersion coefficient (C_{ij}), and finally a damping term ($f_{damp}(R_{ij})$) to ensure that the dispersion

correction is not added at short distance.

$$E_{dispersion} = - \sum_{i=1}^{N_{at}-1} \sum_{k=i+1}^{N_{at}} \frac{C_6^{ij}}{R_{ij}^6} f_{damp}(R_{ij}) \quad (2.17)$$

The damping term is then calculated (2.18), where a is a constant depending on the density functional, and R_r is the van der Waals radius of the two atoms. This damping term ensures that the at short distance (when R_{ij} is close to R_r) there is no dispersion correction as $f_{damp} \rightarrow 0$; whereas at long distance (when R_{ij} is much larger than R_r) the dispersion correction is added as $f_{damp} \rightarrow 1$. For ω B97XD the value of the constant a is 6.¹¹⁴

$$f_{damp}(R_{ij}) = \frac{1}{1 + a(\frac{R_{ij}}{R_r})^{-12}} \quad (2.18)$$

This makes the ω B97XD functional an excellent improvement on other density functionals for the study of systems where non-covalent interactions may be important.

2.3 Basis sets

2.3.1 Introduction

The use of basis sets provides the basis functions for Kohn-Sham orbitals that DFT uses. The basis functions represent orbitals for electrons to populate, and the larger the basis set the greater flexibility of space for the electrons to populate. The molecular orbitals are formed from linear combinations of the individual basis functions provided by the basis set. Ideally an infinite basis set would be used, allowing electrons to have complete freedom in their location, however this is computationally not feasible.¹⁰⁰

2.3.2 Gaussian functions

The basis sets used in this thesis (for all atoms other than Pd) are based on Gaussian functions. Although Gaussian functions in isolation do not provide the most accurate description of atomic orbitals, combinations of these Gaussian functions can accurately reproduce the more accurate (however significantly more computationally expensive) Slater type functions.

The combinations of these primitive Gaussian functions, yield contracted Gaussian functions (ϕ_r) as linear combinations with various coefficients (2.19) where the d_{nr} terms are the coefficients, and g_{nr} are the primitive Gaussians. These contracted Gaussian functions can much more accurately reproduce the desirable Slater type functions.¹⁰⁰

$$\phi_r = d_{1r}g_{1r} + d_{2r}g_{2r} + d_{3r}g_{3r} \quad (2.19)$$

2.3.3 Minimal basis set

The simplest basis set is STO-3G implemented within Gaussian 09, and provides the basis functions to accommodate all electrons, for example for hydrogen and helium would have a 1s orbital to occupy (single basis function). However, elements in period 2, Li→Ne receive 1s, 2s, 2p_x, 2p_y and 2p_z orbitals to occupy (total of 5 basis functions per atom). Despite this STO-3G basis set providing orbitals for all electrons to occupy, it is inadequate for computation due to limited flexibility, and so more basis functions are required for a more accurate treatment of the electronic structure of atoms and molecules.

2.3.4 Double and triple ζ , split-valence basis sets

To increase flexibility double and triple ζ basis sets can be used, to allow different sized orbitals. Double ζ basis sets have two basis functions per basis function in the minimal basis set, and triple ζ basis sets have three basis functions for each basis function in the minimal basis set. Therefore in a double ζ basis set, H and He would

have a total of two basis functions, and for elements in the second period, would now have a total of 10 basis functions.¹⁰⁰ The greater flexibility of double and triple ζ basis sets greatly improves the quality of the calculated results, however there is an extra computational cost of adding additional basis functions. In order to decrease the computational costs, split-valence basis sets take advantage of the greater flexibility for valence electrons, but represent the core electrons with a minimal basis set. For example in a double ζ split-valence basis set, two basis functions are used for valence electrons, and a single basis function for core electrons.¹⁰⁰

2.3.5 Polarisation and diffuse functions

The use of split-valence basis sets allow alterations in size of the atomic orbitals. Polarisation functions can be added to basis sets to allow alterations in the shape of the orbitals (when bonds are polarised etc). This adds extra basis functions to each atom, such as adding d functions to period 2 elements, allowing distorted orbitals to be formed. Finally diffuse functions can be added, which for example allow large s and p type functions for periods 1 and 2, particularly important for lone pairs and anions, as the electrons can be found far from the nucleus.¹⁰⁰

2.3.6 Basis sets used in this thesis for atoms other than palladium

The basis sets used within this thesis for geometry optimisation (for all atoms other than palladium) are Pople type split-valence basis sets, with added diffuse and polarisation functions, of the form 6-31++G(d,p). This basis set separates core from valence electrons, and describes the core electrons with a single contracted Gaussian formed of six primitive Gaussians. The valence electrons are treated with greater flexibility, split into an inner and outer part. The inner part is formed of three Gaussians, and the outer part a single Gaussian.¹⁰⁰ Diffuse and polarisation functions are then added to provide greater flexibility by adding these extra basis functions.

For accurate energy determination, the triple ζ 6-311++G(2df,2p) basis set is used for single point energy calculations, which provide 3 basis functions for the valence electrons, and provide (with the addition of additional polarisation functions) a suitably large basis.¹⁰⁰

2.3.7 Effective core potentials for palladium

For palladium, due to the number of electrons (46), the effect on the computation time is substantial. Another consequence of the larger palladium atom compared to the smaller atoms considered in this thesis, is the effect of special relativity, which also needs to be considered. In order to deal with these issues, the use of effective core potentials is possible. These treat the core of the electrons as an average effect, with the valence electrons treated explicitly. This average core effect also takes into account special relativity, which can have significant influence on bond lengths and energies.¹⁰⁰ Examples of relativistic effective core potentials used in this work include LanL2DZ^{123,124} and SDD.¹²⁵

2.4 Solvation effects in DFT

The effect of solvation can be taken into account in quantum mechanical calculations most efficiently by using a solvation model rather than by the addition of explicit molecules. The most common method of including solvation effects, for example in a DFT calculation, is to use the polarisable continuum model (PCM).¹²⁶ Within Gaussian 09¹⁰⁸ the specific methodology implemented is the Integral Equation Formalism PCM.¹²⁶

In the PCM model, the molecule is placed within a solvent cavity, formed by interlocking spheres around the solute, and the solvent modelled by a uniform dielectric constant representing the solvent.¹²⁷

The use of PCM to correct for solvent effect is very common, including work by Davies and co-workers into solvent effects of C-H bond activation,¹²⁸ the study of

C-H bond activation of benzene by vanadium complexes,¹²⁹ C-H and C-CN bond activation by rhodium complexes,¹³⁰ C-H bond activation with Ir complexes,¹³¹ and O-H bond cleavage in the Wacker process.¹³²

These examples show that the use of PCM as an energy correction to gas-phase structures is widespread, and is therefore suitably accurate for the present studies.

2.5 Atoms in Molecules

2.5.1 Introduction

Bader’s Atoms in Molecules (AIM)^{133,134} has been used frequently to determine the bond strengths and nature of the bond in a variety of contexts. Examples include the investigation of hydrogen bonding between formaldehyde and HF complexes,¹³⁵ Te-N intramolecular interactions,¹³⁶ and intramolecular carbonyl interactions in transition metal complexes.¹³⁷

The basis of quantum theory is that physical observables of molecules can be fully described by the wavefunction (ψ). The goal of the Atoms in Molecules method is to separate the molecule into basins containing individual atoms which still obey the rules of quantum chemistry, with electron density as the physical observable. Then by plotting the electron density within the molecule, to determine its topology, it is possible to obtain chemical insight into bonding and functional group properties.

The plotting of the electron density ρ reveals a number of features which can help us to elucidate the electronic structure. An example of the topology of ρ for cyclopropane (Figure 2.1) shows saddlepoints which can correspond to various features such as atoms, bonds, rings and cages. These saddle points are referred to as critical points.

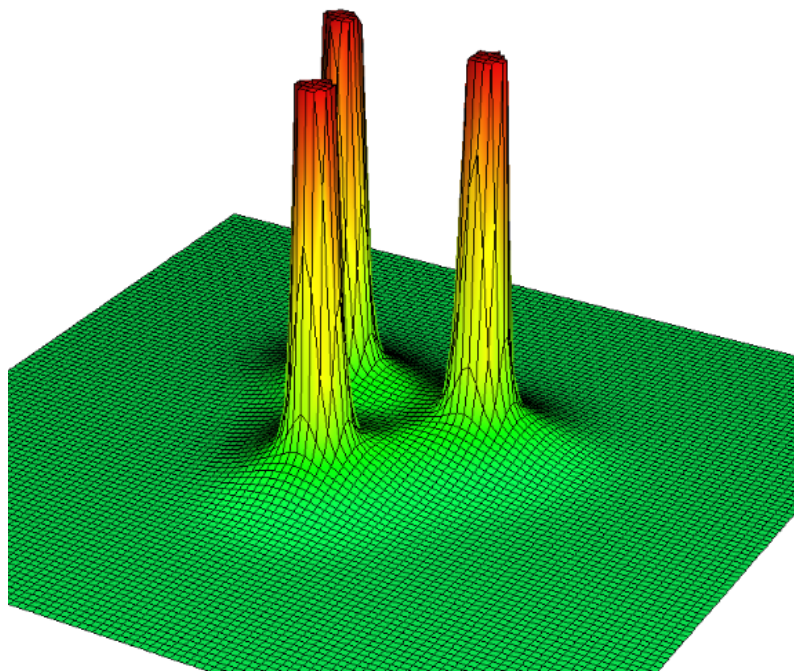


Figure 2.1 Topology of the electron density for cyclopropane.

At a saddle point, the first derivative of the electron density should be 0 along all three principal axes, and the second derivatives in each plane determines the signature of the critical point. When the saddle point has negative curvature in all planes, a (3,-3) nuclear critical point (NCP) is found. These are the atoms that define the basins, and correspond to a local maximum in electron density at the nucleus of the atom, as expected due to the attraction between electrons and nuclei.¹³⁴

When the second derivatives are negative in two axes, and positive in the other then a (3,-1) bond critical point (BCP) is found. This corresponds to a minimum in ρ between the two atoms along the interatomic bond path, and maxima perpendicular to this.¹³⁴

When the second derivative is positive along two axes, and negative in one other, then a (3,1) ring critical point (RCP) is found. This corresponds to a minimum in ρ between three or more atoms forming a ring.¹³⁴ The final type of critical point is the cage critical point (CCP) characterised by positive curvatures in all three planes.¹³⁴

A test to confirm that all critical points have been found is using the Poincaré-Hopf relationship (2.20).¹³⁸

$$n_{NCP} - n_{BCP} + n_{RCP} - n_{CCP} = 1 \quad (2.20)$$

When looking at a molecule, the path between two bonded atoms is known as a bond path, and when the topology of ρ is plotted between these two points, the point along this bond where it reaches a minimum is the location of the BCP.¹³⁸ The chemical insight that can be gained from the properties of electron density and its derivatives at this point will be explained.

At the BCP, the value of $\rho(\mathbf{r})$ can be used to provide a guide to the strength of the interaction. It can also provide information on the nature of the interaction, as greater electron density between atoms suggest a covalent interaction ($\rho(\mathbf{r}) > 0.2$ a.u.), whereas less suggests a closed shell interaction ($\rho(\mathbf{r}) < 0.2$ a.u.). This is intuitive, as in a covalent bond, electrons are shared between the two atoms, and you would expect greater density to be located between the atoms. In a closed shell interaction, the bond is formed by variations in charge, for example between $O^{\delta-}$ and $H^{\delta+}$ in a hydrogen bond, or between Na^+ and Cl^- in an ionic interaction, where there would be significantly less electron density between the two atoms.

When considering BCPs, the saddle point can be characterised by the second derivatives along each axis, giving rise to the curvatures of the $\rho(\mathbf{r})$ along each axis. As $\nabla^2\rho(\mathbf{r})$ is made up from the three curvatures of the $\rho(\mathbf{r})$ (2.21) the values of each of these curvatures determine the shape of the electron density at the bond critical point.

$$\lambda_1 + \lambda_2 + \lambda_3 = \nabla^2\rho(\mathbf{r}) \quad (2.21)$$

λ_1 and λ_2 lie perpendicular to the bond path, and are negative, due to the maximum in electron density at the bond critical point perpendicular to the bond path. The magnitude of the curvature gives an indication of the amount of electron density concentrated at the critical point compared to that located in each of the atomic basins. In a covalent bond a greater $\rho(\mathbf{r})$ is expected at the critical point, and

a larger negative curvature would be expected, having a dominant effect on the total value of $\nabla^2\rho(\mathbf{r})$ making $\nabla^2\rho(\mathbf{r}) < 0$. In an ionic interaction, less electron density is expected to be found between the two atoms, and therefore the positive curvature between the two atoms (λ_3) is expected to be larger than in covalent cases, therefore dominating $\nabla^2\rho(\mathbf{r})$ resulting in values >0 and indicating a closed shell (non-shared) interaction.¹³⁸

Another way to investigate the nature of the bonding between the two atoms is to investigate the potential $V(\mathbf{r})$ and kinetic $G(\mathbf{r})$ electron energy densities. These are related to $\nabla^2\rho(\mathbf{r})$ as an expression of the virial theorem at a stationary state (2.22), and the total electron energy density $H(\mathbf{r})$ (2.23).¹³⁸ $G(\mathbf{r})$ is always positive, and $V(\mathbf{r})$ always negative, and therefore the balance between these two values control both the sign of $\nabla^2\rho$ and $H(\mathbf{r})$. In an interaction where electrons are shared between atoms along the bond path, the movement of electrons is decreased, and therefore $G(\mathbf{r})$ decreases, and the value of $V(\mathbf{r})$ becomes more negative. The domination of $V(\mathbf{r})$ causes $H(\mathbf{r})$ to become negative (as $V(\mathbf{r})$ is negative). Therefore $G(\mathbf{r})$ can be thought of as a measure of 'covalency', whereby the more electron density accumulated at the bond critical point, the less kinetic energy density, and therefore the more negative $H(\mathbf{r})$. In an ionic interaction, there is significantly less charge accumulated along the bond path, and therefore have larger $V(\mathbf{r})$, causing $H(\mathbf{r})$ to become positive and indicate less covalent character. This information about signs also translate across to $\nabla^2\rho$ however in a 2:1 ratio.¹³⁸

$$\left(\frac{\hbar^2}{4m}\right)\nabla^2\rho(\mathbf{r}) = V(\mathbf{r}) + 2G(\mathbf{r}) \quad (2.22)$$

$$H(\mathbf{r}) = V(\mathbf{r}) + G(\mathbf{r}) \quad (2.23)$$

2.5.2 Use of AIM to investigate the strength and nature of bonding

In a study into intramolecular carbonyl interaction in transition metal complexes,¹³⁷ $\rho(\mathbf{r})$ was used to compare the relative strengths of interactions. The positive values of $\nabla^2\rho(\mathbf{r})$ for the carbonyl-carbonyl interactions, were used to suggest a closed shell interaction (ionic, hydrogen bond, or van der Waal).

In a study into non-bonded Te-N interactions,¹³⁶ it was stated that when $\rho(\mathbf{r}) > 0.2$ a.u. then this BCP corresponds to covalent bonding, whereas when $\rho(\mathbf{r}) < 0.2$ a.u. this is characteristic of the closed shell interactions. It was found that these Te-N interactions were predominantly covalent.

In a study by Grabowski and co-workers¹³⁵ they utilised AIM to study hydrogen bonded interactions. They showed that different properties at the BCP could be used to determine bond strengths and the nature of the bonds. They used the principle that $\nabla^2\rho$ corresponds to the concentration ($\nabla^2\rho < 0$) or depletion ($\nabla^2\rho > 0$) of the electron density at the BCP. It was also stated that should $\nabla^2\rho > 0$, but $H_c < 0$ then the interaction has partial covalent character. They also used the ratio of $-G(\mathbf{r})/V(\mathbf{r})$ to characterise the bonding, with values > 1 indicating noncovalent interactions, $1 > -G(\mathbf{r})/V(\mathbf{r}) > 0.5$ indicating partial covalent character, and values < 0.5 a covalent interaction.

The use of ρ to study bond strengths in a study of M-H-B bonds has been undertaken using AIM, studying the strengths of the M-H bond for different metals, Zn, Bi and Ni.¹³⁹ It has also been used to study the strengths of N, S and O interactions with s-block metals.¹⁴⁰

2.6 Method validation results

2.6.1 Introduction

Due to the stated importance of the use of a suitable functional, basis set, and effective core potential, a method validation study has been undertaken. This is focused on previously synthesised, well known, symmetrical pincer palladacycles,^{8,9} which have been characterised by X-ray crystallography.

Previous work within the Cox group by S. Boonseng has focused on symmetrical pincer palladacycles,^{96,141} and this included a method validation study into these PdSCS and PdNCN palladacycles (Figure 2.2) using a number of different density functionals, and several basis sets and effective core potentials. The functionals tested were the GGA functionals: BP86,¹⁰⁷ PBE,^{142,143} and a dispersion corrected example, B97D;¹¹⁶ a GGA-hybrid functional: B3LYP;^{107,113} mGGA functionals: TPSS¹¹⁰ and M06L;¹¹¹ and finally two mGGA-hybrid functionals: ω B97XD,¹¹⁴ and M06.¹¹⁵ These functionals span 3 of the rungs of Jabob’s ladder,¹⁴⁴ shown in Figure 2.3 and their ability to reproduce experimental X-ray crystal structures for the PdSCS⁸ and PdNCN⁹ palladacycles tested. Two different all-electron basis sets were also tested, 6-31G(d) and 6-31+G(d,p), with two effective core potentials for the palladium atom, SDD,¹²⁵ and LanL2DZ.^{123,124} These geometry investigations, using the range of functionals listed above was undertaken by comparing the Pd-L bond lengths between experimental and theoretical structures, and the differences in the cartesian coordinates for each atomic pair using the Quatfit program for all atoms in each molecule.¹⁴⁵

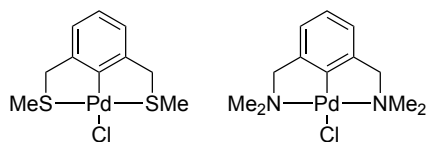


Figure 2.2 Symmetrical palladacycles, PdSCS by van Koten and co-workers, and PdNCN by Lu and co-workers, studied for method validation purposes.

Chemical Accuracy	
Double-Hybrid	
mGGA-hybrid	ω B97XD and M06
GGA-hybrid	B3LYP
mGGA	TPSS, M06-L
GGA	BP86, PBE, B97D
LDA and LSDA	
Hartree world	

Figure 2.3 Classification of DFT functionals with respect to Jacob’s ladder.

The work presented here is an extension of the analysis on these symmetrical pincer palladacycles, to include bond distances of all non-hydrogen atoms, and all non-hydrogen internuclear distances. The original work considered the Pd-L bonds, and inclusion of hydrogen atoms in the analysis. The work presented in this thesis further investigates the ability of the density functionals listed above to reproduce the experimental structures, and to compare to the accuracy reported by other groups.

2.6.2 Quatfit analysis

Experimentally, in X-ray crystallography the position of hydrogen atoms is not precisely known,¹⁴⁶ and therefore performing Quatfit analysis on the entire structure

has the potential to increase the root mean square error (RMS). It is possible in Quatfit analysis to give different weighting to each atom, and this provides the opportunity to only compare the cartesian coordinates for pairs of non-hydrogen atoms. This was the approach employed in this chapter.

The overall RMS error for both the PdNCN (RMS_N) and PdSCS (RMS_S) structures for each methodology is calculated as shown in (2.24), where RMS_N is the RMS error for the PdNCN structure, RMS_S the RMS error for the PdSCS structure; N_N the number of non-hydrogen atoms in the PdNCN structure, and N_S the number of non-hydrogen atoms in the PdSCS structure. The Quatfit analysis performed for this work is presented, and compared to that calculated previously for all atoms (Table 2.1).¹⁴¹

$$RMS = \sqrt{\left(\frac{RMS_N^2 \times N_N + RMS_S^2 \times N_S}{N_N + N_S} \right)} \quad (2.24)$$

Table 2.1 Quatfit analysis for PdNCN and PdSCS structures, to compare cartesian coordinates of experimentally determined and theoretically calculated structures, all numbers quoted in Å.

Functional	RMS for non-hydrogen atoms				RMS for all atoms ¹⁴¹			
	Basis set							
	A	B	C	D	A	B	C	D
B3LYP	0.053	0.044	0.053	0.044	0.151	0.144	0.151	0.146
ω B97XD	0.044	0.039	0.043	0.038	0.162	0.158	0.162	0.158
M06	0.047	0.041	0.047	0.041	0.159	0.155	0.159	0.155
M06-L	0.054	0.047	0.053	0.046	0.161	0.158	0.159	0.155
TPSS	0.040	0.035	0.040	0.035	0.163	0.156	0.162	0.156
B97-D	0.055	0.045	0.054	0.045	0.159	0.153	0.157	0.153
PBE	0.040	0.036	0.040	0.036	0.157	0.151	0.156	0.152
BP86	0.041	0.036	0.041	0.036	0.155	0.149	0.154	0.150

A = 6-31G(d)[LanL2DZ], B = 6-31G(d)[SDD], C = 6-31+G(d,p)[LanL2DZ] and D = 6-31+G(d,p)[SDD]

It can be seen from the results presented in Table 2.1 that the RMS errors found for all atoms are all ≥ 0.144 Å,¹⁴¹ whereas when the hydrogen atoms are excluded are all ≤ 0.055 Å, clearly showing that including hydrogens has a detrimental effect on the overall RMS error calculated by the Quatfit program. This approach was taken by Minenkov and co-workers, to exclude the hydrogens due to the difficulty

in locating their position experimentally.¹⁴⁶ In the X-ray crystal structures from PdNCN and PdSCS, the aromatic C-H bonds are all reported between 0.950 and 0.951 Å, however the optimised structures have aromatic C-H bonds significantly longer at ≈ 1.09 Å, clearly explaining the difference between the Quatfit analysis of all atoms, and excluding the hydrogen atoms.

The RMS errors found by Minenkov and co-workers¹⁴⁶ for 18 DFT optimised ruthenium complexes ranged from ≈ 0.25 Å to ≈ 0.35 Å depending on the functionals tested, the same functionals referred to in this work. Therefore the values presented excluding hydrogen atoms (Table 2.1) are all smaller than the errors found by Minenkov and co-workers.

The results (Table 2.1) reveal several distinct trends; the SDD effective core potential (basis sets B and D) uniformly out-performs the LanL2DZ effective core potential (basis sets A and C) for all functionals tested. There was an insignificant difference between basis sets A and C, and between B and D, and therefore further analysis concentrates on basis set D, 6-31+G(d,p)[SDD], due to the advantage of extra diffuse and polarisation functions.

It can be seen that B3LYP, B97D and M06L are outperformed by all other functionals. It appears that the M06 functional is intermediate in this set of data, and the remaining BP86, PBE, TPSS and ω B97XD functionals all perform extremely well.

2.6.3 Bonded distances

Previously, the Pd-L bond distances were investigated.⁹⁶ In this thesis this analysis has been extended to include all non-hydrogen bonded distances, and all non-hydrogen interatomic distances (calculated by distance matrix of all atoms), using basis set D, 6-31+G(d,p)[SDD] due to this being found to be the best basis set using the Quatfit analysis, in Section 2.6.2.

Firstly, the bonded distances will be discussed, which will be reported as mean signed errors (MSE), calculated as shown in (2.25), and mean unsigned errors (MUE)

calculated as shown in (2.26) for each of PdNCN and PdSCS where R_{ij} is the bond length between atoms i and j , and N_x where $x = \text{N or S}$, is the number of bonds in the molecule.

$$MSE_x = \sum_{i=1, j>i}^{N_x-1} \left(\frac{R_{ij}(\text{DFT}) - R_{ij}(\text{Xray})}{N_x} \right) \quad (2.25)$$

$$MUE_x = \sum_{i=1, j>i}^{N-1} \left| \frac{R_{ij}(\text{DFT}) - R_{ij}(\text{Xray})}{N_x} \right| \quad (2.26)$$

The average MSE and MUE values for PdNCN and PdSCS, MSE_{AV} and MUE_{AV} are calculated as shown in (2.27) and (2.28) respectively for the geometry obtained from each functional.

$$MSE_{AV} = \frac{(MSE_N \times N_N) + (MSE_S \times N_S)}{N_N + N_S} \quad (2.27)$$

$$MUE_{AV} = \frac{(MUE_N \times N_N) + (MUE_S \times N_S)}{N_N + N_S} \quad (2.28)$$

The MSE_{AV} and MUE_{AV} values for each bonded distance and functional are shown in Table 2.2. This data shows that the largest MSE and MUE values are evident (with the exception of B97-D) for functionals that do not accurately model non-covalent interactions, with the lowest errors found for M06, M06-L and ω B97XD which all include these non-covalent interactions. M06 and M06-L include non-covalent interactions as they are parametrised with experimental data sets that include molecules with significant non-covalent character. The best functional for reproducing the experimental X-ray crystal structure for these bonded distances is ω B97XD with an average MSE of 0.005 Å and an MUE of 0.011 Å.

2.6.4 Interatomic distances

To further investigate the ability of functionals to reproduce experimental structures, the interatomic distances have been calculated by generating a distance matrix for

Table 2.2 MSE_{AV} and MUE_{AV} values for bonded distances in PdNCN and PdSCS symmetrical pincer palladacycles.

Functional	Bonded distances	
	$MSE_{AV} / \text{\AA}$	$MUE_{AV} / \text{\AA}$
B3LYP	0.015	0.017
ω B97XD	0.005	0.011
M06	0.007	0.014
M06-L	0.008	0.014
TPSS	0.016	0.019
B97-D	0.021	0.022
PBE	0.014	0.017
BP86	0.016	0.018

each structure from the cartesian coordinates,¹⁴⁷ by using formula (2.29), and then the MSE and MUE values calculated using (2.25) to (2.28).

$$\text{Internuclear distance} = \sqrt{\Delta x^2 + \Delta y^2 + \Delta z^2} \quad (2.29)$$

The errors in these interatomic distances are shown in Table 2.3 and once again show a clear trend (excluding B97-D) that functionals which include non-covalent interactions (M06, M06-L and ω B97XD) achieve optimised structures much closer to experimental structures than those functionals which do not include these interactions. This is in agreement with the bonded distances presented (Table 2.2), suggesting that the non-covalent interactions are indeed important.

Table 2.3 MSE_{AV} and MUE_{AV} values for interatomic distances in PdNCN and PdSCS symmetrical pincer palladacycles.

Functional	Internuclear distances	
	$MSE_{AV} / \text{\AA}$	$MUE_{AV} / \text{\AA}$
B3LYP	0.037	0.039
ω B97XD	0.012	0.024
M06	0.011	0.022
M06-L	0.015	0.028
TPSS	0.033	0.038
B97-D	0.040	0.046
PBE	0.031	0.036
BP86	0.036	0.039

The ability of functionals which include treatment of non-covalent interactions to better predict X-ray crystal structures for transition metal containing complexes

has been shown previously, including in the work by Minenkov and co-workers,¹⁴⁶ where it was shown that those that do not include dispersion corrections systematically overestimate the interatomic distances, and the results presented in Table 2.3 corroborate this finding using these palladium complexes, with all MSE and MUE values positive, but much smaller for M06, M06-L and ω B97XD. It was also found by Minenkov and co-workers¹⁴⁶ that the overall error (MUE) and the signed error (MSE) for the functionals not containing dispersion were similar, evidenced in this data also. The lower MSE values relative to the MUE values for the dispersion corrected functionals is due to cancellation of the over-estimated interatomic distances with a number of underestimated interatomic distances.

The observation of DFT systematically giving expanded structures compared to experimental X-ray structures was also found by Waller and co-workers,¹⁴⁸ in a study into transition metal containing complexes, studied using non-dispersion corrected functionals. This study found that hybrid functionals (however M06 and ω B97XD were not included in this study) achieved the lowest errors, compared to the GGA examples, including BP86.

2.6.5 Analysis

Taking the complete set of data, from the Quatfit analysis, bond distance, and interatomic distance investigations gives the opportunity to choose the most suitable model chemistry for the study of palladacycles. The Quatfit analysis found that the GGA’s BP86, PBE and TPSS gave the smallest RMS errors (<0.041 Å) and ω B97XD also performed very well, with RMS values <0.044 Å. However, all functionals performed well, with little difference between the best and worst performing functionals. It also showed that the SDD effective core potential was better than LanL2DZ across the board, and that the addition of diffuse functions made negligible difference, therefore the 6-31+G(d,p)[SDD] basis set was chosen for further analysis.

For both the bonded and interatomic distances, the functionals (excluding B97-D) which include non-covalent interactions outperformed the other functionals for both

MUE and MSE, with ω B97XD, M06 and M06-L having MSE's at least 0.016 Å smaller than the other functionals. As ω B97XD also performed well in the Quatfit analysis, this provides sufficient confidence in the use of ω B97XD as the functional of choice for geometry optimisation based on this method validation study, with the 6-31+G (d,p)[SDD] basis set.

However, much of the work studied in this thesis often involve key steps where hydrogens play an important role, such as C-H bond activation, it is therefore decided to use extra diffuse functions on hydrogen in the basis set, to include extra flexibility without much computational cost, and therefore geometry optimisation using the ω B97XD/6-31++G(d,p)[SDD] is the methodology used throughout this thesis.

2.7 Computational Details

All calculations present in this thesis were performed using Gaussian 09.¹⁰⁸ Geometry optimisation and frequency analysis was performed using the ω B97XD functional.¹¹⁴ For all atoms other than palladium a double- ζ Pople type basis set, with diffuse and polarisation functions is used, 6-31++G(d,p). For palladium the relativistic effective core potential SDD was used.¹²⁵

Energy minima or transition states were confirmed by the absence or presence of a single imaginary mode, respectively. Additionally transition states were confirmed by eigenvector following calculations to connect the respective energy minima.

Single point energies were then performed at the optimised geometry also using the ω B97XD functional,¹¹⁴ as this functional has been shown to provide accurate energetics.^{149,150} The larger triple- ζ basis set with extra polarisation functions, 6-311++G(2df,2p) was used for all atoms other than palladium. Again the SDD relativistic effective core potential (ECP) was used. At this higher level of theory, when solvent effects are considered, they are calculated using the PCM model,¹²⁶ using acetonitrile ($\epsilon = 35.688$) or *o*-xylene ($\epsilon = 2.5454$) as solvent, as an energy correction to the gas-phase structure.

Geometry optimisation for each experimentally determined structure was per-

formed due to the known inaccuracies in locating the position of hydrogen atoms,¹⁴⁶ and this also allows the calculation of structures for which X-ray crystal structures are not available. It also allows the accurate modelling of the reaction pathways.

Bader’s Atoms in Molecules method^{133,134} was used to perform topological analysis of the electron density using the Multiwfn program.¹⁵¹ As effective core potentials cause problems in this analysis, as bond paths cannot be accurately traced,¹³⁸ the DGDZVP all-electron, relativistic basis set was used for palladium.¹⁵² Therefore, the full computational methodology used for the Atoms in Molecules analysis was ω B97XD/6-311++G(2df,2p)[DGDZVP]// ω B97XD/6-31++G(d,p)[SDD].

Chapter 3

An SCN pincer palladacycle: a DFT pathway and a synthetic route

This chapter describes a new and amenable experimental synthesis to unsymmetrical SCN pincer ligands, with late stage diversification to facilitate library generation; and utilisation of C-H activation to synthesise an unsymmetrical SCN pincer palladacycle. A model formation reaction pathway towards the experimentally synthesised, and model unsymmetrical SCN pincer palladacycle studied using Density Functional Theory is also presented. The stationary points along the pathway towards the experimentally synthesised palladacycle are analysed using Bader's Atoms in Molecules method. The analysis reveals differences in donor atom to palladium bond strengths and nature in key steps such as in the C-H bond activation. It also showed that the model synthetic pathway is energetically favourable, and spontaneous. This work is published in the Royal Society Open Science journal.⁹⁷

3.1 Introduction

3.1.1 SCN pincer palladacycles

The prevalence of unsymmetrical pincer palladacycles is increasing, due to interest into the potential hemilability of the resulting complexes. Early examples of unsymmetrical SCN palladacycles include an intermediate in the biomimetic synthesis of Narwedine (Figure 3.1),¹⁵³ with other examples including the SNC palladacycle synthesised by Spencer *et al.* based on the benzodiazepine framework (Figure 3.2),⁴⁴ an SNC example used in the study into the formation of palladium nanoparticles (Figure 3.3),⁴¹ another SNC example formed from a thioether functionalised iminophosphorane (Figure 3.4),²⁷ and a number of SCN examples synthesised by Odinet and co-workers (Figure 3.5).^{16,154}

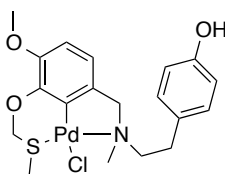


Figure 3.1 Unsymmetrical SCN palladacycle as an intermediate in the synthesis of Narwedine by Holton and co-workers.

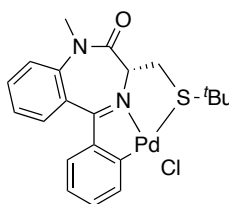


Figure 3.2 SNC pincer palladacycle by Spencer *et al.* with a benzodiazepine backbone.

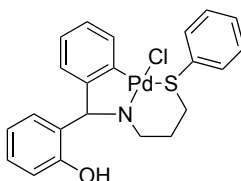


Figure 3.3 SNC pincer palladacycle by Singh and co-workers.

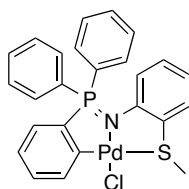


Figure 3.4 SNC pincer palladacycle by Grévy and co-workers.

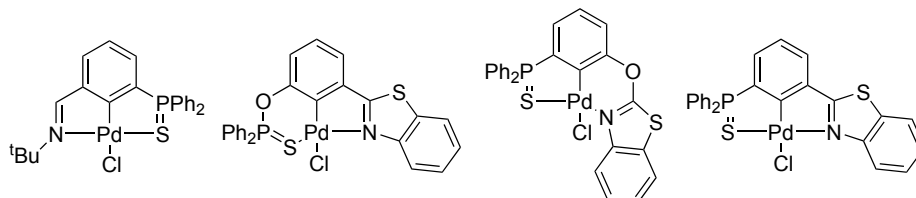
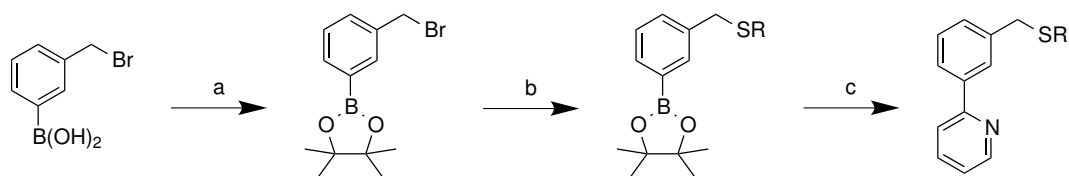


Figure 3.5 SCN pincer palladacycles by Odinets and co-workers.

Despite the increasing interest in these unsymmetrical SCN pincer palladacycles their synthesis is usually more problematic than the much more widely studied symmetrical examples. For example, Figure 3.1 shows an intermediate in a total synthesis of Narwedine; the example in Figure 3.2 requires the synthesis of the benzodiazepine backbone before C-H bond activation is possible;⁴⁴ and the other examples reported often include multi-step syntheses. Therefore the ability to synthesise a library of these unsymmetrical SCN pincer ligands in a few synthetic steps, and the ability to easily vary substituents on the donor atoms would be an advantageous addition to the field of unsymmetrical pincer palladacycle chemistry.

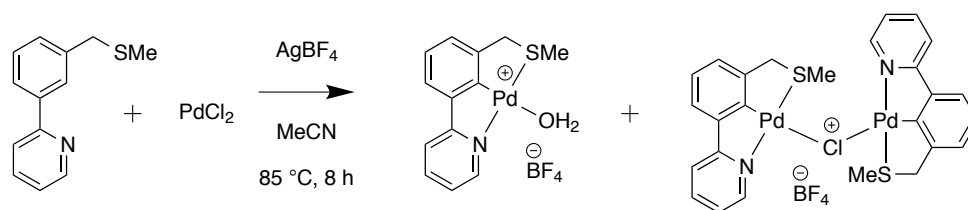
3.1.2 Efforts towards synthesising the SCN ligand and palladacycle presented in this thesis

Previous work by Baltus¹⁵⁵ into library generation of biphenyl compounds synthesised by Suzuki-Miyaura coupling^{156–159} (Scheme 3.1) produced an interesting compound (R=Me, Scheme 3.1). As an unsymmetrical biaryl ligand, it was considered a suitable and convenient candidate to undergo C-H bond activation with a Pd(II) source as a synthetic route to an unsymmetrical pincer palladacycle.



Scheme 3.1 Biaryl synthesis by Baltus. a) Pinacol, MgSO_4 , THF, rt, 1 h. b) HSR, THF, MW 150 °C, 20 min. c) 2-Bromopyridine, Na_2CO_3 , $\text{Pd}(\text{PPh}_3)_4$, toluene, EtOH, H_2O , MW 130 °C, 10 min.

The C-H activation of the unsymmetrical ligand (Scheme 3.1, $\text{R}=\text{Me}$) yielded several products (Scheme 3.2), characterised by X-ray crystallography. One of which was a water bound example (Figure 3.6), and the other a dimeric chlorido bridged example (Figure 3.7).¹⁵⁵ Both of these are cationic with a BF_4^- counterion. Neither of these products were the desired monomeric chloro palladacycle (Figure 3.8).



Scheme 3.2 C-H activation of unsymmetrical SCN ligand by Baltus.

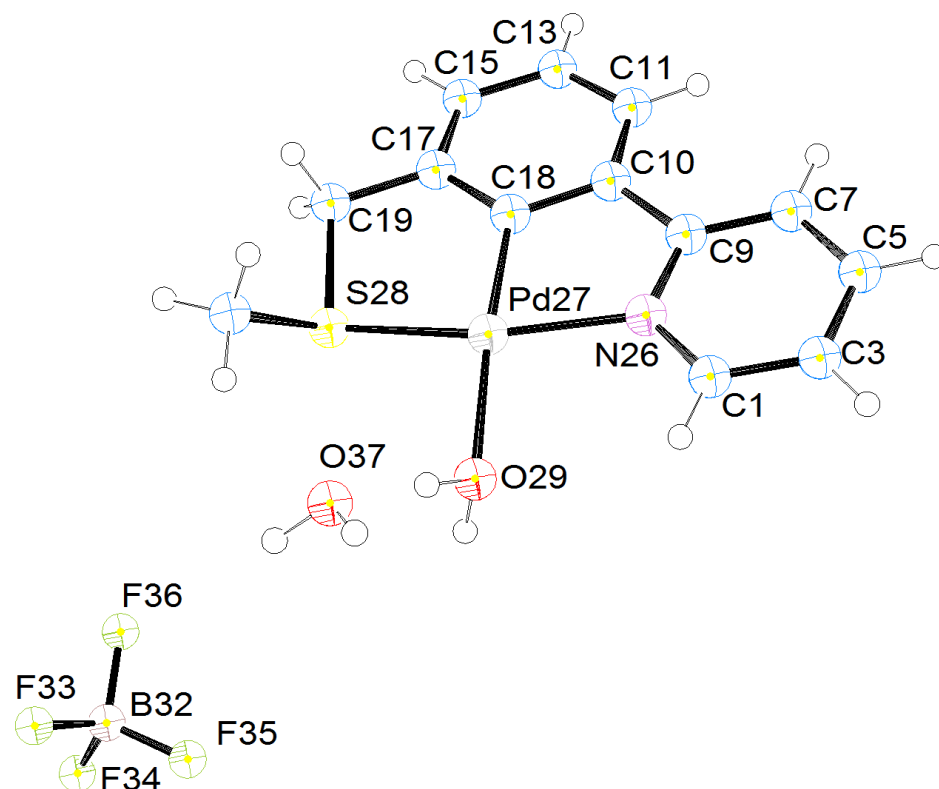


Figure 3.6 Water bound SCN pincer palladacycle X-ray crystal structure from Baltus.

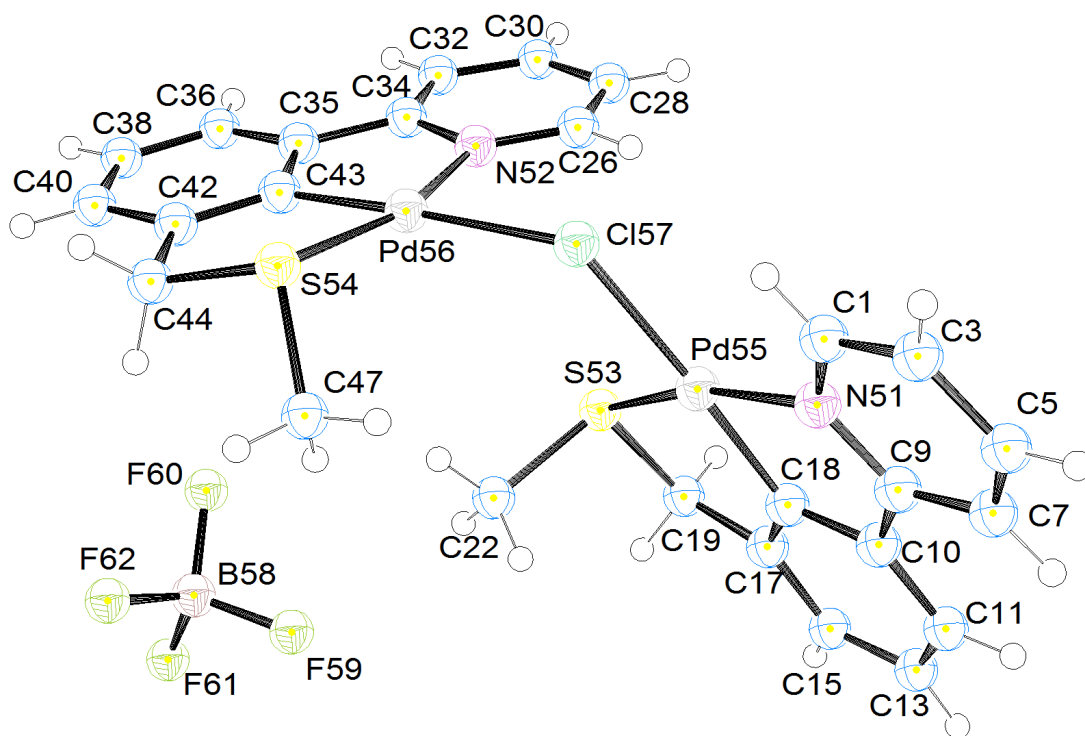


Figure 3.7 Dimeric SCN pincer palladacycle X-ray crystal structure from Baltus.

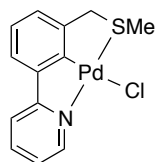


Figure 3.8 Desired SCN palladacycle (R=SMe) from Baltus synthesis, but unobtainable.

3.1.3 Cationic palladacycles, and salt metathesis

Examples of cationic palladacycles are well documented, with examples shown in Figure 3.9 by Herrmann and co-workers,¹⁶⁰ Thirupathi and co-workers,¹⁶¹ and Szabó and co-workers.¹³ Neutral palladacycles, either as monomeric, dimeric or bis-cyclopalladated examples,³¹ are often used in catalytic applications, such as the Suzuki-Miyaura coupling reaction,^{15,16,38,162–165} and in numerous other catalytic applications including C-H bond functionalisation of benzyl nitriles¹⁶⁶ and allyl nitriles,¹⁶⁷ catalytic opening on vinyl epoxides,¹¹ boronation of cinnamyl alcohols,¹¹ conversion of allylic alcohols into allylic boronic esters.¹⁶⁸ Therefore, due to the abundance of literature on catalytic applications on these neutral palladacycles, the conversion of cationic palladacycles into the monomeric chloride via salt metathesis is desirable, and is possible with a large excess of NaCl (Scheme 3.3).¹³

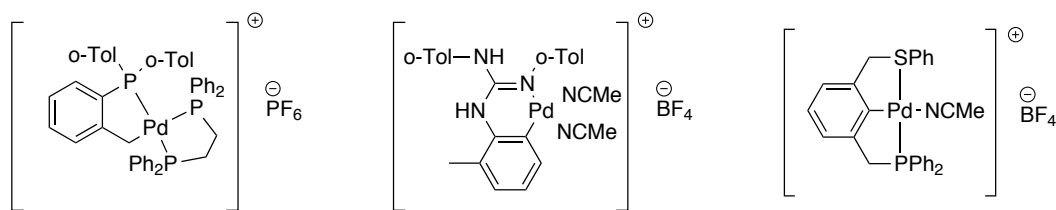
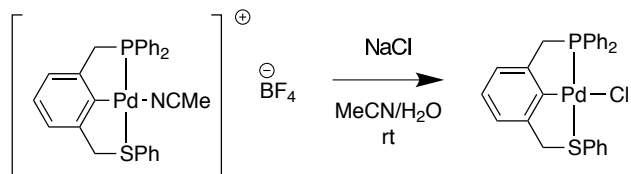


Figure 3.9 Examples of cationic palladacycles by, Herrmann and co-workers (left), Thirupathi and co-workers (middle), and Szabó and co-workers (right).



Scheme 3.3 Salt metathesis of cationic palladacycles by Szabó and coworkers.

An example of this metathesis reaction is provided by Szabó and coworkers¹³

providing the opportunity to synthesise the desired monomeric chloride palladacycle (Figure 3.8). Therefore this synthesis is of interest in order to convert the cationic SMe examples (Figure 3.6 and Figure 3.7)¹⁵⁵ into the monomeric chloride example (Figure 3.8).

Another example of using an excess of a chloride salt in a metathesis reaction is the work by Spencer *et al.* into the conversion of acetate bound palladacycle into a chloride bound palladacycle,⁴⁴ also used by Leung and co-workers.¹⁶⁹

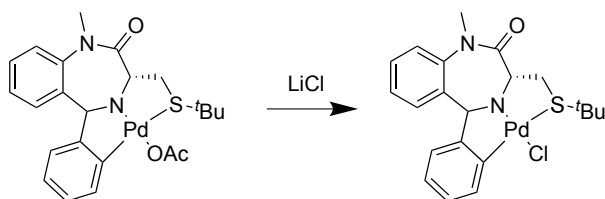
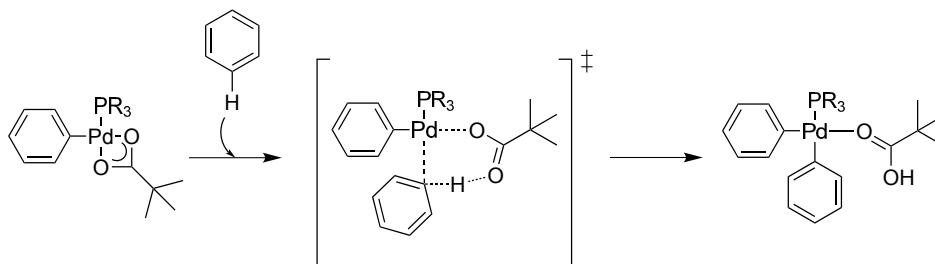


Figure 3.10 LiCl metathesis of acetate bound palladacycle by Spencer *et al.*

3.1.4 C-H bond activation

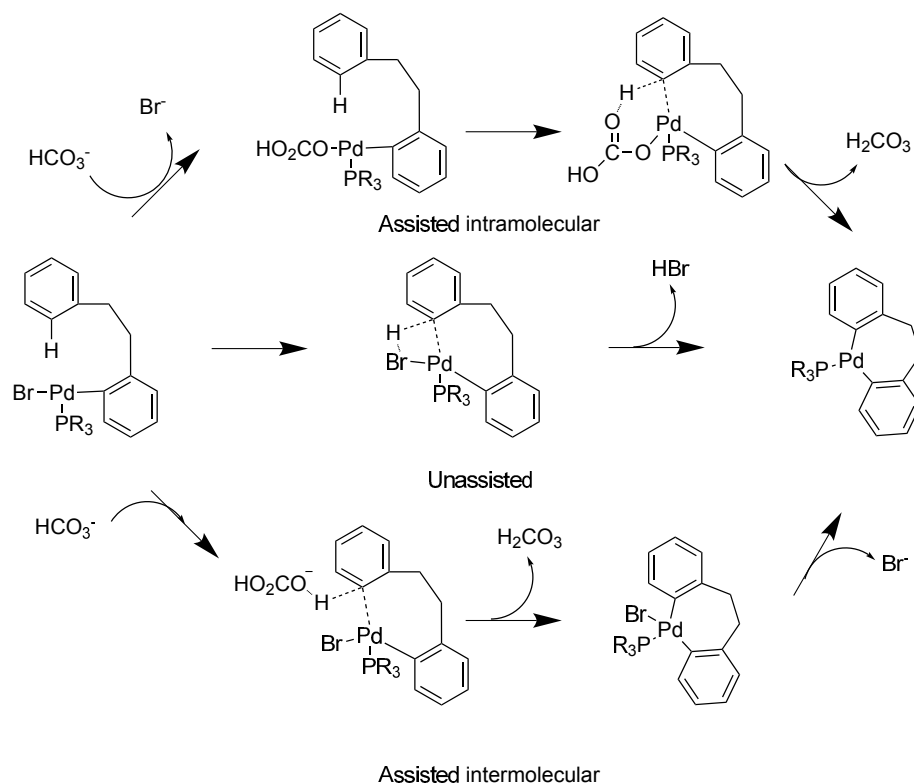
The C-H bond activation procedure is of great importance, due to its significance in catalysis,¹⁷⁰ and as one of the common routes of palladacycle synthesis.^{69,171,172} Existing work into the C-H bond activation mechanism in the cyclometallation to a palladacycle include the seminal work by Davies, Donald and Macgregor¹⁷³ using palladium acetate as the Pd(II) source. This work found that the mechanism proceeds via an agostic C-H interaction to palladium, followed by a six-membered transition state, with the acetate moiety acting as an intramolecular base to abstract the proton, termed ambiphilic metal ligand activation (AMLA).¹⁷⁴

Another investigation into likely C-H bond activation mechanisms was performed by Fagnou and Lafrance using pivalic acid as an additive as an intramolecular base, as shown in Scheme 3.4,¹⁷⁵ and is an example of an AMLA mechanism.



Scheme 3.4 Proposed mechanistic pathway for C-H bond activation with pivalic acid by Fagnou and Lafrance.

Work by Echaverren and co-workers^{176,177} discussed three potential mechanisms for palladium catalysed arylations, involving a C-H bond activation with assisted intramolecular, assisted intermolecular and unassisted pathways. These vary depending on the role of the base, with the assisted intramolecular pathway having an acetate group coordinated to palladium abstracting the proton; the assisted intermolecular pathway, where a free acetate acts as the base; and the unassisted pathway where the acetate base is not involved at all. These three pathways are shown in Scheme 3.5, with the assisted intramolecular mechanism related to the AMLA type mechanism proposed by Davies, Donald and Macgregor,¹⁷³ and that proposed by Fagnou and Lafrance.¹⁷⁵

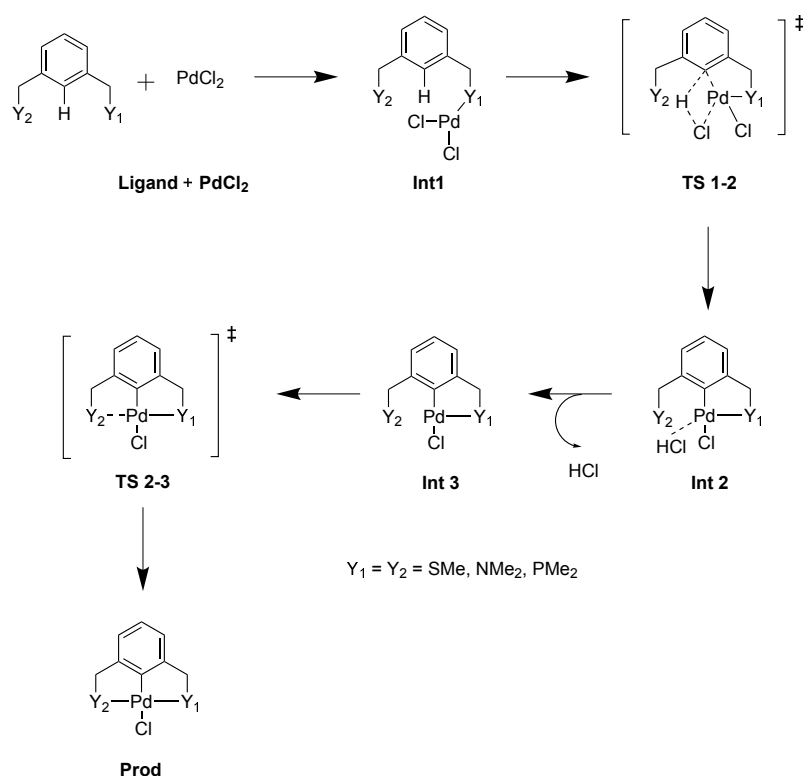


Scheme 3.5 Various C-H bond activation mechanisms suggested by Echaverren and co-workers.

Work within our group has recently focussed on a model formation reaction for symmetrical pincer palladacycles (Scheme 3.6),⁹⁶ in order to study the role of the donor atoms in the pathway, including the key C-H bond activation step. The formation pathway (Scheme 3.7) shows the key steps, and it was found that the PdPCP example had the smallest calculated C-H bond activation barrier (92.5 kJ mol⁻¹), and the PdNCN example had the largest barrier (118.0 kJ mol⁻¹).⁹⁶



Scheme 3.6 Model formation pathway to symmetrical pincer palladacycles.



Scheme 3.7 Symmetrical palladacycle unassisted formation pathway.

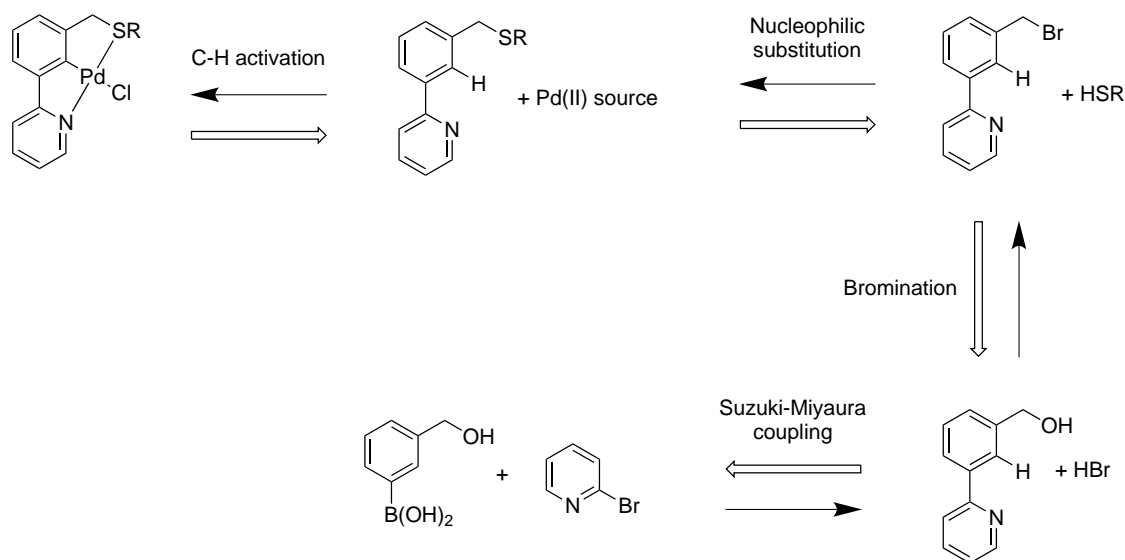
The energy barrier for the C-H bond activation found for the symmetrical pincer palladacycles (Scheme 3.7) are significantly larger ($\Delta E_0^\ddagger \approx 100 \text{ kJ mol}^{-1}$)⁹⁶ than that found for the Davies, Donald and Macgregor example (0.4 kJ mol^{-1})¹⁷³ however smaller than that found for the base unassisted pathway in Scheme 3.5 which had C-H bond activation barriers $\approx 180 \text{ kJ mol}^{-1}$.¹⁷⁷ The assisted intramolecular pathway had a barrier of $\approx 98 \text{ kJ mol}^{-1}$, and the assisted intermolecular pathway a barrier of $\approx 73 \text{ kJ mol}^{-1}$. The likely explanation for this is that for the pathway described in Scheme 3.6,⁹⁶ the lack of base makes the proton abstraction less favourable. However the focus of this study was into the role of the donor atoms, with the absence of effects from base and solvent.

3.2 Results and Discussion

3.2.1 New ligand synthesis with late stage diversification

Due to the desire to synthesise a library of new SCN pincer ligands, this chapter focusses on the design of a new synthetic route to the previously synthesised ligand **1a**, and to synthesise the previously unobtainable SCN pincer palladacycle **2a**. The synthesis of ligand **1a** is known as discussed (Scheme 3.1),^{155,178} however our aim was to devise a synthesis which provides the opportunity for late stage diversification to allow generation of a number of unsymmetrical pincer ligands. In the previous synthesis (Scheme 3.1) there were several key steps, firstly the boronic acid protection as the pinacol, followed by the nucleophilic substitution of the benzyl bromide to install the SMe ligand arm. Next, the Suzuki-Miyaura coupling step was undertaken with 2-bromopyridine, which installed the 2-pyridyl ligand “arm”. In the synthesis described (Scheme 3.1)^{155,178} the nucleophilic displacement step on the pinacol protected boronic acid occurs before the Suzuki-Miyaura step, which means that the Suzuki-Miyaura step is required for each new compound. Therefore the ability to reverse these steps would provide an advantageous synthesis.

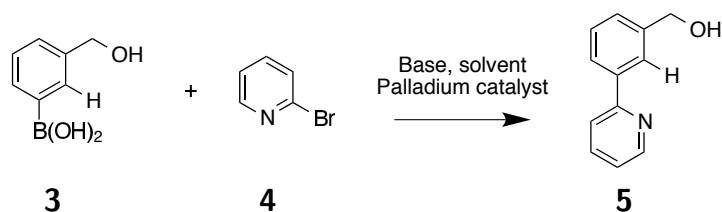
A designed retrosynthetic pathway is shown in Scheme 3.8 which would allow the Suzuki-Miyaura coupling to occur first, which would mean a family of SCN pincer palladacycles could be easily synthesised from a common starting benzyl bromide.



Scheme 3.8 SCN palladacycle retrosynthesis.

3.2.2 Suzuki-Miyaura coupling optimisation

The first step required in the retrosynthetic strategy shown in Scheme 3.8 is the Suzuki-Miyaura coupling required between 3-(hydroxymethyl)phenylboronic acid, **3**, and 2-bromopyridine, **4**, to form [3-(pyridinyl-2-yl)phenyl]methanol, **5**, shown in Scheme 3.9. The choice of base and solvent are vital, as it has been shown that varying the base can have dramatic effects on conversion of the starting materials to products. An example showing choice of base is important, is the study by Bedford and Cazin¹⁶² detailing the coupling of 4-chloroanisole and phenylboronic acid using a nitrogen based palladacycle as the catalyst proceeding in 22% conversion using KF as a base in dioxane, whereas under identical conditions using Cs₂CO₃ proceeds with quantitative conversion. The solvent choice is also important, such as the study by Bedford and co-workers³⁸ showing the coupling of 4-bromoacetophenone with phenylboronic acid using a phosphorous based palladacycle as the catalyst found complete conversion using toluene as a solvent, whereas under identical conditions, only 20% conversion was found using THF.



Scheme 3.9 SCN Suzuki-Miyaura coupling between **3** and **4**, to **5**.

The initial conditions tested for Scheme 3.9 were using $\text{Pd}(\text{PPh}_3)_4$ as the palladium catalyst, aqueous Na_2CO_3 as the base, with toluene and EtOH as co-solvents.^{178,179} Various other bases were tested, along with different reaction conditions, utilising traditional heating and microwave heating (Table 3.1).

Table 3.1 Optimisation of Suzuki-Miyaura coupling shown in Scheme 3.9.

Entry	Catalyst	Base	Conditions	Isolated yield /%
1	$\text{Pd}(\text{PPh}_3)_4$	1 M Na_2CO_3	A	75
2	$\text{Pd}(\text{PPh}_3)_4$	1 M Na_2CO_3	B	27
3	$\text{Pd}(\text{PPh}_3)_4$	0.5 M K_3PO_4	C	51
4	$\text{Pd}(\text{PPh}_3)_4$	1 M NaOH	D	0
5	$\text{Pd}(\text{OAc})_2$	1 M Na_2CO_3	C	57
6	$\text{Pd}(\text{dppf})\text{Cl}_2$	1 M Na_2CO_3	C	49
7 ^a	$\text{Pd}(\text{PPh}_3)_4$	1 M Na_2CO_3	C	77
8 ^a	$\text{Pd}(\text{PPh}_3)_4$	0.5 M K_3PO_4	C	93
9 ^a	$\text{Pd}(\text{PPh}_3)_4$	1 M NaOH	C	12
10 ^b	Buchwald XPhos Pd G2	0.5 M K_3PO_4	C	74

1:2:1 base:toluene:EtOH. A) Thermal, 85 °C, 48 h. B) MW, 150 °C, 10 mins. C) MW, 150 °C, 20 mins. D) Thermal, 85 °C, 24 h. a) 10:7.5:5 base:toluene:EtOH. b) Methodology adapted from Buchwald and co-workers,¹⁸⁰ 1.5 eq of boronic acid, 1 mol % catalyst, 1:2 base:THF.

It can be seen in Table 3.1 that $\text{Pd}(\text{PPh}_3)_4$ was found to be the most effective catalyst under these conditions for this reaction, compared to the others tested: $\text{Pd}(\text{OAc})_2$, $\text{Pd}(\text{dppf})\text{Cl}_2$, and Buchwald's X Phos Pd G2 catalyst (Figure 3.11).¹⁸⁰ By varying the base it was also found that K_3PO_4 proved the most effective choice, and the application of microwave heating was also advantageous as shown in Entry 8. It can also be seen that in Entries 3 and 8, that changing the proportion of base to solvent also has a significant impact on the isolated % yields, with 51 % found for 1:2:1 base:toluene:EtOH, whereas 93 % was achieved with 10:7.5:5 base:toluene:EtOH. Therefore the methodology of choice for the synthesis of ligand precursor **5** is the use

of $\text{Pd}(\text{PPh}_3)_4$ as the catalyst, with aqueous K_3PO_4 as the base, with toluene and EtOH co-solvents in 10:7.5:5 ratio.

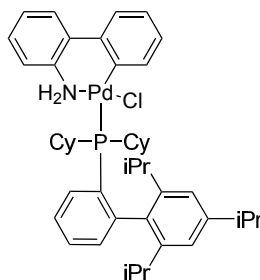
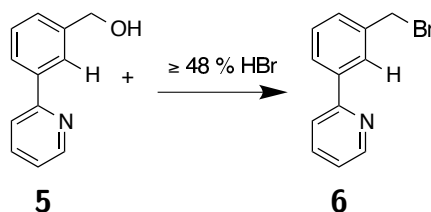


Figure 3.11 Buchwald's catalyst tested in Suzuki-Miyaura coupling optimisation.

3.2.3 Conversion of benzyl alcohol **5** to a benzyl bromide for nucleophilic displacement

The next step in the synthesis is to convert the benzyl alcohol **5** to the corresponding benzyl bromide 2-[3-(bromomethyl)phenyl]pyridine (**6**, Scheme 3.10), in order to facilitate nucleophilic displacement to generate the molecule library. A number of different methods were attempted for this synthesis, including: reaction with a chlorotrimethylsilane/lithium bromide mixture,¹⁸¹ which proved unsuccessful; stirring **5** with PBr_3 ¹⁸² which was low yielding; however the simplest and highest yielding method proved to be refluxing **5** in $\geq 48\%$ hydrobromic acid (Scheme 3.10).¹⁸³ The reaction proceeded in a good yield of 76 %, to give the expected product, **6**.

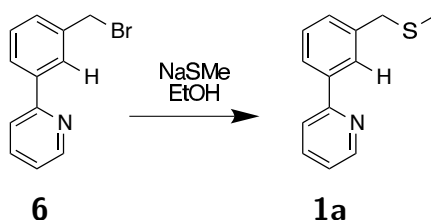


Scheme 3.10 Bromination of **5** using $\geq 48\%$ HBr in H_2O .

The benzyl bromide **6** was found to be unstable when left overnight under bench conditions. It has been shown previously that a sample of 2-chloromethylpyridine decomposes, reacting with the aryl chloride of another molecule, forming polymeric species.¹⁸⁴ However, it was found that keeping **6** at lower temperature or in solution inhibited this degradation.

3.2.4 Benzylic bromide nucleophilic substitution with thiol nucleophiles

Having synthesised **6**, the final step towards the synthesis of the unsymmetrical SCN pincer ligand was the nucleophilic displacement using the desired thiol. To achieve this, sodium thiomethoxide was used as the nucleophile, using ethanol as a solvent,¹⁸⁵ utilising MW heating. This nucleophilic displacement reaction proceeded in 72 % yield (Scheme 3.11), yielding the final product **1a** in an overall yield of 51 %. This overall yield is lower than that found previously to this ligand by Baltus¹⁵⁵ of 78 %, however this new route provides the desired late stage diversification to allow easier library generation of pyridine containing biaryl compounds.



Scheme 3.11 Nucleophilic displacement of **6** with sodium thiomethoxide.

3.2.5 C-H bond activation of ligand **1a**

The method chosen for the synthesis of the palladacycle, **2a** from ligand **1a** is C-H bond activation. The C-H bond to be palladated is ideal for C-H bond activation due to the chelating ability of the two donor atom groups, directing C-H bond activation to the desired position (Figure 3.12). C-H bond activation has been widely used in cyclopalladation, including the first documented synthesis by Cope and Siekman,¹ using PdCl₂ as the Pd(II) source to cyclopalladate azobenzene. Other Pd(II) salts can be used for cyclopalladation, such as Pd(OAc)₂, where the mechanism has been elucidated using DFT.¹⁷³

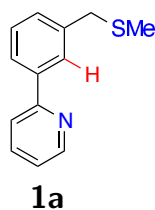
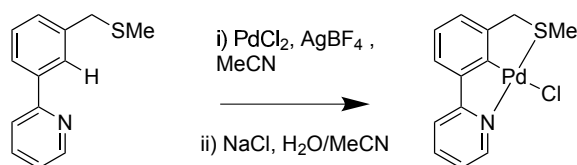


Figure 3.12 C-H bond activation position. C-H bond to be palladated shown in red, and chelating groups for regioselective palladation shown in blue.

The C-H bond activation procedure selected was that used by Baltus in the original synthesis of the mixture of palladacycles,¹⁵⁵ using *in situ* generated $[\text{Pd}(\text{MeCN})_4][\text{BF}_4]_2$. The Pd(II) source $[\text{Pd}(\text{MeCN})_4][\text{BF}_4]_2$ has been used for synthesis of palladacycles,^{13,155,186,187} and acts as a source of highly electrophilic Pd(II).¹⁸⁸ As the previous synthesis by Baltus¹⁵⁵ yielded a mixture of chlorido bridged and aqua complexes (Figure 3.6 and Figure 3.7) the monomeric chloropalladacycle was synthesised by reacting the crude reaction mixture with an excess of NaCl (Scheme 3.12).



Scheme 3.12 C-H bond activation of **1a** with salt metathesis to **2a**.

The combined C-H bond activation and salt metathesis reaction proceeded in 71% yield, giving the desired product, **2a** in overall 36% yield from the starting boronic acid **3** and bromopyridine **4**. The X-ray structure contains two distinct structures, consisting a 50:50 disordered structure, which is shown in Figure 3.13, and separated for clarity, with structure A on the left, and structure B on the right in Figure 3.14. A detailed discussion on the structures are provided in Section 3.2.11.

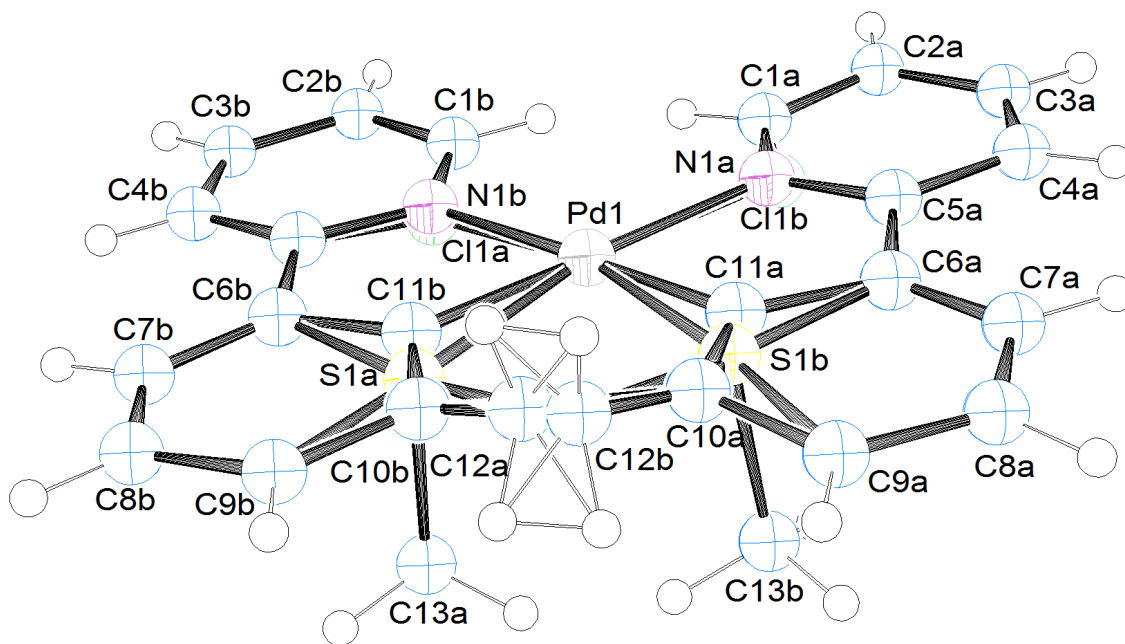


Figure 3.13 Twinned crystal structure of **2a**.

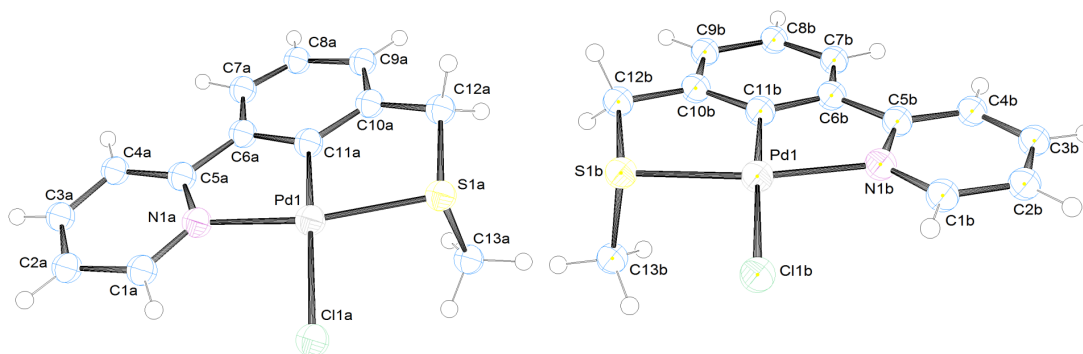


Figure 3.14 Separated crystal structures of **2a**. Left is structure A, right is structure B.

The overall yield for the synthesis of **2a** is comparable to the yields found for other unsymmetrical palladacycles. For example, for the synthesis of the PCS palladacycle shown in Scheme 3.3 the yield is 25%.¹³ Examples of unsymmetrical SCN pincer pincer palladacycles with examples shown in Figure 3.15 have yields for the C-H bond activation step (excluding ligand synthesis) of between 12 and 52 %.¹⁶ The *trans*-chloropalladation of alkynes is another successful route to unsymmetrical palladacycles which for the examples shown proceed between 70 and 95 % yield.¹⁷

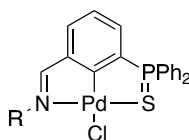


Figure 3.15 Odinets and co-workers SCN pincer palladacycles.

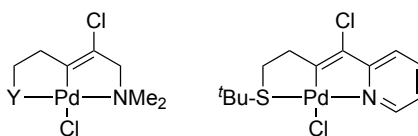


Figure 3.16 Examples of unsymmetrical palladacycles synthesised by chloropalladation by Dupont and co-workers.

3.2.6 Unsymmetrical SCN pincer palladacycle formation reaction pathway

Having synthesised the SCN pincer palladacycle **2a**, the aim of this work was to study the formation pathway for the unsymmetrical SCN pincer palladacycle (Figure 3.8) following the reaction pathways to symmetrical pincer palladacycles performed previously within our group (Scheme 3.6).⁹⁶ The purpose was to investigate the underlying chemical and physical properties with a focus on the role of the donor atoms coordinated to the palladium centre, and establish any differences on the pathway in the transition from symmetric to unsymmetric palladacycles. Any changes in the energetics of the formation pathway would provide evidence that the properties of the donor atoms could have an impact on catalytic applications of the resulting palladacycle.

The structures of interest in this study are shown in Figure 3.17, they are the two symmetrical PdSCS (**I**) and PdNCN examples (**II**), the unsymmetrical pincer ligand **1a**, and the desired PdSCN palladacycle **2a**, all experimentally synthesised. The model formation reaction studied is shown in Scheme 3.13, which like the previous pathway (Scheme 3.6) occurs without the role of base or solvent (initially) in order for comparison, and to easily study the fundamental chemical and physical properties of the ligand.

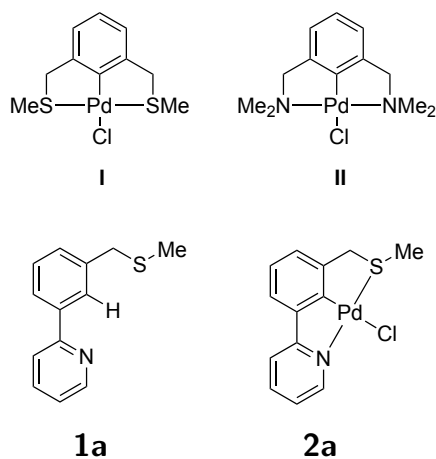
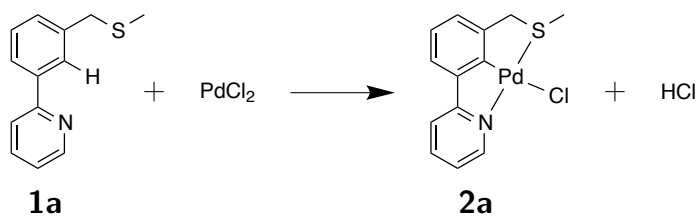


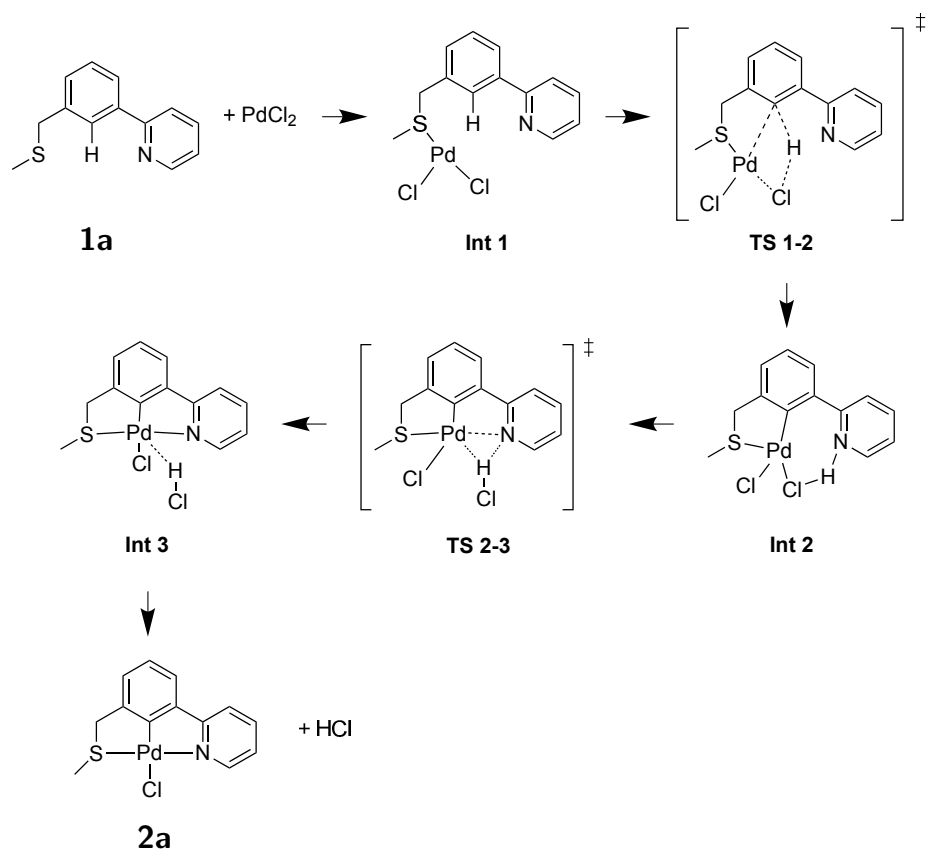
Figure 3.17 Symmetrical pincer palladacycle comparison with unsymmetrical ligand and palladacycle.



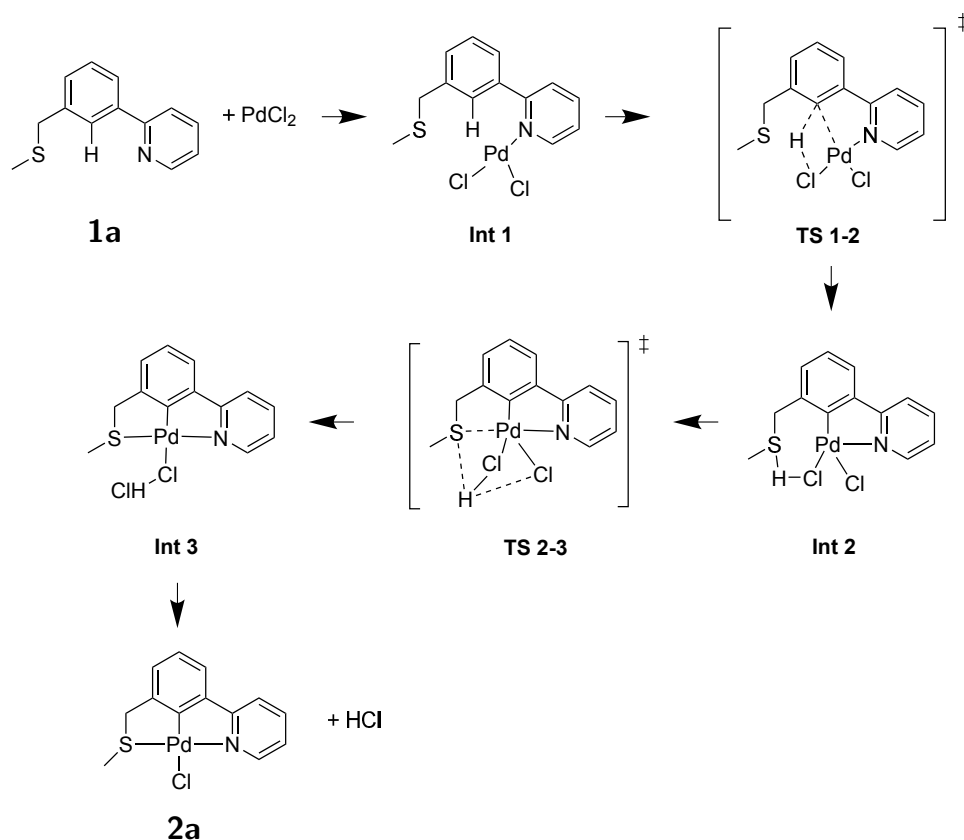
Scheme 3.13 Model formation reaction of **1a** to **2a** by C-H bond activation with PdCl_2 .

3.2.7 Pathway towards **2a** with either N- or S-coordinating to Pd first

The pathway has several possibilities, depending on whether the SMe group or the 2-pyridyl group coordinates to PdCl_2 first. These two pathways will be labelled as *S-coordinates*, where the SMe group coordinates to PdCl_2 first (Scheme 3.14), and *N-coordinates*, where 2-pyridyl coordinates to PdCl_2 first (Scheme 3.15).



Scheme 3.14 Model formation pathway to **2a**, *S*-coordinates, with SMe coordinating to PdCl_2 first.



Scheme 3.15 Model formation pathway to **2a**, *N-coordinates*, with 2-pyridyl coordinating to PdCl₂ first.

The pathways contain several steps, which include the ligand coordination to PdCl₂ either via S- or N-coordinating first in **Int 1**; the C-H bond activation, resulting in the formation of the new Pd-C bond in **TS 1-2**; the ligand coordination step of the other ligand donor atom, which eliminates the bridging HCl unit in **TS 2-3**; and finally the elimination of the coordinated HCl unit to form **2a**.

The energetics, or the energies of the stationary points along each of the pathways, *S-coordinates* (Scheme 3.14) and *N-coordinates* (Scheme 3.15), are shown in Table 3.2 which show that the formation pathway to the unsymmetrical pincer palladacycle **2a** regardless of which donor atom coordinates to the palladium first, is energetically favourable ($\Delta E_0 < -247 \text{ kJ mol}^{-1}$) and thermodynamically stable ($\Delta G < -222 \text{ kJ mol}^{-1}$).

The E_0 values are the zero-point energy corrected values ($E_0 = E_{elec} + ZPE$). The Gibbs free energies, G values are made up of the sum of E (3.1), and the effects of temperature (T) and entropy (S) (3.2 and 3.3), where H is the enthalpy.

Table 3.2 Zero-point corrected (ΔE_0), and Gibbs free (ΔG) energies for *S-coordinates* and *N-coordinates* formation pathways to **2a**.

Structure	ΔE_0 / kJ mol ⁻¹		ΔG / kJ mol ⁻¹	
	<i>S-coordinates</i>	<i>N-coordinates</i>	<i>S-coordinates</i>	<i>N-coordinates</i>
1a + PdCl ₂	0.0	0.0	0.0	0.0
Int 1	-198.8	-216.9	-141.3	-161.1
TS 1-2	-103.3	-91.7	-40.3	-30.5
Int 2	-217.4	-173.2	-153.7	-112.1
TS 2-3	-174.9	-147.0	-114.2	-84.9
Int 3	-277.6	-282.9	-218.9	-226.7
2a + HCl	-250.4	-247.5	-225.3	-222.2

$$E = E_0 + E_{vib} + E_{rot} + E_{trans} \quad (3.1)$$

$$H = E + RT \quad (3.2)$$

$$G = H - TS \quad (3.3)$$

The overall ΔE_0 and ΔG values (Table 3.2) for **2a** are slightly different (<3 kJ mol⁻¹) depending on the pathway, *S-coordinates* or *N-coordinates*, due to minor conformational variations of **1a** and **2a** in the respective pathways. All transition states are confirmed by eigenvector following calculations, resulting in the differing conformers of **1a** and **2a**. The explanation for the divergence of the ΔE_0 and ΔG values is primarily caused by the inclusion of the entropy (S in 3.3) of the system in ΔG . For example in **Int 1** the loss of entropy as the molecules bind makes ΔG less favourable than ΔE_0 by 57.5 kJ mol⁻¹ in the *S-coordinates* pathway. This entropy is regained upon the HCl elimination after **Int 3**.

Comparing the two pathways, several key differences emerge. In the initial Pd-L bond formation in **Int 1**, between ligand **1a** and PdCl₂ with the thioether or pyridine coordinating first, differing energies were found for the two pathways. The *N-coordinates* pathway shows greater stability for **Int 1** ($\Delta G = -161.1$ kJ mol⁻¹)

compared to the *S-coordinates* pathway ($\Delta G = -141.3 \text{ kJ mol}^{-1}$). In the first transition state, **TS 1-2**, the C-H bond activation step, the energy barriers vary between the two pathways, with the *N-coordinates* pathway having a larger barrier ($\Delta G^\ddagger = 130.6 \text{ kJ mol}^{-1}$) than the *S-coordinates* pathway ($\Delta G^\ddagger = 101.0 \text{ kJ mol}^{-1}$). The product of the C-H bond activation, **Int 2**, has significant variations in stability between the pathways, with a difference of 41.6 kJ mol^{-1} between the pathways, with the *S-coordinates* pathway being more stable.

In order to explain the differences between the two pathways discussed, the role of the donor atoms in the pathway has been investigated using Bader’s Atoms in Molecules (AIM) analysis.^{133,134} The key parameters from the AIM analysis are tabulated for the *S-coordinates* (Table 3.3) and *N-coordinates* pathways (Table 3.4). The $\rho(\mathbf{r})$ values indicate the strength of the bond, $\nabla^2\rho(\mathbf{r})$ and $H(\mathbf{r})$ indicate the nature, or the degree of covalency/ionicity of the bonding (see Section 2.5 for more detail).¹³⁸

The greater stability of **Int 1** in the *N-coordinates* pathway (by 19.8 kJ mol^{-1}) can be explained by the strength of the Pd-L bonds, which is investigated using $\rho(\mathbf{r})$ values obtained for each newly formed bond. In the *S-coordinates* pathway a new Pd-S bond is formed in **Int 1**, with a $\rho(\mathbf{r})$ value of 0.087 a.u. (Table 3.3). In comparison, in the *N-coordinates* pathway, the newly formed Pd-N bond has a $\rho(\mathbf{r})$ value of 0.096 a.u. (Table 3.4). The larger $\rho(\mathbf{r})$ value for **Int 1** in the *N-coordinates* pathway is an explanation for the greater stability than the structure in the *S-coordinates* pathway (Table 3.2).

In **TS 1-2**, the C-H bond activation step, the smaller activation barrier in the *S-coordinates* pathway ($\Delta G^\ddagger = 101.0 \text{ kJ mol}^{-1}$) than the *N-coordinates* pathway ($\Delta G^\ddagger = 130.6 \text{ kJ mol}^{-1}$) is unexpected (Table 3.2), due to the relative strength of the Pd-S (0.094 a.u. , Table 3.3) and Pd-N (0.105 a.u. , Table 3.4) bonds in **TS 1-2** for each pathway, respectively. In order to further investigate the difference in these energy barriers, the nature of the bonding was investigated.

The sign and magnitude of the $\nabla^2\rho(\mathbf{r})$ and $H(\mathbf{r})$ values provide information on

Table 3.3 AIM parameters for the *S-coordinates* pathway in the formation reaction pathway of **2a** (Scheme 3.14). All values given in a.u.

Structure	Bond	$\rho(\mathbf{r})$	$\nabla^2\rho(\mathbf{r})$	$H(\mathbf{r})$
Ligand	C-H	0.286	-1.062	-0.306
Int 1	C-H	0.287	-1.065	-0.306
	Pd-S	0.087	0.237	-0.023
	Pd-C	0.042	0.112	-0.007
	Pd-Cl (cleaving)	0.091	0.260	-0.023
TS 1-2	C-H	0.108	-0.090	-0.057
	Pd-S	0.094	0.231	-0.027
	Pd-C	0.105	0.211	-0.035
	Pd-Cl (cleaving)	0.063	0.206	-0.013
Int 2	Pd-S	0.090	0.238	-0.025
	Pd-C	0.123	0.247	-0.044
	Pd-Cl (cleaving)	0.070	0.231	-0.014
	N-H	0.295	-1.690	-0.474
TS 2-3	Pd-S	0.098	0.246	-0.029
	Pd-C	0.141	0.217	-0.058
	Pd-Cl (cleaving)	0.023	0.076	-0.002
	N-H	0.153	-0.246	-0.121
	Pd-N	0.025	0.095	-0.002
Int 3	Pd-S	0.093	0.257	-0.026
	Pd-C	0.147	0.231	-0.062
	Pd-N	0.097	0.453	-0.018
	Pd-H	0.025	0.049	-0.003
2a	Pd-S	0.093	0.264	-0.026
	Pd-C	0.149	0.238	-0.063
	Pd-N	0.096	0.455	-0.017

Table 3.4 AIM parameters for the *N-coordinates* pathway in the formation reaction pathway of **2a**. All values given in a.u.

Structure	Bond	$\rho(\mathbf{r})$	$\nabla^2\rho(\mathbf{r})$	$H(\mathbf{r})$
Ligand	C-H	0.289	-1.085	-0.309
Int 1	C-H	0.283	-1.035	-0.299
	Pd-N	0.096	0.459	-0.017
	Pd-C	0.044	0.124	-0.009
	Pd-Cl (cleaving)	0.093	0.263	-0.023
TS 1-2	C-H	0.097	-0.050	-0.046
	Pd-N	0.105	0.467	-0.023
	Pd-C	0.110	0.217	-0.038
	Pd-Cl (cleaving)	0.014	0.048	0.002
Int 2 ,	Pd-N	0.107	0.478	-0.023
	Pd-C	0.125	0.224	-0.046
	Pd-Cl (cleaving)	0.062	0.229	-0.010
	S-H	0.072	-0.002	-0.027
TS 2-3	Pd-N	0.109	0.481	-0.024
	Pd-C	0.133	0.212	-0.052
	Pd-Cl (cleaving)	0.046	0.163	-0.007
	S-H	0.016	0.042	0.001
	Pd-S	0.009	0.028	0.001
Int 3	Pd-N	0.097	0.455	-0.018
	Pd-C	0.149	0.229	-0.064
	Pd-S	0.090	0.251	-0.025
2a	Pd-N	0.097	0.457	-0.018
	Pd-C	0.148	0.240	-0.063
	Pd-S	0.091	0.257	-0.025

the degree of covalency and/or ionicity of bonds (see Section 2.5).^{152,189} In **TS 1-2** the Pd-S bond in the *S-coordinates* pathway has a $\nabla^2\rho(\mathbf{r})$ value of 0.231 a.u., and a $H(\mathbf{r})$ value of -0.027 a.u. (Table 3.3). These values suggest a partial ionic, partial covalent character, as a positive $\nabla^2\rho(\mathbf{r})$ suggests an ionic interaction, whereas a negative $H(\mathbf{r})$ suggests a covalent interaction. These partial ionic and partial covalent interactions are typical for many metal-donor atom bonds.^{152,190–194}

In comparison, in the *N-coordinates* pathway, the Pd-N bond in **TS 1-2** has a $\nabla^2\rho(\mathbf{r})$ value of 0.467 a.u., and a $H(\mathbf{r})$ value of -0.023 a.u. (Table 3.4). The larger $\nabla^2\rho(\mathbf{r})$ and less negative $H(\mathbf{r})$ values for the Pd-N bond compared to the Pd-S bond in the *S-coordinates* pathway discussed above both indicate that the Pd-N bond for **TS 1-2** has greater ionic character than the Pd-S bond. A key consequence of this differing nature of the bonding could be the charge distribution within the pathway, which could have implications in the stability of key structures. The finding that the Pd-N bond is more ionic than the Pd-S bond is also borne out in all other structures in the pathway.

In order to further investigate the effect of the nature of the bonding, the Bader charges have been tabulated for each atom in each structure along each of the pathways (Table 3.5). The values are slightly different for **2a** depending on the pathway, due to the small conformational differences. A striking feature of the charge data is that for all structures in the *S-coordinates* pathway, the palladium charge is always lower than when N-coordinates first. For example, in **Int 1** the Pd charge in the *S-coordinates* pathway is 0.610 a.u. (Table 3.5), whereas in the *N-coordinates* pathway this charge is increased to 0.709 a.u, this in comparison to the Pd charge in PdCl_2 of 0.683 a.u.

These differences in charge suggest a greater electron donating ability of the thioether arm, compared to that of the pyridine. For example, in the formation of **Int 1**, in the *S-coordinates* pathway, the S charge goes from -0.009 a.u. in **1a**, to 0.117 a.u. in **Int 1**, clearly showing a net donation of electron density from the S atom to the Pd atom. In comparison, in the *N-coordinates* pathway the N atom

Table 3.5 Bader charges for the formation reaction pathway of **2a**. All charges are given in a.u.

Structure	Atom	S-coordinates first	N-coordinates first
PdCl ₂	Pd	0.683	
1a	S	-0.009	-0.013
	N	-1.135	-1.137
	C	-0.032	-0.019
	H	0.009	0.048
Int 1	Pd	0.610	0.709
	S	0.117	0.007
	N	-1.135	-1.175
	C	-0.064	-0.096
	H	0.029	0.054
TS 1-2	Pd	0.587	0.706
	S	0.122	-0.002
	N	-1.132	-1.149
	C	-0.274	-0.252
	H	0.328	0.318
Int 2	Pd	0.565	0.661
	S	0.104	-0.021
	N	-1.274	-1.149
	C	-0.126	-0.145
	H	0.528	0.347
TS 2-3	Pd	0.570	0.658
	S	0.137	-0.042
	N	-1.233	-1.145
	C	-0.120	-0.139
	H	0.483	0.316
Int 3	Pd	0.554	0.575
	S	0.094	0.116
	N	-1.157	-1.153
	C	-0.133	-0.122
	H	0.285	0.340
2a	Pd	0.575	0.578
	S	0.098	0.105
	N	-1.154	-1.152
	C	-0.125	-0.126

in **1a** has a charge of -1.137 a.u., which decreases to -1.175 a.u., gaining electron density from the Pd atom, contrary to the *S-coordinates* pathway.

Therefore the greater electron donating ability of the S atom has greater ability to quench the palladium charge than the N atom of the pyridine donor arm. Hence the ability to stabilise the electrophilic palladium atom¹⁷⁴ in **TS 1-2** is the likely explanation for the decrease in the energy barrier for the C-H bond activation step, despite the weaker Pd-S bond, compared to that in the *N-coordinates* pathway.

There is a significant difference between the energies for **Int 2** depending on the pathway (41.6 kJ mol⁻¹, Table 3.2), which has implications on the second energy barrier for the coordination of the second donor atom and the cleavage of the Pd-Cl bond. In this intermediate, one of either two stabilising interactions is formed, an N-H interaction in the *S-coordinates* pathway, or an S-H interaction in the *N-coordinates* pathway (Figure 3.18). The $\rho(\mathbf{r})$ values of the N-H and S-H interactions can be used to explain the significantly different stabilities of the different structures. The N-H interaction has $\rho(\mathbf{r}) = 0.295$ a.u. (Table 3.3), whereas the S-H interaction has $\rho(\mathbf{r}) = 0.072$ a.u. (Table 3.4), clearly showing the strong N-H interaction stabilises **Int 2** in the *S-coordinates* pathway, explaining the 41.6 kJ mol⁻¹ energy difference between the two structures.

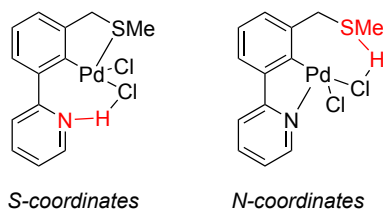


Figure 3.18 **Int 2** structures with N-H and S-H stabilising bonds, highlighted in red.

For **TS 2-3** there is a larger energy barrier in the *S-coordinates* pathway ($\Delta G^\ddagger = 39.5$ kJ mol⁻¹) than in the *N-coordinates* pathway ($\Delta G^\ddagger = 27.2$ kJ mol⁻¹, Table 3.2). There are several factors affecting these differing energy barriers, including the nature of the transition state and the cleavage of the N-H or S-H bonds. For both systems, the major component of the imaginary mode in this transition state is the cleavage of the strong N-H bond in the *S-coordinates* pathway (Figure 3.19), and the weaker

S-H bond in the *N-coordinates* pathway (Figure 3.20), respectively. Therefore, the cleavage of the stronger N-H bond as discussed earlier, is likely to be a major factor in the increased transition state barrier for **TS 2-3** for S-coordinates first.

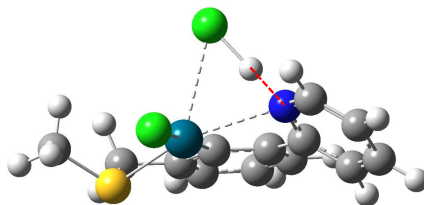


Figure 3.19 **TS 2-3** for the *S-coordinates* pathway, with the cleaving N-H bond shown in red.

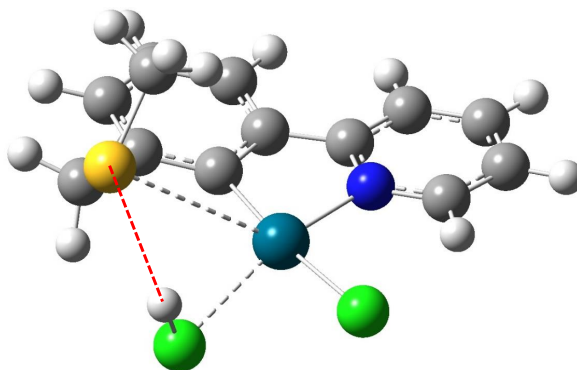


Figure 3.20 **TS 2-3** for the *N-coordinates* pathway, with the cleaving S-H bond shown in red.

The values for **Int 3** and the final product **2a** are very similar for both pathways due to their very similar structures, and as discussed previously any small differences are due to the slightly different conformers of **1a** and **2a**.

3.2.8 Comparison to previously studied PdSCS and PdNCN palladacycles

In this section, the results for the model formation pathway to **2a** are compared with that published previously for the symmetrical PdSCS, **I**, and PdNCN, **II**, examples (Figure 3.17),⁹⁶ and for the unsymmetrical PdSCN example (Figure 3.21).⁹⁷

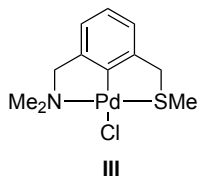
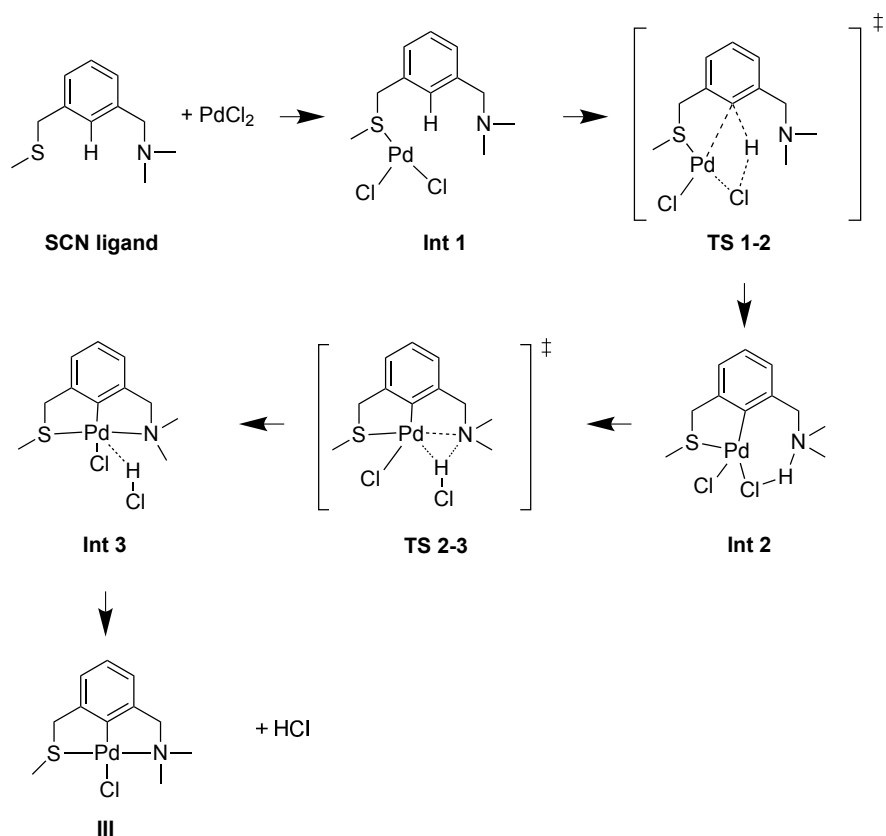


Figure 3.21 A model unsymmetrical PdSCN palladacycle.

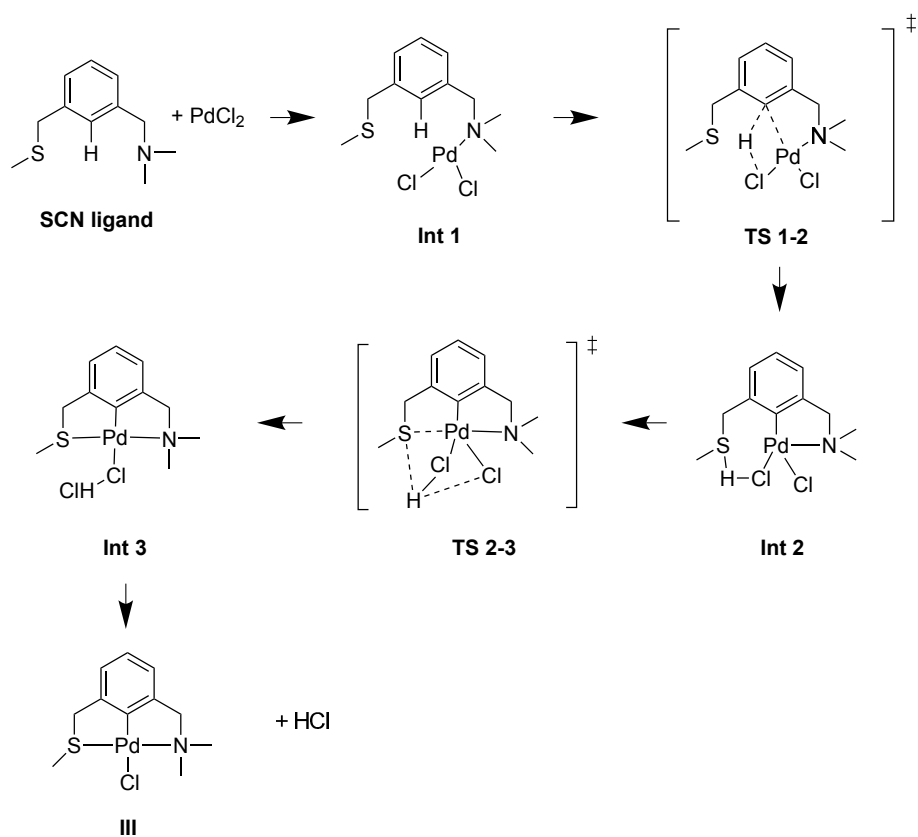
The energy values published for the symmetrical PdSCS and PdNCN structures were calculated using the ω B97XD/6-311++G(2df,2p)[SDD]//PBE/6-31+G(d,p)[SDD] model chemistry.⁹⁶ In this thesis, all calculations are performed using ω B97XD/6-311++G(2df,2p)[SDD]// ω B97XD/6-31++G(d,p)[SDD] with the use of the dispersion corrected functional ω B97XD and the extra diffuse functions for the hydrogen atoms for geometry optimisation. Therefore to provide the most accurate comparison the previous pathways towards **I** and **II** have been reoptimised, and single point energies calculated using the ω B97XD/6-311++G(2df,2p)[SDD]// ω B97XD/6-31++G(d,p)[SDD] model chemistry.

In the present work with unsymmetrical pincer palladacycles **2a** and **III**, it was found that the HCl elimination occurs at **Int 3** (Scheme 3.14 and Scheme 3.15), whereas in the formation of **I** and **II** the elimination occurs after **Int 2** (Scheme 3.7).⁹⁶ This has implications only when considering **TS 2-3**, as the initial and rate-determining transition state **TS 1-2** in each pathway are identical for all structures.

The pathway for the formation of the PdSCN example **III** (Figure 3.21) has the same pathway and methodology as found for **2a** and therefore with a *S-coordinates* pathway (Scheme 3.16) and a *N-coordinates* pathway (Scheme 3.17).



Scheme 3.16 Model formation pathway to **(III)**, *S*-coordinates first.



Scheme 3.17 Model formation pathway to **(III)**, *N*-coordinates first.

The energy barriers for the key C-H bond activation step for the symmetrical PdSCS (**I**) and PdNCN (**II**), along with the unsymmetrical PdSCN (**III**, Figure 3.21), and for **2a** are tabulated (Table 3.6). The results show that for the key C-H bond activation step **TS 1-2**, in all cases the barrier for the *S-coordinates* pathway is lower than that for the *N-coordinates* pathway, in line with that found for **2a**. The formation of PdSCS (**I**) has a slightly lower barrier ($\Delta G^\ddagger = 111.6 \text{ kJ mol}^{-1}$) than that of PdNCN (**II**, $\Delta G^\ddagger = 123.1 \text{ kJ mol}^{-1}$); and for the unsymmetrical PdSCN example (Figure 3.21) the *S-coordinates* pathway is lower in energy ($\Delta G^\ddagger = 124.0 \text{ kJ mol}^{-1}$) than the *N-coordinates* pathway ($\Delta G^\ddagger = 129.2 \text{ kJ mol}^{-1}$). These results are in agreement with that found for the formation of **2a**, i.e. the *S-coordinates* pathway barrier is lower than that of the *N-coordinates* pathway.

Table 3.6 C-H bond activation energy barrier comparison between various symmetrical and unsymmetrical pincer palladacycles.

Structure	$\Delta G^\ddagger / \text{kJ mol}^{-1}$	
	<i>S-coordinates</i>	<i>N-coordinates</i>
PdSCS, I	111.6	n/a
PdNCN, II	n/a	123.1
PdSCN, III	124.0	129.2
2a	101.0	130.6

Other comparisons between the two pathways include the relative energetic stability of the first Pd-L interaction, in the formation of **Int 1** in each case (Table 3.7). In all cases, for PdSCS, **I** (Figure 3.17), PdSCN, **III** (Figure 3.21) and **2a** in the *S-coordinates* pathway, the formation of the Pd-S bond is less energetically favourable than that of the Pd-N bond, i.e. for PdNCN, **II**, PdSCN, **III** and **2a** in the *N-coordinates* pathway.

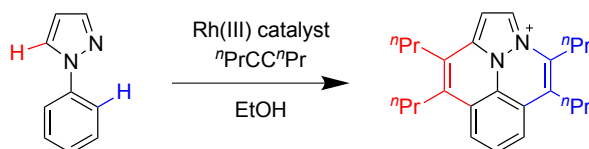
Table 3.7 Energy of **Int 1** comparison between various symmetrical and unsymmetrical pincer palladacycles .

Structure	$\Delta G / \text{kJ mol}^{-1}$	
	<i>S-coordinates</i>	<i>N-coordinates</i>
PdSCS, I	-157.5	n/a
PdNCN, II	n/a	-170.2
PdSCN, III	-148.5	-170.5
2a	-141.3	-161.1

It can be seen that the observations found in the formation pathway of **2a** for the varying energies of **Int 1** depending on the pathway and the varying C-H bond activation barriers is mirrored in that for pathways of **I**, **II** and **III**. Also, moving to unsymmetrical examples provides a significant alteration in the energetics of the formation pathways, as it has been shown that moving to unsymmetrical examples, PdSCN **III** and **2a** provide the opportunity to have two different pathways to vary the C-H bond activation barrier. Having the presence of the other ligand could be beneficial in catalysis, such as in the catalyst activation pathway, due to the different bond strengths and natures.

3.2.9 Solvation effects

All of the calculations discussed to this point have been performed in the gas-phase, without the inclusion of solvation effects. To investigate such effects, calculations were performed with the inclusion of solvent to investigate any differences in the energetics and kinetics of the pathways. It has been shown that inclusion of solvent effects can have a significant influence on the energetic pathways for C-H bond activation processes. For example, that shown by Macgregor and co-workers on the regioselectivity of the C-H bond activation, with significantly different energetic profiles depending on whether EtOH or xylene were used as the solvent, where the C-H bond activation of the blue C-H bond yields a cationic complex, favoured by the polar solvent, EtOH, and the red C-H bond activation is favoured in the non-polar solvent, xylene (Scheme 3.18).¹²⁸ A popular method for inclusion of solvent effects is the polarisable continuum model (PCM),¹²⁶ discussed more fully in Section 2.4 which is normally applied as an energy correction to the gas-phase structure.



Scheme 3.18 Solvent dependent C-H bond activation by Macgregor and co-workers.

In order to investigate the solvation effects, the formation pathways were calculated using MeCN as the solvent, using the PCM model due to the use of MeCN in the experimental synthesis. As the solvation effects are added as an energy correction the structures in the pathways remain the same as shown in Scheme 3.14 and Scheme 3.15. The energies are given in Table 3.8 which show the solvent corrected energies are different to those without solvent (Table 3.2). However, we are interested in the trends in the values, such as the change in the coordination and C-H bond activation energies in order to compare the two sets of data (Table 3.9, Table 3.10 and Table 3.11).

Table 3.8 Solvent corrected ΔE_{0S} and ΔG_S energies for each pathway to **2a**.

Structure	$\Delta E_{0S} / \text{kJ mol}^{-1}$		$\Delta G_S / \text{kJ mol}^{-1}$	
	<i>S-coordinates</i>	<i>N-coordinates</i>	<i>S-coordinates</i>	<i>N-coordinates</i>
1a + PdCl ₂	0.0	0.0	0.0	0.0
Int 1	-148.9	-161.0	-91.4	-105.2
TS 1-2	-28.2	-12.3	34.8	48.9
Int 2	-177.2	-93.0	-113.5	-31.8
TS 2-3	-123.1	-64.1	-62.4	-2.1
Int 3	-194.2	-199.9	-135.5	-143.7
2a + HCl	-175.8	-175.5	-150.8	-150.3

Firstly the coordination energies are compared with and without solvent, and the values are shown in Table 3.9. There is a decrease in energy when the effects of the solvation are included, of between 57 and 58 kJ mol⁻¹, for ΔE_0 and ΔG . Therefore the solvation effects are consistent for each pathway.

Table 3.9 **Int 1** coordination energy of **1a** to PdCl₂ comparison with (ΔX_S) and without (ΔX) MeCN solvent (where $X = E_0$ or G).

	Energy / kJ mol ⁻¹	
	<i>S-coordinates</i>	<i>N-coordinates</i>
ΔE_0	-211.7	-230.6
ΔE_{0S}	-154.5	-172.7
ΔG	-155.8	-170.5
ΔG_S	-98.6	-112.6

Despite the changes due to the solvation energy shown (Table 3.9) the trend that the *N-coordinates* pathway is more favourable than the *S-coordinates* pathway is still

evident, with the *N-coordinates* pathway with solvation included being 14.0 kJ mol^{-1} more favourable than the *S-coordinates* pathway for ΔG_S (Table 3.9). This compares to a difference of 14.7 kJ mol^{-1} for ΔG , therefore despite the overall energy values changing, the trends in the results are the same with and without the inclusion of solvent effects for the ligand **2a** coordination to PdCl_2 .

The energy values can also be compared for the C-H bond activation energy barriers (Table 3.10). In this case the energy barriers increase by between 23 and 25 kJ mol^{-1} for ΔE_{0S}^\ddagger and ΔG_S^\ddagger , respectively. Despite these increases, the trends in the differences between the pathways remains the same, as the difference is 29.7 kJ mol^{-1} for ΔG^\ddagger and 27.6 kJ mol^{-1} for ΔG_S^\ddagger . Again the inclusion of the solvent changes the absolute energy values, but not the overall trends.

Table 3.10 TS 1-2 C-H bond activation energy barrier comparison with and without MeCN solvent.

	Energy / kJ mol^{-1}	
	<i>S-coordinates</i>	<i>N-coordinates</i>
ΔE_0^\ddagger	95.5	125.2
ΔE_{0S}^\ddagger	120.7	148.7
ΔG^\ddagger	101.0	130.7
ΔG_S^\ddagger	126.2	154.1

Finally the overall formation energies can be compared, which are tabulated (Table 3.11) and show that solvation significantly decreases formation energy, decreasing by 70 to 75 kJ mol^{-1} when solvent corrections are added to ΔE_0 or ΔG .

Table 3.11 Overall formation energy with and without MeCN solvent.

	Energy / kJ mol^{-1}	
	<i>S-coordinates</i>	<i>N-coordinates</i>
ΔE_0^\ddagger	-250.4	-247.5
ΔE_{0S}^\ddagger	-175.8	-175.5
ΔG^\ddagger	-225.3	-222.2
ΔG_S^\ddagger	-150.8	-150.3

3.2.10 Summary

These results show that the unsymmetrical pincer ligands significantly effect key steps in the formation reaction pathway, such as ligand coordination and C-H bond activation. It was found that the Pd-N bonds are stronger (larger $\rho(\mathbf{r})$ values), however the S donor atom is more electron donating (stabilises electrophilic Pd centre) than the N donor atom, resulting in smaller C-H bond activation barriers. It was also shown that the model formation reactions studied were energetically and thermodynamically favourable. The effect of solvation was also investigated, showing the significant differences in energy values when the solvent energy corrections are added, however the trends found without solvent inclusion remain, and the energy profile is shown for both pathways (Figure 3.22) including corrections for Gibbs free energy and solvent.

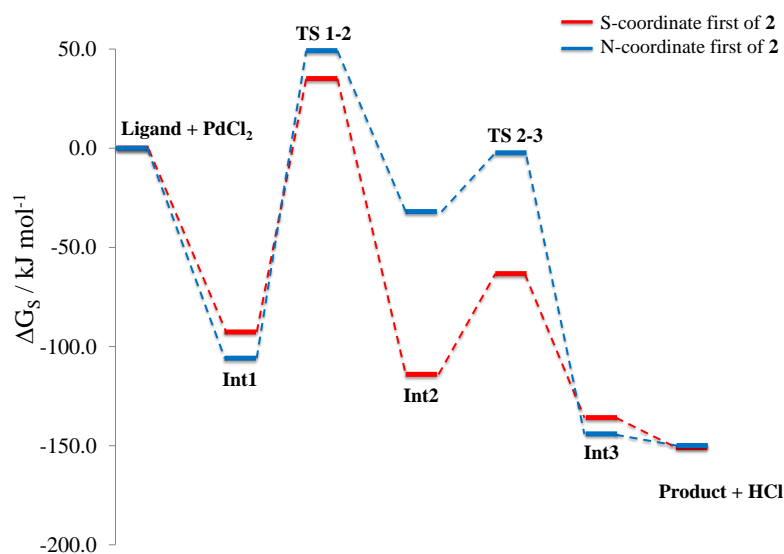


Figure 3.22 Gibbs free and solvent corrected energetic profile for the formation reaction pathway to **2a**.

3.2.11 Comparison of theoretically determined and experimental solid state geometry of **2a**

With the experimentally determined X-ray crystal structure, further validation of the chosen DFT methodology can be undertaken. The DFT methodology has previously

been validated in the study into the symmetrical PdSCS (**I**)⁸ and PdNCN (**II**)⁹ palladacycles (Figure 3.17) however as an additional check into the validity in the choice of methodology the solid state X-ray crystal structures are compared here to the theoretically calculated structures.

The solid state X-ray crystal structure (Figure 3.13) which has been separated into two structures (Figure 3.14) can be used to compare the experimental and theoretical structures. Geometry optimisation from the experimental structure is important as the location of the hydrogen atoms are not precisely known from experiment,¹⁴⁶ and as the aim is to also study structures without crystal structure data, the gas-phase energy minima will be calculated. The accuracy of reproduction of the X-ray structure will be compared by calculating the mean unsigned errors (MUE), found by Minenkov and co-workers *et al.*¹⁴⁶ for metal containing bond lengths in ruthenium complexes to range from 0.020 to 0.045 Å.

The palladacycles display a distorted square planar geometry, with the experimental and theoretical Pd-L bond lengths tabulated for both structures (Table 3.12). Variations between experiment and theory range from 0.000 to 0.026 Å which is comparable to that found previously by Minenkov and co-workers,¹⁴⁶ and that found for the PBE functional in the previous method validation study (0.025 Å) for symmetrical pincer palladacycles.⁹⁶ Also the bond, and dihedral angles around the palladium centre are very close to the experimental values (Table 3.13), with bond angle differences within 1.0° and the dihedral within 4.0°. The combination of these two sets of data provide confidence in the accuracy of the theoretical calculations to model the experimental geometries of the Pd-L environment.

Table 3.12 Experimental and theoretical Pd-L bond distance comparison for **2a**.

Bond	Exp. A	Exp. B	Opt. A	Opt. B	Δ A	Δ B
	Distance / Å					
Pd-S	2.291	2.291	2.314	2.314	0.023	0.023
Pd-N	2.082	2.080	2.080	2.080	0.002	0.000
Pd-Cl	2.423	2.403	2.397	2.397	0.026	0.007
Pd-C	1.951	1.974	1.954	1.954	0.004	0.020

Table 3.13 Experimental and theoretical bond angle and dihedral comparison for **2a** around the palladium centre.

Bond	Exp. A	Exp. B	Opt. A	Opt. B	Δ A	Δ B
	Angle / °					
N-Pd-S	165.2	164.9	165.7	165.7	0.6	0.9
N-Pd-C	80.5	80.4	80.5	80.5	0.0	0.1
S-Pd-C	84.8	84.6	85.2	85.2	0.5	0.6
N-Pd-S-C	7.9	-8.6	4.8	-4.8	-3.1	3.8

3.3 Conclusions

In this chapter, it has been shown that for the model formation reaction to **2a** calculated using density functional theory the donor atoms have a significant effect on the energetics of the pathway, including the different stability of the ligand coordination to PdCl₂, the varying C-H bond activation, and the HCl elimination barriers depending on whether N- or S-coordinates to the PdCl₂ first. This suggests clearly that having different donor atoms present in the palladacycle is having an impact on bond strength and the nature of the interactions as determined using Bader’s Atoms in Molecules theory, leading to the desire to synthesise unsymmetrical SCN palladacycle. A new versatile synthetic route to unsymmetrical SCN ligands was devised with late stage diversification possible as the last step is a nucleophilic substitution allowing library generation. The desired SCN ligand **1a** was successfully synthesised in an overall yield of 51 %, and then underwent cyclopalladation with [Pd(MeCN)₄][BF₄]₂ yielding the desired SCN palladacycle **2a** in an overall 36 % yield. It was also found that our choice of DFT methodology reproduces experimentally determined structures. This work has been published in Royal Society Open Science.⁹⁷

3.4 Experimental details

3.4.1 General Details

Solvents and chemicals were purchased from commercial suppliers and used without further purification, with most reactions taking place open to atmosphere and

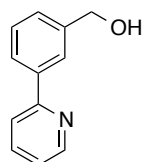
moisture. C-H activation reactions were undertaken using Schlenk techniques, under nitrogen, in dry acetonitrile.

3.4.2 Instrumentation

^1H and $^{13}\text{C}\{^1\text{H}\}$ spectra were recorded on a Varian 500, or 400 MHz spectrometer. HRMS has been obtained on an ESI mass spectrometer using a Bruker Daltonics Apex III, with ESI source Apollo ESI, using methanol as the spray solvent by Dr. Alaa K. Abdul-Sada of the University of Sussex Mass Spectrometry Centre. GC measurements were obtained using a Perkin Elmer Autosystem XL Gas Chromatograph, utilising a flame ionisation detector, and a Supelco MDN-5S 30 m x 0.25 mm x 0.25 μm column, with a He mobile phase. Elemental analyses were run by the London Metropolitan University Elemental Analysis Service. Crystal structures were obtained by the UK National Crystallography Service at the University of Southampton.¹⁹⁵

3.4.3 Experimental Procedures

3-(Pyridin-2-yl)phenyl]methanol, **5**



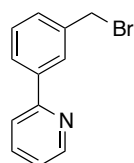
3-[(Hydroxymethyl)phenyl]boronic acid (4.04 mmol, 614 mg), 2-bromopyridine (4.04 mmol, 0.393 mL), $\text{Pd}(\text{PPh}_3)_4$ (0.16 mmol, 182 mg), 0.5 M K_3PO_4 (10 ml), toluene (7.5 ml), EtOH (5 ml) were added to a sealed 35 ml microwave vial and stirred under microwave irradiation (maximum power 300 W, using dynamic heating) at 150 °C for 20 minutes. The reaction was cooled, and the volatiles removed *in vacuo*. The mixture was diluted with H_2O (25 ml) and EtOAc (25 ml), washed with H_2O (2 x 25 ml) and brine (25 ml). The combined organic layers were dried over anhydrous MgSO_4 , filtered, and concentrated *in vacuo*. The crude material was purified using flash column chromatography (7:3 DCM:EtOAc) yielding 694 mg of the expected product **5** as a white solid in 93 % yield.

^1H NMR (500 MHz, Chloroform-*d*) δ (ppm): 8.70 (d, $J = 4.9$ Hz, 1H), 8.02 (s, 1H), 7.90 (d, $J = 7.6$ Hz, 1H), 7.78 - 7.74 (m, 2H), 7.48 (dd, $J = 7.6, 7.6$ Hz, 1H), 7.44 (d, $J = 7.6$ Hz, 1H), 7.24 (ddd, $J = 7.3, 4.9, 2.7$ Hz, 1H), 4.80 (d, $J = 6.0$ Hz, 2H), 1.79 (t, $J = 6.0$ Hz, 1H).

$^{13}\text{C}\{^1\text{H}\}$ NMR (126 MHz, Chloroform-*d*) δ (ppm): 157.3, 149.7, 141.5, 139.7, 136.8, 129.0, 127.5, 126.2, 125.5, 122.2, 120.6, 65.4.

HRMS (m/z). Calc. for $[\text{C}_{12}\text{H}_{11}\text{NO} + \text{Na}]^+$ 208.0733. Found 208.0731.

2-[3-(Bromomethyl)phenyl]pyridine, **6**

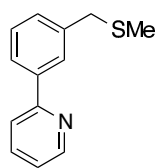


[3-(Pyridin-2-yl)phenyl]methanol, **5** (3.03 mmol, 561 mg) and $\geq 48\%$ HBr in H_2O (5 ml) were added to a 10 ml round bottomed flask and stirred at 150°C for 8 hours, then left to stir overnight at room temperature. The reaction mixture pH was carefully adjusted to approximately 7.5 by careful addition of a saturated NaHCO_3 solution. The crude product was extracted with EtOAc (3 x 50 ml), washed with H_2O (3 x 50 ml) and brine (50 ml). The organic layers were dried over anhydrous MgSO_4 , filtered and the solvent removed *in vacuo*. The crude product was purified using flash column chromatography (9:1 DCM:EtOAc) yielding 568 mg of the expected product **6** as a yellow oil in 76 % yield.

^1H NMR (500 MHz, Chloroform-*d*) δ (ppm): 8.70 (d, $J = 4.9$ Hz, 1H), 8.06 (s, 1H), 7.93 - 7.89 (m, 1H), 7.79 - 7.73 (m, 2H), 7.48 - 7.44 (m, 2H), 7.25 (ddd, $J = 6.7, 4.9, 1.7$ Hz, 1H), 4.58 (s, 2H).

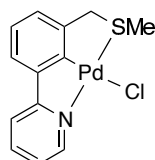
$^{13}\text{C}\{^1\text{H}\}$ NMR (126 MHz, Chloroform-*d*) δ (ppm): 156.7, 149.7, 134.0, 138.4, 136.8, 129.6, 129.2, 127.6, 126.9, 122.4, 120.6, 33.4.

HRMS (m/z). Calc. for $[\text{C}_{12}\text{H}_{10}\text{BrN} + \text{H}]^+$ 248.0069. Found 248.0071.

2-3-[(Methylsulfanyl)methyl]phenylpyridine, 1a

2-[3-(Bromomethyl)phenyl]pyridine, **6** (1.33 mmol, 331 mg), sodium thiomethoxide (1.62 mmol, 114 mg) and EtOH (4 ml) were added to a sealed microwave vial and stirred under microwave irradiation (maximum power 300 W, dynamic heating) at 150 °C for 20 minutes. After cooling, the solvent was removed *in vacuo*, and the crude mixture was diluted with H₂O (25 ml) and EtOAc (25 ml). The crude product was extracted with EtOAc (2 x 25 ml), washed with H₂O (2 x 25 ml) and brine (25 ml). The organic layers were dried over anhydrous Na₂SO₄, filtered and concentrated *in vacuo*. The crude product was purified by flash chromatography (9:1 DCM:EtOAc) yielding 207 mg of the expected product **5** as a yellow oil in 72 % yield.

¹H and ¹³C{¹H}NMR spectra are in agreement with prior literature values.¹⁷⁸

2-3-[(Methylsulfanyl)methyl]phenylpyridine chloro palladacycle, 2a

Under an argon atmosphere, palladium (II) chloride (1.05 mmol, 186 mg) was dissolved in dry MeCN (8 ml) and heated under reflux until a red solution had formed. Silver tetrafluoroborate (2.10 mmol, 409 mg) dissolved in dry MeCN (8 ml) was added to the palladium (II) chloride solution and heated under reflux for 2 hours, forming a white precipitate. The precipitate was removed by filtration and discarded, and 2-3-[(methylsulfanyl)methyl]phenylpyridine, **1a** (0.96 mmol, 207 mg) in dry acetonitrile (8 mmol) added to the filtrate, and heated under reflux for 6 hours. The flask was cooled to room temperature, filtered over celite and the solvent removed *in vacuo*.

The crude intermediate was dissolved in MeCN (5 ml), and sodium chloride (19.9 mmol, 1.17 g) dissolved in H₂O (5 ml) was added, and the mixture was stirred at room temperature for 3 hours. The solvent was removed *in vacuo*, and the crude mixture dissolved in DCM (35 ml) and H₂O (35 ml). The crude product was extracted with DCM (2 x 35 ml), washed with H₂O (2 x 35 ml) and brine (35 ml). The organic layers were dried over MgSO₄, filtered over celite, and the solvent removed *in vacuo*.

The crude product was purified by flash column chromatography (100 % → 98:2 DCM:MeOH) yielding 244 mg of the expected product **2a** as a yellow solid in 71 % yield.

¹H NMR (500 MHz, Chloroform-*d*) δ (ppm): 9.06 (d, J = 5.4 Hz, 1H), 7.83 (dd, J = 7.9, 7.9 Hz, 1H), 7.61 (d, J = 7.9 Hz, 1H), 7.30 (d, J = 7.6 Hz, 1H), 7.22 (m, 1H), 7.06 (dd, J = 7.6, 7.6 Hz, 1H), 7.01 (d, J = 7.6 Hz, 1H), 4.30 (m, 2H), 2.84 (s, 3H).

¹³C{¹H}NMR (126 MHz, Chloroform-*d*) δ (ppm): 165.7, 165.2, 150.4, 147.8, 144.3, 138.9, 125.1, 124.7, 122.8, 122.2, 118.7, 49.4, 23.7.

HRMS (m/z). Calc. for [C₁₃H₁₂NPdS]⁺ 319.9720. Found 319.9710.

Elemental Analysis. Calc. (%) for C₁₃H₁₂NPdS₂Cl: C 43.84, H 3.40, N 3.93; found: C 43.71, H 3.48, N 3.93.

Chapter 4

Expanding the scope: A family of SCN pincer palladacycles

This chapter details the synthesis of a number of novel unsymmetrical SCN pincer ligands, using the synthetic pathway described in Chapter 3. C-H bond activation of the unsymmetrical SCN pincer ligands is presented, yielding a family of novel unsymmetrical SCN pincer palladacycles. The catalytic evaluation of these unsymmetrical palladacycles in the Suzuki-Miyaura reaction is presented, revealing differences in catalytic activity depending on the thioether substituent. A potential catalyst activation pathway is studied for the Suzuki-Miyaura coupling reaction using DFT.

4.1 Introduction

The previous chapter included the design of a new route towards unsymmetrical pincer SCN ligands, with an emphasis on the synthesis of an SCN pincer ligand (Figure 4.1) with a thiomethyl substituent. The aim of the work presented in this chapter is to vary the substituent on the sulphur atom to synthesise a library of these unsymmetrical pincer ligands, to expand the scope of the synthetic chemistry, and to vary the steric and electronic effects of the sulphur ligand.

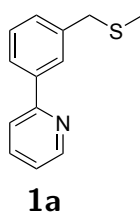
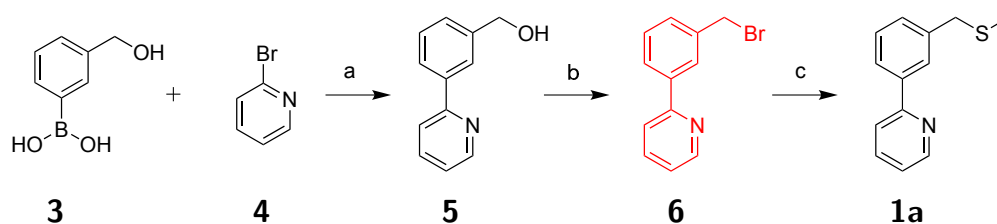


Figure 4.1 SCN pincer ligand, **1a**, with a methyl thioether substituent.

The full synthetic pathway to **1a** is shown in Scheme 4.1 with the key benzyl bromide (**6**) highlighted in red. Varying the sulphur nucleophile at this ligand synthesis stage provides the opportunity for a ligand library to be synthesised.



Scheme 4.1 Full reaction scheme to **1a**. a) $\text{Pd}(\text{PPh}_3)_4$, K_3PO_4 , Tol, EtOH, H_2O . b) HBr. c) NaSMe, EtOH.

4.1.1 Steric and electronic ligand effects

The changing of thioether substituents provides the opportunity to vary the steric and electronic properties on the sulphur atom, this in turn provides the opportunity to fine tune the palladium environment. For example, in a study into selenium pincer palladacycles (Figure 4.2),¹¹ it was envisaged that adding electron donating groups into the para-position of the Se donor group, would result in a changing of the electronics of the palladium centre, and hence could have implications in catalysis. However it was found that OMe substitution on the selenium donor group made little difference in catalytic activity, however substitution on the ligand backbone, para to the palladium, provided a four-fold activity increase.

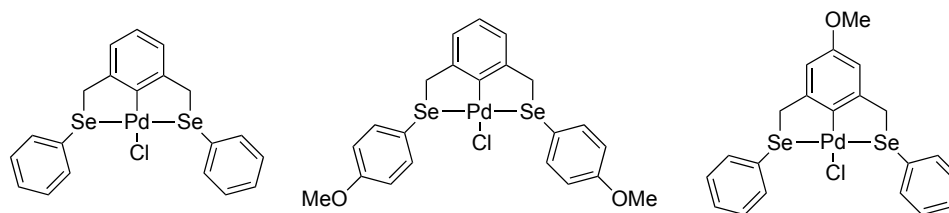


Figure 4.2 Selenium palladacycles by Szabó and co-workers, with ligand electronic fine tuning on Se donor group (middle), and the ligand backbone (right).

The effect of adding electron rich OMe groups and electron poor NO₂ groups to the ligand backbone has also been investigated for the IrPCP pincer palladacycles. By changing the Y donor group (Figure 4.3), differences in catalysis were found in various small molecule additions to the IrPCP complex, with increasing electron density disfavouring H-H or C-H bond addition,⁷⁶ or alkane dehydrogenation for 16e pincer complexes.¹⁹⁶

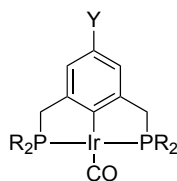


Figure 4.3 Substituent effects on IrPCP pincer complexes by Krogh-Jespersen *et al.*

There has also been investigation into the ability to fine tune the steric effects of groups on the donor atoms (Figure 4.4),¹⁹⁷ where increasing the steric bulk on the donor groups has the potential to influence halogenation reactions. Studies have also been undertaken using guanidine based palladacycles,¹⁹⁸ chiral phosphapalladacycles,¹⁶⁹ and in aryl-aryl coupling reactions using palladium norbornene palladacycles.¹⁹⁹

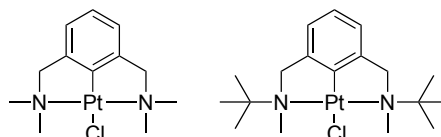


Figure 4.4 Adding additional steric bulk to symmetrical NCN pincer platinum complexes by van Koten.

Studies into the combinations of steric and electronic effects has been performed

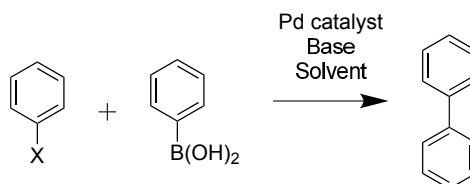
on unsymmetrical nitrogen based palladium complexes²⁰⁰ and O,N-based palladium complexes.²⁰¹

The ability to utilise unsymmetrical pincer palladacycles to combine different electronic and steric effects of the different ligand arms provides an excellent way to study these effects.^{23,202}

These investigations into varying the steric and electronic properties of the groups on the palladium atom provide the desire to synthesise a family of SCN palladacycles related to **1a** with varying electronic and steric character.

4.1.2 Suzuki-Miyaura catalysis

The Suzuki-Miyaura coupling reaction,^{156,203} is the palladium catalysed C-C cross coupling reaction utilising transmetalation with boron reagents, with a general example shown in Scheme 4.2. The Suzuki-Miyaura coupling reaction has evolved into a very widely used reaction, and in a recent analysis of the reactions used in medicinal chemistry, is the most commonly used synthetic procedure for palladium catalysed C-C bond formations,²⁰⁴ clearly showing its importance in modern chemistry.



Scheme 4.2 General Suzuki-Miyaura coupling.

The coupling of aryl iodides and aryl bromides is reported frequently, with that of iodides and electronically activated bromides often performed with simple palladium species such as $\text{Pd}(\text{OAc})_2$ or $\text{Pd}(\text{PPh}_3)_4$, however the coupling of electronically deactivated aryl bromides and aryl chlorides is desirable. Aryl chlorides are more desirable as substrates, due to their lower cost, lower molecular weight (hence “greener” due to less waste production) and greater availability, relative to the analogous bromides and iodides.²⁰⁵ However, the drawback of using aryl chlorides is that Ar-Cl bonds are stronger than equivalent Ar-Br and Ar-I bonds. For example, bond dissociation ener-

gies for phenyl halide bonds decrease from Ar-F (527 kJ mol^{-1}) > Ar-Cl (402 kJ mol^{-1}) > Ar-Br (339 kJ mol^{-1}) > Ar-I (272 kJ mol^{-1}), resulting in more difficult oxidative addition of the Ar-Cl bond in the first step of the Suzuki-Miyaura coupling reaction, compared to Ar-Br and Ar-I examples.²⁰⁶ Adding electron withdrawing groups to the aryl substituent of the aryl halide, such as NO_2 increases their activity, by weakening the Ar-X bond, however if the substituents are not required in the final product, adds increasing complexity to the reaction procedure.²⁰⁶

The development of new catalysts for the Suzuki-Miyaura reaction is a very active research field,¹⁵⁹ and the application of palladacycles as precatalysts is widespread. The seminal work by Herrmann, Beller and co-workers utilised their Herrmann-Beller palladacycle (Figure 4.5) in the Suzuki-Miyaura coupling.³² Other examples of palladacycles being utilised in the Suzuki-Miyaura coupling include the diverse work by Buchwald, using NC palladacycles (Figure 4.6);^{180,207} with other examples widespread, including NC^{31,44,162,208,209} and PC palladacycles.^{31,36–38,163,164,210}

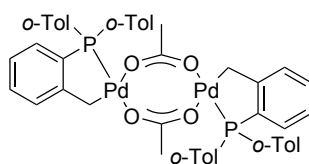


Figure 4.5 Herrmann-Beller palladacycle.

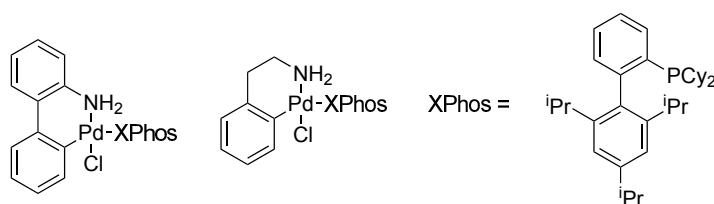


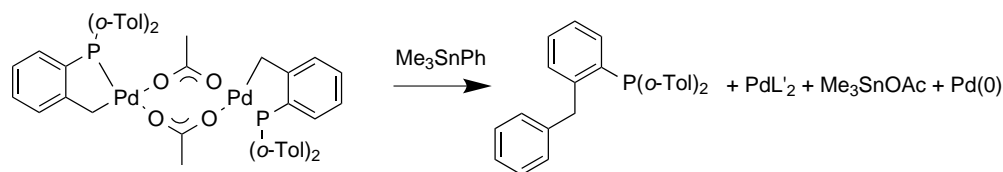
Figure 4.6 Buchwald and co-workers' palladacycle precatalysts.

A plethora of pincer palladacycles have been utilised in the Suzuki-Miyaura coupling reaction, including both symmetrical,^{39,40,42,165,211} and unsymmetrical examples,^{15,27,34,35,41,154,212} providing a suitable benchmark to study newly synthesised palladacycles in catalytic applications.

4.1.3 Suzuki-Miyaura coupling mechanistic insight

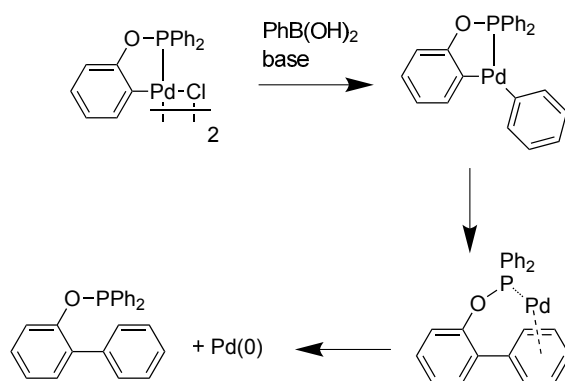
Palladacycle catalyst activation

In the initial application of palladacycles in C-C bond coupling reactions (Suzuki-Miyaura and Heck olefination), a mechanism involving a Pd(II)/Pd(IV) pathway was suggested,^{32,213} however very quickly it was postulated that the palladacycles were likely acting as a catalyst via another mechanism, and perhaps act as a precatalyst to generate Pd(0) species (Scheme 4.3).⁵² Reviews covering the active species in the Suzuki-Miyaura coupling reaction suggest that in most cases catalysis occurs via a Pd(0)/Pd(II) mechanism, and therefore the palladacycle must be activated into a form of Pd(0), with the nature of this species causing further debate.²¹⁴⁻²¹⁶ The idea of "Homeopathic Ligand-Free Palladium" was discussed by de Vries and co-workers, showing that palladacycles act as a source of Pd(0), and Pd(OAc)₂ also acts as ligand free palladium in the Heck reaction.⁴⁵



Scheme 4.3 Generation of Pd(0) from a palladacycle precatalyst, by Louie and Hartwig.

An important contribution to the field was made by Bedford *et al.*³⁷ on the generation of the catalytically active Pd(0) species. A PC phosphinite palladacycle was exposed to various components of the Suzuki reaction to show that the generation of Pd(0) and an *ortho*-arylated biphenyl occurred when the palladacycle was exposed to base and phenylboronic acid (Scheme 4.4).



Scheme 4.4 Bedford *et al.*'s investigation into generation of Pd(0) from a PC palladacycle.

The likely role of Pd(0) from palladacycle precatalysts sheds light upon the reports of palladacycle catalyst recyclability. Examples include that by Lin and Luo,²¹⁷ where it was found that a polystyrene supported PC palladacycle could act as a catalyst in the Heck, Suzuki and Sonogashira coupling reactions, with reported recyclability, over numerous couplings (up to 7). The catalyst retained its reactivity, albeit only for aryl iodides and bromides. The recyclability of palladacycle catalysis was also investigated by Bedford *et al.*²¹⁸ where it was found that the silica supported NC catalysts achieved poor recyclability in the Suzuki-Miyaura reaction, attributed to the likely reduction of the palladacycle to a Pd(0) species. This is possibly the explanation why recyclable catalysts fail to achieve the excellent results achieved using solution based examples. However, an interesting report was published by Karami *et al.*²¹⁹ on the use of an NC palladacycle as a recyclable catalyst for the Heck reaction, where the palladacycle acts as a reservoir of palladium nanoparticles, stabilised by polyethylene glycol, achieving recyclability, for aryl iodides, and activated aryl bromides.

Other investigations include the room temperature Suzuki-Miyaura coupling of aryl bromides by phosphorus based palladium complexes;²²⁰ and the coupling of aryl bromides by PCN pincer palladacycles including the use of the mercury drop test as an investigation into possible mechanisms.¹⁶⁴

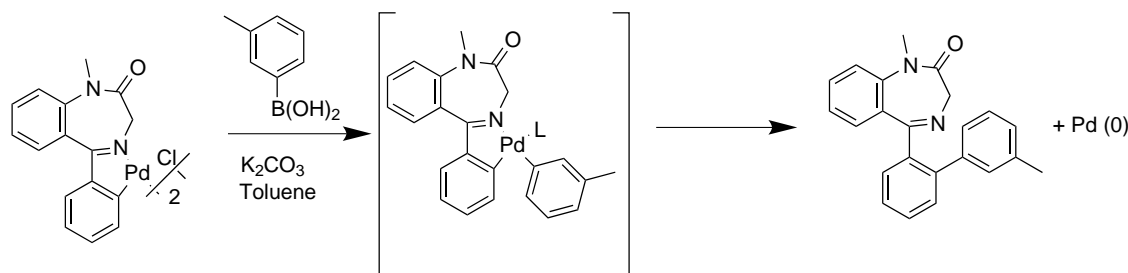
Despite the plethora of examples of palladacycle application into Suzuki-Miyaura catalysis, no papers provide a comprehensive mechanistic investigation into the

catalyst activation step. Experimental evidence is widespread for the process, with proposed key intermediates, however a comprehensive theoretical investigation is lacking.

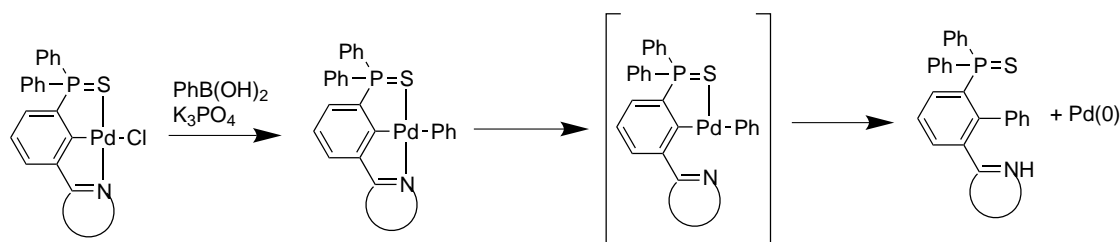
Several review articles cover the nature of the active catalyst, including work by Astruc,²²¹ covering the use of palladium nanoparticles as catalysts (either heterogeneous or homogeneous). In a number of excellent reviews,^{214,215} the authors cover the recent research into the active catalysts generated from Pd(II) complexes, including palladacycles, summarising the various efforts to ascertain the true catalyst.

Much debate is still present on the actual true catalyst, whether it be ligand free Pd(0), palladium nanoparticles, low-ligated Pd(0) etc, however it is generally accepted that palladacycles are reduced to Pd(0) in the absence of strong oxidising agents, and therefore the direction of design of palladium catalysts have to take into account the mechanism by which this occurs, and how to alter the kinetics and thermodynamics of this catalyst activation step to increase the catalytic activity.

Along with the previous examples discussed,^{37,52} further work on the generation of the catalytically active species has been undertaken, such as the work by Spencer *et al.* (Scheme 4.5),⁴⁴ and the work by Odinet and co-workers (Scheme 4.6).¹⁶ In the latter case, the effect of the hemilability of the unsymmetrical SCN pincer palladacycle on the decoordination of one of the donor arms was raised. This effect of hemilability,²⁴ is well discussed,^{17,35,172} and the varying donor atoms may have an effect on the rate of generation of the Pd(0) species, and therefore on the catalytic activity of the palladacycles in catalysis where Pd(0) is the active species.



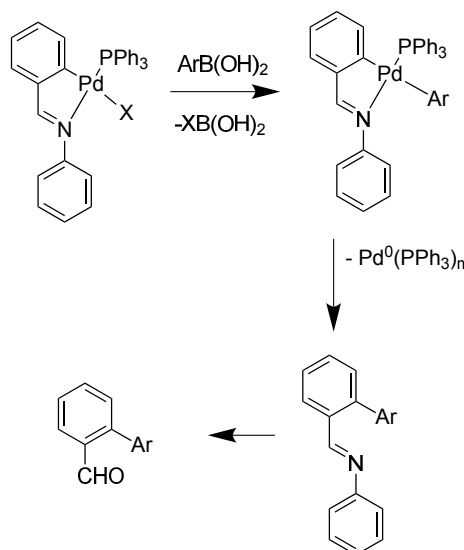
Scheme 4.5 Generation of Pd(0) from palladacycles by Spencer *et al.*



Scheme 4.6 Generation of Pd(0) by Odinet and co-workers.

Most recently, the work by Fairlamb and co-workers,²²² discusses the palladacycle precatalyst activation step, and stated “Controlling and understanding the precatalyst activation step is however, absolutely critical - an aspect that is poorly understood”.²²² It was shown that in a catalyst activation step, transmetalation with a boronic acid occurs as shown previously, with reductive elimination of a Pd(0) species, with the arylated ligand remaining (which readily undergoes hydrolysis) (Scheme 4.7).

In a paper by d’Orly  and Jutand,²²³ the generation of Pd(0) from a PC palladacycle is discussed, *via* a reductive elimination of Pd(0) involving the bridging acetate group, which was investigated using cyclic voltammetry to observe the presence of the Pd(0) generated *in situ* from the palladacycle.



Scheme 4.7 Reductive elimination of Pd(0) proposed by Fairlamb and co-workers.

4.1.4 Comparison of catalyst activation to previous DFT studies

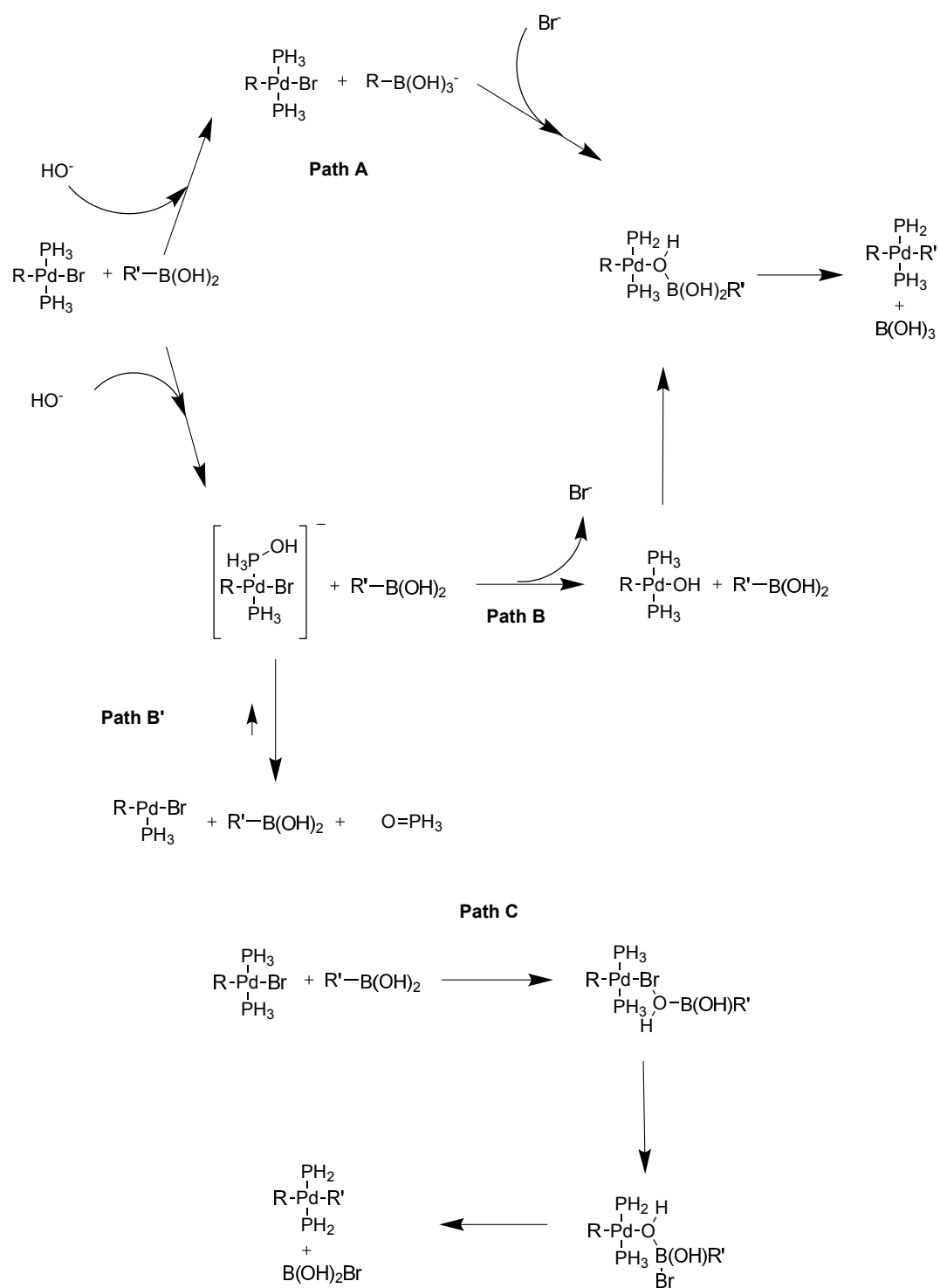
Despite the catalyst activation pathway for palladacycles having not been studied previously using DFT, comparisons can be made between similar processes, such as in the Suzuki-Miyaura coupling reaction. Two of the key steps in the catalyst activation pathway are transmetallation and reductive elimination, which also occur in the Suzuki-Miyaura coupling reaction.

There have been several studies on the role of the base in the transmetallation, and the effect on the kinetics of the transmetallation step, which has been reviewed including theoretical and experimental investigations.^{224,225}

Role of the base in transmetallation

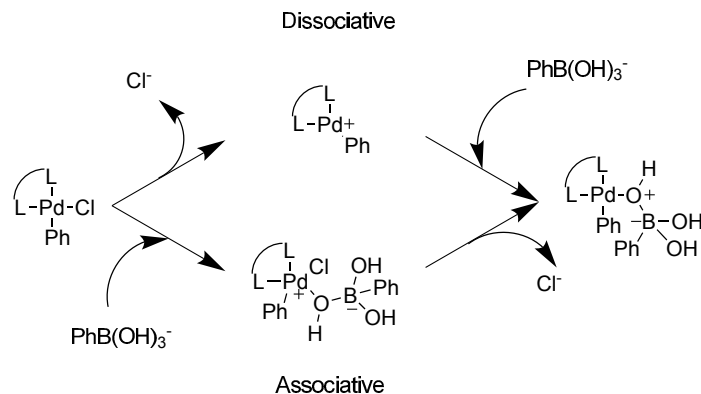
Several different roles of the base in transmetallation of the Suzuki-Miyaura coupling reaction have been studied, such as that by Maseras and co-workers²²⁶ into the transmetallation step of the Suzuki-Miyaura coupling, yielding several different pathways (Scheme 4.8). The pathways A and B differ in the role of the base (HO^-), wherein pathway A the base forms a phenylboronate species; and in pathway B forms an oxo-palladium species. Pathway C is the transmetallation pathway taking place without base. It was found that pathway C was most endothermic ($\Delta E_0 = 135.1 \text{ kJ mol}^{-1}$), with an energy barrier of $243.1 \text{ kJ mol}^{-1}$, therefore proving an unlikely pathway. Pathway A was deemed most likely, as an exothermic process ($\Delta E_0 -62.3 \text{ kJ mol}^{-1}$) with a significantly lower energy barrier of 92.9 kJ mol^{-1} . Pathway B was ruled out, as it was found the HO^- would oxidise the PH_3 group, rather than substitute the halide.

The role of the base, analogous to pathway A in Scheme 4.8²²⁶ was also studied in transmetallation involving diimine palladium species by Weng and Hong;²²⁷ and an investigation of phosphine effects on transmetallation by Harvey and co-workers.²²⁸ Chelating N- and P- based ligands were studied by Hong and co-workers,²²⁹ with both an associative and a dissociative pathway (Scheme 4.9). The dissociative pathway



Scheme 4.8 Transmetallation mechanisms by Maseras and co-workers.

was found to be infeasible as it was extremely endergonic ($\Delta G = 528.0 \text{ kJ mol}^{-1}$) for the dissociation step.



Scheme 4.9 Transmetalation step by Hong and co-workers.

The associative pathway was significantly more feasible, with a halide substitution barrier of 77.4 kJ mol^{-1} , and removal of the resultant chloride anion having an energy cost of $156.9 \text{ kJ mol}^{-1}$. It was also found the base-free transmetalation had a significantly larger energy barrier of $143.9 \text{ kJ mol}^{-1}$.²²⁹

A pathway analogous to pathway B in Scheme 4.8²²⁶ was favoured when studied by electrochemical techniques by Amatore *et al.*,²³⁰ showing the oxo-palladium species was favoured over the phenylboronate pathway, also found by Carrow and Hartwig.²³¹

Another study involved using vinylboronic acid, and a vinyl substituted palladium complex by Maseras and co-workers.²³² The boronate pathway analogous to pathway A (Scheme 4.8) was studied with both associative and dissociative pathways considered. Barriers for the transmetalation step of between 38.1 and 51.9 kJ mol^{-1} depending on the pathway were found. However for the dissociative pathway, the energetic cost of the chloride dissociation was not included. The pathway also included the reductive elimination step, with a barrier of 20.1 kJ mol^{-1} .

The boronate pathway was also postulated to be the favoured pathway in an experimental study by Lima *et al.*,²³³ when studying the pK_a effects on catalysis. It was concluded that, despite not being able to completely rule out the possibility of the boronic acid reacting with a palladium oxo-species, the most reactive species is

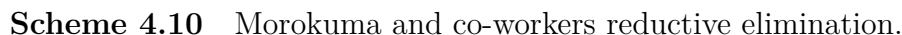
likely to be the boronate in transmetallation.

Effect of solvent on the transmetallation step

In another investigation into the role of the base in the transmetallation step, work by Ortuño *et al.*²³⁴ into the role of the base and solvent was studied on $(\text{PPh}_3)_2\text{Pd}(\text{Ph})(\text{Br})$ using DFT (M06/6-31(d,p)[SDD]). It was found that in the transmetallation step, the route via phenylboronate was more energetically feasible than via the oxo-palladium species. All calculations were performed in THF solvent using the SMD continuum methodology. The role of water molecules within the structures was also investigated. It was found that the phenylboronate pathway,²³⁴ analogous to the pathway A in Scheme 4.8²²⁶ with the presence of three explicit water molecules in the structure, in continuum THF solvent had a Gibbs free energy barrier of 79.1 kJ mol^{-1} . This compares to that of the oxo-palladium pathway whereby a barrier of $104.6 \text{ kJ mol}^{-1}$ was found for the displacement of the bromide by the hydroxide anion, and a barrier of 35.6 kJ mol^{-1} for the coordination of the phenylboronic acid to the oxo-palladium species. It was found that the addition of extra water molecules had little effect on the phenylboronate pathway, however for the oxo-palladium pathway, without the three water molecules, the barrier was increased for the bromide displacement to $137.2 \text{ kJ mol}^{-1}$ indicating that solvent is more important in the oxo-palladium pathway.

Reductive elimination

In addition to the previously discussed study by Maseras and co-workers (Scheme 4.8),²³² an excellent investigation was undertaken by Morokuma and co-workers²³⁵ into the kinetics and thermodynamics of various C-C coupling reactions. The reductive elimination studied various R groups, including vinyl, phenyl, methyl and ethynyl groups (Scheme 4.10). It was found that the energy barrier decreased in the order methyl > ethynyl > phenyl > vinyl. The Gibbs free energy barriers to reductive elimination ranged from 25.1 kJ mol^{-1} for the formation of buta-1,3-diene from the vinyl



4.2 Experimental results

4.2.1 SCN ligand library synthesis

In order to investigate the steric and electronic influence of substitution on the thioether group, a number of different sulphur nucleophiles (Figure 4.7) have been used in the nucleophilic displacement of **6** in Scheme 4.1. These nucleophiles provide the opportunity to increase electron density on the palladium by inductive electron donation with increasing chain length (HSC₂H₅, **7b**, and HSC₃H₇, **7c**). Steric demand can also be increased (HSC₆H₅, **7d**), and then the electronic effects can be varied on **7d** by increasing electron density mesomerically by the OMe group on the phenyl ring in 4-HSC₆H₄OCH₃, **7f**; decreasing electron density mesomerically on the phenyl ring with the NO₂ group in 4-HSC₆H₄NO₂, **7g**, and inductively increasing electron density on the ring with the para methyl group in 4-HSC₆H₄CH₃, **7e**.

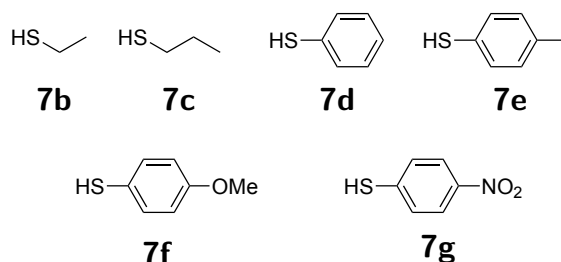


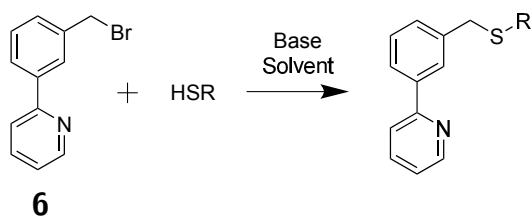
Figure 4.7 Sulphur based nucleophiles studied in this thesis.

These variations in sulphur based nucleophiles provide a number of opportunities to change the electron density on the sulphur atom, and potentially thereby the palladium atom. Also, this allowed the modification of the steric bulk of the thioether donor arm. It will then be interesting to observe if this has any effect on any catalytic applications of the resulting SCN pincer palladacycles.

In the initial synthesis of **1a** (Scheme 4.1), NaSMe was used as the nucleophile in the nucleophilic substitution of **6**, however in the cases presented in Figure 4.7 none of the sulphur nucleophiles are negatively charged, and therefore a base or proton scavenger is required for the reaction to proceed smoothly to increase the nucleophilicity of the thioether, in this case either NaH, NEt₃ or Hunig's base. Also

a different solvent is required for use with NaH, as originally the protic solvent EtOH was used, and therefore a non-protic solvent is required.

The reactions performed (Scheme 4.11) yielded a number of novel unsymmetrical SCN pincer ligands (Figure 4.8), in addition to the previously discussed example, **1a**. The ligand **1d** has previously been synthesised via the original Baltus route.²⁴² The yields and synthetic conditions are presented in Table 4.1.



Scheme 4.11 Nucleophilic displacement of **6** by a range of sulphur based nucleophiles.

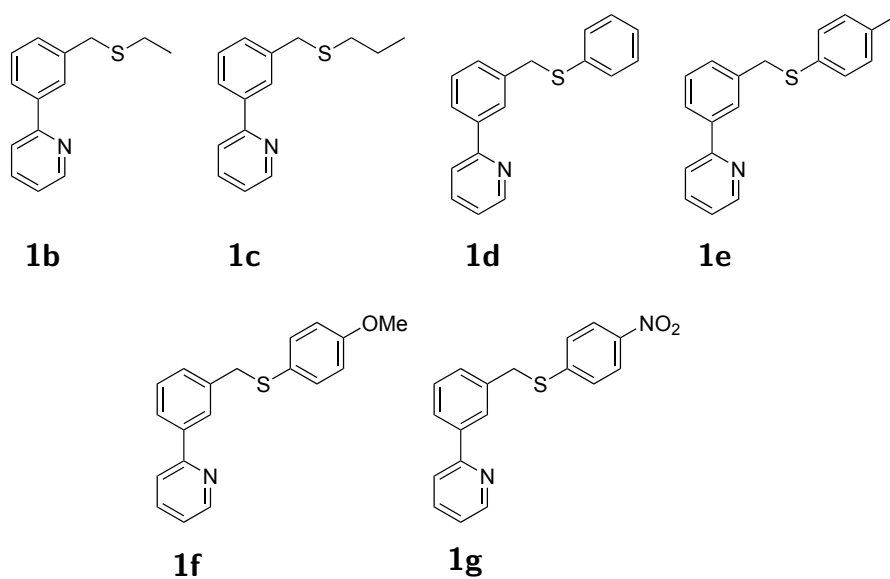


Figure 4.8 Unsymmetrical SCN pincer ligands.

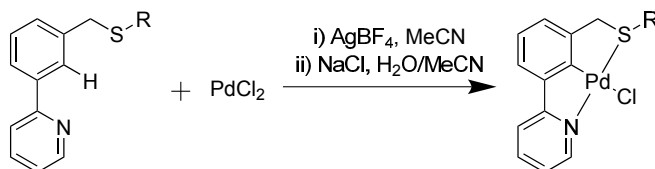
It was found that the optimum reaction conditions for most sulphur nucleophiles was using NaH as the base, with DMF as the solvent, with the exception of the synthesis of **1e**, where it can be seen that in entry 5, that NEt₃ in EtOH provided a higher yield. Hunig's base was used for the synthesis of **1g** as a precaution against potential undesired reactions between NaH and the NO₂ group.²⁴³

Table 4.1 SCN ligand synthesis yields.

Entry	Product	Conditions	Isolated yield / %
1	1b	NaH, DMF, MW 150 °C, 15 min	72
2	1c	NaH, DMF, MW 150 °C, 20 min	>99
3	1c	NaH, THF, MW 130 °C, 15 min	55
4	1d	NaH, DMF, MW 150 °C, 20 min	99
5	1e	NEt ₃ , EtOH, MW 150 °C, 20 min	51
6	1e	NaH, DMF, MW 150 °C, 15 min	39
7	1f	NaH, DMF, MW 150 °C, 20 min	60
8	1g	Hunig's base, DMF, MW 150 °C, 20 min	73

4.2.2 SCN pincer palladacycle synthesis

With the small library of novel SCN pincer ligands synthesised (Figure 4.8) the next step is to synthesise the related SCN pincer palladacycles, as per the route described previously for **2a**, using *in situ* generated Pd(NCMe)₄(BF₄)₂ (Scheme 4.12).

**Scheme 4.12** C-H bond activation of SCN pincer ligands.

The newly synthesised palladacycles are shown in Figure 4.9, with **2d** previously synthesised,²⁴² and their yields are presented in Table 4.2 in good to excellent yield.

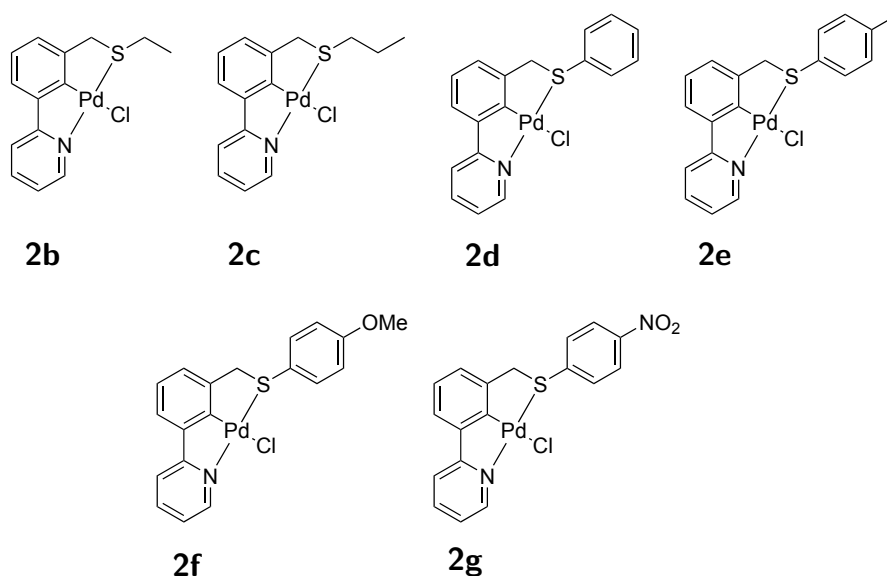
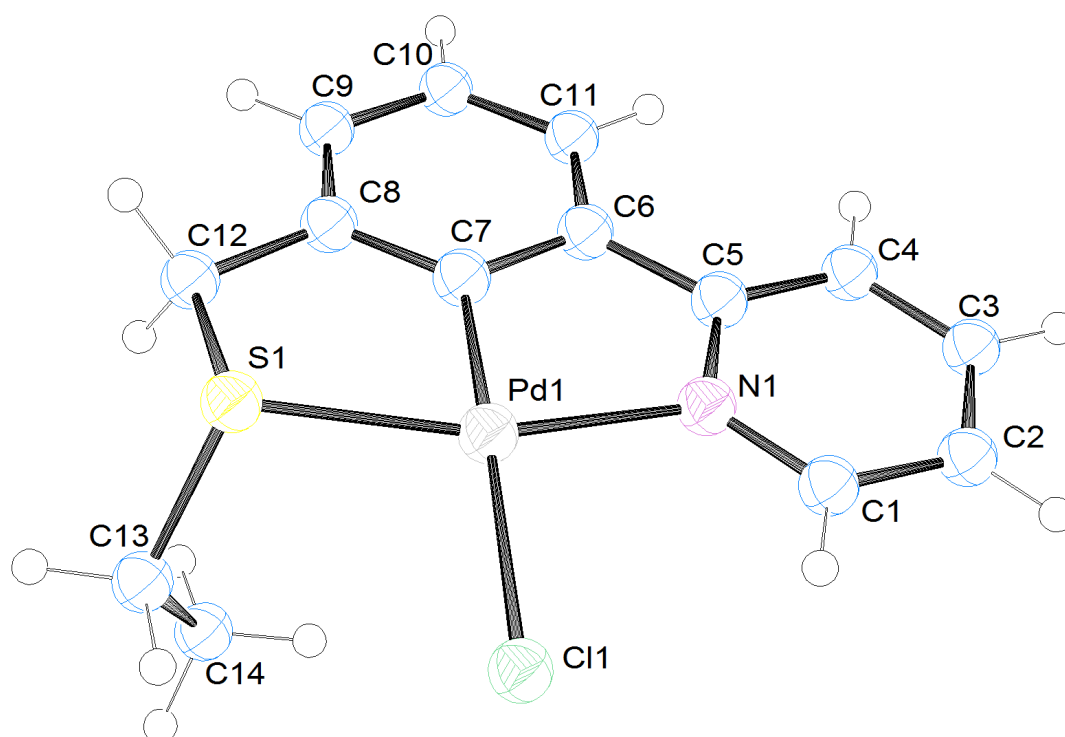
**Figure 4.9** Experimentally synthesised unsymmetrical SCN pincer palladacycles.

Table 4.2 SCN pincer palladacycle synthesis yields.

Entry	Ligand	Palladacycle	Yield / %
1	1b	2b	83
2	1c	2c	85
3	1d	2d	71
4	1e	2e	89
5	1f	2f	54
6	1g	2g	34

Crystal structures are provided for **2b** (Figure 4.10), **2c** (Figure 4.11) and **2f** (Figure 4.12), visualised using the Ortep3 program.²⁴⁴

**Figure 4.10** Crystal structure of **2b**.

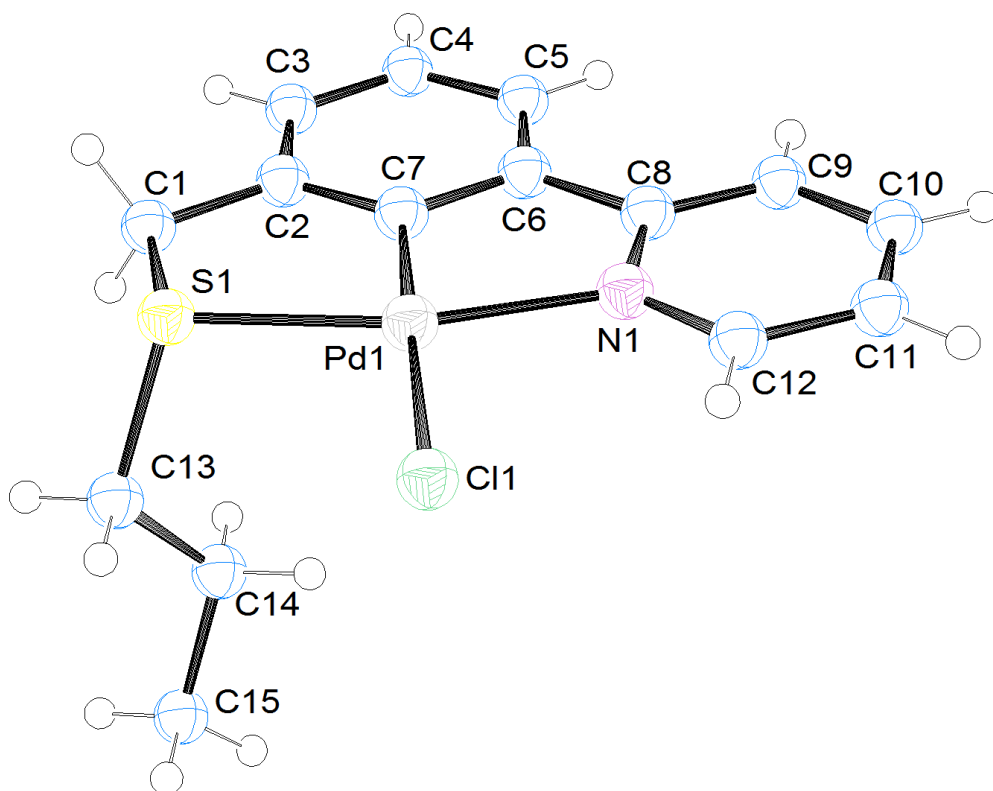


Figure 4.11 Crystal structure of **2c**.

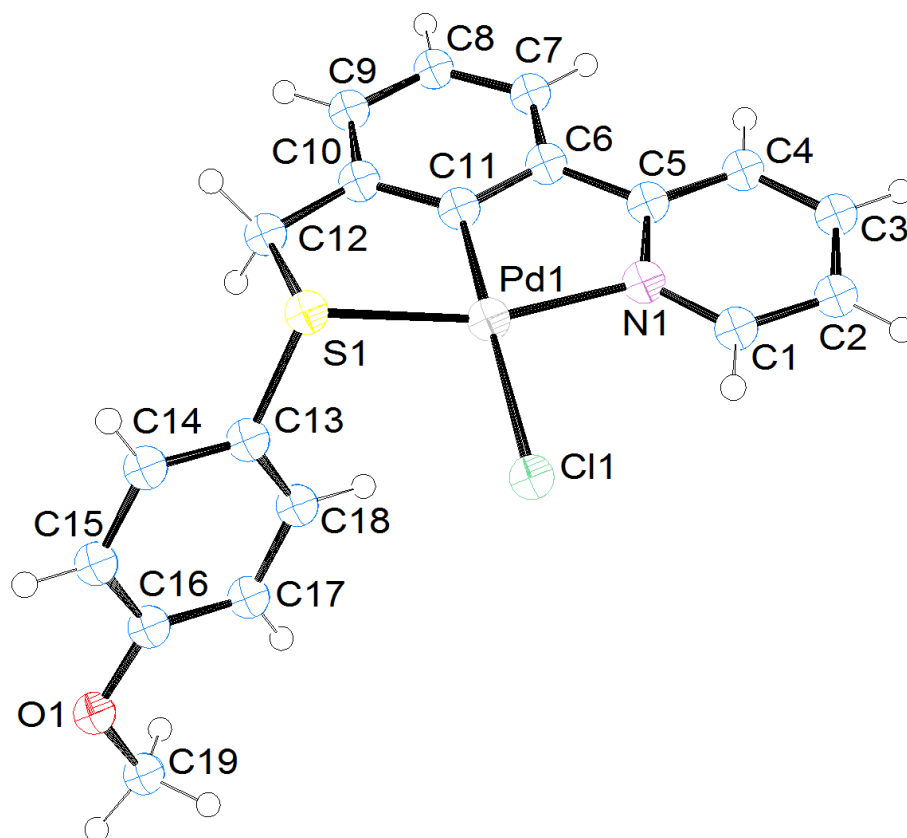
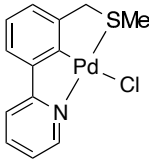
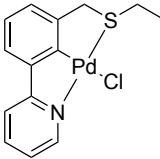
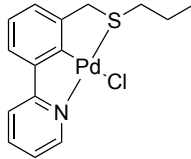
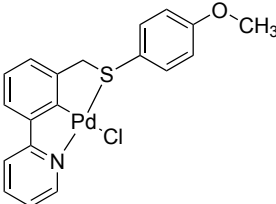


Figure 4.12 Crystal structure of **2f**.

The structures of the SCN pincer palladacycles can be investigated, observing any differences in Pd-L bond lengths, as the substituent of the thioether group is changed (Table 4.3). All structures exhibit a distorted square-planar geometry. The bond distances for **2a** contain significantly larger estimated standard deviations (e.s.d.) in comparison the other structures, making comparison with this structure difficult. For the remaining structures (**2b,c,f**), within the 5 x e.s.d. limits, no significant differences in the experimental bond lengths can be observed.

Table 4.3 SCN pincer palladacycle X-ray crystal structure Pd-L bond lengths.

Bond	Bond length / Å			
	2a 	2b 	2c 	2f 
Pd-S	2.291(8)	2.2638(4)	2.2705(7)	2.2674(5)
Pd-N	2.09(3)	2.0672(13)	2.066(2)	2.0708(15)
Pd-C	1.95(3)	1.9489(15)	1.950(2)	1.950(2)
Pd-Cl	2.423(8)	2.4095(4)	2.3961(5)	2.4093(5)

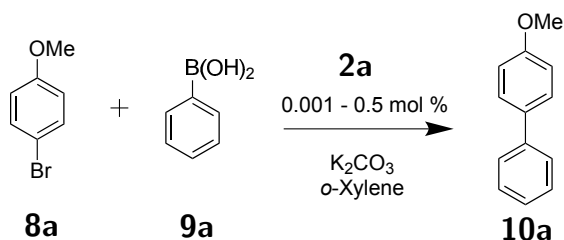
4.2.3 Suzuki-Miyaura coupling catalysis

These newly synthesised SCN pincer palladacycles were next tested in a potential catalytic application, the Suzuki-Miyaura coupling reaction, as precatalysts, in order to investigate any difference in their catalytic activity depending on the sulphur atom substituent.

Catalyst loading investigation using **2a**

The initial catalytic investigation focused on using **2a** as the precatalyst for the coupling of an electronically deactivated aryl bromide, 4-bromoanisole, **8a** with phenylboronic acid, **9a** (Scheme 4.13). The conditions used were analogous to that used for the initial work with the Herrmann-Beller catalyst.³² This utilises K₂CO₃ as the base, with *o*-xylene as the solvent, with various catalyst loadings of **2a**. The

reaction was performed at 130 °C. The first investigation is into the catalyst loading required for catalysis, and what effect decreasing the catalytic loading has on the product conversion rates. The reactions were monitored using gas-chromatography (GC), with aliquots taken at 2 h and 4 h, measuring the % conversion from the starting bromide **8a** to the final product, **10a**. The results are presented in Table 4.4, along with a range of literature examples for comparison.



Scheme 4.13 Catalyst loading investigation for Suzuki-Miyaura coupling using **2a**.

Table 4.4 Catalyst loading investigation for Suzuki-Miyaura coupling using **2a** GC conversions.

Entry	Catalyst loading / mol % ^a	GC conversion / % ^a		
		2 h	4 h	Literature
1	0.5	94	96	
2	0.1	95	96	
3	0.05	93	94	
4	0.01	85	87	
5	0.001	6	7	
6 ^b	1			93
	0.1			78
	0.01			5
7 ^c	1			91
	0.1			84
	0.01			3
8 ^d	0.5			98
	0.05			92
	0.005			43
9 ^e	1			61

a) Average of 2 runs, based on **8a** and **10a**. b) 5 h using SCN palladacycle A.¹⁶ c) 5 h using SCN palladacycle B.³⁵ d) 27 h using SCN palladacycle C.⁴⁴ e) 5 h using SCN palladacycle D.²⁷ Literature palladacycles are shown in Figure 4.13.

It can be seen from the results in Table 4.4 that at catalyst loadings of 0.001 mol %, in entry 5, only a small conversion of **8a** to **10a** is evident (only 7 % conversion after

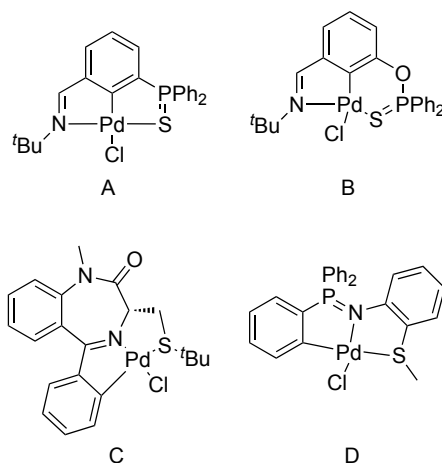


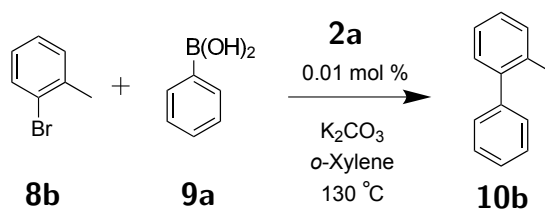
Figure 4.13 Literature palladacycles compared in Table 4.4.

4 h). However good conversion is found for 0.01 mol % in entry 4, suggesting this is a reasonable catalyst loading for further catalytic investigations.

These catalyst loadings are favourable in comparison to other reported SCN pincer palladacycles. Entries 6 and 7 by Aleksanyan and co-workers^{16,35} provided lower GC conversions than presented in this work; similar conversions were found at equivalent catalyst loadings for the benzodiazpene based palladacycles by Spencer *et al.* in entry 8;⁴⁴ and the work presented here achieves significantly higher GC conversions that shown in entry 9.²⁷ Therefore the catalytic loadings achieved are comparable to that reported previously.

Reaction time optimisation using **2a**

With the optimum catalyst loading of 0.01 mol % the next step was to investigate the optimal reaction times required for the catalytic reaction to proceed to completion. For this, another electronically deactivated, and sterically hindered aryl bromide, 2-bromotoluene, **8b**, was coupled with phenylboronic acid, **9a** (Scheme 4.14), and monitored by GC every 15 min.



Scheme 4.14 Catalyst reaction time optimisation using **2a**, an average of two separate runs.

The results for this study are shown in Figure 4.14, where it can be seen that after ≈ 45 min the % conversion plateaus, and the reaction is almost complete, with only small increases in conversion as time progress through to 4 h.

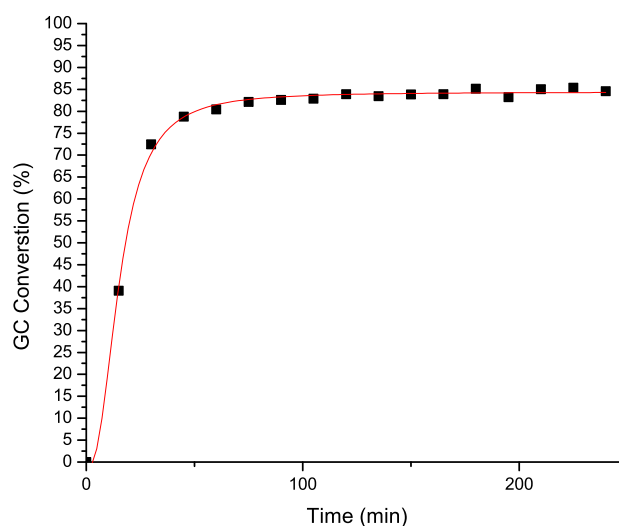


Figure 4.14 Reaction time optimisation for Suzuki-Miyaura coupling reaction using **2a**, average of two runs.

Sterically demanding coupling reactions using **2a**

In this section, the scope of the reaction is expanded to sterically demanding and electronically deactivated aryl bromides. The different coupling reactions studied are shown in Figure 4.15, with the results shown in Table 4.5. **2a** is the precatalyst used in these reactions, and for the reaction in entry 4, are compared to a symmetric SCS pincer palladacycle (Figure 4.16),^{245,246} and the Herrmann-Beller catalyst (Figure 4.5).³²

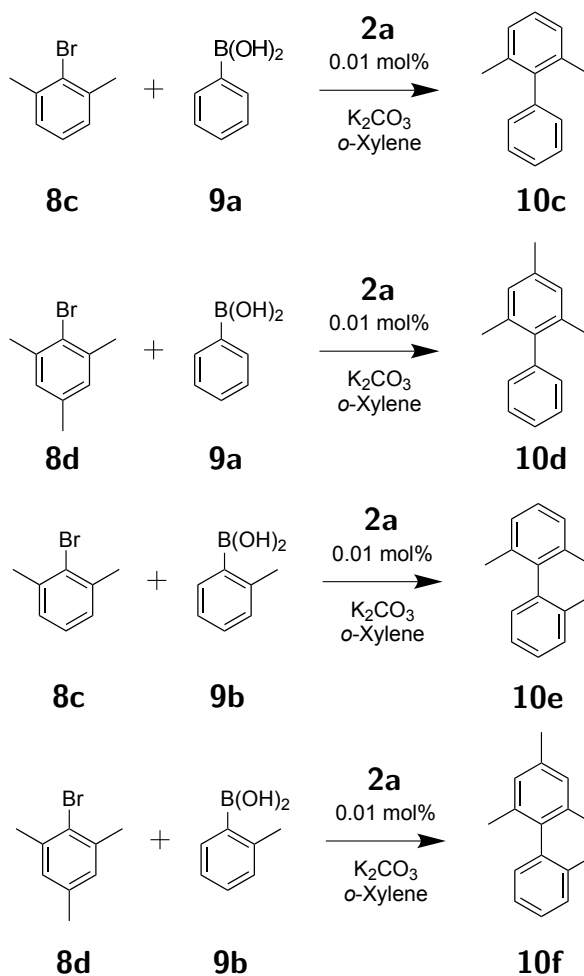


Figure 4.15 Suzuki-Miyaura coupling reactions of sterically hindered substrates undertaken using **2a**.

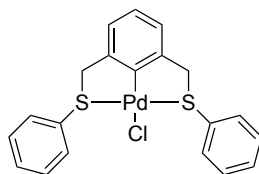
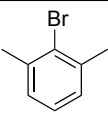
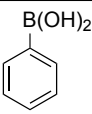
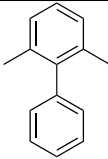
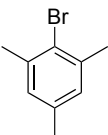
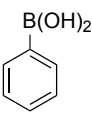
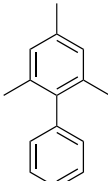
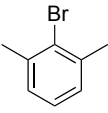
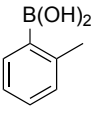
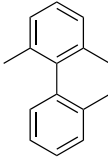
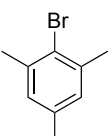
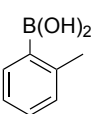
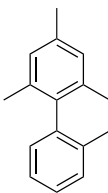


Figure 4.16 Symmetric PdSCS pincer palladacycle.

It can be seen (Table 4.5) that **2a** successfully couples these sterically demanding coupling partners. The comparison between the symmetric and unsymmetric pincer palladacycles in entry 4, also shows that the unsymmetric palladacycle **2a** is slightly more efficient than the symmetric palladacycle tested. Under these catalytic conditions **2a** also provides higher GC conversions than the Herrmann-Beller palladacycle.

Examples of these sterically demanding coupling reactions are widespread in the

Table 4.5 Suzuki-Miyaura coupling reactions of sterically hindered substrates undertaken using **2a**.

Entry	Bromide	Boronic acid	Product	GC Conversion / %		
				2 h	4 h	6 h
1				61	64	67
2				57	59	62
3				23	31	39
4				67	74	79
				37 ^a	43 ^a	47 ^a
				51 ^b	51 ^b	57 ^b

Reactions performed in duplicate and results are the average of both runs. a) Symmetrical SCS pincer palladacycle (Figure 4.16) as catalyst. b) Herrmann-Beller palladacycle as catalyst (Figure 4.5).³²

literature using palladacycles, with examples shown in Figure 4.17 including the coupling of **8c** with phenylboronic acid, **9a**. These include the application of PC palladacycle A providing 48 % conversion, however at a lower catalyst loading of 0.001 mol %;¹⁶³ PCP pincer palladacycle B using the same 0.01 mol % catalyst loading presented in this work, achieving % conversion of 30 % after 18 h;³⁹ and another PCP example C achieved impressive conversions of 62 % at 0.001 mol % catalyst loading.²¹¹ Symmetrical NCN pincer palladacycle D has also been shown to achieve inferior results to those presented here achieving conversions of 99 % however at the higher catalyst loading of 0.1 mol %;¹⁵ in another example NCN pincer palladacycle E achieved 45 % yield at 0.01 mol % catalyst loading.⁴⁰ PCP phosphinite pincer F has also been shown to successfully couple **8d** and **9b** in 87 % yield, however at 1 mol % catalyst loading.¹⁶⁵

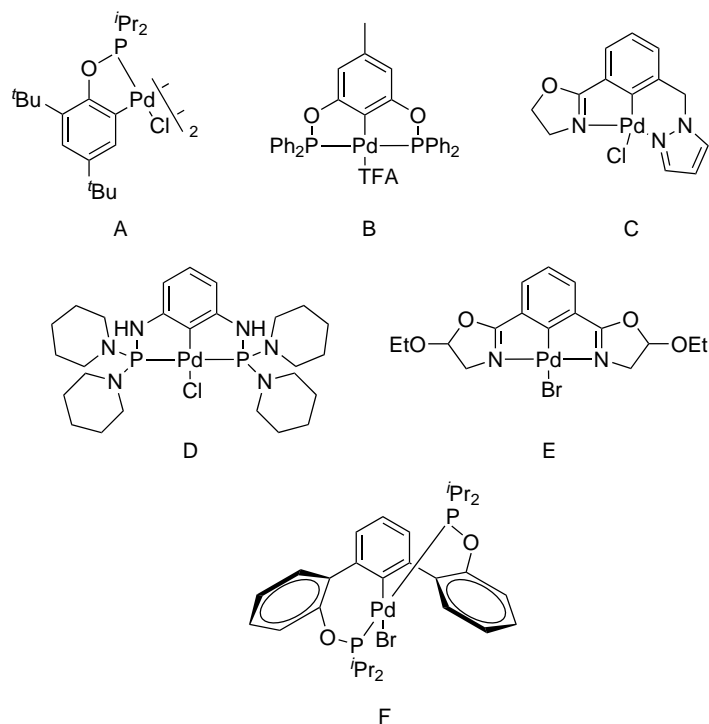


Figure 4.17 Literature sterically hindered Suzuki coupling palladacycle examples.

SCN pincer palladacycles

In order to investigate the effect of varying the substituents on the sulphur on their catalytic activity, the coupling of the sterically hindered aryl bromide, **8d** with the

sterically hindered arylboronic acid, **9b** was undertaken with a number of SCN pincer palladacycles, **2a–c,e,f** (Figure 4.18) and presented in Table 4.6. These results were also compared to the symmetrical SCS pincer palladacycle Figure 4.16^{245,246} and the Herrmann-Beller palladacycle (Figure 4.5).³²

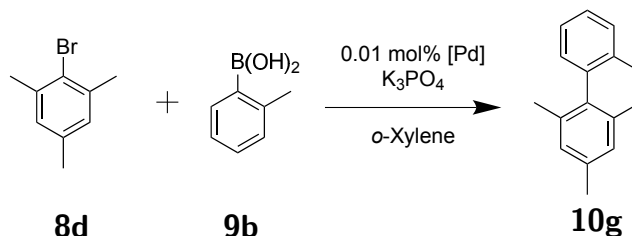


Figure 4.18 Suzuki-Miyaura coupling of **8d** and **9b** with various palladacycle catalysts.

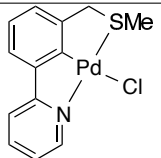
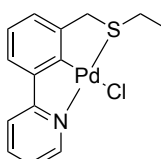
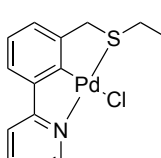
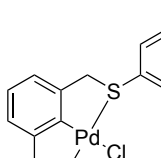
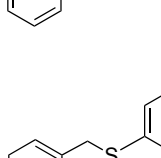
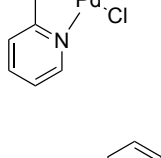
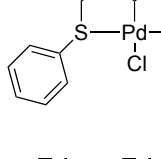
The results presented in Table 4.6 show that there are differences in the catalytic activity in the Suzuki-Miyaura coupling depending on the thioether substituent. The results suggest that substituting the thioether with alkyl groups (entries 1-3) achieve higher % conversions, than the aryl substituted thioethers (entries 4 and 5). The symmetrical aryl substituted SCS pincer palladacycle shown in Figure 4.16 also achieves lower % conversion than the alkyl substituted examples, and the Herrmann-Beller palladacycle (entry 7) achieves % conversions intermediate between the aryl and alkyl substituted SCN pincer palladacycles (entries 1-3).

Clearly the thioether substituent has a significant effect on the catalytic activity, and therefore investigating these differences is desirable to understand the catalytic properties of the unsymmetrical pincer palladacycles.

4.3 Theoretical results

Following on from the discussion in Section 4.1.3, in this section the catalyst activation pathway of palladacycles to Pd(0) for the application in the Suzuki-Miyaura coupling reaction was investigated. From the investigation by Odinet and co-workers,¹⁶ which provided proposed intermediates in the formation of Pd(0) from unsymmetrical pincer SCN palladacycles (Scheme 4.6), the full pathway was calculated including all

Table 4.6 Suzuki-Miyaura coupling of **8d** and **9b** with SCN pincer palladacycles, symmetrical SCS palladacycle and the Herrmann-Beller palladacycle.

Entry	Palladacycle	GC conversion / %		
		2 h	4 h	6 h
1		69	76	79
2		-	62	64
3		76	77	79
4		24	34	39
5		-	32	37
6		37	43	47
7		50	50	57

stationary points along the pathway. The pathway includes two key steps studied in the Suzuki-Miyaura coupling reaction, transmetallation and reductive elimination, providing guidance into likely mechanistic pathways.

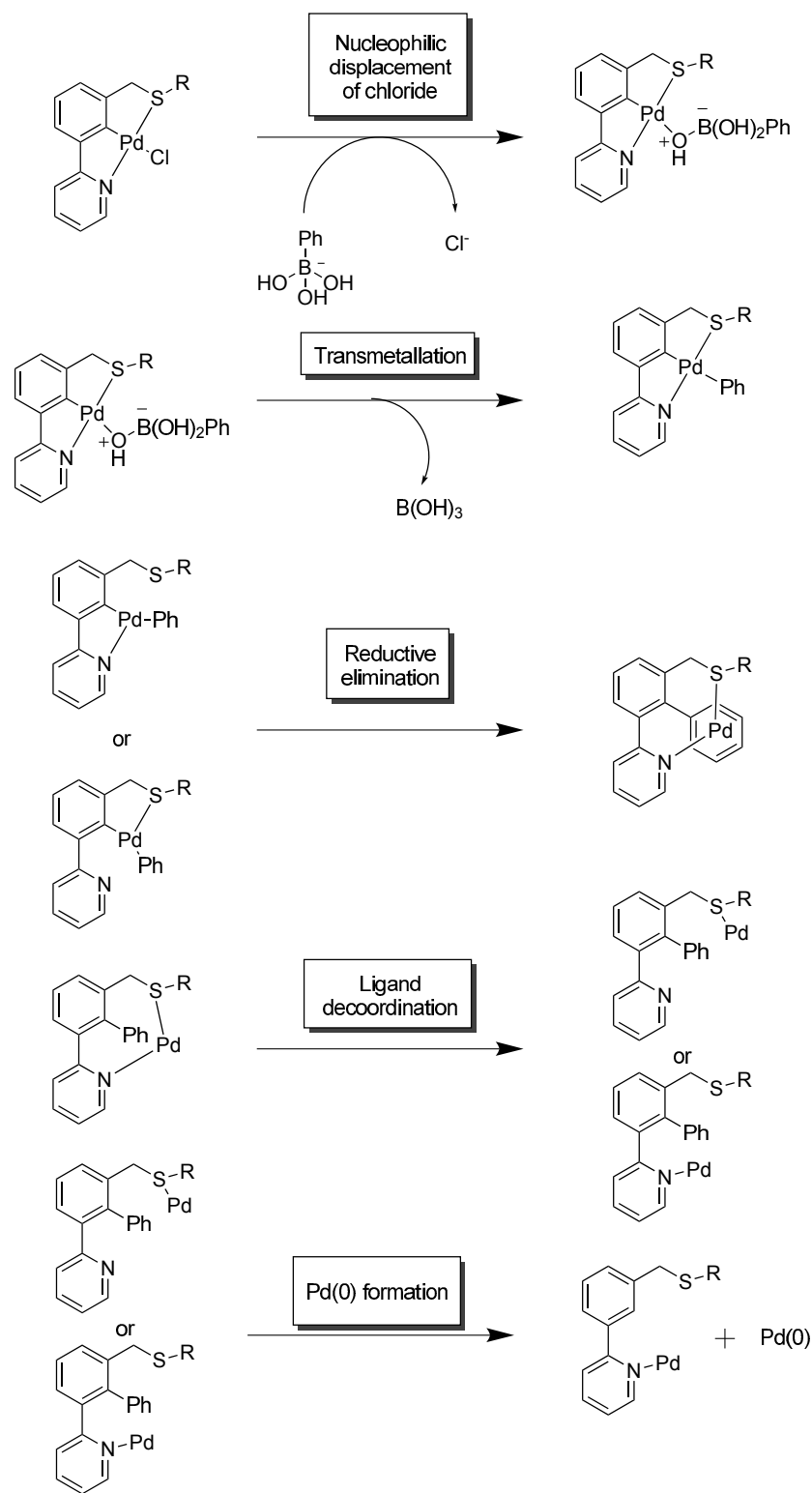
Discussed in Section 4.1.4 is the role of the base in the transmetallation pathway, where it was found a possible pathway includes the base (HO^-) precoordinating to the boronic acid, forming the phenylboronate species, which then displaces the halide present on the palladium atom.²⁴⁷ Therefore in the study presented here, the phenylboronate is used as the transmetallation partner.

4.3.1 Catalyst activation pathway

In this section, solvent corrections were performed using *o*-xylene to compare to the experimental Suzuki-Miyaura coupling results.

The proposed catalytic activation pathway includes several key steps. The nucleophilic substitution of the halide by the phenylboronate, the transmetallation step with the formation of the new Pd-C bond; and finally the reductive elimination of the Pd with the formation of the new C-C bond.

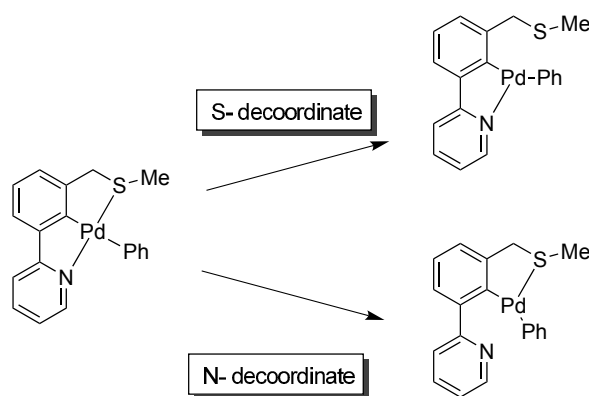
A general scheme detailing key steps in this pathway is provided in Scheme 4.15 where it can be seen that for the reductive elimination there are two different possibilities, depending on whether S- or N- remains coordinated to the palladium atom. One of the Pd-L bonds requires cleavage to facilitate reductive elimination, as this is not possible in the *trans* configuration. Likewise, in the ligand decoordination step (Scheme 4.15) either S- or N- can decoordinate first.



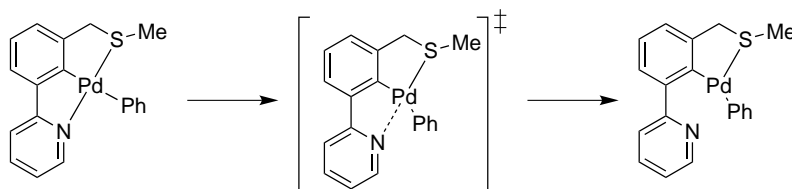
Scheme 4.15 Key steps in the catalyst activation pathway.

For the ligand decoordination in the reductive elimination step (Scheme 4.15) for $\text{R} = \text{Me}$, palladacycle **2a**, two possibilities are shown (Scheme 4.16), and the cleavage of the Pd-S bond is slightly more favourable than the cleavage of the Pd-N

bond (by 10.5 kJ mol^{-1}), however a reductive elimination transition state does not exist on the potential energy surface for the Pd-S decooordination pathway, therefore in this pathway, the Pd-N bond must cleave. The transition state leading to Pd-N bond decooordination (Scheme 4.17) as expected is large ($\Delta G^\ddagger = 172.2 \text{ kJ mol}^{-1}$), however in the real experimental system this is likely to be drastically reduced due to the presence of additional coordinating groups, such as the phenylboronate, or solvent to occupy the now empty coordination site. To test this, acetonitrile, a more polar solvent was chosen as solvent in the PCM model. A lower barrier of $161.7 \text{ kJ mol}^{-1}$ was found, and therefore even though this is not an explicit solvent molecule decreases the barrier. Therefore despite the large barrier for this step, it is unlikely to be rate determining experimentally due to the presence of other coordinating groups.



Scheme 4.16 Ligand decooordination leading to reductive elimination.

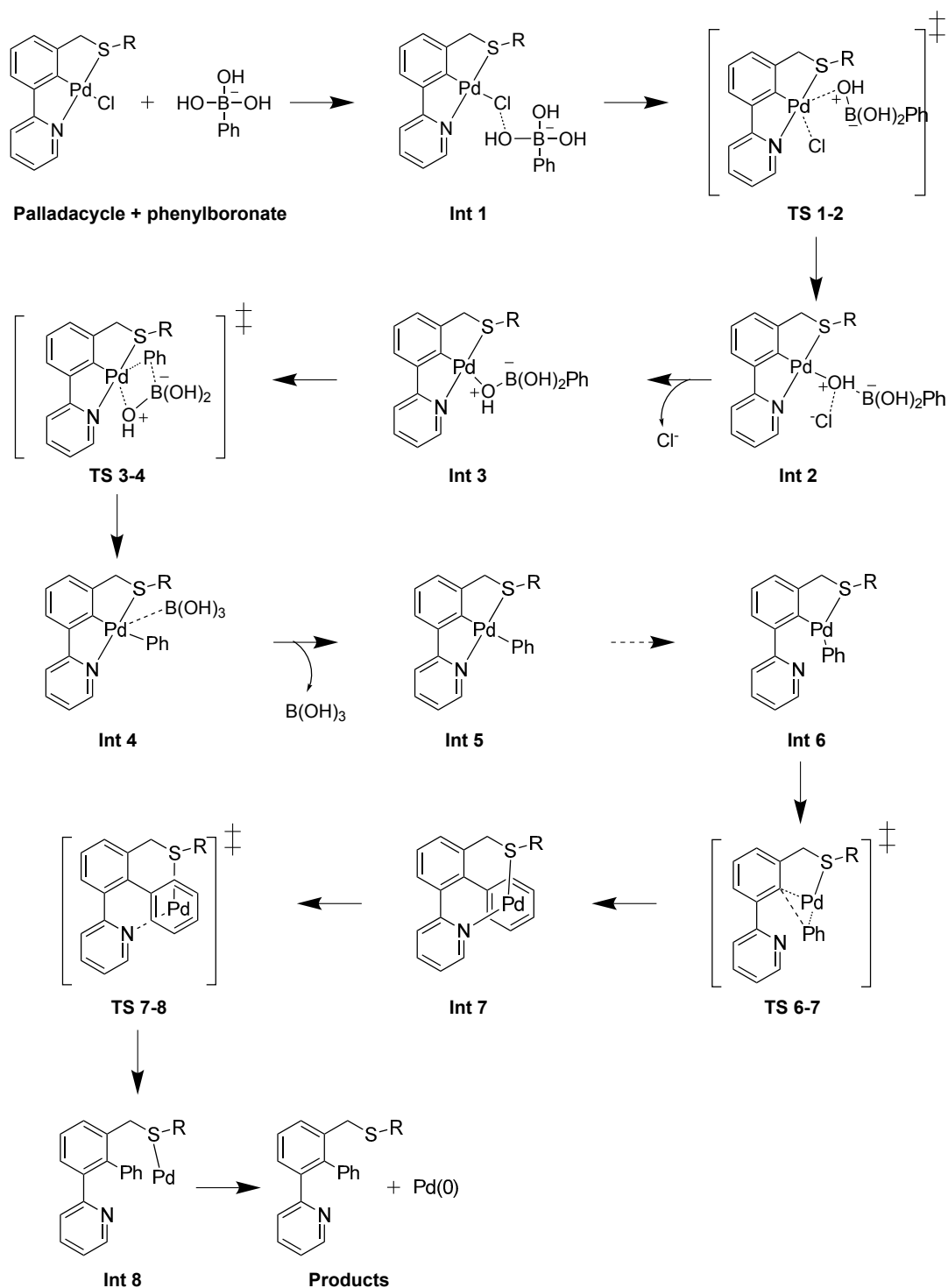


Scheme 4.17 N-decoordination transition state.

Similarly, in the final ligand decooordination step (Scheme 4.15), two possibilities exist, with either S- or N- decoordinates from the palladium. For **2a**, N- decoordinates has a lower energy barrier (14.3 kJ mol^{-1}) than when S- decoordinates from palladium (39.7 kJ mol^{-1}), with N- decoordinates also yielding a more stable singly coordinated

palladium structure, by 70.3 kJ mol^{-1} . This is due to the greater flexibility of the thioether arm, allowing π -interactions between the Ph group and the palladium atom. Therefore the N- decoordination pathway is more favourable.

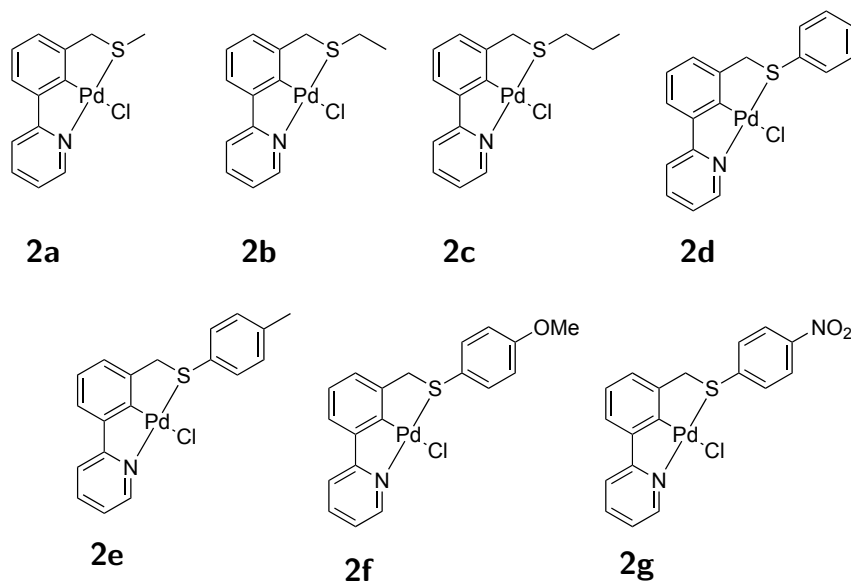
Considering the possibilities discussed, the most likely pathway is shown in Scheme 4.18. The first step is the nucleophilic substitution of the halide in **TS 1-2** by the phenylboronate, the second step is transmetallation in **TS 3-4** with the formation of the new Pd-C bond; and the third step is reductive elimination of the Pd in **TS 6-7** with the formation of the new C-C bond. The Gibbs free energies for each SCN pincer palladacycle, **2a-g** are presented in Table 4.7.



Scheme 4.18 Full catalyst activation pathway for SCN pincer palladacycles in the generation of Pd(0). For R \neq Me barrier not calculated for **TS 5-6**, denoted by the dashed arrow.

The energies are shown in Figure 4.19 with the key sections of the reaction included; the nucleophilic chloride substitution by the phenylboronate, transmetalation, reductive elimination, and ligand decoordination.

Table 4.7 Gibbs free energies, ΔG_S , the energies including a solvent correction, for the catalyst activation pathway of SCN pincer palladacycles.



	ΔG_S / kJ mol ⁻¹						
	2a	2b	2c	2d	2e	2f	2g
Palladacycle	0.0	0.0	0.0	0.0	0.0	0.0	0.0
Int 1	8.0	13.0	11.1	2.8	4.2	9.5	-10.0
TS 1-2	43.0	35.4	33.2	47.2	41.2	48.1	33.2
Int 2	9.7	9.3	4.9	4.0	6.1	9.1	6.2
Int 3	20.3	23.8	16.0	13.9	15.4	19.5	14.5
TS 3-4	120.0	121.2	117.4	118.1	119.8	117.7	112.4
Int 4	-8.6	-3.9	-12.0	-17.5	-17.4	-11.3	-25.8
Int 5	-24.2	-25.1	-30.8	-28.9	-30.9	-31.2	-34.7
Int 6	35.9	46.3	43.2	26.1	27.7	24.4	21.4
TS 6-7	131.3	130.1	131.4	118.1	119.4	121.0	106.8
Int 7	-1.0	1.7	0.7	-15.9	-14.2	-12.2	-22.2
TS 7-8	13.3	13.0	13.4	-1.3	-2.5	1.2	-12.2
Int 8	-51.1	-47.6	-47.2	-67.5	-64.6	-64.7	-71.9
Ligand	72.4	83.0	84.1	62.0	59.9	61.6	54.9

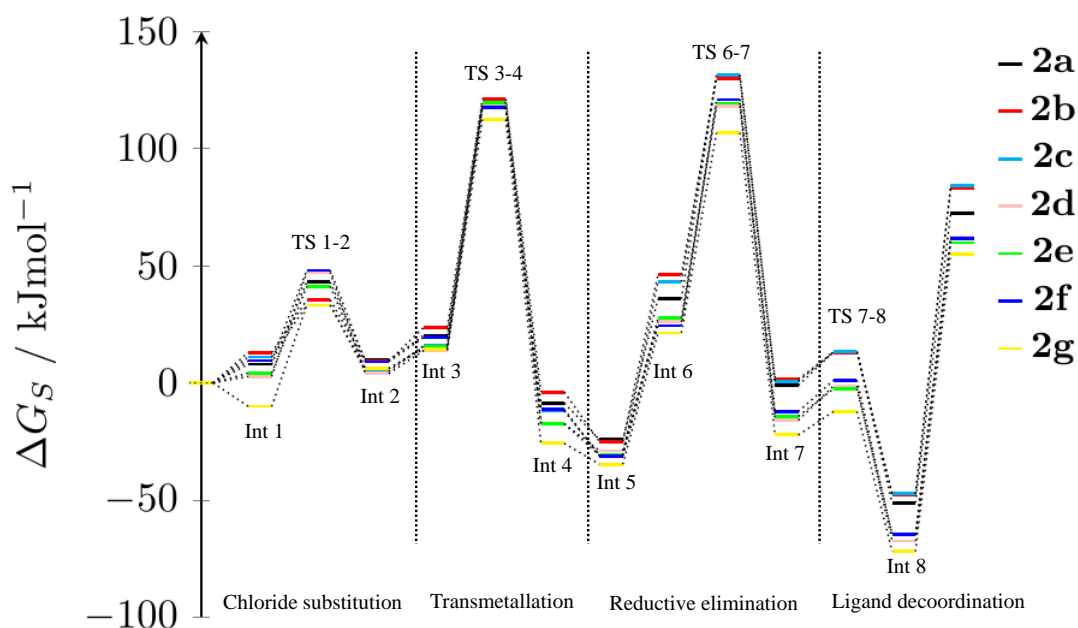


Figure 4.19 Gibbs free energies (ΔG_s) for SCN pincer palladacycle catalyst activation pathway.

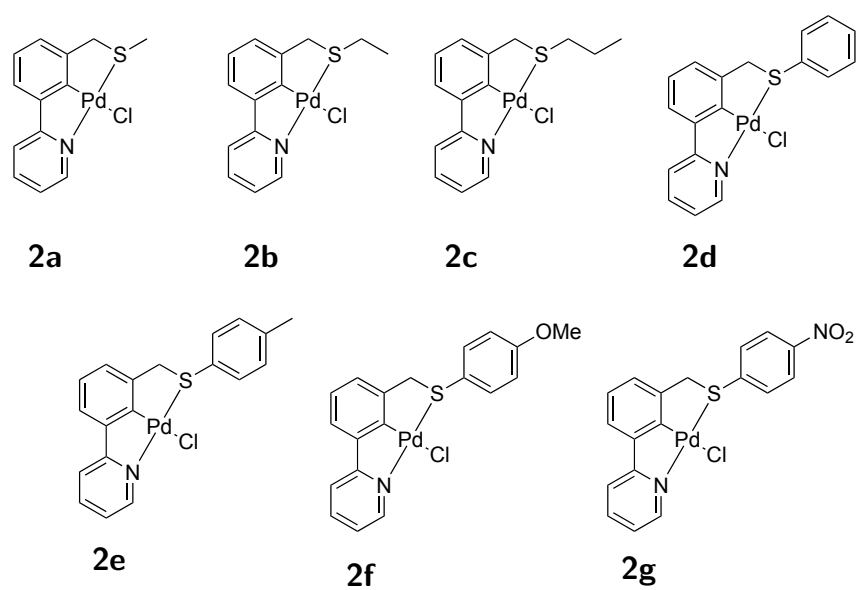
Due to the presence of two different donor atoms, different scenarios are possible in the various stages of the reaction pathway. For example, at **Int 6** either the S- or the N- can decoordinate from the square planar palladium atom to provide the desired geometry for reductive elimination. The energy difference for **2a** is only 10 kJ mol^{-1} .

The activation energy barriers (ΔG_s^\ddagger) for the chloride substitution (**TS 1-2**), transmetallation (**TS 3-4**), reductive elimination (**TS 6-7**) and ligand decooordination (**TS 7-8**) steps are tabulated in Table 4.8. In all cases, the transmetallation barriers (**TS 3-4**) are larger than the reductive elimination barriers (**TS 6-7**) to varying degrees, making it the rate determining step in the reaction pathway. The chloride substitution (**TS 1-2**) and ligand dissociation steps (**TS 7-8**) have significantly lower barriers ($<36 \text{ kJ mol}^{-1}$).

There is no discernible difference between the rate determining step in each pathway, regardless of the substituent on the thioether arm, with a difference of only 6.9 kJ mol^{-1} between the lowest rate determining step (**TS 3-4** for **2b**) and the largest (**TS 3-4** for **2d**).

The transmetallation (**TS 3-4**) barriers presented in this work ($\approx 100 \text{ kJ mol}^{-1}$)

Table 4.8 Gibbs free activation energy barriers (ΔG_S^\ddagger) for key steps for the SCN pincer palladacycle catalyst activation pathways.



	$\Delta G_S^\ddagger / \text{kJ mol}^{-1}$						
	2a	2b	2c	2d	2e	2f	2g
TS 1-2	35.0	22.3	22.0	44.5	37.0	38.6	43.2
TS 3-4	99.7	97.4	101.3	104.2	104.3	98.1	97.9
TS 6-7	95.4	83.8	88.2	92.0	91.7	96.5	85.4
TS 7-8	14.3	11.3	12.7	14.6	11.6	13.4	10.0

can be compared to similar studies into the transmetallation step in the Suzuki-Miyaura coupling reaction, with the same use of phenylboronate as the transmetallation partner. The pathway by Braga and co-workers shown in Scheme 4.8, where a barrier of 92 kJ mol^{-1} was found, albeit without solvent corrections;²²⁶ Zhang and Li,²⁴⁸ found a barrier of 81 kJ mol^{-1} for the step shown in Figure 4.20, using THF as a continuum solvent; barriers found by Harvey and co-workers,²²⁸ for the transmetallation step shown in Figure 4.21, were between 60 and 82 kJ mol^{-1} depending on the R group in the PR_3 ligand, again using continuum THF as solvent;²²⁸ and between 71 and 97 kJ mol^{-1} for the study for chelated palladium complexes by Huang, Weng and Hong, calculated in the gas phase.²²⁹

Clearly the barriers presented in this work for the transmetallation step are only slightly larger than most of the ones found in the theoretical study of potential mechanisms for Suzuki-Miyaura catalysis, and show that the mechanism presented is feasible.

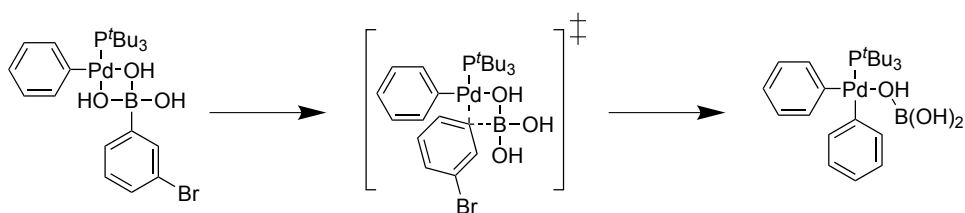


Figure 4.20 Zhang and Li transmetallation pathway.

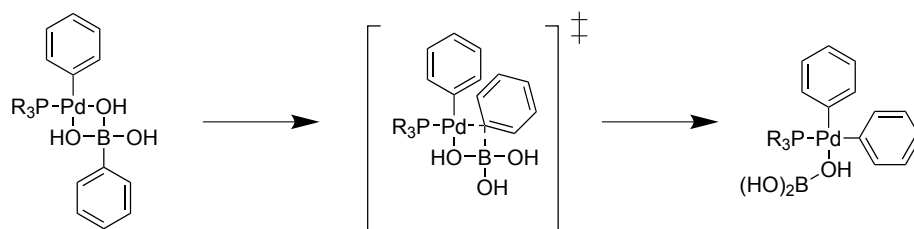


Figure 4.21 Harvey and co-workers transmetallation pathway.

For the reductive elimination step, many studies have been previously presented. Activation energies for reductive elimination of ethane from $\text{PdMe}_2(\text{PMe}_3)\text{L}$ complexes ranged from 25 to 96 kJ mol^{-1} depending on the L group in a study by Espinet and co-workers;²³⁶ and in an excellent study into reductive elimination of

ethane from $\text{PdMe}_2(\text{PR}_3)_2$ reveals the electronic effects of the PR_3 ligands on the activation barrier, and PMe_3 ligands having the largest energy barriers (110 kJ mol^{-1}), with PPh_3 having the smallest barriers (75 kJ mol^{-1}).²³⁷ A similar investigation was performed by Sajith and Suresh, revealing barriers ranging from 63 kJ mol^{-1} for PCl_3 ligands, to 132 kJ mol^{-1} for PEt_3 ligands, with a barrier found of 100 kJ mol^{-1} for PPh_3 ligands.¹⁵²

These results also show that the reductive elimination barriers of between 90.3 and $103.3 \text{ kJ mol}^{-1}$ presented in this work are reasonable when compared to similar reactions presented in the literature.

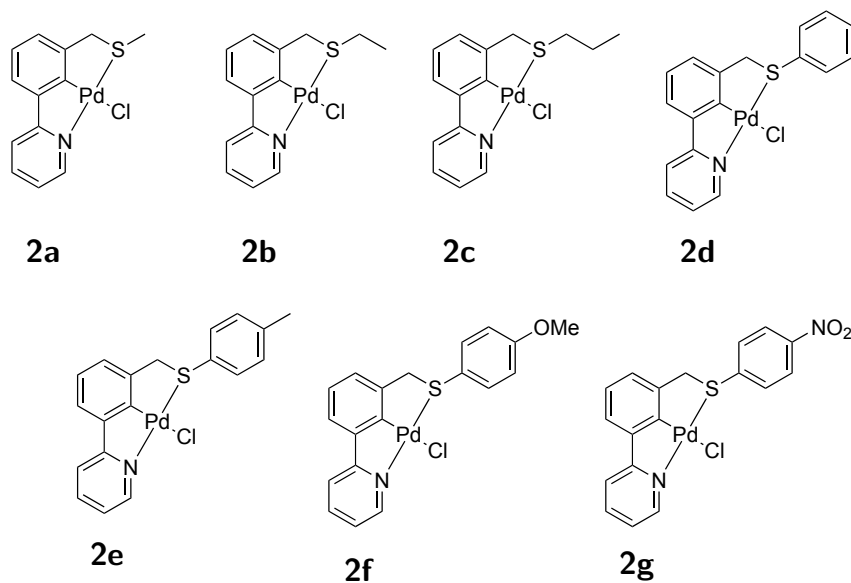
The overall pathway to ligand free $\text{Pd}(0)$ is endergonic in all cases, with $\Delta G_S > 42.5 \text{ kJ mol}^{-1}$, however differences emerge dependent on the thioether substituent, with the alkyl substituted examples (**2a–c**) being more endergonic (**2a** = 54.7 kJ mol^{-1} , **2b** = 65.1 kJ mol^{-1} and **2c** = 65.8 kJ mol^{-1}) than the aryl examples (**2d–g** with values $< 46.4 \text{ kJ mol}^{-1}$).

4.3.2 Bader charge analysis

As the aim of changing the substituent on the thioether arm was to investigate the effect on the sulphur charge and consequently the palladium atom. Bader charge analysis has been performed on the pathway shown in Scheme 4.18 for all SCN pincer palladacycles, with the S (Table 4.9) and Pd (Table 4.10) charges presented.

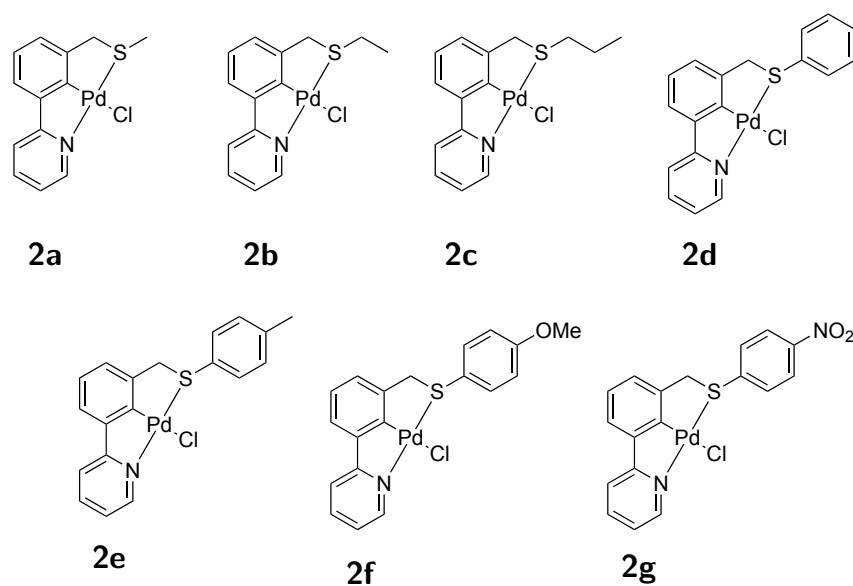
The charge analysis for the S atom (Table 4.9) shows that the alkyl substituted examples, with: Me, Et or Pr thioether substituents (**2a–c**) have a greater electron density on the sulphur atom in the palladacycle (charges of 0.079 to 0.107 a.u.) with the Pr substituent having the greatest electron density, as expected, with a charge of 0.079 a.u. In comparison, the aryl thioether substituents (**2d–g**) provide less electron density on the S atom (0.110 to 0.130 a.u.), with the mesomerically donating OMe group in **2f**, and inductively donating CH_3 groups providing a little additional electron density to the S atom, as compared to **2d**. However the electron withdrawing NO_2 group provides a more electron rich sulphur atom in **2g** than in

Table 4.9 Bader charge analysis of S atom in the catalyst activation pathway of SCN pincer palladacycles.



Structure	Bader charge / a.u.						
	2a	2b	2c	2d	2e	2f	2g
Palladacycle	0.107	0.080	0.079	0.130	0.110	0.111	0.118
Int 1	0.136	0.092	0.095	0.156	0.155	0.156	0.216
TS 1-2	0.159	0.080	0.080	0.172	0.171	0.176	0.195
Int 2	0.075	0.073	0.074	0.157	0.155	0.156	0.126
Int 3	0.127	0.068	0.106	0.160	0.157	0.162	0.137
TS 3-4	0.121	0.092	0.084	0.144	0.144	0.148	0.117
Int 4	0.088	0.068	0.065	0.101	0.101	0.110	0.115
Int 5	0.086	0.064	0.067	0.108	0.109	0.109	0.124
Int 6	-0.006	-0.026	-0.026	0.013	0.013	0.016	0.023
TS 6-7	0.002	-0.018	-0.017	0.023	0.022	0.024	0.028
Int 7	0.007	-0.014	-0.018	0.031	0.050	0.032	0.051
TS 7-8	0.036	0.015	0.010	0.057	0.057	0.059	0.069
Int 8	0.006	-0.015	-0.017	0.025	0.026	0.026	0.034
Product	-0.003	-0.025	-0.031	0.019	0.017	0.019	0.034

Table 4.10 Bader charge analysis of Pd atom in the catalyst activation pathway of SCN pincer palladacycles.



Structure	Bader charge / a.u.						
	2a	2b	2c	2d	2e	2f	2g
Palladacycle	0.572	0.574	0.574	0.586	0.577	0.576	0.583
Int 1	0.623	0.621	0.620	0.625	0.670	0.625	0.633
TS 1-2	0.643	0.658	0.656	0.646	0.646	0.645	0.647
Int 2	0.664	0.672	0.672	0.670	0.670	0.670	0.677
Int 3	0.622	0.634	0.623	0.623	0.636	0.636	0.637
TS 3-4	0.564	0.563	0.555	0.573	0.573	0.573	0.584
Int 4	0.557	0.539	0.552	0.557	0.556	0.551	0.529
Int 5	0.542	0.542	0.543	0.547	0.530	0.547	0.553
Int 6	0.372	0.372	0.372	0.372	0.372	0.373	0.368
TS 6-7	0.277	0.277	0.280	0.272	0.273	0.272	0.239
Int 7	-0.033	-0.029	-0.022	-0.028	-0.059	-0.029	-0.027
TS 7-8	-0.036	-0.034	-0.033	-0.024	-0.027	-0.029	-0.015
Int 8	0.065	0.067	0.063	0.073	0.072	0.073	0.072
Product	-	-	-	-	-	-	-

2d.

These changes in electron density on the sulphur atom, induce very small differences on the palladium atom in the palladacycle. For example, all palladium charges are between 0.572 and 0.586 a.u. (Table 4.10). However, all alkyl substituted thioethers (**2a–c**) have slightly more electron rich palladium atoms (0.572 - 0.574 a.u.) than the aryl substituted thioethers (**2d–g**, 0.576 - 0.586 a.u.).

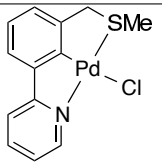
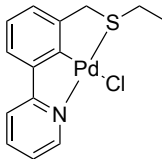
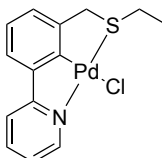
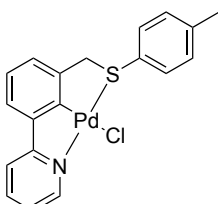
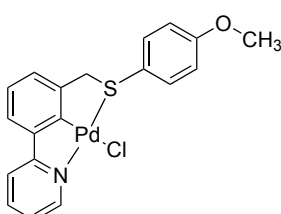
In the rate determining transmetallation step, differences are evident in the palladium charge, with the more electron rich alkyl examples (**2a–c**) inducing more electron density onto the palladium (0.555 - 0.563 a.u.), as compared to 0.573 - 0.584 a.u. for the aryl substituted examples (**2d–g**), however do not effect the energy barriers, as all transmetallation barriers are comparable with no discernible trend (Table 4.8).

In the reductive elimination step, for the S charge (Table 4.9) the same trend emerges for that of the transmetallation step, but less pronounced, with greater electron density on the S for alkyl substituents (**2a–c**) of -0.018 to 0.002 a.u. compared to the aryl substituted examples (**2d–g**) of 0.022 to 0.024 a.u., however they are insignificant, and therefore have negligible difference. This explains the very similar reductive elimination barriers (Table 4.8).

4.4 Rationalisation of the catalysis results

It has been found (Section 4.2.3) that in the application of palladacycles, **2a–c,e,f**, in the Suzuki-Miyaura catalysis that differences emerged in their catalytic activity. It was found that the aryl substituted examples, **2e** and **2f** achieved lower % conversion than the alkyl substituted examples, **2a–c** (Table 4.6). The full catalyst activation pathway was studied using DFT revealing key steps and barriers, including transmetallation and reductive elimination, however these revealed little difference between the different pathways, with no discernible trend. More significant differences were observed between the palladacycles for the overall reaction energies. The final catalytic results and overall reaction energies are summarised in Table 4.11.

Table 4.11 SCN pincer palladacycle catalysis results, compared to overall catalyst activation pathway energy.

Palladacycle	6 h GC conversion / %	Overall pathway energy / kJ mol ⁻¹
	79	72.4
	64	83.0
	79	84.1
	39	59.9
	37	61.6

The least endergonic reactions, and therefore more favourable are the palladacycles bearing the aryl substituents (**2e** and **2f**, 59.9 and 61.6 kJ mol⁻¹, respectively), and also achieve lower % conversions compared to the alkyl substituted examples (**2a-c**, 72.4 - 84.1 kJ mol⁻¹, respectively). This correlation between results can be explained by the likely role of the catalytically active Pd(0) species.

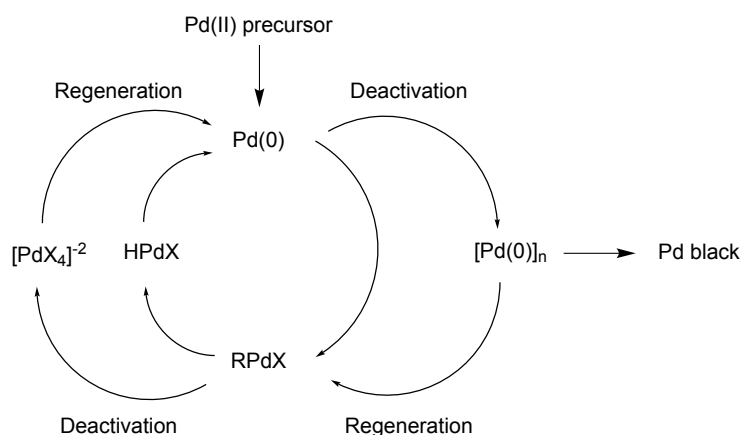
In work by de Vries *et al.* into the role of ligand free palladium in the Heck reaction, it was found pallacycles act as a source of ligand-free palladium, with investigations into catalyst loading of Pd(OAc)₂ on the catalytic activity.^{45,249} The results showed that at higher catalyst loadings, palladium black forms, stopping the reaction, as shown in Scheme 4.19, as higher concentrations of the ligand free palladium produces more catalytically inactive Pd(0).



Scheme 4.19 Proposed role of Pd(0) in catalysis by de Vries *et al.*

In a detailed study by Dupont and co-workers²⁵⁰ into the study of possible catalysis in the Heck reaction, and the active Pd(0) species, they propose possible deactivation routes, shown in Scheme 4.20 with a key deactivation route to the agglomeration of palladium nanoparticles to form catalytically inactive palladium black. The same was proposed by de Vries for pincer palladacycles in the Heck reaction,²⁵¹ again providing possible routes to catalyst deactivation due to palladium black.

The decreased catalytic activity of the aryl based SCN pincer palladacycles (**2e** and **2f**) and less endergonic pathway towards ligand free palladium (Table 4.11) can be explained by the fate of the resulting ligand free palladium as discussed in the reports above. The less endergonic pathway results in more Pd(0) being formed due to the pathway being more favourable than for palladacycles **2a-c**, which in turn provides a greater likelihood of the Pd(0) agglomerating to form the catalytically



Scheme 4.20 Proposed catalyst deactivation by Dupont and co-workers.

inactive palladium black. The less favourable pathway towards ligand free palladium from **2a–c** yields less Pd(0), resulting in less palladium black, and leaving more catalytically active Pd(0) species, increasing the % conversions in Suzuki-Miyaura catalysis. Work by Bedford *et al.* attributed the greater activity of phosphinite palladacycles to increased catalyst longevity provided by π acidity of the arylated ligand, which is a similar principle as presented here where the palladacycle is able to greater stabilise the Pd(0) species, increasing activity.²⁵²

These findings suggest that the ability to allow slow, controlled release of Pd(0) is a possible way to improve results in catalytic Suzuki-Miyaura coupling, and changing the donor atoms and groups to achieve this is a possible way to improve catalytic performance in catalysis where palladacycles act as sources of ligand free palladium, such as the Suzuki-Miyaura coupling.

4.5 Conclusion

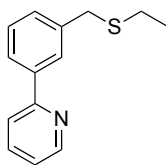
This chapter has summarised the synthesis of a family of novel SCN pincer ligands, which *via* C-H bond activation yielded their palladacycles. These palladacycles were tested in the Suzuki-Miyaura catalysis where it was found they achieved reasonable conversion of electronically demanding and sterically hindered aryl bromides into their biaryl products, with differences emerging depending on the thioether substituent. Aryl substituted examples were found to achieve lower conversions than the

alkyl substituted examples. In order to investigate the effect of changing thioether substituent, a potential catalyst activation pathway was reported involving key transmetallation, reductive elimination, and ligand decoordination steps studied using DFT. Different possibilities were examined for S- or N- decoordination before the reductive elimination, and the final ligand decoordination steps, with N- decoordination forming a complete and more energetically favourable pathway. It was found the different thioether substituents had little effect on the kinetics of the pathway, however the thermodynamics were effected, with the aryl substituted thioether based palladacycles being less endergonic than the alkyl substituted examples. The easier release of catalytically active Pd(0) by the aryl examples potentially increases Pd(0) concentration resulting in undesirable palladium black formation, therefore the alkyl based palladacycles, which provide less favourable ligand free palladium generation are preferable, and act as more efficient precatalysts.

4.6 Experimental details

4.6.1 Experimental procedures

2-3-[(Ethylsulfanyl)methyl]phenylpyridine, **1b**.



Under an argon atmosphere, ethanethiol (2.42 mmol, 0.179 mL) and sodium hydride (2.41 mmol, 58 mg) were dissolved in dry DMF (3 mL) and the mixture was stirred at room temperature in a sealed microwave vial for 15 min. **6** (1.61 mmol, 400 mg) in dry DMF (3 mL) was then added, and stirred under microwave irradiation (maximum power, 300 W, dynamic heating) at 150 °C for 15 min. After cooling, the solvent was removed *in vacuo* and the crude mixture was diluted in H₂O (25 mL) and DCM (25 mL). The product was extracted with DCM (2 × 25 mL), washed with H₂O (5 × 25 mL) and brine (25 mL). The organic layers were dried over anhydrous

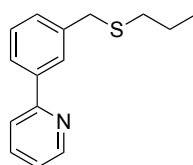
MgSO₄, filtered, and concentrated *in vacuo*. The crude product was purified using flash column chromatography (7:3 DCM:EtOAc) yielding 263 mg of the expected product, **1b**, as a yellow oil in 71 % yield.

¹H NMR (500 MHz), Chloroform-*d* δ (ppm): 8.70 (d, J = 4.8 Hz, 1H), 7.96 (s, 1H), 7.86 (d, J = 7.5 Hz, 1H), 7.77 - 7.73 (m, 2H), 7.43 (dd, J = 7.5, 7.5 Hz, 1H), 7.39 (d, J = 7.5 Hz, 1H), 7.24 (ddd, J = 6.3, 4.8, 2.3 Hz, 1H), 3.81 (s, 2H), 2.48 (q, J = 7.5 Hz, 2H), 1.25 (t, J = 7.5 Hz, 3H).

¹³C{¹H}NMR (126 MHz, Chloroform-*d*) δ : 157.3, 149.7, 139.6, 139.2, 136.7, 129.4, 128.9, 127.4, 125.5, 122.1, 120.6, 36.0, 25.4, 14.4.

HRMS (m/z). Calc. for [C₁₄H₁₅NS + H]⁺ 230.0998. Found 230.0998.

2-3-[(Propylsulfanyl)methyl]phenylpyridine, **1c**.



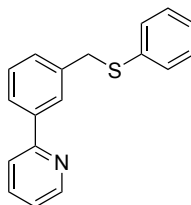
Under an argon atmosphere, propane-1-thiol (1.97 mmol, 0.178 ml) and sodium hydride (1.97 mmol, 47 mg) were dissolved in dry DMF (2 ml) and stirred at room temperature in a sealed microwave vial for 15 min. **6** (1.23 mmol, 304 mg) in dry DMF (2 ml) was then added and then the mixture stirred under microwave irradiation (maximum power, 300 W, dynamic heating) at 150 °C for 20 min. After cooling, the crude product was extracted with DCM (3 × 25 ml) and washed with H₂O (5 × 25 ml) and brine (25 ml). The organic layers were dried over anhydrous Na₂SO₄, filtered and concentrated *in vacuo* yielding 300 mg of the expected product, **1c**, as a yellow oil in >99 % yield.

¹H NMR (500 MHz, Chloroform-*d*) δ (ppm): 8.70 (d, J = 4.8 Hz, 1H), 7.96 (s, 1H), 7.86 (d, J = 7.5 Hz, 1H), 7.78 - 7.73 (m, 2H), 7.43 (dd, J = 7.5, 7.5 Hz, 1H), 7.39 (d, J = 7.5 Hz, 1H), 7.24 (ddd, J = 6.5, 4.8, 2.1 Hz, 1H), 3.79 (s, 2H), 2.44 (t, J = 7.2 Hz, 2H), 1.64 - 1.57 (m, 2H), 0.96 (t, J = 7.3 Hz, 3H).

$^{13}\text{C}\{^1\text{H}\}$ NMR (126 MHz, Chloroform-*d*) δ (ppm): 157.2, 149.6, 139.6, 139.3, 136.7, 129.4, 128.8, 127.4, 125.5, 122.1, 120.6, 36.3, 33.6, 22.6, 13.5.

HRMS (*m/z*). Calc. for $[\text{C}_{15}\text{H}_{17}\text{NS} + \text{H}]^+$ 244.1154. Found 244.1155.

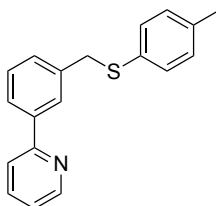
2-3-[(Phenylsulfanyl)methyl]phenylpyridine, 1d.



Under an argon atmosphere, benzenethiol (1.86 mmol, 0.190 ml) and sodium hydride (1.82 mmol, 44 mg) were dissolved in dry DMF (2 ml) and the mixture stirred at room temperature in a sealed microwave vial for 15 min. **6** (1.53 mmol, 379 mg) in dry DMF (2 ml) was then added and the mixture was stirred under microwave irradiation (maximum power, 300 W, dynamic heating) at 150 °C for 20 min. After cooling, the product was extracted with EtOAc (3 × 35 ml) and washed with H₂O (7 × 35 ml) and brine (35 ml). The organic layers were dried over anhydrous Na₂SO₄, filtered and concentrated *in vacuo* yielding 418 mg of the expected product, **2d** as a yellow oil in 99 % yield.

^1H and $^{13}\text{C}\{^1\text{H}\}$ NMRs are in agreement with previous values.²⁴²

2-(3-[(4-Methylphenyl)sulfanyl]methylphenyl)pyridine, 1e.



Under an argon atmosphere, 4-methylbenzenethiol (0.70 mmol, 87 mg) and triethylamine (0.70 mmol, 0.099 ml) were dissolved in dry EtOH (2 ml) and stirred at room temperature in a sealed microwave vial for 15 min. **6** (0.44 mmol, 110 mg) in dry EtOH (2 mmol) was then added and the mixture was stirred under microwave irradiation (maximum power, 300 W, dynamic heating) at 150 °C for 20 min. After

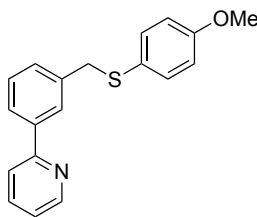
cooling, the solvent was removed *in vacuo* and the crude mixture diluted in H₂O (25 mL) and EtOAc (25 mL). The product was extracted with EtOAc (2 × 25 mL), washed with H₂O (2 × 25 mL) and brine (25 mL). The organic layers were dried over anhydrous MgSO₄, filtered and concentrated *in vacuo*. The crude product was purified by flash chromatography (8:2 C₆H₁₂:Et₂O) yielding 65 mg of the expected product, **1e** as a yellow oil in 51 % yield.

¹H NMR (500 MHz, Chloroform-*d*) δ (ppm): 8.70 (d, J = 4.8 Hz, 1H), 7.90 (s, 1H), 7.87 (d, J = 7.6 Hz, 1H), 7.72 (m, 1H), 7.65 (d, J = 8.0 Hz, 1H), 7.39 (dd, J = 7.6, 7.6 Hz, 1H), 7.32 (d, J = 7.6 Hz, 1H), 7.25 (d, J = 8.1 Hz, 2H), 7.21 (ddd, J = 7.4, 4.8, 1.2 Hz, 1H), 7.06 (d, J = 8.1 Hz, 2H), 4.15 (s, 2H), 2.30 (s, 3H).

¹³C{¹H}NMR (100 MHz, Chloroform-*d*) 157.2, 149.6, 139.6, 138.3, 136.6, 132.4, 131.5, 130.9 (2C), 129.6 (2C), 129.3, 128.8, 127.4, 125.7, 122.1, 120.5, 39.9, 21.0.

HRMS (m/z). Calc. for [C₁₉H₁₇NS⁺H]⁺ 292.1154. Found 292.1151.

2-(3-[(4-Methoxyphenyl)sulfanyl]methylphenyl)pyridine, **1f**.



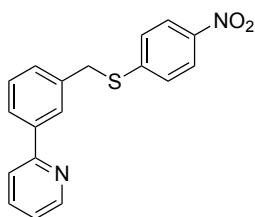
Under an argon atmosphere, 4-methoxybenzenethiol (1.10 mmol, 0.136 mL) and sodium hydride (1.10 mmol, 27 mg) were dissolved in dry DMF (2 mL) and stirred at room temperature in a sealed microwave vial for 15 min. **6** (1.24 mmol, 308 mg) in dry DMF (2 mL) was then added and the mixture stirred under microwave irradiation (maximum power, 300 W, dynamic heating) at 150 °C for 20 min. After cooling, the product was extracted with DCM (3 × 25 mL), washed with water (5 × 25 mL) and brine (25 mL). The organic layers were dried over anhydrous Na₂SO₅, filtered and concentrated *in vacuo*. The crude product was purified by flash column chromatography (9:1 DCM:C₆H₁₂) yielding 203 mg of the expected product, **1f** as a yellow oil in 60 % yield.

^1H NMR (500 MHz, Chloroform-*d*) δ (ppm): 8.69 (ddd, $J = 4.8, 1.8, 0.9$ Hz, 1H), 7.86 (d, $J = 7.7$ Hz, 1H), 7.81 (s, 1H), 7.73 (ddd, $J = 9.7, 7.9, 1.8$ Hz, 1H), 7.65 (d, $J = 7.7$ Hz, 1H), 7.37 (dd, $J = 7.7, 7.7$ Hz, 1H), 7.28 (d, $J = 8.8$ Hz, 2H), 7.25 - 7.21 (m, 2H), 6.79 (d, $J = 8.8$ Hz, 2H), 4.07 (s, 2H), 3.76 (s, 3H).

$^{13}\text{C}\{^1\text{H}\}$ NMR (126 MHz, Chloroform-*d*) δ (ppm): 159.3, 157.2, 149.6, 139.5, 138.6, 136.6, 134.2 (2C), 129.4, 128.8, 127.5, 126.0 (2C), 125.6, 122.1, 120.6, 114.5, 55.3, 41.3.

HRMS (m/z). Calc. for $[\text{C}_{19}\text{H}_{17}\text{NOS} + \text{H}]^+$ 308.1104. Found 308.1109.

2-(3-[(4-Nitrophenyl)sulfanyl]methylphenyl)pyridine, **1g**.

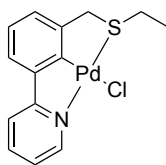


Under an argon atmosphere, 4-nitrobenzenethiol (2.15 mmol), Hunig's base (2.15 mmol, 0.37 ml) were dissolved in dry DMF (2 ml) and stirred at room temperature in a sealed microwave vial for 15 min. **6** (2.30 mmol, 570 mg) in dry DMF (2 ml) was then added and the mixture stirred under microwave irradiation (maximum power, 300 W, dynamic heating) at 150 °C for 20 min. After cooling, the product was extracted with DCM (3×25 ml), washed with H_2O (5×25 ml) and brine (25 ml). The organic layers were dried over anhydrous Na_2SO_4 , filtered and concentrated *in vacuo*. The crude product was purified by flash column chromatography (DCM) yielding 507 mg of the expected product, **1g** as a yellow oil in 73% yield.

^1H NMR (500 MHz, Chloroform-*d*) δ (ppm): 8.69 (d, $J = 4.8$ Hz, 1H), 8.08 - 8.06 (m, 3H) 7.88 (ddd, $J = 4.8, 4.8, 1.7$ Hz, 1H), 7.74 (ddd, 7.9, 7.9, 1.9 Hz, 1H), 7.70 (d, $J = 7.9$ Hz, 1H), 7.43 (m, 2H), 7.34 (d, $J = 9.0$ Hz, 2H), 7.23 (ddd, $J = 7.1, 4.8, 1.7$ Hz, 1H), 4.31 (s, 2H).

$^{13}\text{C}\{^1\text{H}\}$ NMR (126 MHz, Chloroform-*d*) δ (ppm): 156.7, 149.7, 147.1, 145.3 (2C), 140.0, 136.8, 136.1, 129.2, 129.1, 127.4, 126.7, 126.3 (2C), 123.9, 122.4, 120.6, 37.1.

HRMS (m/z). Calc. for $[\text{C}_{18}\text{H}_{14}\text{N}_2\text{O}_2\text{S} + \text{H}]^+$ 323.0849. Found 323.0850.

2-3-[(Ethylsulfanyl)methyl]phenylpyridine chloro-palladacycle, 2b.

Under an argon atmosphere, PdCl_2 (1.17 mmol, 208 mg) was dissolved in dry MeCN (10 ml) and heated under reflux until a red solution had formed. AgBF_4 (2.36 mmol, 460 mg) in dry MeCN (5 ml) was added to the PdCl_2 solution and heated under reflux for 2 h, forming a white precipitate. The precipitate was filtered off, and **1b** (1.13 mmol, 260 mg) dissolved in dry MeCN (10 ml), was added to the filtrate, and heated under reflux for 4 h. The solution was cooled to room temperature, filtered over celite, and the solvent removed *in vacuo*.

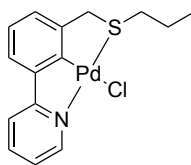
The crude solid was dissolved in MeCN (5 ml), and NaCl (26.0 mmol, 1.52 g) dissolved in H_2O (5 ml) was added, and stirred at room temperature for 3 h. The solvent was removed *in vacuo*, and the crude mixture dissolved in DCM (25 ml) and H_2O (25 ml). The crude product was extracted with DCM (2×25 ml), washed with H_2O (2×25 ml) and brine (25 ml), and dried over anhydrous Na_2SO_4 . The mixture was filtered over celite, and the solvent removed *in vacuo*, yielding 347 mg of the expected product, **2b** as a yellow solid in 83 % yield.

^1H NMR (500 MHz, Chloroform-*d*) δ (ppm): 9.15 (d, $J = 5.5$ Hz, 1H), 7.84 (ddd, $J = 7.8, 7.8, 1.7$ Hz, 1H), 7.64 (d, $J = 7.8$ Hz, 1H), 7.33 (d, $J = 7.7$ Hz, 1H), 7.26 - 7.23 (m, 1H), 7.08 (dd, $J = 7.7, 7.7$ Hz, 1H), 7.03 (d, $J = 7.7$ Hz, 1H), 4.25 (bs, 2H), 3.20 (q, $J = 7.4$ Hz, 2H), 1.57 (t, $J = 7.4$ Hz, 3H).

$^{13}\text{C}\{^1\text{H}\}$ NMR (126 MHz, Chloroform-*d*) δ (ppm): 165.5, 165.3, 150.5, 148.1, 144.4, 139.0, 125.0, 124.7, 122.9, 122.2, 118.7, 45.8, 33.8, 14.8.

HRMS (m/z). Calc. for $[\text{C}_{14}\text{H}_{14}\text{NPdS}]^+$ 333.9876. Found 333.9878.

Elemental Analysis. Calc. (%) for $\text{C}_{14}\text{H}_{14}\text{NPdS}$: C 45.42, H 3.81, N 3.78; found C 45.50, H 3.75, N 3.83.

2-3-[(Propylsulfanyl)methyl]phenylpyridine chloro-palladacycle, 2c.

Under an argon atmosphere, PdCl₂ (0.56 mmol, 99 mg) was dissolved in dry MeCN (10 ml) and heated under reflux until a red solution had formed. AgBF₄ (1.14 mmol, 223 mg) in dry MeCN (5 ml) was added to the PdCl₂ solution and heated under reflux for 2 h, forming a white precipitate. The precipitate was filtered off, and **1c** (0.55 mmol, 113 mg) dissolved in dry MeCN (10 ml), was added to the filtrate, and heated under reflux for 6 h. The solution was cooled to room temperature, filtered over celite, and the solvent removed *in vacuo*.

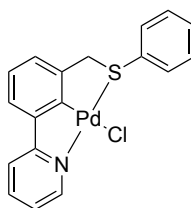
The crude solid was dissolved in MeCN (5 ml), and NaCl (10.9 mmol, 638 mg) dissolved in H₂O (5 ml) was added, and stirred at room temperature for 3 h. The solvent was removed *in vacuo*, and the crude mixture dissolved in DCM (25 ml) and H₂O (25 ml). The crude product was extracted with DCM (2 × 25 ml), washed with H₂O (2 × 25 ml) and brine (25 ml), and dried over anhydrous Na₂SO₄. The mixture was filtered over celite, and the solvent removed *in vacuo*, yielding 179 mg of the expected product, **2c** as a yellow solid in 85 % yield.

¹H NMR (500 MHz, Chloroform-*d*) δ (ppm): 9.11 (d, *J* = 5.5 Hz, 1H), 7.82 (ddd, *J* = 7.8, 7.8, 1.7 Hz, 1H), 7.62 (d, *J* = 7.7 Hz, 1H), 7.30 (d, *J* = 7.8 Hz, 1H), 7.22 (ddd, *J* = 7.8, 5.5, 1.3 Hz 1H), 7.05 (dd, *J* = 7.7, 7.7 Hz, 1H), 7.00 (d, *J* = 7.7 Hz, 1H), 4.27 (bs, 2H), 3.15 (t, *J* = 7.8 Hz, 2H), 1.96 (m, 2H), 1.07 (t, *J* = 7.4 Hz, 3H).

¹³C{¹H}NMR (126 MHz, Chloroform-*d*) δ (ppm): 165.5, 165.3, 150.5, 148.1, 144.4, 139.0, 125.0, 124.6, 122.9, 122.1, 118.7, 46.6, 41.4, 23.3, 13.3.

HRMS (*m/z*). Calc. for [C₁₅H₁₆NPdS]⁺ 348.0033. Found 348.0032.

Elemental Analysis. Calc. (%) for C₁₅H₁₆NPdS: C 46.89, H 4.20, N 3.65; found: C 47.02, H 4.08, N 3.56.

2-3-[(Phenylsulfanyl)methyl]phenylpyridine chloro-palladacycle, 2d.

Under an argon atmosphere, PdCl₂ (1.52 mmol, 270 mg) was dissolved in dry MeCN (10 ml) and heated under reflux until a red solution had formed. AgBF₄ (3.05 mmol, 593 mg) in dry MeCN (5 ml) was added to the PdCl₂ solution and heated under reflux for 2 h, forming a white precipitate. The precipitate was filtered off, and **1d** (1.51 mmol, 418 mg) dissolved in dry MeCN (15 ml), was added to the filtrate, and heated under reflux for 6 h. The solution was cooled to room temperature, filtered over celite, and the solvent removed *in vacuo*.

The crude solid was dissolved in MeCN (5 ml), and NaCl (30.1 mmol, 1.76 g) dissolved in H₂O (5 ml) was added, and stirred at room temperature over night. The solvent was removed *in vacuo*, and the crude mixture dissolved in DCM (25 ml) and H₂O (25 ml). The crude product was extracted with DCM (2 × 25 ml), washed with H₂O (2 × 25 ml) and brine (25 ml), and dried over anhydrous MgSO₄. The mixture was filtered over celite, and the solvent removed *in vacuo*.

The crude product was purified by flash column chromatography (100 % → 98:2 DCM:MeOH), yielding 446 mg of the expected product, **2d** as a yellow solid in 71 % yield.

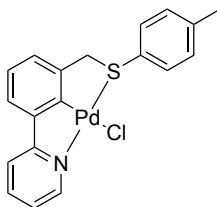
¹H NMR (500 MHz, Chloroform-*d*) δ (ppm): 9.14 (d, *J* = 5.5 Hz, 1H), 7.91 - 7.89 (m, 2H), 7.83 (ddd, *J* = 7.7, 7.7 1.7 Hz, 1H), 7.62 (d, *J* = 7.7 Hz, 1H), 7.36 - 7.33 (m, 3H), 7.29 (d, *J* = 7.7 Hz, 1H), 7.20 (ddd, *J* = 7.7, 5.5, 1.2 Hz, 1H), 7.06 (dd, *J* = 7.7, 7.7 Hz, 1H), 7.00 (d, *J* = 7.7 Hz, 1H) 4.63 (s, 2H).

¹³C{¹H}NMR (126 MHz, Chloroform-*d*) δ (ppm): 166.0, 165.5, 150.8, 147.8, 144.6, 139.1, 132.8, 131.9 (2C), 129.9, 129.6 (2C), 124.9, 124.8, 122.9, 122.3, 118.8, 53.1.

HRMS (*m/z*). Calc. for [C₁₈H₁₄NPdS]⁺ 381.9876. Found 381.9876.

Elemental Analysis. Calc. (%) for $C_{18}H_{14}NPdSCl$: C 51.69, H 3.37, N 3.35; found C 51.50, H 3.28, N 3.41.

2-(3-[(4-Methylphenyl)sulfanyl]methylphenyl)pyridine chloro-palladacycle, **2e.**



Under an argon atmosphere, $PdCl_2$ (1.09 mmol, 194 mg) was dissolved in dry MeCN (10 ml) and heated under reflux until a red solution had formed. $AgBF_4$ (2.18 mmol, 425 mg) in dry MeCN (5 ml) was added to the $PdCl_2$ solution and heated under reflux for 2 h, forming a white precipitate. The precipitate was filtered off, and **1e** (0.54 mmol, 158 mg) dissolved in dry MeCN (10 ml), was added to the filtrate, and heated under reflux for 6 h. The solution was cooled to room temperature, filtered over celite, and the solvent removed *in vacuo*.

The crude solid was dissolved in MeCN (5 ml), and NaCl (10.9 mmol, 638 mg) dissolved in H_2O (5 ml) was added, and stirred at room temperature for 3 h. The solvent was removed *in vacuo*, and the crude mixture dissolved in DCM (25 ml) and H_2O (25 ml). The crude product was extracted with DCM (2×25 ml), washed with H_2O (2×25 ml) and brine (25 ml), and dried over anhydrous Na_2SO_4 . The mixture was filtered over celite, and the solvent removed *in vacuo*, yielding 179 mg of the expected product, **2e** as a yellow solid in 89 % yield.

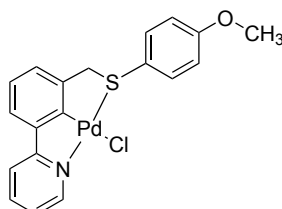
1H NMR (500 MHz, Chloroform-*d*) δ (ppm): 9.19 (d, $J = 5.5$ Hz, 1H), 7.84 (dd, $J = 7.6, 7.6$ Hz, 1H), 7.79 (d, $J = 8.1$ Hz, 2H), 7.64 (d, $J = 7.6$ Hz, 1H), 7.33 (d, $J = 7.6$ Hz, 1H), 7.23 - 7.21 (m, 1H), 7.16 (d, $J = 8.1$ Hz, 2H), 7.08 (dd, $J = 7.6, 7.6$ Hz, 1H), 7.00 (d, $J = 7.6$ Hz, 1H) 4.60 (bs, 2H), 2.32 (s, 3H).

$^{13}C\{^1H\}$ NMR (126 MHz, Chloroform-*d*) δ (ppm): 166.0, 165.5, 150.7, 147.9, 144.5, 140.4, 139.1, 132.0 (2C), 130.3 (2C), 129.4, 124.8, 124.8, 122.9, 122.2, 118.8, 53.5, 21.2.

HRMS (m/z). Calc. for $[C_{19}H_{16}NPdS]^+$ 396.033. Found 396.0050.

Elemental Analysis. Calc. (%) for $C_{19}H_{16}NPdSCl$: C 52.63, H 3.84, N 3.29; found C 52.79, H 3.73, N 3.24.

2-(3-[(4-Methoxyphenyl)sulfanyl]methylphenyl)pyridine chloro-palladacycle, **2f.**



Under an argon atmosphere, $PdCl_2$ (0.67 mmol, 119 mg) was dissolved in dry MeCN (10 ml) and heated under reflux until a red solution had formed. $AgBF_4$ (1.35 mmol, 263 mg) in dry MeCN (5 ml) was added to the $PdCl_2$ solution and heated under reflux for 2 h, forming a white precipitate. The precipitate was filtered off, and **1f** (0.62 mmol, 190 mg) dissolved in dry MeCN (10 ml), was added to the filtrate, and heated under reflux for 6 h. The solution was cooled to room temperature, filtered over celite, and the solvent removed *in vacuo*.

The crude solid was dissolved in MeCN (5 ml), and NaCl (6.09 mmol, 356 mg) dissolved in H_2O (5 ml) was added, and stirred at room temperature for 3 h. The solvent was removed *in vacuo*, and the crude mixture dissolved in DCM (25 ml) and H_2O (25 ml). The crude product was extracted with DCM (2×25 ml), washed with H_2O (2×25 ml) and brine (25 ml), and dried over anhydrous Na_2SO_4 . The mixture was filtered over celite, and the solvent removed *in vacuo*, yielding 179 mg of the expected product, **2f** as a yellow solid in 54 % yield.

1H NMR (500 MHz, Chloroform- d) δ (ppm): 9.18 (d, $J = 5.5$ Hz, 1H), 7.86 - 7.83 (m, 3H), 7.65 (d, $J = 7.9$ Hz, 1H), 7.33 (d, $J = 7.6$ Hz, 1H), 7.23 (ddd, $J = 7.6, 5.5, 1.4$ Hz, 1H), 7.08 (dd, $J = 7.6, 7.6$ Hz, 1H), 6.99 (d, $J = 7.6$ Hz, 1H), 6.87 (d, $J = 8.9$ Hz, 1H), 4.58 (s, 2H), 3.77 (s, 3H).

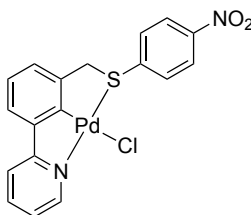
$^{13}C\{^1H\}$ NMR (126 MHz, Chloroform- d) δ (ppm): 165.9, 165.5, 161.2, 150.8, 147.8, 144.5, 139.1, 134.0 (2C), 124.8, 123.5, 122.9, 122.2, 118.8, 115.1 (2C), 55.5,

54.4. Missing one carbon.

HRMS (m/z). Calc. for $[C_{19}H_{16}NOPdS]^+$ 411.9982. Found 411.9991.

Elemental Analysis. Calc. (%) for $C_{19}H_{16}NOPdS$: C 50.91, H 3.60, N 3.12; found C 50.80, H 3.47, N 3.19.

2-(3-[(4-Nitrophenyl)sulfanyl]methylphenyl)pyridine chloro palladacycle, 2g.



Under an argon atmosphere, $PdCl_2$ (0.99 mmol, 178 mg) was dissolved in dry MeCN (6 ml) and heated under reflux until a red solution had formed. $AgBF_4$ (1.99 mmol, 387 mg) in dry MeCN (6 ml) was added to the $PdCl_2$ solution and heated under reflux for 2 h, forming a white precipitate. The precipitate was filtered off, and **1g** (0.87 mmol, 281 mg) dissolved in dry MeCN (12 ml), was added to the filtrate, and heated under reflux for 6 h. The solution was cooled to room temperature, filtered over celite, and the solvent removed *in vacuo*.

The crude solid was dissolved in MeCN (5 ml), and NaCl (10.7 mmol, 626 mg) dissolved in H_2O (5 ml) was added, and stirred at room temperature for 3 h. The solvent was removed *in vacuo*, and the crude mixture dissolved in DCM (25 ml) and H_2O (25 ml). The crude product was extracted with DCM (2×25 ml), washed with H_2O (2×25 ml) and brine (25 ml), and dried over anhydrous Na_2SO_4 . The mixture was filtered over celite, and the solvent removed *in vacuo*.

The crude product was purified by recrystallisation from hot MeCN, yielding 139 mg of the expected product, **2g** as a yellow solid in 34 % yield.

1H NMR (500 MHz, Chloroform- d) δ (ppm): 8.96 (d, $J = 6.3$ Hz, 1H), 8.29 (d, $J = 10.7$ Hz, 2H), 8.14 - 8.09 (m, 4H), 7.66 - 7.64 (m, 1H), 7.51 (dd, $J = 8.7, 8.7$ Hz, 1H), 7.21 - 7.18 (m, 2H), 5.02 (s, 2H).

Compound was too insoluble to obtain $^{13}C\{^1H\}$ and HRMS.

MS (m/z). Calc. for $[\text{C}_{18}\text{H}_{13}\text{N}_2\text{O}_2\text{PdS}]^+$ 428. Found 428.

Elemental Analysis. Calc. (%) for $\text{C}_{18}\text{H}_{13}\text{N}_2\text{O}_2\text{PdSCl}$: C 46.67, H 2.83, N 6.05;
found C 46.58, H 2.79, N 6.14.

Chapter 5

Beyond sulphur: N'CN unsymmetrical pincer palladacycles

This chapter summarises the synthesis of a number of novel N'CN unsymmetrical pincer ligands, and their C-H bond activation to the pincer palladacycles. Several different C-H bond activation procedures were investigated, in order to maximise yields. Their catalytic application in the Suzuki-Miyaura coupling reaction was investigated, demonstrating excellent activity in the coupling of a sterically demanding and electronically deactivated aryl bromide. The study into the catalyst activation pathway for the Suzuki-Miyaura coupling is extended to these N'CN pincer palladacycles, revealing little difference between the palladacycles tested experimentally.

5.1 Introduction

5.1.1 N'CN pincer palladacycles

A plethora of examples of NCN pincer palladacycles have been reported, mainly symmetrical examples. One of the simplest examples include that shown in Figure 5.1 synthesised by van Koten and co-workers.²⁵³ Another family include the bis(oxazole) or bis(thiazole) based palladacycles, with symmetrical examples as shown by Reiser and co-workers,⁴⁰ and Xiao and co-workers;²⁵⁴ and unsymmetrical examples as reported by Song and co-workers (Figure 5.2).¹⁵ Other examples of bis(oxazole) ligands, termed ‘Phebox ligands’^{172,202} have also been reported by Stark and Richards,⁵⁷ and related compounds were reported by Denmark *et al.*²⁵⁵ Examples using the same ligand backbone have also been used with other transition metals, including chiral rhodium Phebox complexes by Nishiyama and co-workers.²⁵⁶

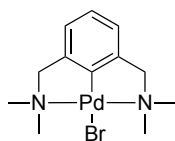


Figure 5.1 Symmetrical NCN pincer palladacycle by van Koten and co-workers.

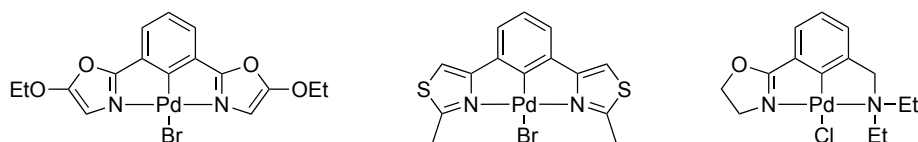


Figure 5.2 Symmetrical bis(oxazole) palladacycle by Reiser and co-workers (left), bis(thiazole) palladacycle by Xiao and co-workers (centre), and unsymmetrical oxazole palladacycle by Song and co-workers (right).

A difficulty arises in the synthesis of NCN pincer palladacycles as competition between kinetic and thermodynamic products is experienced when undergoing C-H bond activation. In a study by van Koten and co-workers,²⁵⁷ they found C-H activation of an NCN ligand yielded a double C-H bond activated structure, which was isolated as a dimeric pyridine complex. The monomeric palladacycle was synthesised from the C-SiMe₃ complex, rather than *via* C-H bond activation (Figure 5.3).

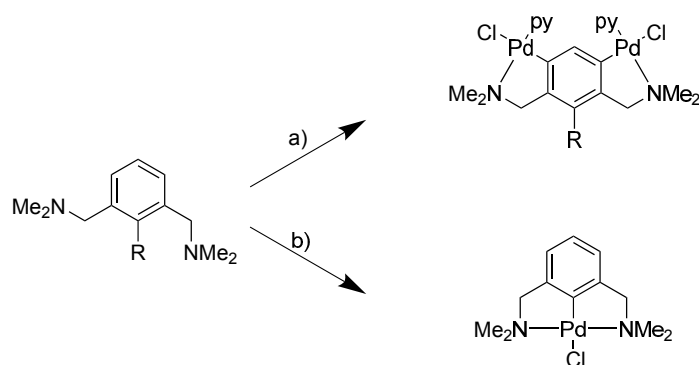
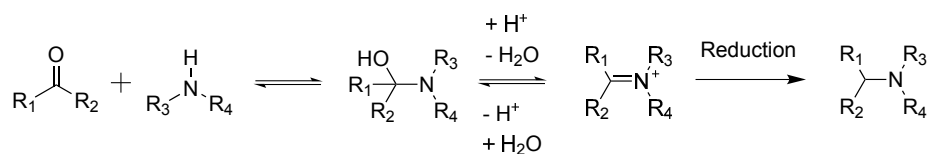


Figure 5.3 Products from palladacycle formation of van Koten and co-workers. Kinetic product (a), R=H, i) Pd(OAc)₂, MeOH, NEt₃, ii) LiCl, iii) py (pyridine). Thermodynamic product (b), R=SiMe₃, i) Li₂[PdCl₄].

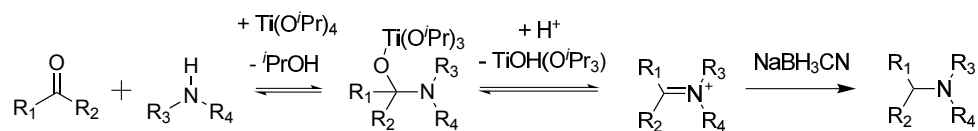
Hence, incorporating functional groups in the mutual *ortho* position, such as SiMe₃ or Br can be beneficial in their synthesis, compared to C-H bond activation routes.³¹ However this is less attractive synthetically, since an additional synthetic step is required to make the functionalised ligand.

5.1.2 Reductive amination

A potential synthetic strategy towards amine containing biaryl ligands required for this study, includes the use of the reductive amination procedure, the conversion of aldehydes or ketones into amines. A general procedure is shown in Scheme 5.1. The choice of a suitable reducing agent is vital, with the ability to reduce the iminium ion, in preference to any other groups in the molecule. A number of methods have been reported, including the use of Zn/AcOH, NaBH₄/Mg(ClO₄)₂, Zn(BH₄)₂/ZnCl₂ and NaBH(OAc)₃.²⁵⁸ Another widely discussed method includes the use of Ti(O^{*i*}Pr)₄/NaBH₃CN.²⁵⁹ The general scheme is shown in Scheme 5.2 with Ti(O^{*i*}Pr)₄ acting as a Lewis acid in the reaction.



Scheme 5.1 General reductive amination.

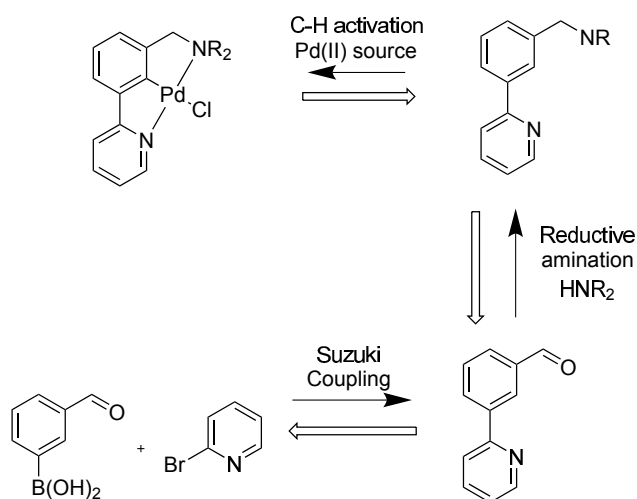


Scheme 5.2 Reductive amination using Ti(OiPr)_4 .

5.2 Results and discussion

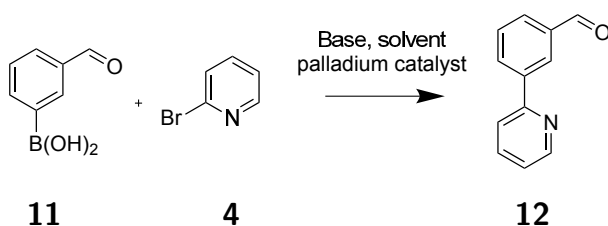
5.2.1 N'CN ligand synthesis

The biaryl motif discussed in Chapter 3 and Chapter 4, with their late stage diversification synthetic route provide an opportunity to modify to amine functionalities in the molecule. A potential retrosynthesis is shown in Scheme 5.3 utilising the initial Suzuki-Miyaura coupling step, reductive amination, and C-H bond activation.



Scheme 5.3 N'CN pincer palladacycle retrosynthesis.

The first step in the synthesis is the Suzuki-Miyaura coupling of the 3-formylphenylboronic acid (**11**) with 2-bromopyridine (**4**) to form the biaryl motif, 3-(pyridin-2-yl)benzaldehyde (**12**) shown in Scheme 5.4.



Scheme 5.4 N'CN Suzuki-Miyaura coupling between **11** and **4**.

A number of palladium catalysts were tested for this coupling reaction, including $\text{Pd}(\text{PPh}_3)_4$, $\text{Pd}(\text{dppf})\text{Cl}_2$, $\text{Pd}(\text{OAc})_2$ and Buchwald's XPhos G2 catalyst (Figure 3.11).¹⁸⁰ Reactions were undertaken under thermal and microwave irradiation (Table 5.1).

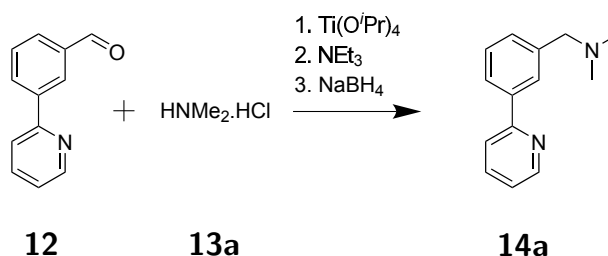
Table 5.1 Optimisation of the Suzuki-Miyaura coupling to form biaryl ligand **12**.

Entry	Catalyst	Base	Reaction conditions	Isolated yield / %
1	$\text{Pd}(\text{PPh}_3)_4$	1 M Na_2CO_3	A	65
2	$\text{Pd}(\text{PPh}_3)_4$	1M Na_2CO_3	B	72
3	$\text{Pd}(\text{PPh}_3)_4$	1M Na_2CO_3	C	58
4	$\text{Pd}(\text{dppf})\text{Cl}_2$	1M Na_2CO_3	C	79
5	$\text{Pd}(\text{OAc})_2$	1M Na_2CO_3	C	37
6	Buchwald XPhos Pd G2	0.5M K_3PO_4	C	22

A = Thermal, 85 °C, 18 h. B = Thermal, 85 °C, 48 h. C = MW, 150 °C, 20 min. Entries 1-5, 4 mol % catalyst, 1:2:1 base:toluene:EtOH. Reaction 6, 2 mol %, 1:2 base:THF.

The catalyst of choice was found to be $\text{Pd}(\text{dppf})\text{Cl}_2$ (entry 4) achieving a 79 % yield under microwave irradiation, allowing the reaction to proceed in only 20 min as opposed to 48 h thermally.

With the successful synthesis of **12**, the next step in the synthesis was the attempted reductive amination with $\text{HNMe}_2 \cdot \text{HCl}$ to furnish an N'CN unsymmetrical pincer ligand. The application of the commonly used $\text{NaBH}(\text{OAc})_3$ proved unsuccessful,²⁵⁸ yielding the benzyl alcohol synthesised previously, **5** introduced in Chapter 3. The use of $\text{Ti}(\text{O}^i\text{Pr})_4$ as a Lewis acid,²⁵⁹ and NaBH_4 as the reducing agent yielded the expected product, **14a** in 81 % yield (Scheme 5.5).

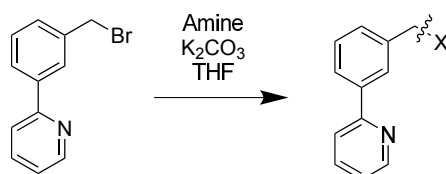


Scheme 5.5 Synthesis of **14a**.

Following on, in order to investigate the effect of changing the amine substituents, diethylamine was used in the reductive amination procedure, however proved un-

successful with both $\text{Ti}(\text{OiPr})_4$ and $\text{NaBH}(\text{OAc})_3$. Morpholine was also used as the amine group, again yielding the alcohol, rather than the aminated product. Therefore, another synthetic procedure was investigated in order to obtain the desired products.

The strategy employed was altering the synthesis of SCN pincer palladacycles, by using amine nucleophiles as opposed to thioether nucleophiles as discussed in Chapter 3 and Chapter 4. The reactions performed (Scheme 5.6) yielded the N'CN ligands **14a–c** shown in Table 5.2.



Scheme 5.6 Nucleophilic displacement of bromide by amine nucleophiles, where X is a range of amine donor groups.

Table 5.2 N'CN pincer ligand synthesis yields.

Amine	N'CN ligand	X, Scheme 5.6	Conditions	Yield / %
		14a		A 81
		14b		B 99
		14c		B 68

A = **12**, $\text{Ti}(\text{OiPr})_4$, EtOH, NaBH_4 , rt, overnight. B = **6**, K_2CO_3 , THF, MW, 150 °C, 30 min.

The range of N'CN ligands provide opportunity to increase the electron density on the nitrogen by the increased inductive effect of longer alkyl chain in **14b** and increasing the steric demands in **14c**.

5.2.2 C-H bond activation

The first N'CN pincer ligand selected for C-H bond activation, is the example bearing the morpholinyl group, **14c**. The first method tested included that used previously in the synthesis of SCN pincer palladacycles, *in situ* generated $[\text{Pd}(\text{MeCN})_4][\text{BF}_4]_2$ as the Pd(II) source.^{186–188} This achieved yields of 12%, which is disappointing, and during the reaction, significant amounts of Pd black formation was observed, which upon workup was filtered off. Therefore, a number of C-H bond activation techniques were tested, in order to increase the yield for this reaction. $\text{Pd}(\text{OAc})_2$ is often used as palladating agent, including the use of solvents such as MeOH,¹⁷¹ or AcOH.^{44,69,260} Another option is transcyclopalladation using $\text{Pd}_2(\text{dmdba})_2\text{Cl}_2$ (Figure 5.4),²⁶¹ whereby the ligands bound to palladium are exchanged in toluene, with the dmdba ligand displaced by the new ligand.

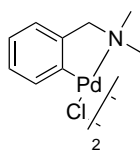


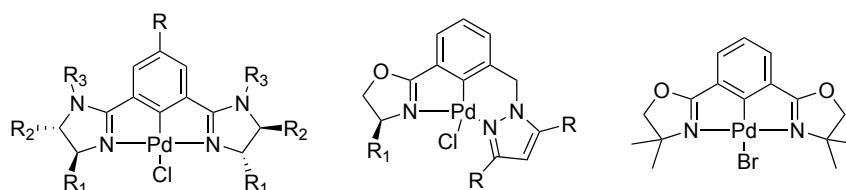
Figure 5.4 $\text{Pd}_2(\text{dmdba})_2\text{Cl}_2$ palladacycle used in transcyclopalladation.

These methods were tested for **14c** in order to synthesise the unsymmetrical N'CN pincer palladacycle **15c** (Table 5.3), showing that all syntheses provide low yields. The highest yielding synthesis included the use of $\text{Pd}(\text{OAc})_2$ in AcOH, however even in this synthesis, a significant amount of palladium black is formed, resulting in the low yielding synthesis.

Despite these disappointing yields, literature precedence shows that synthesis of nitrogen based pincer palladacycles are often synthesised in low yield via C-H bond activation. For example, the NCN and N'CN pincer palladacycles shown in Figure 5.5 by Song and co-workers,^{15,172,262} and Richards and Fossey,²⁶³ were synthesised with yields presented in Table 5.4. Therefore whilst the yields presented in this work are disappointing, they are comparable to similar work presented using the same C-H bond activation techniques.

Table 5.3 Optimisation of palladation of **14c**.

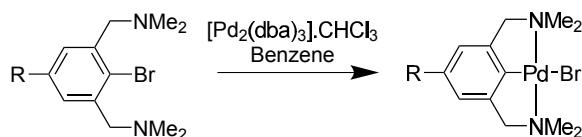
Entry	Palladium source	Solvent	Time / h	Temp / °C	Isolated yield / %
1	$[\text{Pd}(\text{MeCN})_4][\text{BF}_4]_2$	MeCN	6	85	12
2	$\text{Pd}(\text{OAc})_2$	MeOH	4	65	2
3	$\text{Pd}(\text{OAc})_2$	AcOH	4	130	24
4	$\text{Pd}_2(\text{dmba})_2\text{Cl}_2$	Toluene	4	85	0

**Figure 5.5** NCN pincer palladacycles synthesised by Song and co-workers (left and centre), and Richards and Folley (right).**Table 5.4** Literature yields for palladation of NCN ligands.

Entry	Palladacycle (Figure 5.5)	Yield / %
1	Left	12-54
2	Centre	17-70
3	Right	3

For the palladacycle by Richards and Folley (right, Figure 5.5) synthesised in 3 % yield by C-H bond activation, the yield was increased to 41 % by employing a different synthetic strategy, in this case via lithiation, followed by transmetalation with $\text{PdBr}_2(1,5\text{-COD})$. Clearly in this synthesis, the yield is significantly higher, and led us to investigate other synthetic routes towards **15c**.

Another commonly used method for synthesis of palladacycles is via oxidative addition,^{7,31} however a halide is required in the position of palladation. An example of this synthetic route is provided by van Koten and co-workers,⁶⁷ with the use of $[\text{Pd}_2(\text{dba})_3] \cdot \text{CHCl}_3$, acting upon the ligand, with a bromide in the palladation position (Scheme 5.7).



Scheme 5.7 Palladacycle formation *via* oxidative addition by van Koten and co-workers.

In order to attempt a similar synthetic route to that shown by van Koten and co-workers,⁶⁷ the N'CN ligand needs to be brominated in the mutual *ortho* position.

Under normal bromination conditions, several possible sites exist, and therefore a regioselective route is required to selectively brominate in the mutual *ortho* position. One potential method is via an intermediate palladacycle, using Pd(OAc)₂. This method provides the opportunity to brominate selectively in the *ortho* position, for anilides. It was proposed that a key intermediate, and the likely active catalyst, formed *in situ* from Pd(OAc)₂ and TsOH-H₂O, is shown in Figure 5.6.²⁶⁴

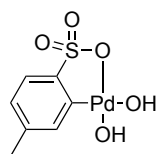


Figure 5.6 Likely active catalyst in *ortho* selective bromination by Bedford *et al.*

The reaction shown in Figure 5.7 was attempted using **14c**, however unfortunately it did not prove successful, leaving only starting material.

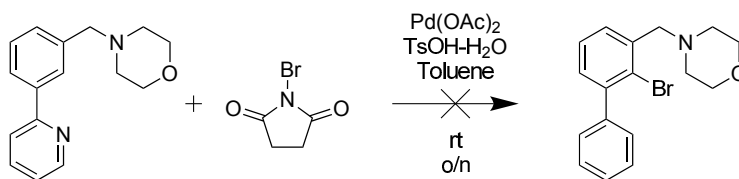


Figure 5.7 Attempted *ortho* bromination of **14c**.

In order to investigate the stability of the palladacycle in the harsh conditions employed in the C-H bond activation of refluxing in AcOH, **14c** was heated in *d*₄AcOH, and the palladacycle monitored *via* ¹H NMR, which showed no degradation of the palladacycle over time, showing that the final palladacycle is stable under the synthetic conditions. The stability of the ligand to the refluxing acetic acid was also tested by monitoring in *d*₄AcOH showing no change.

Additionally, the C-H bond activation procedure was also repeated in d_4 AcOH with $\text{Pd}(\text{OAc})_2$ revealing a reaction taking place, evidenced by the changing ligand signals. Thus it can be shown that the harsh 130°C AcOH is not the reason behind the disappointing yields.

Therefore despite the low yields, the C-H bond activation procedure was used on the unsymmetrical N'CN pincer ligands **14a** and **14b** (Figure 5.8).

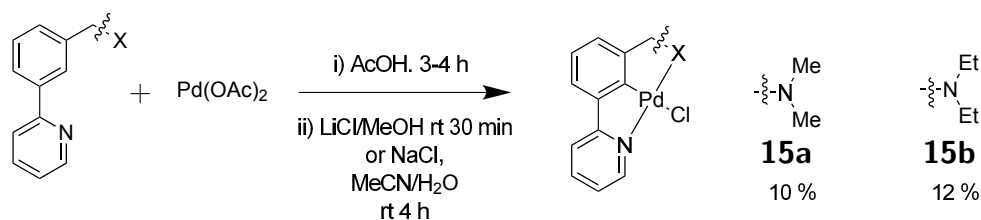


Figure 5.8 N'CN pincer palladacycles.

The yields for the synthesis of **15a** (10 %) and **15b** (12 %) are again disappointing, and further work could focus on designing a higher yielding process, rather than the poor yielding C-H bond activation techniques.

X-ray crystal structures were obtained for **15a–c**, in Figure 5.9, Figure 5.10 and Figure 5.11 respectively. Both **15a** and **15b** have two molecules in the unit cell, and **15c** has a single molecule in the unit cell.

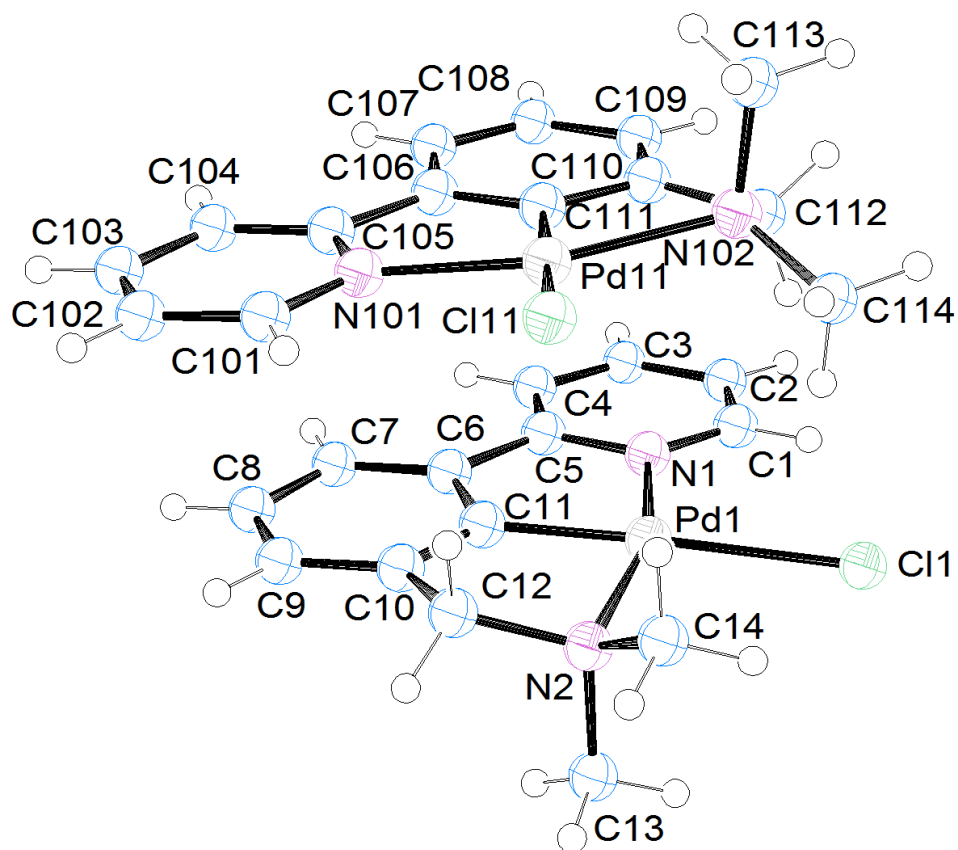


Figure 5.9 X-ray crystal structure of 15a.

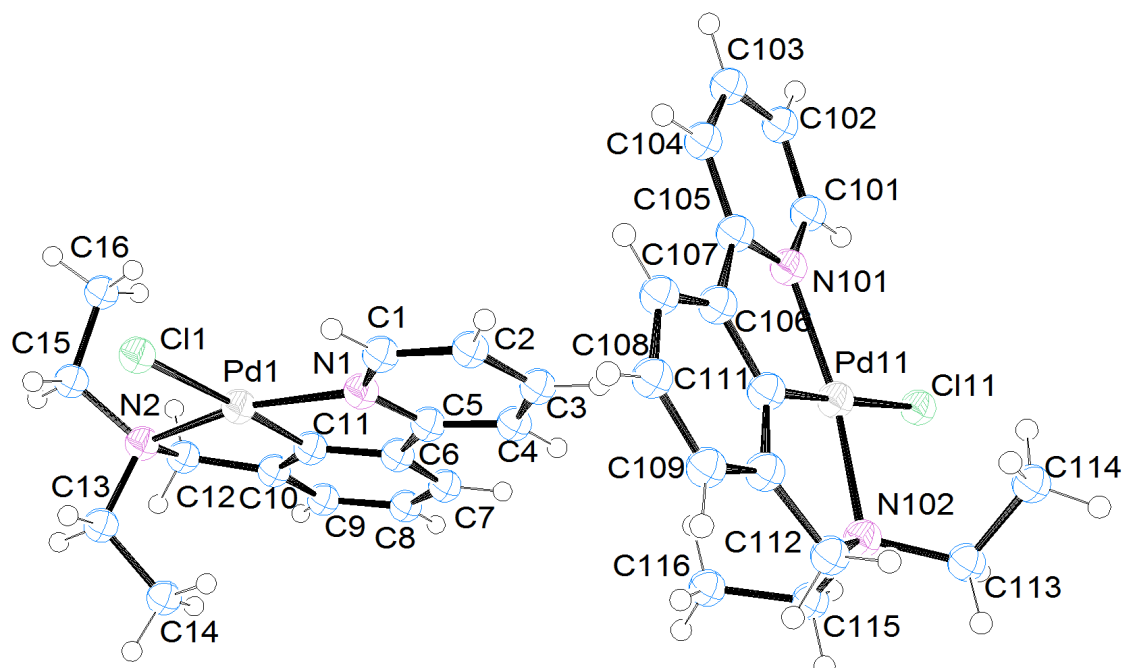


Figure 5.10 X-ray crystal structure of 15b.

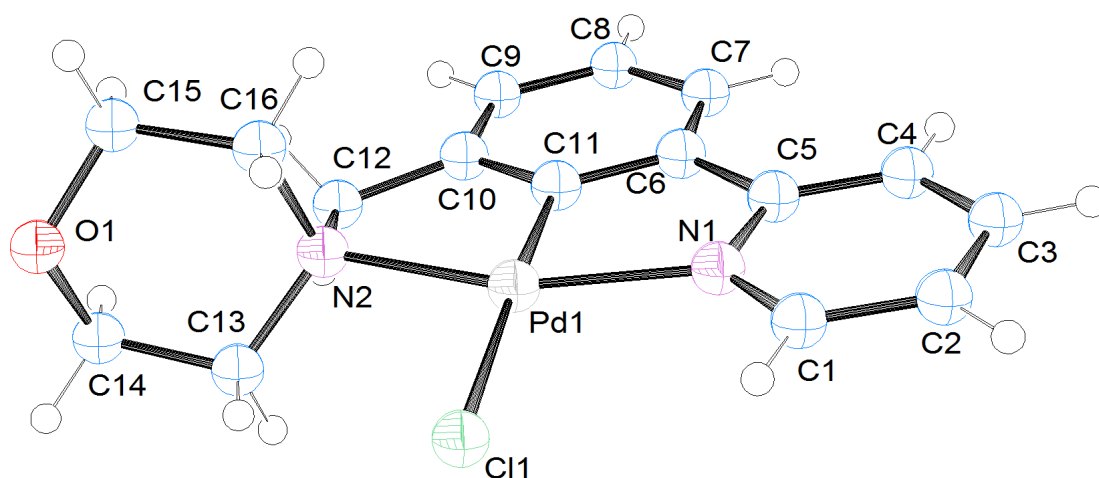


Figure 5.11 X-ray crystal structure of **15c**.

The structures of these N'CN pincer palladacycles can be investigated (only one molecule per unit cell will be studied), with the key palladium ligand bonds shown in Table 5.5, revealing insignificant differences in bond lengths depending on the structure, analogous to that found for the SCN pincer palladacycle (Chapter 4).

Table 5.5 N'CN pincer palladacycle X-ray crystal structure Pd-L bond lengths.

Bond	Bond length / Å		
	15a 	15b 	15c
Pd-N _{amine}	2.105(6)	2.1145(16)	2.1239(19)
Pd-N _{pyr}	2.062(5)	2.0639(5)	2.0521(19)
Pd-C	1.917(6)	1.9184(18)	1.913(2)
Pd-Cl	2.4260(17)	2.4231(5)	2.4327(6)

5.2.3 Suzuki-Miyaura catalysis

In order to compare the relative catalytic activity of the unsymmetrical N'CN pincer palladacycles, they were tested in the Suzuki-Miyaura coupling reaction, in order to compare with the unsymmetrical SCN pincer palladacycles (Section 4.2.3).

The coupling reaction studied is shown again for clarity in Figure 5.12, with the N'CN palladacycle catalysts, **15b** and **15c** along with comparisons against a symmetrical NCN pincer palladacycle by van Koten and co-workers,²⁵³ and the Herrmann-Beller palladacycle.

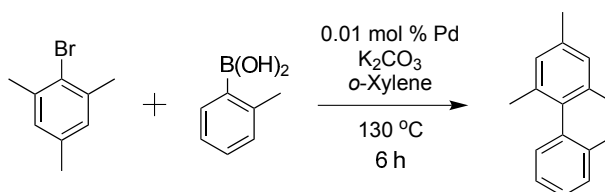


Figure 5.12 Suzuki-Miyaura coupling testing with N'CN pincer palladacycles.

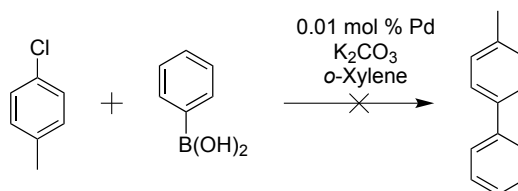
The results presented in Table 5.6 show that there is little difference in catalytic activity between **15b** and **15c** and the symmetrical NCN palladacycle, with conversions >95 %, which was significantly higher than that found for the Herrmann-Beller palladacycle (entry 3). Palladacycle **15a** was not tested as insufficient quantity was synthesised to test in catalysis.

Table 5.6 Suzuki-Miyaura coupling test using N'CN and NCN pincer palladacycles, and the Herrmann-Beller palladacycle.

Entry	Catalyst	GC conversion / %		
		2 h	4 h	6 h
1		95	96	98
2		97	98	99
3		50	50	57
4		96	97	98

Clearly, the N'CN palladacycles achieve very high conversions for these sterically

hindered couplings, and were therefore tested using a significantly more difficult to couple aryl chloride (Scheme 5.8). Unfortunately this was unsuccessful, with no coupling occurring. The use of TBAB as a phase transfer catalyst and palladium nanoparticle stabiliser was also tested, again proving unsuccessful.



Scheme 5.8 Attempted Suzuki-Miyaura coupling of an aryl chloride using N'CN pincer palladacycles.

5.2.4 Suzuki-Miyaura catalyst activation pathway

The catalyst activation pathway studied for the SCN pincer palladacycles (Section 4.3.1) is also considered for the N'CN pincer palladacycles, in order to understand the catalytic Suzuki-Miyaura coupling results presented (Table 5.6). The key steps in the pathway are shown for **15a–c** in Figure 5.13 showing the chloride substitution, transmetallation and reductive elimination steps. Likewise as for the SCN pathway, at **Int 5**, either the amine or the pyridine arm can decoordinate, however, unlike found for the SCN pathways, two different reductive elimination pathways are revealed leading to either a bridged palladium species (pathway a) as in the SCN pathway, or a singly coordinated structure for **15a** and **15c** (pathway b).

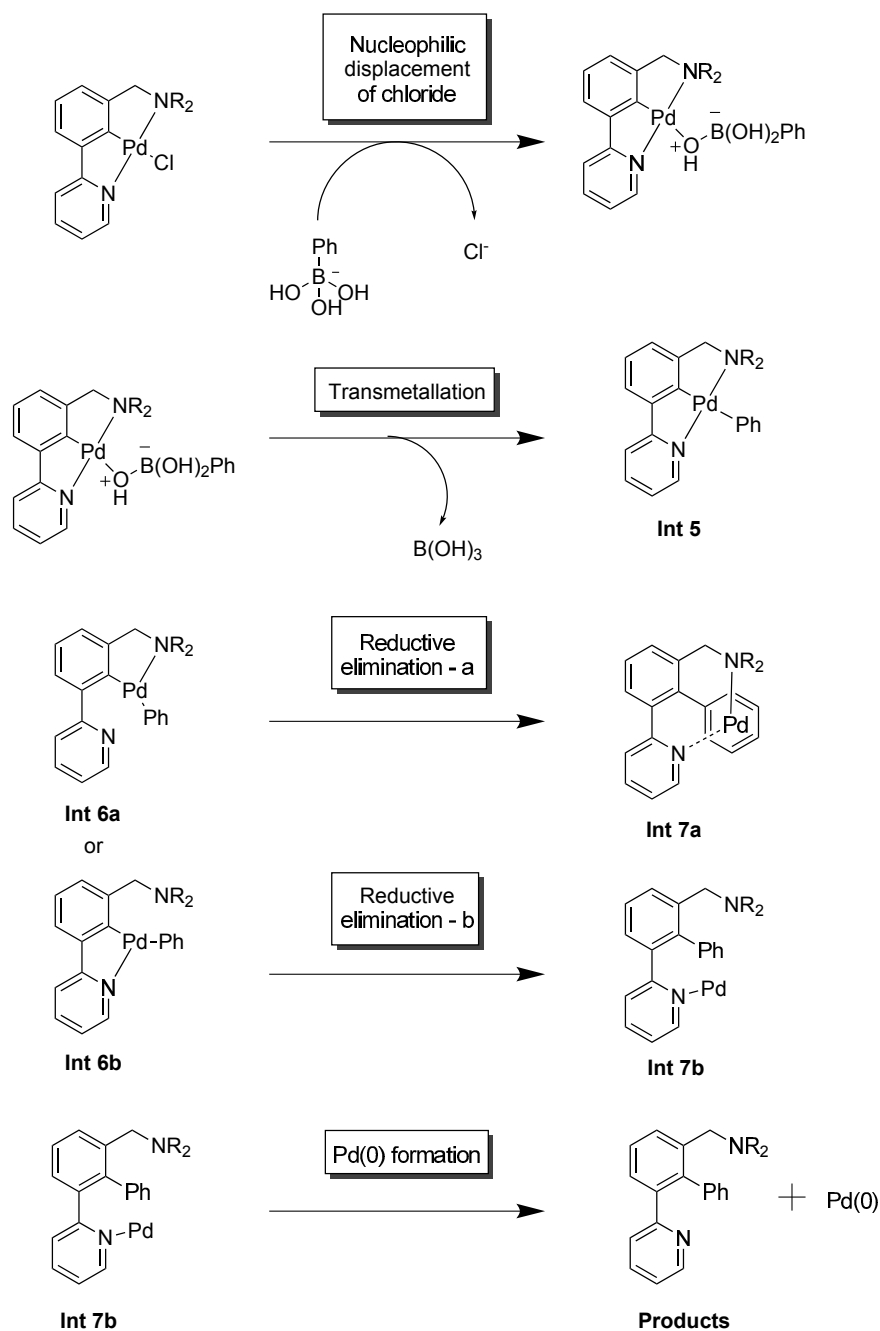


Figure 5.13 Key steps in the catalyst activation pathway of N'CN pincer palladacycles for the Suzuki-Miyaura coupling reactions.

When at **Int 5** the pyridine arm decoordinates from palladium, the reductive elimination yields the bridged palladium species (**Int 6a**) analogous to the SCN pathways (Figure 5.14). For **15a** and **15c**, when the amine decoordinates (**Int 6b**) reductive elimination step does not yield the bridged species, rather the palladium is only coordinated to the pyridine group (Figure 5.15).

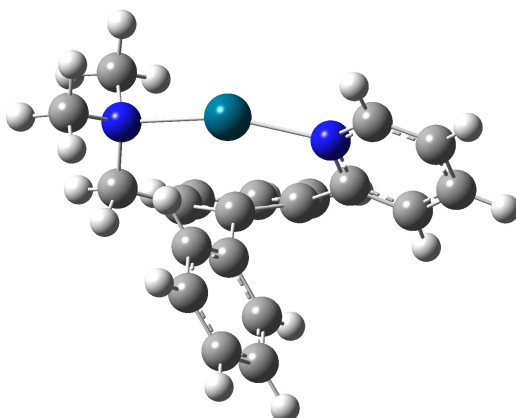


Figure 5.14 Bridging structure of **Int 7a** for **15a**.

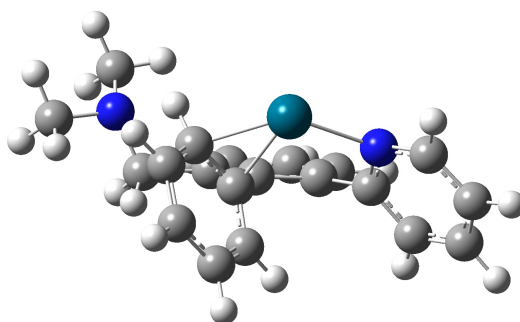
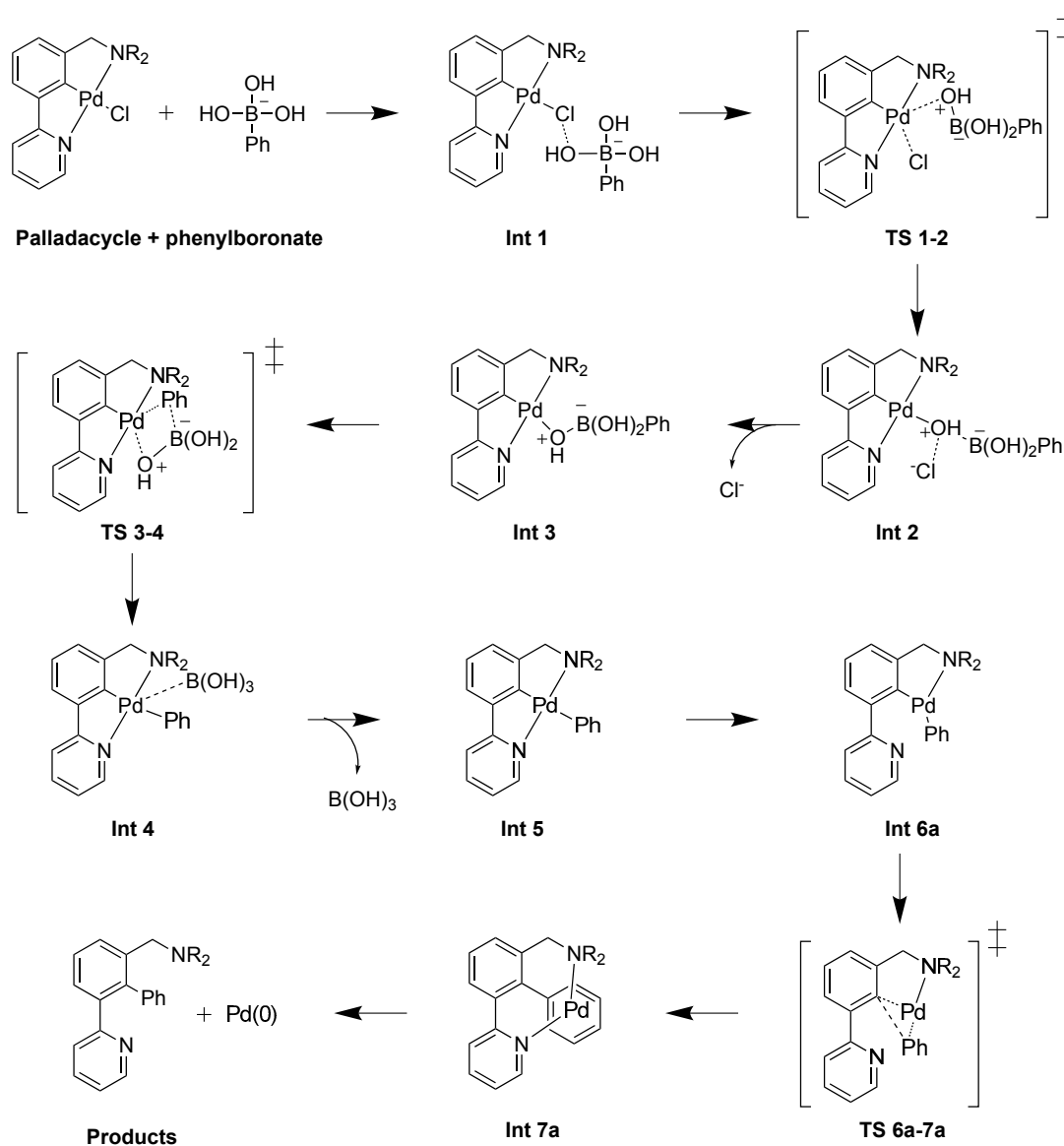


Figure 5.15 Singly coordinated structure of **Int 7b** for **15a**.

For the bridged structure, **Int 7a**, there are two ligand decooordination possibilities, however, transition states could not be found for either of these possibilities, however it was shown in the SCN catalyst activation pathway the transmetallation and reductive elimination energy barriers would be significantly larger, and therefore

these ligand decoordination transition states are insignificant for the overall pathway.

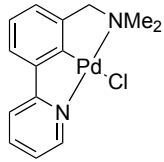
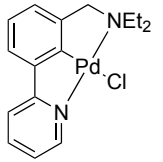
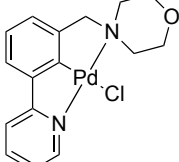
The first pathway considered, pathway a, is that analogous to the SCN pathway, containing the bridged palladium species after reductive elimination (Figure 5.14). This is shown in Scheme 5.9 and lead to the Pd(0) species likely involved in catalysis. The energies are presented in Table 5.7 and Figure 5.16.



Scheme 5.9 Pathway a for the Suzuki-Miyaura catalyst activation pathway for unsymmetrical N'CN pincer palladacycles.

The data show that the overall reaction energy is slightly different for the three palladacycles, with a difference between **15b** and **15c** of 16.8 kJ mol^{-1} , with **15a** intermediate. However parallels can only be made with the experimental catalytic data of **15b** and **15c** as **15a** was not tested in catalysis due to the small amounts

Table 5.7 Gibbs free energies, ΔG_S for the catalyst activation pathway of N'CN pincer palladacycles (pathway a).

	$\Delta G_S / \text{kJ mol}^{-1}$		
	15a	15b	15c
			
Palladacycle	0.0	0.0	0.0
Int 1	10.0	12.3	3.8
TS 1-2	33.3	42.0	27.8
Int 2	2.7	11.4	6.8
Int 3	13.6	19.9	12.4
TS 3-4	135.5	149.0	139.3
Int 4	5.7	16.8	2.4
Int 5	-10.2	-3.8	-13.2
Int 6	25.8	40.0	24.1
TS 6-7	140.4	152.0	136.0
Int 7	26.4	38.8	25.1
Ligand + Pd(0)	75.5	88.3	71.5

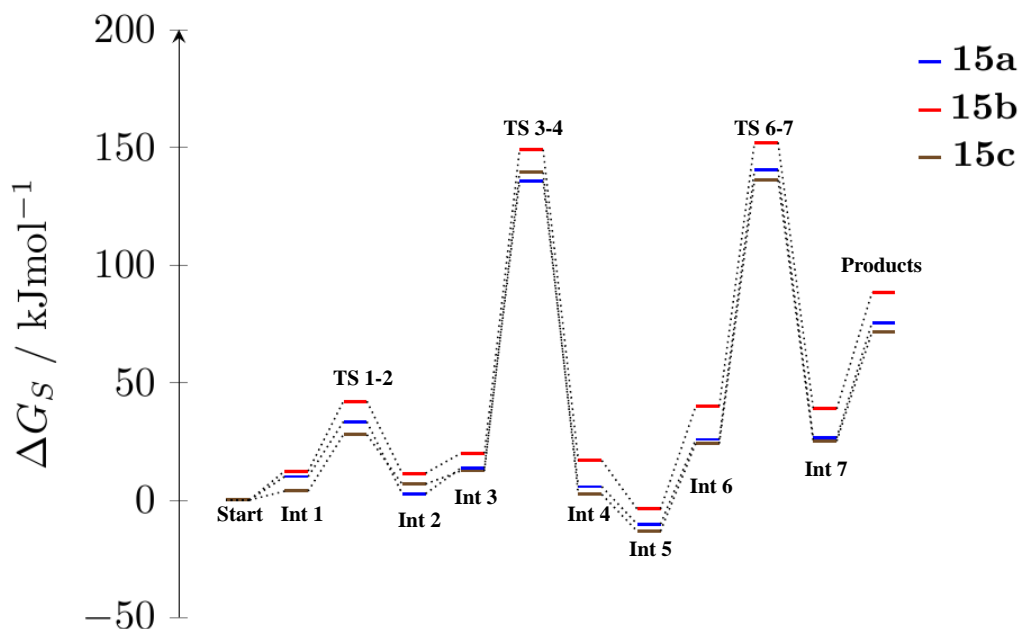
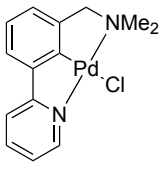
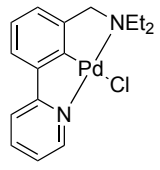
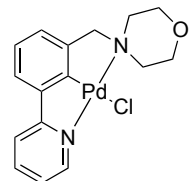


Figure 5.16 Gibbs free energies, ΔG_S for the catalyst activation pathway of N'CN pincer palladacycles (pathway a).

available.

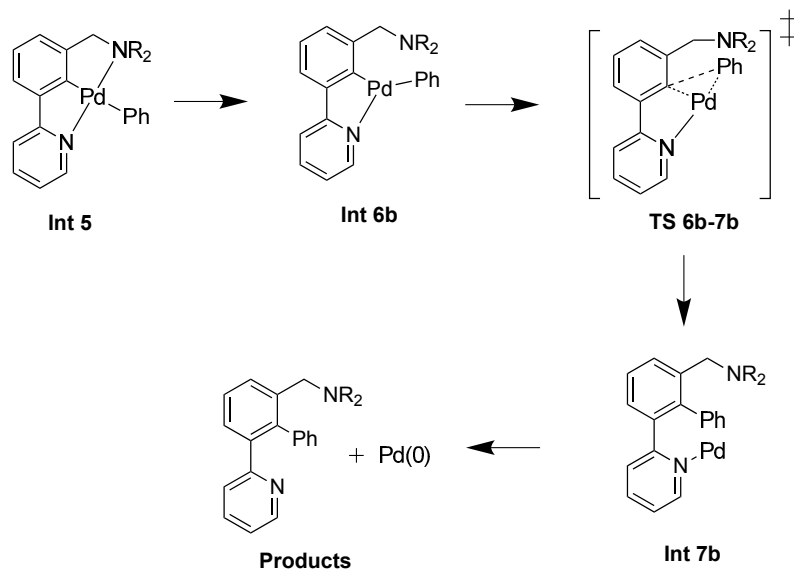
There is no discernible difference between the catalytic activities of **15b** and **15c** (Table 5.6), therefore the energy barriers in the key transmetalation (**TS 3-4**) and reductive elimination (**TS 6-7**) steps can be compared. These are tabulated in Table 5.8 revealing that the energy barriers for both **15b** and **15c** are very similar for the rate determining transmetalation step (**TS 3-4**), with a difference of only 2.0 kJ mol⁻¹, supporting the data that their catalytic activity are almost identical. As the overall reaction energy is different for both **15b** and **15c** (Table 5.7), it suggests that in this case, the energy barriers influence the catalytic activity, rather than the overall thermodynamics.

Table 5.8 Gibbs free activation energy barriers (ΔG_S^\ddagger) for key steps for the N'CN pincer palladacycle catalyst activation pathways.

	ΔG_S^\ddagger / kJ mol ⁻¹		
	15a 	15b 	15c 
TS 1-2	23.3	29.7	24.1
TS 3-4	121.9	129.1	127.0
TS 6-7	114.6	112.1	111.9

A comparison between the catalytic activity, and the reaction pathways for both the SCN and N'CN pincer palladacycles will be discussed in Chapter 7, in order to rationalise the different catalytic activities.

The other pathway possibility, pathway b affects the reductive elimination step, where the amine arm decoordinates from the palladium in the formation of **Int 6b** (Figure 5.13), and results in the singly coordinated palladium species after reductive elimination (Figure 5.15). This pathway was found for **15a** and **15c**, and is shown in Scheme 5.10 from **Int 5**.



Scheme 5.10 Possible reductive elimination pathway for **15a,c** in the Suzuki-Miyaura reaction.

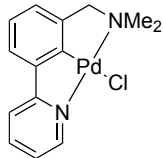
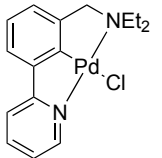
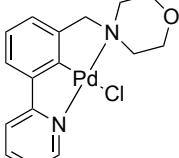
The energy difference between pathway a and pathway b are minimal for **Int 6** and **TS 6-7**, and are less than 7 kJ mol^{-1} , and therefore both pathways are possible, and likely to occur for both **15a** and **15c**, however the transition state, **TS 6b-7b** was not found for **15b**.

In order to investigate the effect of changing the amine substituent on the palladium atom, the charges on the key atoms in the palladacycle are investigated using Bader's Atoms in Molecules analysis. The charges in **15a-c** are shown in Table 5.9 and show that the effect on the palladium atom of the amine group is negligible, with very little difference on any of the charges. The only charge to show even slight differences are the amine nitrogen atoms (N_{amine}), however even then they only vary between -0.895 and -0.905 a.u. These little differences in charge further support the analysis that both **15b** and **15c** achieve very similar catalytic activities in the Suzuki-Miyaura coupling reaction.

5.3 Conclusion

This chapter has detailed the synthesis of novel unsymmetrical N'CN pincer ligands, and their consequential C-H bond activation to the unsymmetrical N'CN pincer

Table 5.9 Bader charges for N'CN pincer palladacycles.

Atom	15a	15b	15c
			
	Charge / a.u.		
Pd	0.639	0.638	0.638
N _{amine}	-0.905	-0.895	-0.902
N _{pyr}	-1.140	-1.143	-1.140
Cl	-0.728	-0.727	-0.726
C	-0.117	-0.112	-0.116

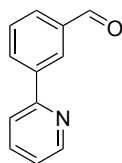
palladacycles. The yields of these syntheses were disappointing, albeit reasonable when compared to other published NCN pincer palladacycle syntheses.

The N'CN pincer palladacycles were tested in a Suzuki-Miyaura coupling reaction of sterically demanding and electronically deactivated aryl bromide, revealing excellent catalytic activity. No difference in catalytic activity was found between the two N'CN pincer palladacycles tested. The palladacycles were not active in the coupling of the more challenging aryl chlorides, even in the presence of the phase transfer catalyst and nanoparticle stabiliser TBAB.

The catalyst activation pathway was investigated for the N'CN pincer palladacycles, revealing no significant difference in the energy barriers for the transmetalation and reductive elimination steps, with small differences in the overall reaction energy. Following on, the Bader charges were investigated also revealing no difference between the different palladacycles. These data explain the failure of the different N'CN palladacycles to exhibit different catalytic activity in the Suzuki-Miyaura coupling reaction.

5.4 Experimental details

3-(Pyridin-2-yl)benzaldehyde, **12**



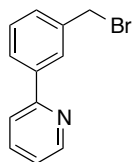
3-Formylphenylboronic acid (4.24 mmol, 635 mg), 2-bromopyridine (4.24 mmol, 0.412 ml), Pd(dppf)Cl₂ (0.17 mmol, 122 mg), 1M Na₂CO₃ (5 ml), toluene (10 ml) and EtOH (5 ml) were added to a sealed microwave vial and irradiated (maximum power, 300 W, dynamic heating) for 20 min at 150 °C. After cooling, the solvent was removed *in vacuo*. The crude mixture was diluted with H₂O (25 ml) and extracted with EtOAc (3 x 25 ml), washed with H₂O (2 x 25 ml) and brine (25 ml). The organic layers were dried over anhydrous MgSO₄, filtered, and the solvent removed *in vacuo*. The crude product was purified using flash column chromatography (7:3 DCM:EtOAc) yielding 402 mg of the expected product, **12**, as a yellow oil in 74 % yield.

¹H NMR (500 MHz, Chloroform-*d*) δ (ppm): 10.13 (s, 1H), 8.74 (d, J = 4.8 Hz, 1H), 8.52 (s, 1H), 8.30 (d, J = 7.7 Hz, 1H), 7.94 (d, J = 7.7 Hz, 1H), 7.82 - 7.79 (m, 2H), 7.65 (dd, J = 7.7, 7.7 Hz, 1H), 7.32 - 7.28 (m, 1H).

¹³C{¹H}NMR (126 MHz, Chloroform-*d*) δ (ppm): 192.2, 155.9, 149.9, 140.3, 137.0, 136.9, 132.7, 129.7, 129.5, 128.4, 122.8, 120.6.

HRMS (m/z). Calc. for [C₁₂H₉NO + H]⁺ 184.0757. Found 184.0761.

2-[3-(Bromomethyl)phenyl]pyridine, **6**



[3-(Pyridin-2-yl)phenyl]methanol, **5** (3.03 mmol, 561 mg) and \geq 48% HBr in H₂O (5 ml) were added to a 10 ml round bottomed flask and stirred at 150 °C for 8 hours, then left to stir overnight at room temperature. The reaction mixture pH was

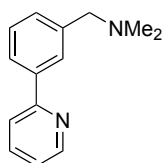
carefully adjusted to approximately 7.5 by careful addition of a saturated NaHCO_3 solution. The crude product was extracted with EtOAc (3 x 50 ml), washed with H_2O (3 x 50 ml) and brine (50 ml). The organic layers were dried over anhydrous MgSO_4 , filtered and the solvent removed *in vacuo*. The crude product was purified using flash column chromatography (9:1 DCM:EtOAc) yielding 568 mg of the expected product **6** as a yellow oil in 76 % yield.

^1H NMR (500 MHz, Chloroform-*d*) δ (ppm): 8.70 (d, $J = 4.9$ Hz, 1H), 8.06 (s, 1H), 7.93 - 7.89 (m, 1H), 7.79 - 7.73 (m, 2H), 7.48 - 7.44 (m, 2H), 7.25 (ddd, $J = 6.7$, 4.9, 1.7 Hz, 1H), 4.58 (s, 2H).

$^{13}\text{C}\{^1\text{H}\}$ NMR (126 MHz, Chloroform-*d*) δ (ppm): 156.7, 149.7, 134.0, 138.4, 136.8, 129.6, 129.2, 127.6, 126.9, 122.4, 120.6, 33.4.

HRMS (m/z). Calc. for $[\text{C}_{12}\text{H}_{10}\text{BrN} + \text{H}]^+$ 248.0069. Found 248.0071.

N,N-Dimethyl-1-[3-(pyridin-2-yl)phenyl]methanamine, **14a**



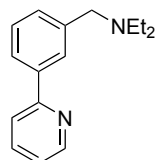
3-(Pyridin-2-yl)benzaldehyde, **12** (5.76 mmol, 1.06 g), $\text{HNMe}_2 \cdot \text{HCl}$ (12.1 mmol, 987 mg), $\text{Ti}(\text{OiPr})_4$ (11.6 mmol, 3.30 g) and EtOH (50 ml) were added to a round bottomed flask and stirred at rt overnight. NaBH_4 (8.63 mmol, 327 mg) was then added to the flask and the mixture stirred at rt for 24 h. The mixture was quenched using aqueous ammonia (35 % in H_2O , 30 ml) and filtered. The solid residue was washed with DCM (50 ml) and the product was extracted from the filtrate using DCM (3 x 35 ml). The organic layers were dried over anhydrous MgSO_4 and the solvent was removed *in vacuo* yielding 0.99 g of the expected product **14a** as a green oil in 81 % yield.

^1H NMR (400 MHz, Chloroform-*d*) δ (ppm): 8.62 (d, $J = 4.8$ Hz, 1H), 7.91 (s, 1H), 7.84 (d, $J = 7.5$ Hz, 1H), 7.67 - 7.60 (m, 2H), 7.38 - 7.31 (m, 2H), 7.12 - 7.10 (m, 1H), 3.45 (s, 2H), 2.20 (s, 6H).

$^{13}\text{C}\{^1\text{H}\}$ NMR (126 MHz, Chloroform-*d*) δ (ppm): 157.4, 149.5, 139.4, 136.6, 129.7, 128.6, 127.6, 125.7, 122.0, 120.6, 64.3, 45.3 (2C). 1 carbon missing.

HRMS (*m/z*). Calc. for $[\text{C}_{14}\text{H}_{16}\text{N}_2 + \text{H}]^+$ 213.1386. Found 213.1384.

N,N-Diethyl-1-[3-(pyridin-2-yl)phenyl]methanamine, **14b**



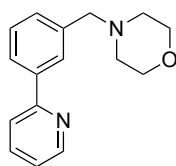
2-[3-(Bromomethyl)phenyl]pyridine, **6** (2.78 mmol, 690 mg), HNEt₂ (4.17 mmol, 0.43 ml), K₂CO₃ (12.1 mmol, 1.67 g) and THF (8 ml) were added to a microwave vial and then stirred under microwave irradiation (maximum power 300 W, dynamic power) at 150 °C for 30 min. After cooling, the solvent was removed *in vacuo*, and the reaction mixture was added to H₂O (25 ml) and the crude product was extracted using EtOAc (3 x 25 ml), washed with H₂O (2 x 25 ml) and brine (25 ml). The combined organic layers were dried over anhydrous Na₂SO₄, filtered and the solvent was removed *in vacuo* yielding 665 mg of the expected product **14b** as a yellow oil in 99 % yield.

^1H NMR (400 MHz, Chloroform-*d*) δ (ppm): 8.69 (d, J = 4.8 Hz, 1H), 7.94 (s, 1H), 7.86 (ddd, J = 5.3, 5.3, 1.9 Hz, 1H), 7.75 - 7.74 (m, 2H), 7.43 - 7.41 (m, 2H), 7.24 - 7.20 (m, 1H), 3.66 (s, 2H), 2.56 (q, J = 7.1 Hz, 4H), 1.06 (t, J = 7.1 Hz, 6H).

$^{13}\text{C}\{^1\text{H}\}$ NMR (100 MHz, Chloroform-*d*) δ (ppm): 157.7, 149.6, 140.7, 139.3, 136.6, 129.5, 128.5, 127.4, 125.3, 121.9, 120.6, 57.6, 46.8 (2C), 11.8 (2C).

HRMS (*m/z*). Calc. for $[\text{C}_{16}\text{H}_{20}\text{N}_2 + \text{H}]^+$ 241.1699. Found 241.1692.

4-(3-(Pyridin-2-yl)benzyl)morpholine, **14c**



2-[3-(Bromomethyl)phenyl]pyridine, **6** (2.50 mmol, 611 mg), **13b** (7.58 mmol, 0.66 ml), K₂CO₃ (7.49 mmol, 1.03 g) and THF (8 ml) were added to a microwave

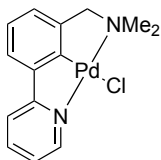
vial and then stirred under microwave irradiation (maximum power 300 W, dynamic power) at 150 °C for 30 min. After cooling, the solvent was removed *in vacuo*, and the reaction mixture was added to H₂O (25 ml) and the crude product was extracted using EtOAc (3 x 25 ml), washed with H₂O (2 x 25 ml) and brine (25 ml). The combined organic layers were dried over anhydrous Na₂SO₄, filtered and the solvent was removed *in vacuo* yielding 638 mg of the expected product **14c** as a yellow oil in 99 % yield.

¹H NMR (500 MHz, Chloroform-*d*) δ (ppm): 8.70 (d, J = 4.9 Hz, 1H), 7.96 (s, 1H), 7.87 (ddd, J = 7.3, 1.7, 1.7 Hz, 1H), 7.77 - 7.73 (m, 2H), 7.45 - 7.40 (m, 2H), 7.23 (dd, J = 7.3, 4.9 Hz, 1H), 3.72 (t, J = 4.6 Hz, 4H), 3.59 (s, 2H), 2.48 (t, J = 4.6 Hz, 4H).

¹³C{¹H}NMR (100 MHz, Chloroform-*d*) δ (ppm): 157.5, 149.7, 139.5, 138.2, 136.8, 129.9, 128.8, 127.9, 126.0, 122.2, 120.8, 67.0 (2C), 63.5, 53.7 (2C).

HRMS (m/z). Calc. for [C₁₆H₁₈N₂O + H]⁺ 255.1492. Found 255.1484.

N,N-Dimethyl-1-[3-(pyridin-2-yl)phenyl]methanamine chloro palladacycle, **15a**



N,N-Dimethyl-1-[3-(pyridin-2-yl)phenyl]methanamine (**14a**) (0.80 mmol, 170 mg) and Pd(OAc)₂ (0.83 mmol, 186 mg) were dissolved in AcOH (15 ml) and stirred at 125 °C for 3 hours. After cooling, the solvent was removed *in vacuo*, and reconcentrated with DCM (5 x 50 ml) to remove any residual AcOH. The crude mixture was dissolved in MeOH (10 ml) and LiCl (excess) was added. The mixture was stirred at rt for 30 min. The solvent was removed *in vacuo*, and the crude mixture dissolved in DCM (25 ml) and H₂O (25 ml). The crude product was extracted using DCM (2 x 25 ml), washed with H₂O (2 x 25 ml) and brine (25 ml). The combined organic layers were dried over anhydrous MgSO₄, filtered, and the solvent removed *in vacuo*. The

crude product was purified by recrystallisation from DCM/hexane yielding 82 mg of the expected product as a yellow solid in 10 % yield.

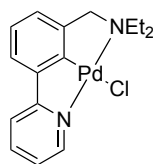
^1H NMR (500 MHz, Chloroform-*d*) δ (ppm): 9.02 (ddd, $J = 5.6, 1.7, 0.7$ Hz, 1H), 7.81 (ddd, $J = 7.8, 7.8, 1.7$ Hz, 1H), 7.58 (d, $J = 7.8$ Hz, 1H), 7.27 - 7.25 (m, 1H), 7.17 (ddd, $J = 7.6, 5.6, 1.4$ Hz, 1H), 7.09 (dd, $J = 7.6, 7.6$ Hz, 1H), 6.92 (d, $J = 7.6$ Hz, 1H), 4.13 (s, 2H), 3.08 (s, 6H).

$^{13}\text{C}\{^1\text{H}\}$ NMR (126 MHz, Chloroform-*d*) δ (ppm): 165.1, 164.6, 152.4, 145.9, 142.4, 138.6, 124.5, 123.4, 122.7, 121.1, 118.6, 74.9, 53.1 (2C).

HRMS (m/z). Calc. for $[\text{C}_{14}\text{H}_{15}\text{N}_2\text{Pd}]^+$ 317.0259. Found 317.0269.

Elemental Analysis. Calc. (%) for $\text{C}_{14}\text{H}_{15}\text{N}_2\text{PdCl}$: C 47.61, H 4.28, N 7.93; found C 47.54, H 4.34, N 7.84.

N,N-Diethyl-1-[3-(pyridin-2-yl)phenyl]methanamine chloro palladacycle, 15b



N,N-Diethyl-1-[3-(pyridin-2-yl)phenyl]methanamine (**14b**) (1.25 mmol, 301 mg) and $\text{Pd}(\text{OAc})_2$ (1.26 mmol, 310 mg) were dissolved in AcOH (4 ml) and stirred at 125 °C for 4 hours. After cooling, the solvent was removed *in vacuo*, and reconcentrated with DCM (5 x 50 ml) to remove any residual AcOH. The crude mixture was dissolved in MeCN (10 ml) and H_2O (10 ml), and NaCl (13.0 mmol, 761 mg) was added. The mixture was stirred at rt for 3 h. The solvent was removed *in vacuo*, and the crude mixture dissolved in DCM (35 ml) and H_2O (35 ml). The crude product was extracted using DCM (2 x 35 ml), washed with H_2O (2 x 35 ml) and brine (35 ml). The combined organic layers were dried over anhydrous MgSO_4 , filtered, and the solvent removed *in vacuo*. The crude product was purified by flash column chromatography (9:1 DCM:EtOAc) yielding 59 mg of the expected product as a yellow solid in 12 % yield.

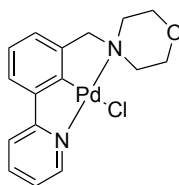
^1H NMR (500 MHz, Chloroform-*d*) δ (ppm): 9.06 (d, $J = 5.5$ Hz, 1H), 7.80 (ddd, $J = 7.8, 7.8, 1.6$ Hz, 1H), 7.57 (d, $J = 7.8$ Hz, 1H), 7.23 (d, $J = 7.8$ Hz, 1H), 7.17 (ddd, $J = 7.6, 5.5, 1.3$ Hz, 1H), 7.06 (dd, $J = 7.6, 7.6$ Hz, 1H), 6.89 (d, $J = 7.6$ Hz, 1H), 4.16 (s, 2H), 3.51 - 3.44 (m, 2H), 2.85 - 2.78 (m, 2H), 1.61 (t, $J = 7.1$ Hz, 6H).

$^{13}\text{C}\{^1\text{H}\}$ NMR (126 MHz, Chloroform-*d*) δ (ppm): 165.0, 163.4, 152.2, 148.1, 142.4, 138.5, 124.2, 122.7, 122.4, 120.8, 118.4, 67.2, 58.1 (2C), 14.1 (2C).

HRMS (m/z). Calc. for $[\text{C}_{16}\text{H}_{19}\text{N}_2\text{Pd}]^+$ 345.0578. Found 345.0564.

Elemental Analysis. Calc. (%) for $\text{C}_{16}\text{H}_{19}\text{N}_2\text{PdCl}$: C 50.41, H 5.02, N 7.35; found C 50.34, H 4.92, N 7.46.

4-(3-(Pyridin-2-yl)benzyl)morpholine chloro palladacycle, **15c**



4-(3-(Pyridin-2-yl)benzyl)morpholine (**14c**) (1.10 mmol, 279 mg) and $\text{Pd}(\text{OAc})_2$ (1.21 mmol, 272 mg) were dissolved in AcOH (4 ml) and stirred at 125°C for 4 hours. After cooling, the solvent was removed *in vacuo*, and reconcentrated with DCM (5 x 50 ml) to remove any residual AcOH. The crude mixture was dissolved in MeCN (10 ml) and H_2O (10 ml), and NaCl (11.2 mmol, 652 mg) was added. The mixture was stirred at rt for 3 h. The solvent was removed *in vacuo*, and the crude mixture dissolved in DCM (35 ml) and H_2O (35 ml). The crude product was extracted using DCM (2 x 35 ml), washed with H_2O (2 x 35 ml) and brine (35 ml). The combined organic layers were dried over anhydrous MgSO_4 , filtered, and the solvent removed *in vacuo*. The crude product was purified by flash column chromatography (7:3 DCM:EtOAc) yielding 103 mg of the expected product as a yellow solid in 24 % yield.

^1H NMR (500 MHz, Chloroform-*d*) δ (ppm): 9.16 (d, $J = 5.6$ Hz, 1H), 7.80 (dd, $J = 7.8, 7.8$ Hz, 1H), 7.56 (d, $J = 7.8$ Hz, 1H), 7.23 (d, $J = 7.8$ Hz, 1H), 7.17 (dd, $J = 7.6, 5.6$ Hz, 1H), 7.09 (dd, $J = 7.6, 7.6$ Hz, 1H), 6.96 (d, $J = 7.6$ Hz, 1H), 4.38 (s, 2H), 4.30 - 4.28 (m, 2H), 4.10 - 4.06 (m, 2H), 3.90 - 3.86 (m, 2H), 3.01 - 2.97 (m,

2H).

$^{13}\text{C}\{^1\text{H}\}$ NMR (126 MHz, Chloroform-*d*) δ (ppm): 165.1, 163.6, 152.4, 144.5, 142.4, 138.7, 124.8, 123.6, 122.6, 121.2, 118.5, 69.9, 62.8 (2C), 59.64 (2C).

HRMS (m/z). Calc. for $[\text{C}_{16}\text{H}_{17}\text{N}_2\text{OPd}]^+$ 359.0370. Found 359.0359.

Elemental Analysis. Calc. (%) for $\text{C}_{16}\text{H}_{17}\text{N}_2\text{OPdCl}$: C 48.63, H 4.34, N 7.09; found C 48.59, H 4.42, N 6.97.

Chapter 6

Unsymmetrical phosphorus containing palladacycles, and Pd(II) catalysis

This chapter summarises the synthesis of novel unsymmetrical PCN and PCS pincer ligands, followed by the C-H bond activation to the associated pincer palladacycles. These palladacycles were tested in the Suzuki-Miyaura coupling of sterically demanding and electronically deactivated aryl bromides, revealing excellent catalytic activity.

The catalytic application of the PCN and PCS pincer palladacycles, along with the SCN and N'CN catalysts discussed previously, were tested in several other catalytic applications. The coupling between a vinyl epoxide and phenylboronic acid was achieved catalytically, revealing different ratios between linear and branched products. A catalytic aldol condensation between methylisocyanoacetate with benzaldehyde, yielding oxazole products was also performed, with varying cis/trans ratios depending on the palladacycle. DFT was also utilised to study the catalyst activation pathway for the Suzuki-Miyaura coupling reaction for the PCN and PCS pincer palladacycles.

6.1 Introduction

6.1.1 Phosphorus containing palladium catalysis

Many of the widely available and successful palladium catalysts contain phosphorus donor ligands, examples include $\text{Pd}(\text{PPh}_3)_4$, $\text{Pd}(\text{dppf})\text{Cl}_2$,²⁶⁵ Pd-118 and Buchwald's XPhos ligand and related examples,²⁶⁶ shown in Figure 6.1.

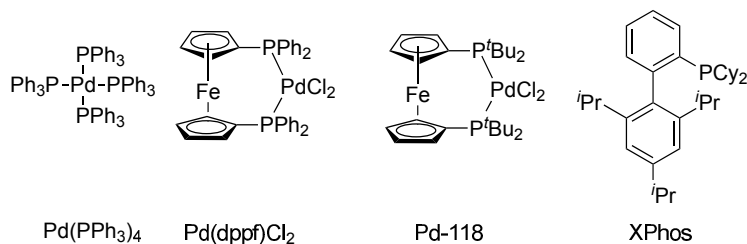


Figure 6.1 Phosphorus containing palladium complexes and ligands.

The use of palladacycles containing phosphorus donor ligands is also widespread in catalytic applications such as the Suzuki-Miyaura coupling reaction shown in Figure 6.2, such as that by Karami *et al.*,²⁶⁷ Trzeciak and co-workers,¹⁶⁴ and SanMartin and co-workers.²¹²

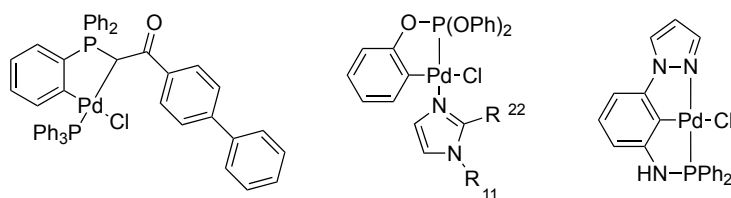
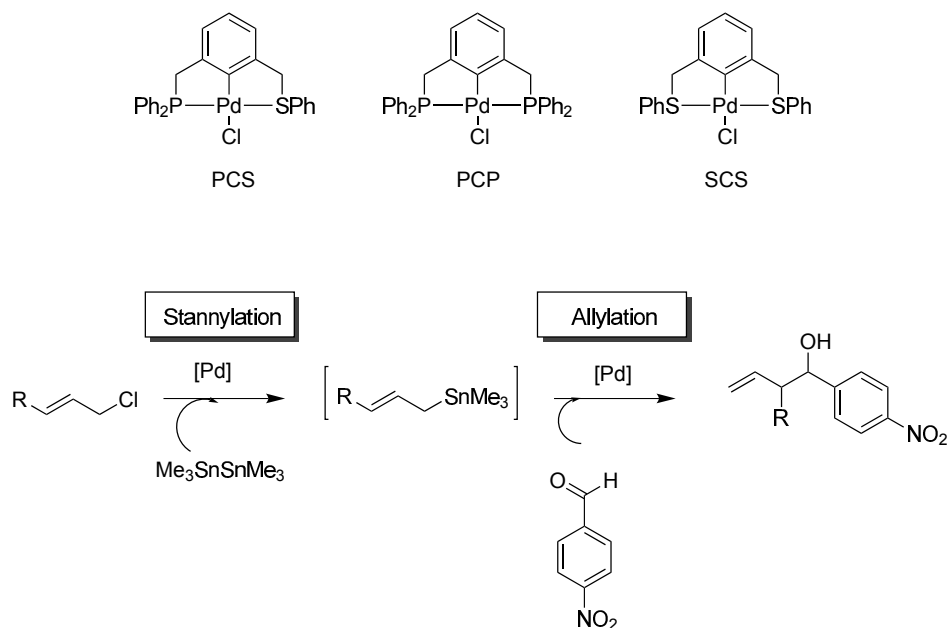
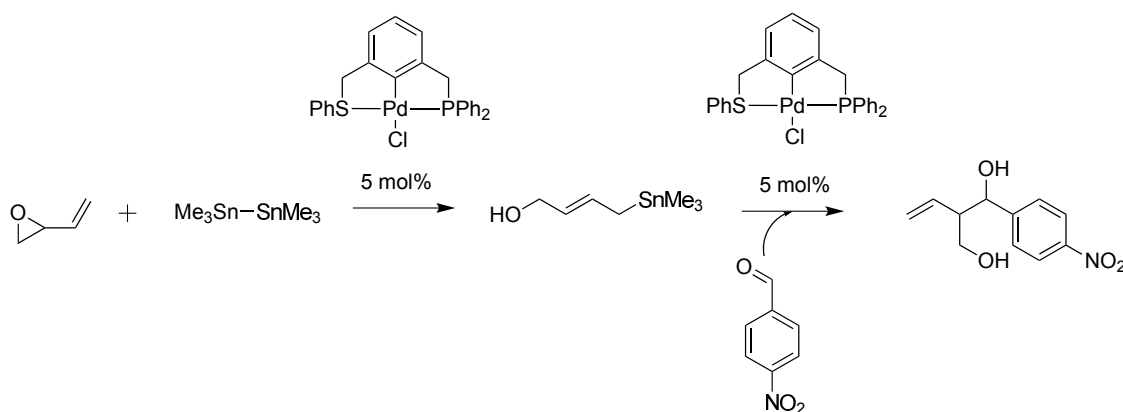


Figure 6.2 Phosphorus containing palladacycles utilised in Suzuki-Miyaura catalysis.

Phosphorus containing palladacycles have also been utilised in a diverse range of catalytic applications, including the tandem catalytic stannylation and allyl chlorides discussed previously by Szabó and co-workers (Scheme 6.1),¹³ along with other examples such as a tandem catalytic allylation of vinyloxirane with an aldehyde in the same publication (Scheme 6.2).

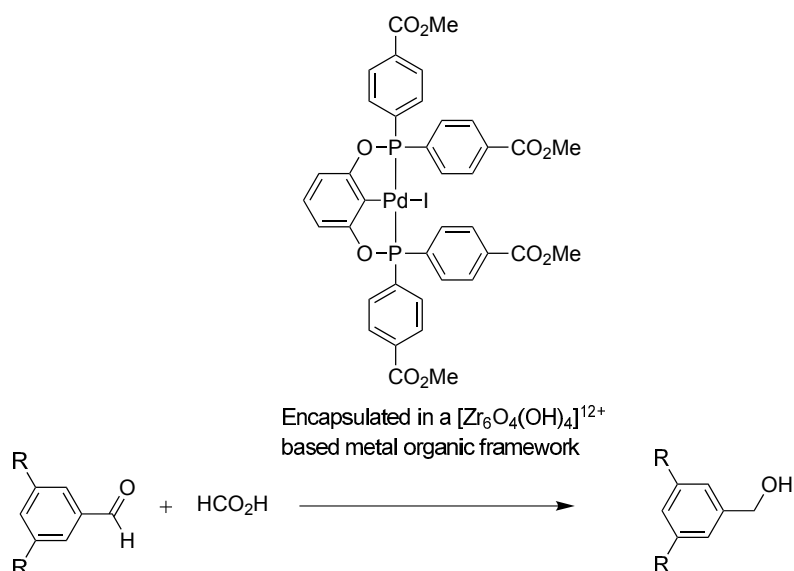


Scheme 6.1 Tandem stannylation and allylation by Szabó and co-workers.



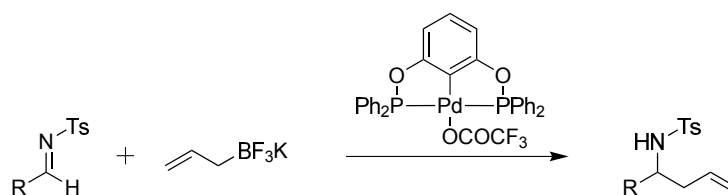
Scheme 6.2 Tandem coupling between vinyloxirane and an aldehyde by Szabó and co-workers.

Another example of catalysis utilising phosphorus containing palladacycles includes the interesting study by Wade and co-workers into the development of a PCP pincer palladacycle incorporated in a metal organic framework (MOF). This palladacycle acted as a catalyst in a simple transfer hydrogenation from acetic acid to various benzaldehydes (Scheme 6.3), which would not proceed using the non-MOF encapsulated palladacycle due to catalyst instability. This highlights the potential benefit of immobilised catalysts.²⁶⁸

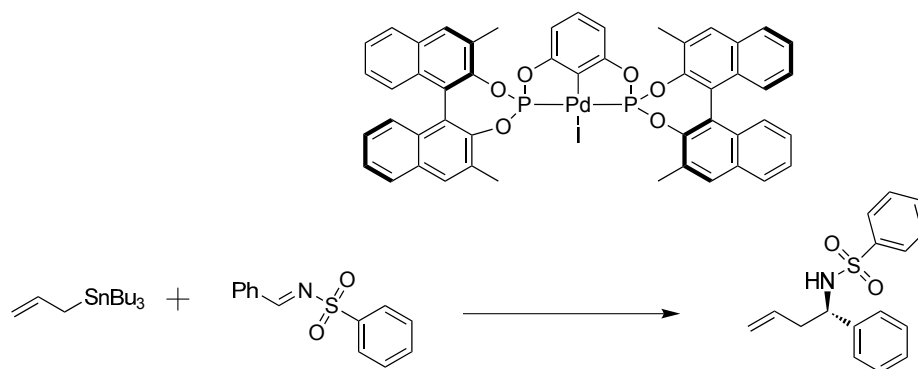


Scheme 6.3 Metal organic framework encapsulated PCP pincer palladacycle in a transfer hydrogenation catalyst application by Wade and co-workers.

In addition to the tandem allylation reactions discussed above, phosphorus containing palladacycles have found application in several allylation reactions, such as that by Szabó and co-workers using the less toxic allylborates (Scheme 6.4);²⁶⁹ also involving enantioselective variations, such as that also by Szabó and co-workers of the allylation of tributyl allylstannane and sulfonimine in up to 59% ee using a PCP palladacycle with BINOL substituents (Scheme 6.5).²⁷⁰ Also by Bedford and Pilarski utilising PCP palladacycles for the allylation of aldehydes and imines,²⁷¹ and C-H functionalisation of benzylnitriles by Szabó and coworkers.¹⁶⁶



Scheme 6.4 Allylation using less toxic allylborates by Szabó and co-workers.



Scheme 6.5 Asymmetric allylation of sulfonimines by Szabó and co-workers.

A likely reason for the interest in phosphorus as a donor atom to palladium, and hence phosphorus containing palladacycles is the strong Pd-P bond. Unlike other common donor atoms such as N or S, there is a greater possibility for metal back-bonding to the phosphorus atom, increasing the strength of the Pd-P bond. The traditional orbital diagram is shown in Figure 6.3 adapted from the paper by Orpen and Connolly,²⁷² showing π back-donation from the occupied palladium d orbital, into an empty d orbital on phosphorus. However the authors suggest a modified diagram, where the back-donation actually occurs into a hybrid of phosphorus σ^* and d orbitals.²⁷²

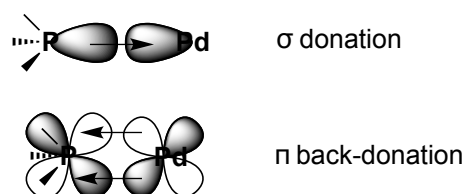


Figure 6.3 Traditional π back-donation orbital diagram for M-P bond.

This back-donation contributes to the stronger Pd-P bond, leading to the extremely high thermal stability of palladacycles, as shown in the Herrmann-Beller palladacycle.^{32,213}

6.1.2 Phosphorus containing palladacycles

In addition to the examples listed above, phosphorus containing pincer palladacycles are becoming increasingly widespread. A range of these palladacycles are shown

in Figure 6.4, with an unsymmetrical PCN examples by Rosa and co-workers,⁴⁸ Wendt and co-workers,¹⁴ Punji and co-workers,²⁷³ and by Dupont and co-workers synthesised by chloropalladation.¹⁷

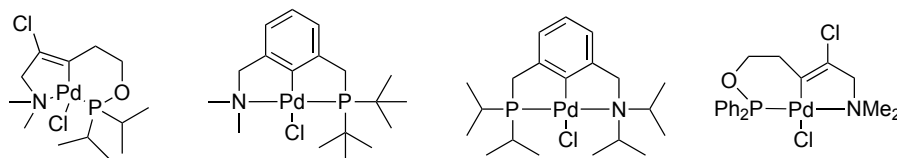


Figure 6.4 PCN pincer palladacycle examples by SanMartin, Wendt, Punji and Dupont and co-workers.

Other phosphorus containing pincers are shown in Figure 6.5, including that by Szabó and co-workers, an unsymmetrical PCS palladacycle, symmetrical PCP pincers by Bedford and co-workers,³⁹ a mixed 5-,6- PCP pincer by Eberhard *et al.*,²⁷⁴ and another cyclohexyl containing symmetrical PCP example by Wendt and Olsson.⁴²

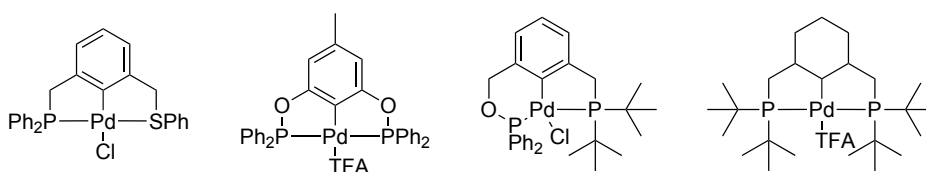
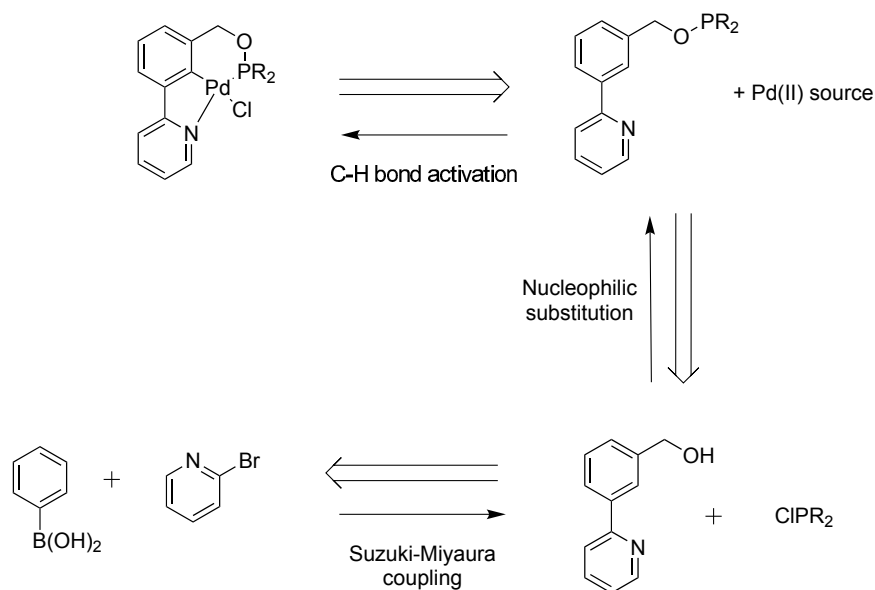


Figure 6.5 Other phosphorus containing pincer palladacycles by Szabó, Bedford, Wendt and co-workers.

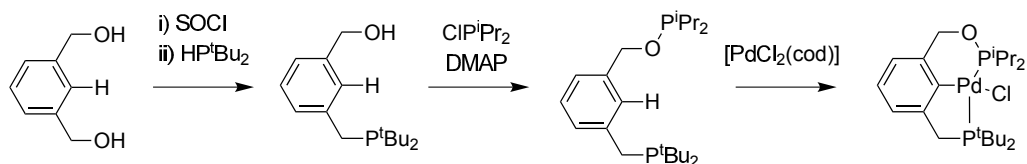
6.2 Results and discussion

6.2.1 Phosphorus containing palladacycle synthesis

A retrosynthetic pathway towards PCN pincer palladacycles, bearing a phosphinite donor group is shown in Scheme 6.6 revealing a possible route from the benzylic alcohol intermediate, **5** in the route towards SCN and N'CN pincer palladacycles shown in Chapter 3 and Chapter 5. The nucleophilic substitution of the chloride on a ClPR_2 by a benzylic alcohol has been demonstrated by Eberhard *et al.* shown in Scheme 6.7 in the synthesis of a PCP palladacycle with mixed phosphine and phosphinite phosphorus donor groups.²⁷⁵

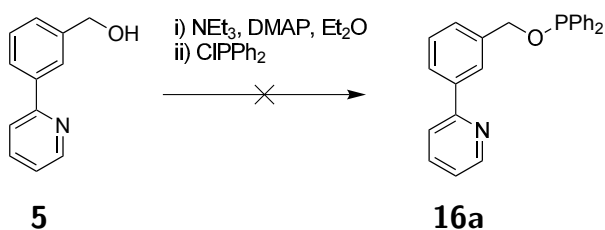


Scheme 6.6 Retrosynthetic pathway towards PCN pincer palladacycle.



Scheme 6.7 Mixed phosphine and phosphinite PCP pincer palladacycle synthesis by Eberhard *et al.*

Therefore, using **5** synthesised previously, the attempted synthesis of PCN pincer ligand **16a** was performed under an argon atmosphere as shown in Scheme 6.8, however ³¹P analysis proved the reaction to be unsuccessful. The actual product of the reaction was likely to be the oxidised phosphinite product shown in Figure 6.6. Therefore this suggested the reaction was successful, however the product was not stable under standard laboratory conditions.



Scheme 6.8 Attempted synthesis of PCN pincer ligand.

Due to the instability of **16a** under standard laboratory conditions, the Pd(II)

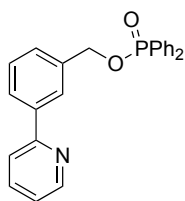
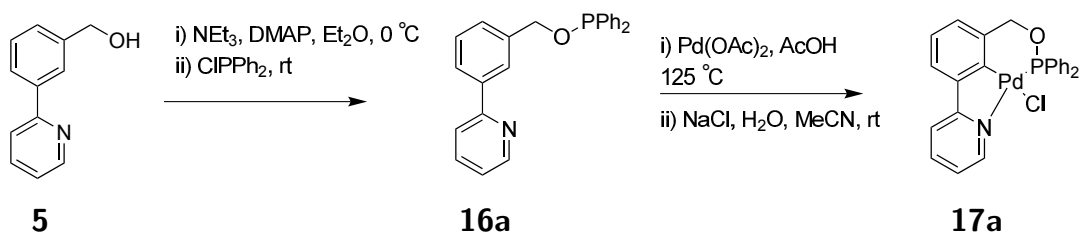


Figure 6.6 Proposed product from reaction shown in Scheme 6.8.

source was added *in situ* to inhibit oxidation of the ligand. This synthesis is shown in Scheme 6.9, proceeding in a 29% yield from the starting alcohol.



Scheme 6.9 Synthesis of PCN pincer palladacycle.

The PCN pincer compound **17a** is a mixed 5-,6- ring compound, with the phosphorus contained within a 6-membered ring, and the pyridine remaining in a 5 membered ring. The X-ray crystal structure is shown in Figure 6.7 revealing a boat-type structure in the 6-membered palladacycle ring.

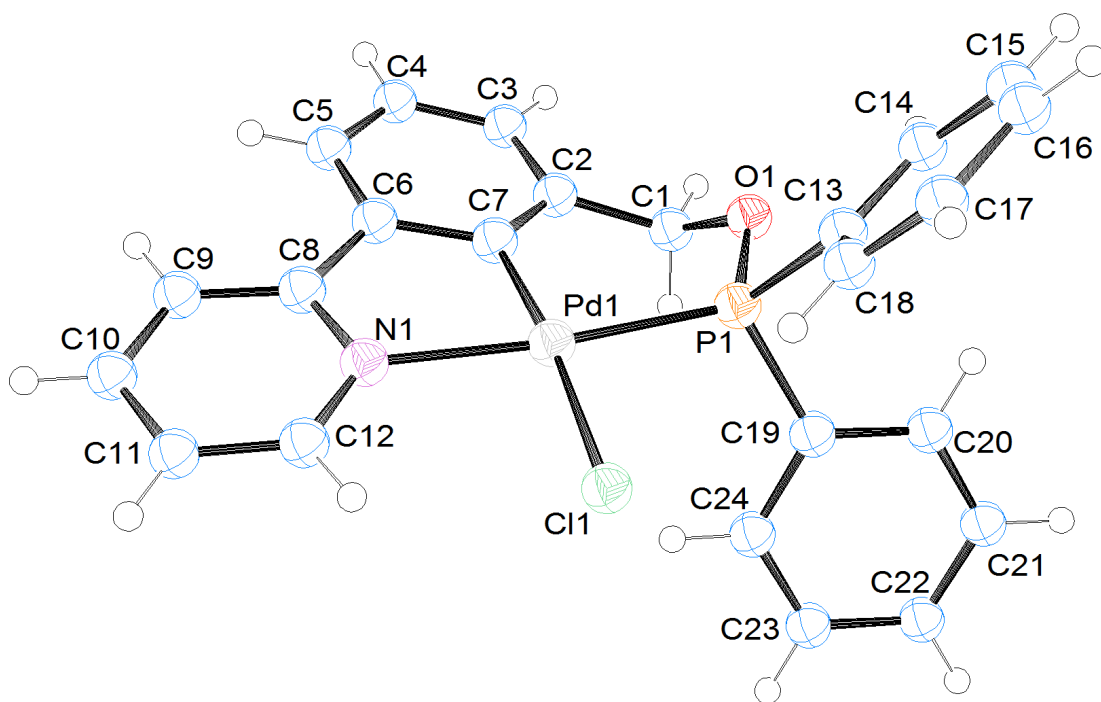
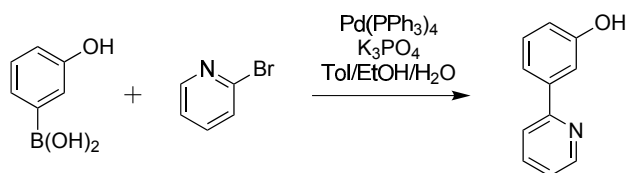


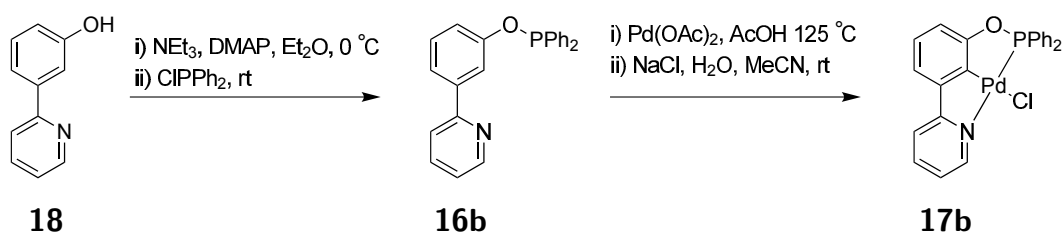
Figure 6.7 X-ray crystal structure of **17a**.

In order to obtain a phosphinite bound palladacycle with two 5-membered rings, a different starting compound is required. In order to achieve this, a new intermediate was synthesised, as shown in Scheme 6.10, proceeding in 73 % yield, with the desired phenol group. This then allows the formation of a 5-membered phosphorus containing ring Scheme 6.11.



Scheme 6.10 Phenol intermediate synthesis.

Analogous to the synthetic pathway discussed towards **17a**, the synthesis of the *in situ* generated ligand **16b** followed by the C-H bond activation was achieved in 22 % yield as shown in Scheme 6.11.



Scheme 6.11 Synthesis of 5-,5- membered ring PCN pincer palladacycle.

The PCN pincer palladacycle was also characterised by X-ray crystallography, with the structure depicted in Figure 6.8, with the less distorted 5-membered rings shown, as compared to the 5-,6- membered palladacycle.

With previous chapters within this thesis focussing on SCN pincer palladacycles, Chapter 3 and Chapter 4, unsymmetrical N'CN pincer palladacycles, Chapter 5, and now PCN pincer palladacycles, all with the pyridine donor group, the ability to alter the synthesis to introduce different groups in this position can also be investigated. By altering the original 2-bromopyridine in the Suzuki-Miyaura coupling, different donor groups can be introduced. Therefore, a synthesis towards a PCS pincer palladacycle was investigated, in order to complement previous PCS pincer palladacycles published, such as that by Szabó and co-workers shown in Figure 6.5. The synthesis towards

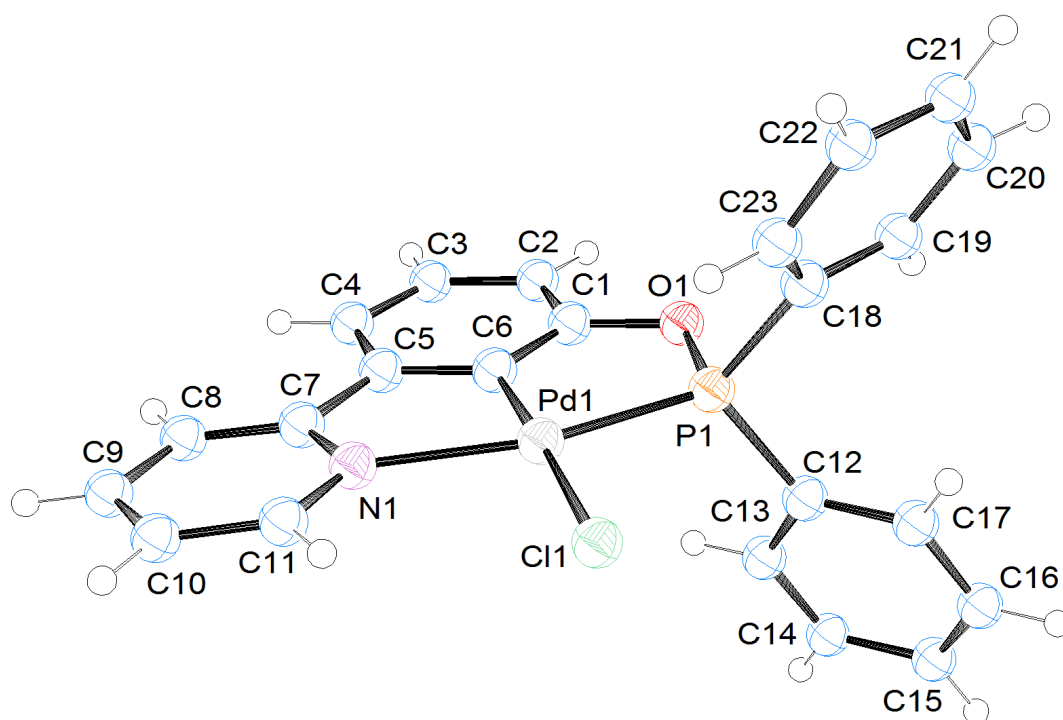
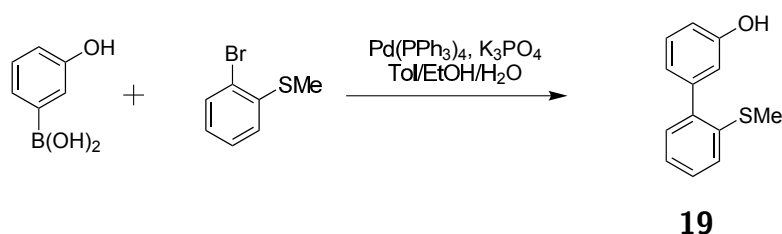


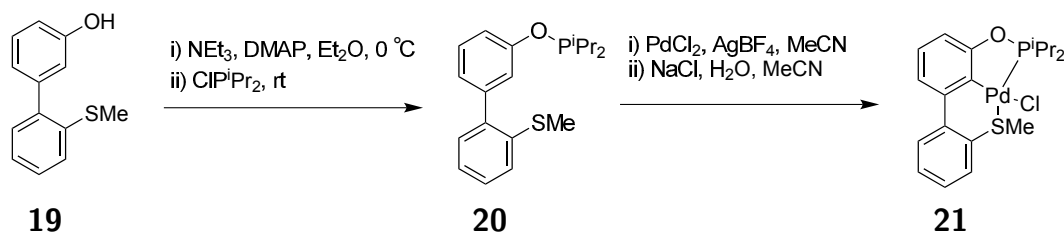
Figure 6.8 X-ray crystal structure of **17b**.

a sulfur donor atom PCS pincer palladacycle is shown in Scheme 6.12, with the synthesis of the phenol intermediate **19** which proceeds in 55 % yield.



Scheme 6.12 Suzuki-Miyaura coupling leading to an intermediate in the synthesis of a PCS pincer palladacycle.

With the intermediate **19**, the corresponding PCS pincer palladacycle (**21**) was synthesised as shown in Scheme 6.13. In this case, *in situ* generated $[\text{Pd}(\text{MeCN})_4][\text{BF}_4]_2$ was used,^{13,155,186,187} due to its success in the formation of SCN pincer palladacycles (Chapter 3 and Chapter 4) due to its highly electrophilic nature. This reaction was very successful, proceeding in 73 % yield from **19**.



Scheme 6.13 PCS pincer palladacycle synthesis.

The X-ray crystal structure of **21** is shown in Figure 6.9, again with a mixed 5-,6- ring system, exhibiting the distorted boat type structure of the 6-membered ring. In order to compare the effect of 5-,5- and 5-,6- rings for the PCN pincer palladacycles, and changing from pyridine to a thioether, the crystal structure bond lengths for key Pd-L bonds are compared (Table 6.1).

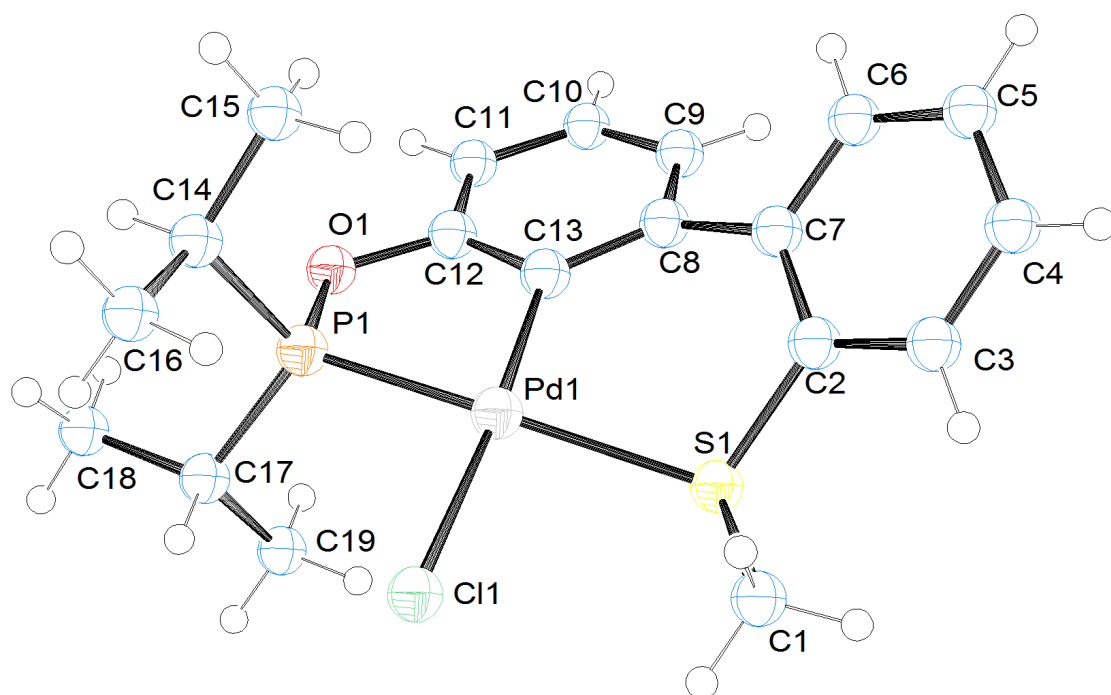
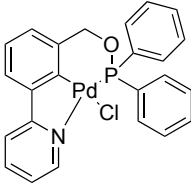
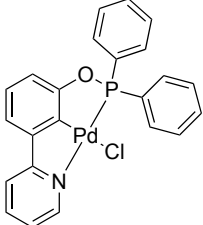
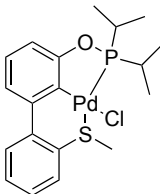


Figure 6.9 X-ray crystal structure of PCS palladacycle, **21**.

Differences in the phosphorus containing palladacycles (Table 6.1) for Pd-L bond lengths occur for the Pd-C bond lengths, with the bond being shortest in **17b** at 1.961(2) Å, and longest in **21** at 2.0159(16) Å. The Pd-C bonds in the SCN palladacycles are ≈ 1.95 Å (Chapter 4), and N'CN palladacycles ≈ 1.92 Å (Chapter 5), more closely resembling the 5-,5- membered palladacycle **17b** at 1.96 Å, with

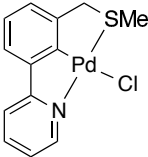
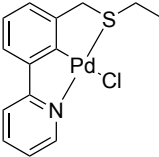
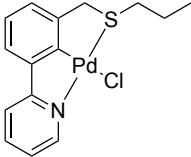
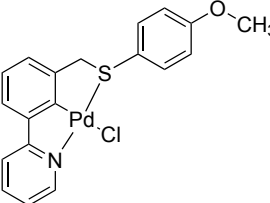
Table 6.1 Phosphorus containing pincer palladacycle X-ray crystal structure Pd-L bond lengths.

Bond	Bond length / Å		
	17a	17b	21
			
Pd-S	n/a	n/a	2.3672(5)
Pd-N	2.103(2)	2.1216(18)	n/a
Pd-P	2.2159(7)	2.2028(6)	2.2060(5)
Pd-C	2.005(3)	1.961(2)	2.0159(16)
Pd-Cl	2.3830(7)	2.3942(5)	2.3678(5)

the mixed 5-,6- rings having longer Pd-C bond distances of $> 2 \text{ Å}$, likely due to the increased steric demand in the 6 membered ring.

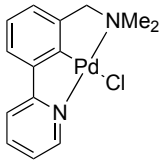
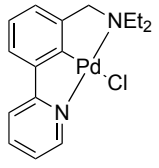
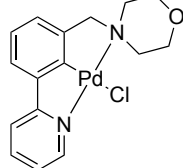
Another interesting trend emerging in the experimental X-ray crystal structures are in the Pd-N bond distances for the pyridine donor group. In order for easy comparison, the key metal-ligand bond lengths for the SCN and N'CN pincer palladacycles are shown in Table 6.2 and Table 6.3 respectively.

Table 6.2 SCN pincer palladacycle X-ray crystal structure Pd-L bond lengths.

Bond	Bond length / Å			
	2a	2b	2c	2f
				
Pd-S	2.291(8)	2.2638(4)	2.2705(7)	2.2674(5)
Pd-N	2.09(3)	2.0672(13)	2.066(2)	2.0708(15)
Pd-C	1.95(3)	1.9489(15)	1.950(2)	1.950(2)
Pd-Cl	2.423(8)	2.4095(4)	2.3961(5)	2.4093(5)

The experimental and DFT optimised Pd-N bond distances for the pyridine donor group are shown in Table 6.4 for all the X-ray crystallographically determined palladacycles. It can be seen that the longest Pd-N_{pyr} bonds in the experimental X-ray crystal structures are in the PCN pincer palladacycles (**17a** and **17b**) at $>$

Table 6.3 N'CN pincer palladacycle X-ray crystal structure Pd-L bond lengths.

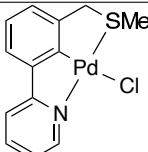
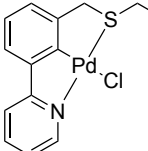
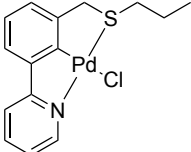
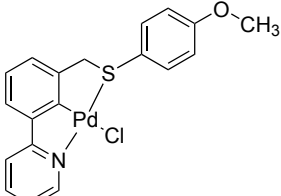
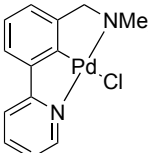
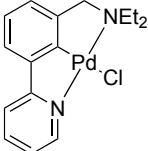
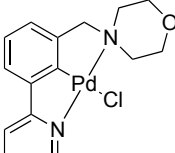
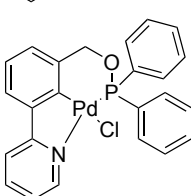
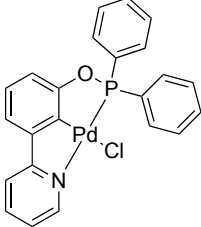
Bond	Bond length / Å		
	15a 	15b 	15c 
Pd-N _{amine}	2.105(6)	2.1145(16)	2.1239(19)
Pd-N _{pyr}	2.062(5)	2.0639(5)	2.0521(19)
Pd-C	1.917(6)	1.9184(18)	1.913(2)
Pd-Cl	2.4260(17)	2.4231(5)	2.4327(6)

2.103(2) Å, and the N'CN pincer palladacycles having the shortest Pd-N_{pyr} bond lengths at < 2.0639(5) Å. The Pd-N_{pyr} bond length for the SCN pincer palladacycles are intermediate. The optimised distances for the SCN and N'CN pincer palladacycles are all 2.08 Å, which is appreciably shorter than the > 2.13 Å distances for the PCN pincer palladacycle.

The likely reasoning behind these differing Pd-N_{pyr} bond lengths is the *trans* influence, which is the effect of a donor ligand on the M-L bond *trans* to it. A study by Sajith and Suresh^{276,277} has shown that DFT can correctly predict the *trans* influence of a range of crystallographically determined Pd(II) complexes. They also then studied the *trans* influence of a wide range of ligands, with Pd-Cl bond lengths for PR₃ of 2.438 Å demonstrating the strongest *trans* influence. It was found that SMe₂ was intermediate, with a shorter Pd-Cl bond length of 2.354 Å, and the weakest *trans* influence exhibited by NH₃ with the shortest Pd-Cl bond length of 2.343 Å.

The *trans* influence trends, PMe₃ > SMe₂ > NH₃^{276,277} perfectly correlate with the experimental findings on Pd-N_{pyr} bond lengths (Table 6.4) with the longest bonds shown in PCN palladacycles, and the shortest in the N'CN pincer palladacycles.

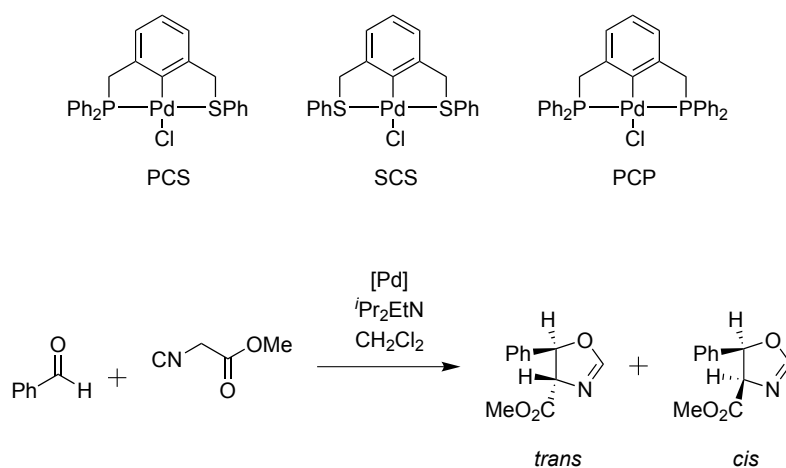
Table 6.4 Pd-N_{pyr} experimental and theoretical bond lengths.

Palladacycle		Pd-N bond length / Å	
		Experimental	DFT
2a		2.09(3)	2.08
2b		2.0672(13)	2.08
2c		2.066(2)	2.08
2f		2.0708(15)	2.08
15a		2.062(5)	2.08
15b		2.0639(5)	2.08
15c		2.0521(19)	2.08
17a		2.103(2)	2.13
17b		2.1216(18)	2.14

6.2.2 Catalytic investigation

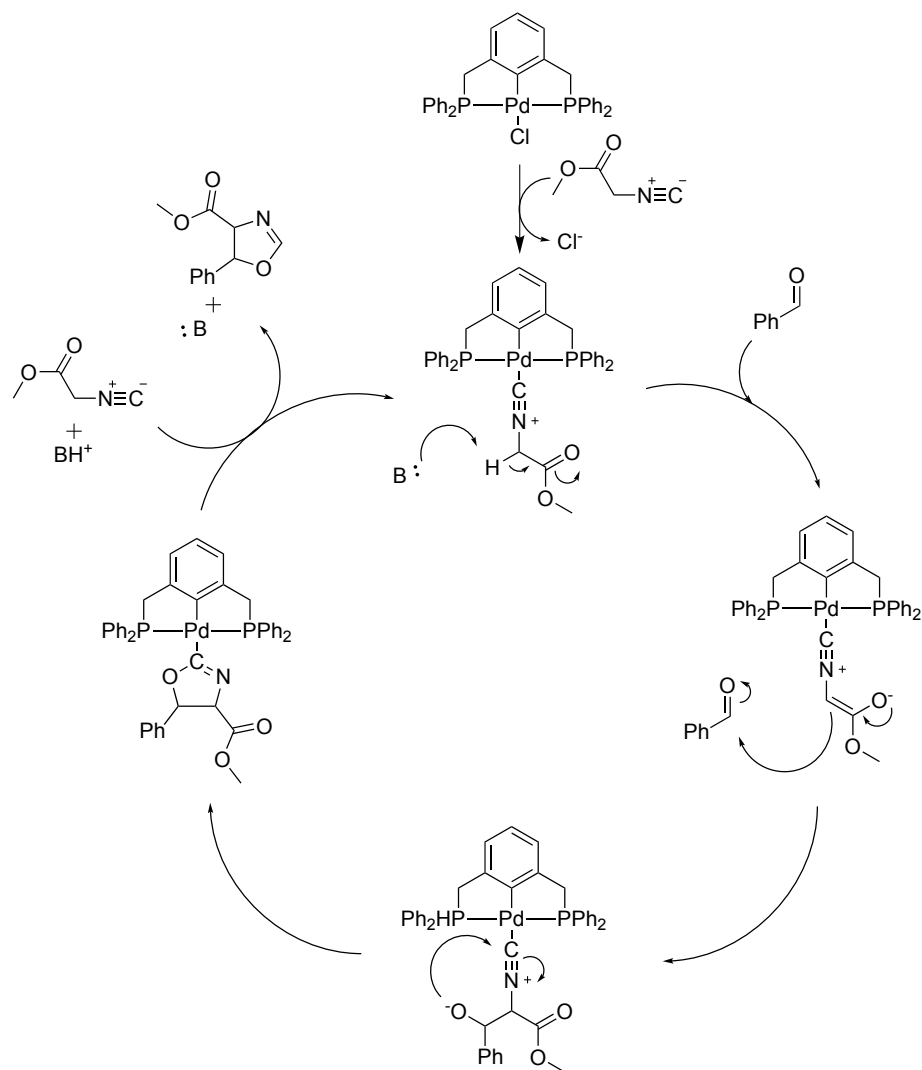
Aldol condensation

An interesting catalytic application of unsymmetrical pincer palladacycles is that reported by Szabó and co-workers¹³ discussed in Chapter 1, and shown again for clarity in Scheme 6.14. It was found that the turnover frequency (TOF / mol h⁻¹) was highest for the PCS palladacycle (75) compared to the SCS (46) and the PCP (17), however different *cis* to *trans* ratios of product were found when using different catalysts, with the PCS and SCS examples achieving $\approx 60\%$ *trans*, whereas the PCP example gave 82% of the *trans* product.



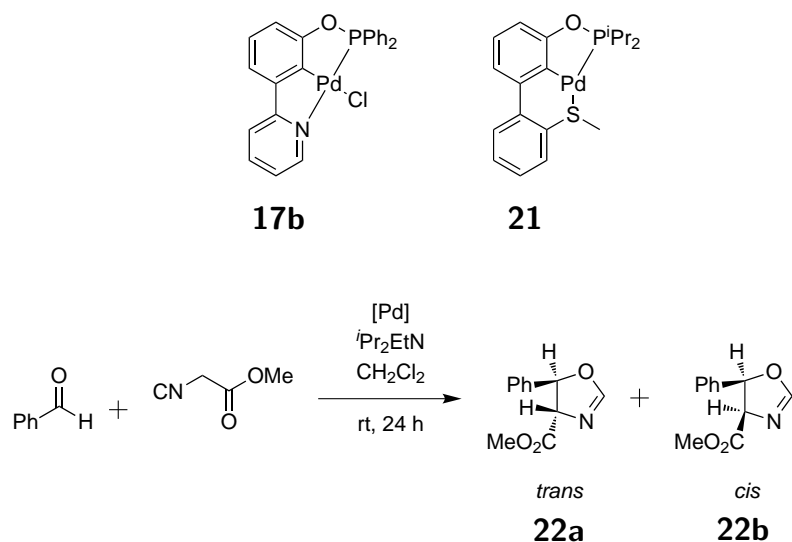
Scheme 6.14 Aldol condensation investigation by symmetrical, SCS and PCP, and unsymmetrical PCS pincer palladacycles by Szabó and co-workers.

A potential catalytic cycle is proposed in Scheme 6.15, and likely sterics of the pendant groups on the donor atoms are likely to have a substantial effect on the stereochemical outcomes of the reaction.



Scheme 6.15 Proposed catalytic cyclic of aldol condensation.

In order to investigate the catalytic activity of the PCN and PCS pincer palladacycles, these were used as catalysts for the reaction shown in Scheme 6.16. To compare the role of the donor atoms, the catalytic reaction was also tested using SCN and N'CN palladacycles shown in Figure 6.10.



Scheme 6.16 Catalytic aldol condensation using phosphorus containing palladacycles.

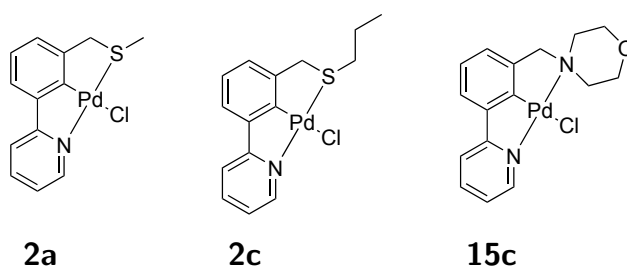
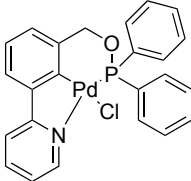
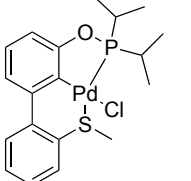
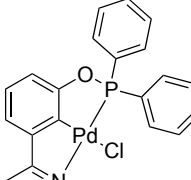
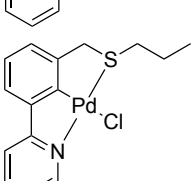
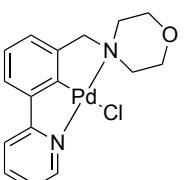
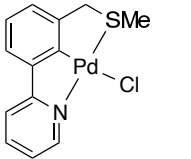


Figure 6.10 Other SCN and N'CN palladacycles tested in the aldol condensation reaction.

The reaction was also tested using $\text{Pd}(\text{OAc})_2$ and Pd-118, with its structure shown in Figure 6.1. It was found that after 24 h, benzaldehyde remained in the reaction vessel, as shown by NMR and TLC, however the product can clearly be identified in the crude ^1H NMR, and compared to literature values, in order to compare the *cis/trans* ratios, with that found by Szabó and co-workers.¹³ The crude ^1H NMR is shown with the easily distinguishable non-aromatic protons in Figure 6.11 performed using **15c** achieving a *trans/cis* ratio of 58/42.

The results for the novel unsymmetrical pincer palladacycles are shown in Table 6.5, in order of decreasing *trans* ratio for the range of palladacycles. Literature and known compound results are presented in Table 6.6 with literature examples taken from the work by Szabó and co-workers.¹³ The results for Pd-118 and $\text{Pd}(\text{OAc})_2$ are also shown.

Table 6.5 Novel palladacycle aldol condensation catalysis results, crude ^1H NMR ratios, with reactions performed in duplicate.

Entry	Catalyst	Trans/Cis ^a
1	17a 	85/15
2	21 	74/26
3	17b 	73/27
4	2c 	68/32
5	15c 	59/41
6	2a 	57/43

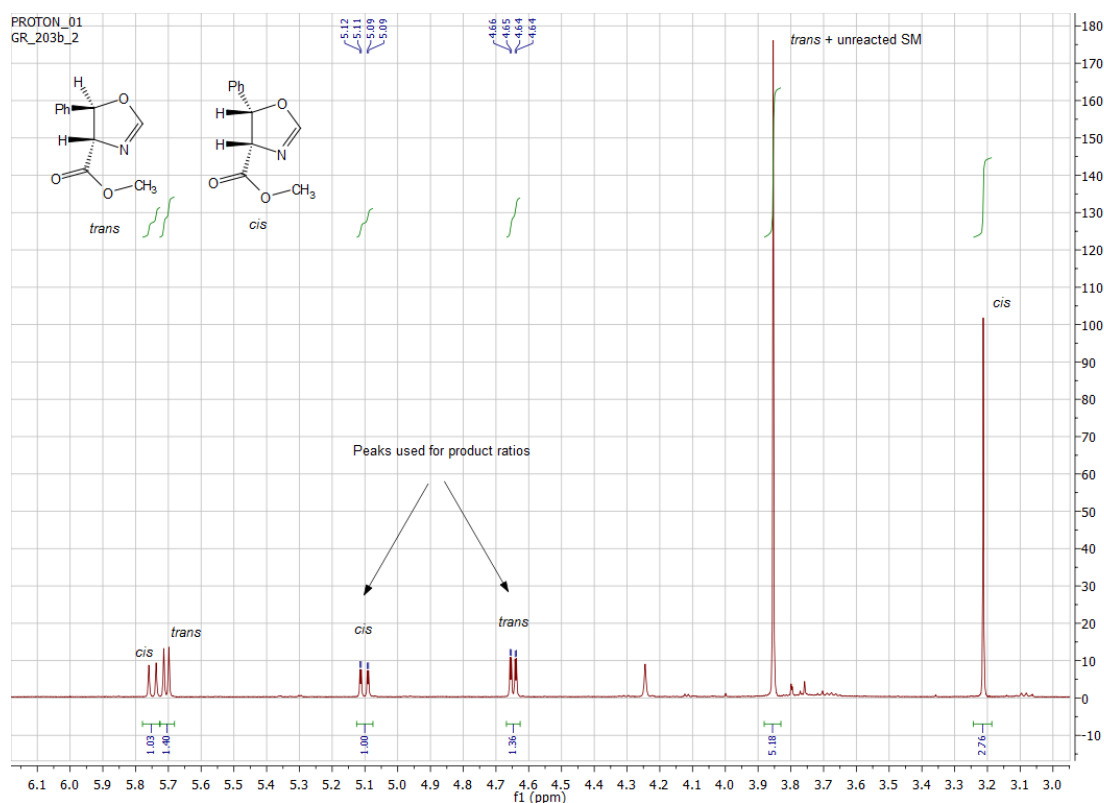


Figure 6.11 Crude ^1H NMR of the non-aromatic region of the aldol condensation reaction performed using **15c** achieving a *trans/cis* ratio of 58/42.

Table 6.6 Literature and known compound aldol condensation catalysis results, crude ^1H NMR ratios, with reactions performed in duplicate.

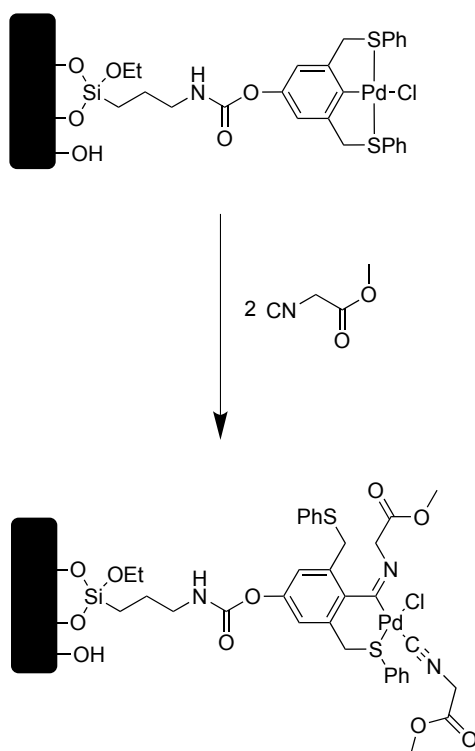
Entry	Catalyst	Trans/Cis ^a
1 ¹³		82/18
2 ¹³		59/41
3 ¹³		57/43
4 ^b		52/48
5	$\text{Pd}(\text{OAc})_2$	58/42
6	Pd-118	56/44

^a = Average of 2 duplicate runs within 5%, performed by ^1H NMR. ^b = Performed as a validation of the method and to compare to the literature value.

The results presented (Table 6.5 and Table 6.6) reveal some interesting trends. As a test, initially the literature value for the SCS pincer palladacycle shown in entry 2, Table 6.6 was repeated to confirm the reaction was successful, and as a benchmark for the novel results presented in this thesis. The literature ratio (entry 2, Table 6.6) achieved 59% *trans* selectivity, and when replicated in our laboratory (entry 4, Table 6.6), a *trans* selectivity of 52% was achieved, confirming that the reaction was successful, and a similar selectivity was established.

The highest *trans* selectivity (entry 1, Table 6.5) is found for the unsymmetrical PCN pincer palladacycle **17a**, slightly higher than that found for the symmetrical PCP palladacycle by Szabó and co-workers (entry 1, Table 6.6),¹³ and the lowest for the symmetrical SCS example shown in entry 4, Table 6.6. The novel palladacycles tested (Table 6.5) also reveal an interesting feature, with the phosphorus containing palladacycles achieving greater *trans* selectivity at >73%, contrasting with the SCN in entry 6, Table 6.5, achieving a greater proportion of *cis* selectivity, at 57% *trans*. The increased chain length in the SCN palladacycle, with a pendant propyl chain also has an effect on the product ratio, with the propyl chain (entry 4, Table 6.5) achieving greater *trans* selectivity than the pendant methyl group in entry 6, Table 6.6. Finally it can be seen that the non-palladacyclic Pd(II) catalysts Pd(OAc)₂ and Pd-118 (entries 5 and 6, Table 6.6) show less selectivity between *trans/cis* than the SCN propyl example (entry 4) and the PCN examples (Table 6.5) reported here.

It is clear that changing the donor atoms and donor atom substituents on the palladacycle can have an influence on the stereochemical outcome of the reaction, with the ratio of *trans/cis* selectivity being influenced. Previous studies by van Koten and co-workers,²⁷⁸ showed that for an immobilised symmetrical SCS pincer palladacycle the active catalyst was formed by insertion of the methylisocyanoacetate into the Pd-C bond, with one of the Pd-S bonds cleaving, shown in Scheme 6.17.



Scheme 6.17 Methylisocyanoacetate insertion into Pd-C bond of a silica immobilised symmetrical SCS pincer palladacycle by van Koten and co-workers.

In the work by Szabó and co-workers¹³ it was found that the Pd-P bond was significantly stronger than that of the Pd-S bond, resulting in a different active catalytic species. The hemilabile nature of the Pd-L bonds, resulting in decooordination of the S- donor group from palladium, and the methylisocyanoacetate inserting into the Pd-C bond, yielding the active catalytic species shown in Figure 6.12, analogous to that found by van Koten and co-workers (Scheme 6.17). The much stronger Pd-P bonds result in no Pd-L bond dissociation, yielding the catalytically active PCS species shown in Figure 6.12.

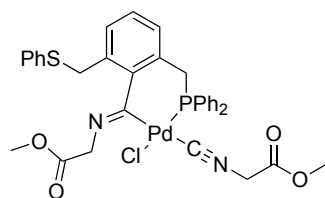

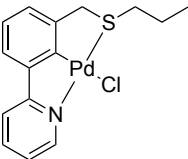
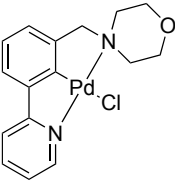
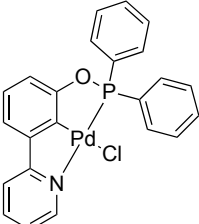


Figure 6.12 Active catalytic species in catalytic aldol condensation by Szabó and co-workers.

Therefore different catalytically active species are likely present depending on the donor atom groups. The potential hemilability arising from the diverse range

of palladacycles presented in this thesis appears to have an effect in this pathway, resulting in different *trans/cis* ratios. In order to probe the hemilability, the Pd-L bond strengths of each of the palladacycles has been investigated using Bader's Atoms in Molecules analysis, using the $\rho(\mathbf{r})$ value,¹³⁸ as discussed in Section 2.5.

Table 6.7 Pd-L bond $\rho(\mathbf{r})$ values (a.u.) for palladacycles tested in the catalytic aldol condensation.

	Palladacycle	Bond	$\rho(r)$
2a		Pd-S	0.093
		Pd-N	0.096
2c		Pd-S	0.093
		Pd-N	0.096
15c		Pd-N _{amine}	0.084
		Pd-N _{pyr}	0.098
17b		Pd-P	0.113
		Pd-N	0.085

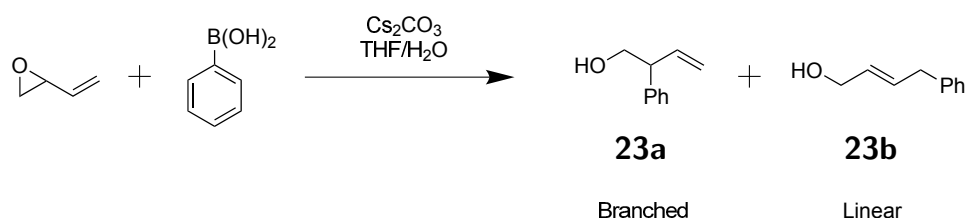
The data in Table 6.7 show that the Pd-S and Pd-N bonds are significantly weaker than the Pd-P bonds, evidenced by the smaller $\rho(\mathbf{r})$ values. The difference in *trans/cis* ratio for **2a** (entry 6, Table 6.5) and **2c** (entry 3) cannot be explained by different bond strengths as shown by the Atoms in Molecules analysis as the bonds have the same $\rho(\mathbf{r})$ values, and therefore the steric influence of the propyl chain is likely having an influence on the *trans/cis* selectivity. Also the high *trans* selectivity for **17b** (entry 2) is likely due to the significantly stronger Pd-P bond, and achieves very similar results to the symmetrical PCP palladacycle result (entry 1).

Further work following on from this thesis could focus on the rationalisation of these catalytic results, by studying the reaction mechanism to understand how

reaction barriers and the pathway change as the donor groups and atoms are altered.

Vinyl epoxide and boronic acid coupling

Another catalytic application tested includes a coupling between a vinyl epoxide and phenylboronic acid. This is another example of a catalytic application where the palladium remains in the +2 oxidation state, thereby retaining the ligand structure of the palladacycle, as opposed to the Suzuki-Miyaura coupling reactions studied in previous chapters where the palladacycle acts as a source of catalytically active Pd(0). The vinyl epoxide coupling was investigated by Szabó and co-workers,⁷¹ and one example of this reaction is tested to determine the role of the donor atoms and groups on the coupling reaction shown in Scheme 6.18.



Scheme 6.18 Vinyl epoxide coupling to phenylboronic acid catalysed by palladium catalysts.

Szabó and co-workers⁷¹ found 92 % linear selectivity in the coupling reaction, achieved in 94 % yield, with a symmetrical PdSeCSe palladacycle, shown in Figure 6.13. A series of unsymmetrical pincer palladacycles synthesised in this thesis are tested in the reaction shown in Scheme 6.18, along with a symmetrical pincer palladacycle, and several other common Pd containing palladacycles and palladium catalysts. The results are shown in Table 6.8 for the pincer palladacycles, and in Table 6.9 for other common palladium containing catalysts.

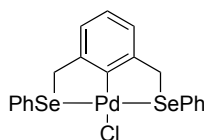


Figure 6.13 Symmetrical PdSeCSe palladacycle by Szabó and co-workers.

Table 6.8 Vinyl epoxide coupling to phenylboronic acid pincer palladacycle results.

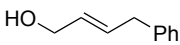
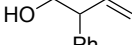
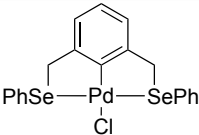
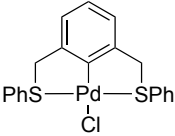
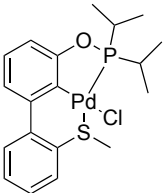
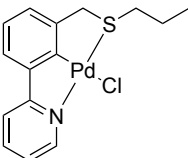
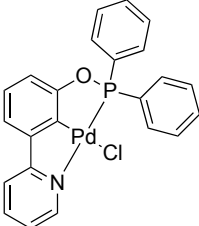
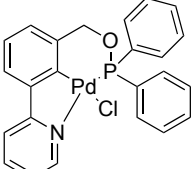
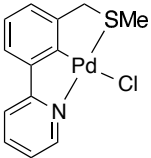
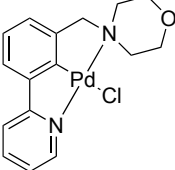
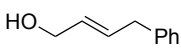
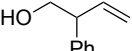
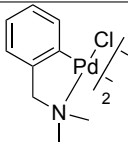
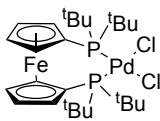
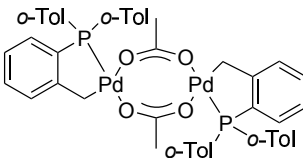
Entry	Palladacycle			Yield / %
1		92	8	94 ⁷¹
2		78	22	>99
3	21 	68	32	76
4	2c 	68	32	89
5	17b 	66	34	66
6	17a 	64	36	96
7	2a 	64	36	96
8	15c 	60	40	84

Table 6.9 Vinyl epoxide coupling with phenylboronic acid other palladium catalyst results.

Entry	Palladium catalyst			Yield / %
1		78	22	97
2	$\text{Pd}(\text{PPh}_3)_4$	68	32	89
3		59	41	>99
4		55	45	>99

A crude ^1H NMR for the mixture of the linear (**23b**) and branched (**23a**) products is shown in Figure 6.14 with the non-aromatic protons of the products shown. The linear product NMR spectrum agrees with that of Uozumi and co-workers,²⁷⁹ and when the $^{13}\text{C}\{^1\text{H}\}$ NMR is considered, the peaks for the *cis* isomer of the linear product is also visible, however is not clearly distinguishable in the ^1H NMR. The branched product NMR agrees with that of Bower and co-workers.²⁸⁰

The pincer palladacycle results show that the symmetrical SCS pincer palladacycle (entry 2, Table 6.8) achieves the highest linear selectivity of the new results. The unsymmetrical pincer palladacycles achieve increasing proportions of the branched product, with **15c** achieving the highest proportion of the branched product (entry 8, 40 %), with the other pincer palladacycles achieving increasing linear selectivity. All of the unsymmetrical pincer palladacycles achieve significantly greater proportions of the branched product as compared to the symmetrical pincer palladacycles.

Of the other common palladium containing catalysts for this reaction (Table 6.9) $\text{Pd}(\text{dmba})_2\text{Cl}_2$ (entry 1) achieves highest linear selectivity at 78 %, and the Herrmann-Beller palladacycle (entry 4) achieves the highest proportion of the branched product

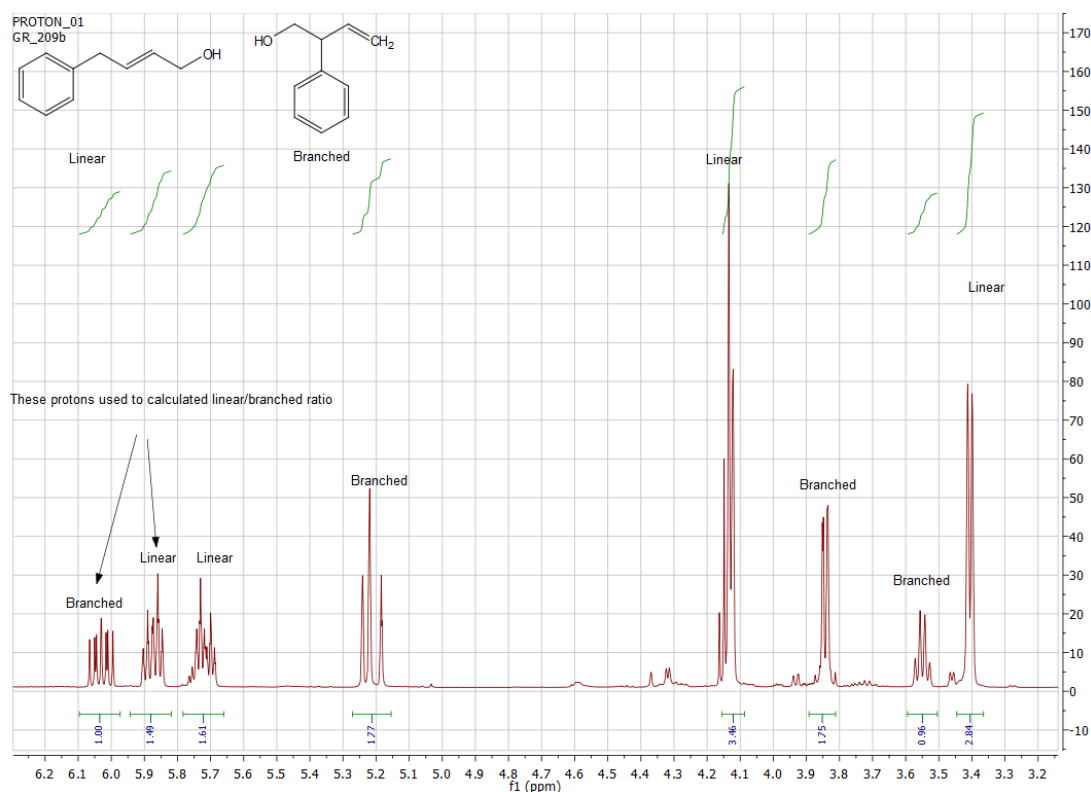
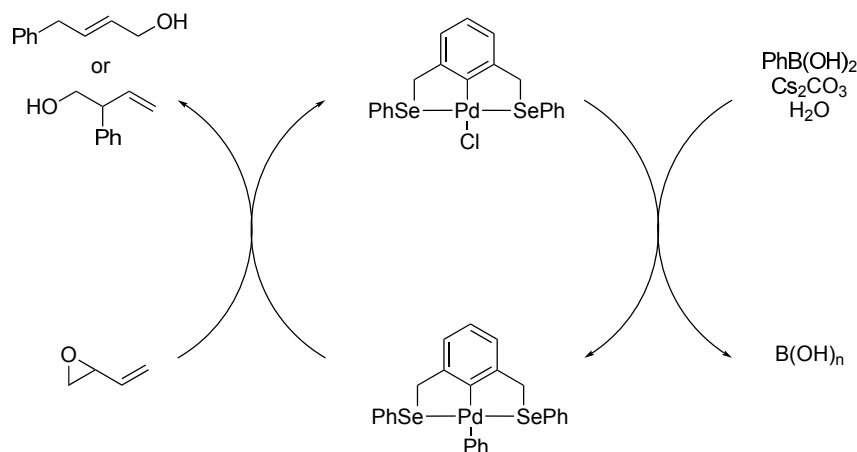


Figure 6.14 Crude ^1H NMR of linear/branched mixture of **23** performed using **15c** in 60/40 linear/branched ratio.

(45 %).

This data suggests that the use of unsymmetrical pincer palladacycles provide the opportunity to tune the selectivity of the vinyl epoxide coupling reaction to phenylboronic acid, in order to achieve greater proportion of the branched coupling product.

In the original work by Szabó and co-workers,⁷¹ a pathway was proposed which is shown in Scheme 6.19. The mechanism includes a transmetallation step between the boronic acid and the palladacycle. This step is analogous to the transmetallation step which has been extensively studied in this thesis (Chapter 4, Chapter 5, and later in this chapter). Further work could include studying the mechanism by which the vinyl epoxide reacts with the transmetallated species, and the variations between the symmetrical and unsymmetrical pincer palladacycles. Effects could range from different transmetallation barrier heights, different steric demands at the palladium centre, and potential hemilability affecting the different structural isomerism.

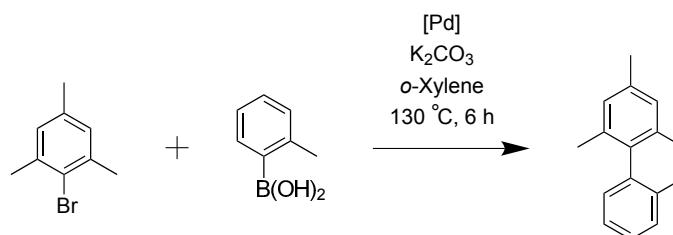


Scheme 6.19 Proposed mechanism for the coupling of vinyl epoxide and phenylboronic acid by Szabó and co-workers.

Suzuki-Miyaura catalysis

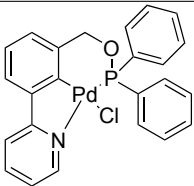
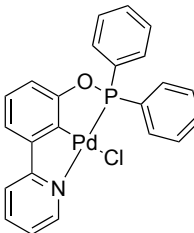
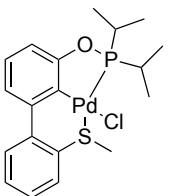
The final catalytic application tested for the PCN and PCS pincer palladacycles presented in this chapter is in the Suzuki-Miyaura coupling reaction in order to compare with the catalytic activities of the other unsymmetrical SCN and N'CN pincer palladacycles presented in this thesis.

The sterically demanding coupling reaction tested is shown in Scheme 6.20, and was performed using 0.01 mol % catalyst loading of **17a**, **17b** and **21**. The results shown in Table 6.10 reveal excellent catalytic activity of all palladacycles. The catalytic activity of the PCN pincer palladacycles (entries 1 and 2) are slightly higher than that of the PCS pincer palladacycle (entry 3). Analogous to that studied for the N'CN pincer palladacycles, the coupling of the much more challenging aryl chloride chloroanisole was attempted, including with the use of TBAB, and again proved unsuccessful.



Scheme 6.20 Suzuki-Miyaura coupling reaction tested using PCN and PCS pincer palladacycles.

Table 6.10 PCN and PCS pincer palladacycle Suzuki-Miyaura coupling testing.

Entry	Palladacycle	GC conversion ^a / %		
		2 h	4 h	6 h
1	17a 	92	95	97
2	17b 	90	93	94
3	21 	83	84	85

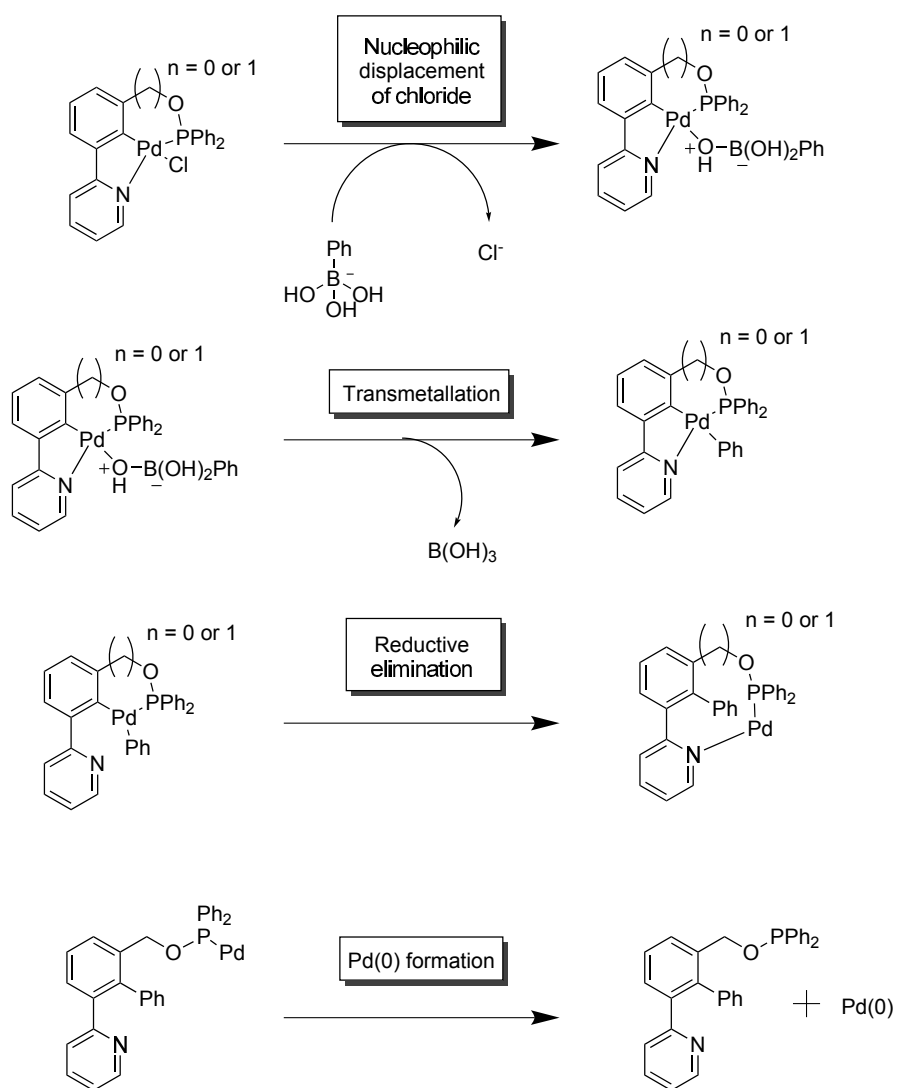
^a = Average of 2 runs.

In order to validate the GC conversion data presented in this thesis, the various coupling reactions tested in this thesis were performed using **17a**, and ^1H and $^{13}\text{C}\{^1\text{H}\}$ NMR, and HRMS analysis were performed on the crude product, revealing reasonable to excellent yields of the corresponding biaryl products. The reactions tested and the % yields are presented in Table 6.11.

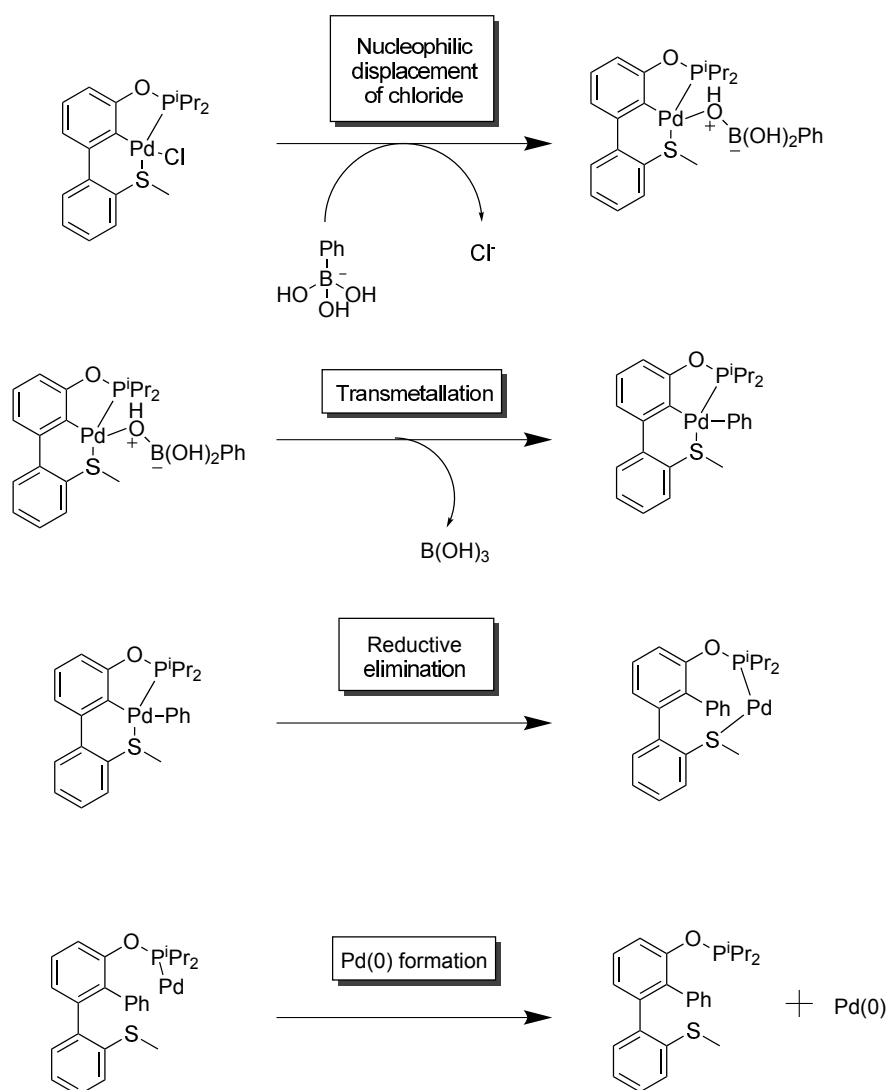
6.2.3 Suzuki-Miyaura coupling rationalisation

As performed for the SCN (Chapter 4) and N'CN (Chapter 5) pincer palladacycles, the Suzuki-Miyaura catalyst activation pathway has been studied, in order to obtain likely key intermediates along the reaction pathway, and to determine energetic barriers for the key transmetallation and reductive elimination steps, and the overall reaction energy yielding catalytically active Pd(0). The key steps in the reaction for the PCN pincer palladacycles are shown in Scheme 6.21. The key steps for the PCS pincer palladacycles are shown in Scheme 6.22.

In these pathways the initial chloride displacement transition state could not be

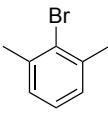
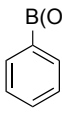
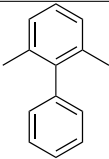
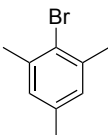
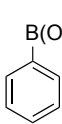
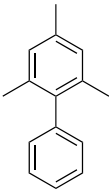
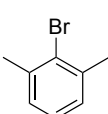
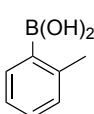
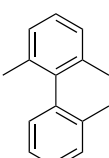
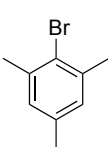
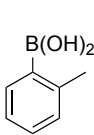
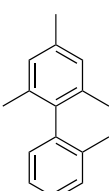


Scheme 6.21 Key steps in the Suzuki-Miyaura coupling catalyst activation pathway for PCN pincer palladacycles.



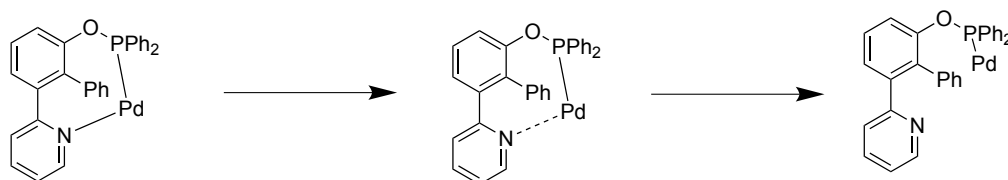
Scheme 6.22 Key steps in the Suzuki-Miyaura coupling catalyst activation pathway for the PCS pincer palladacycle.

Table 6.11 Suzuki-Miyaura coupling reactions performed using **17a** to obtain % yield and analytical data.

Entry	Bromide	Boronic acid	Product	Yield / %
1				70
2				79
3				57
4				82

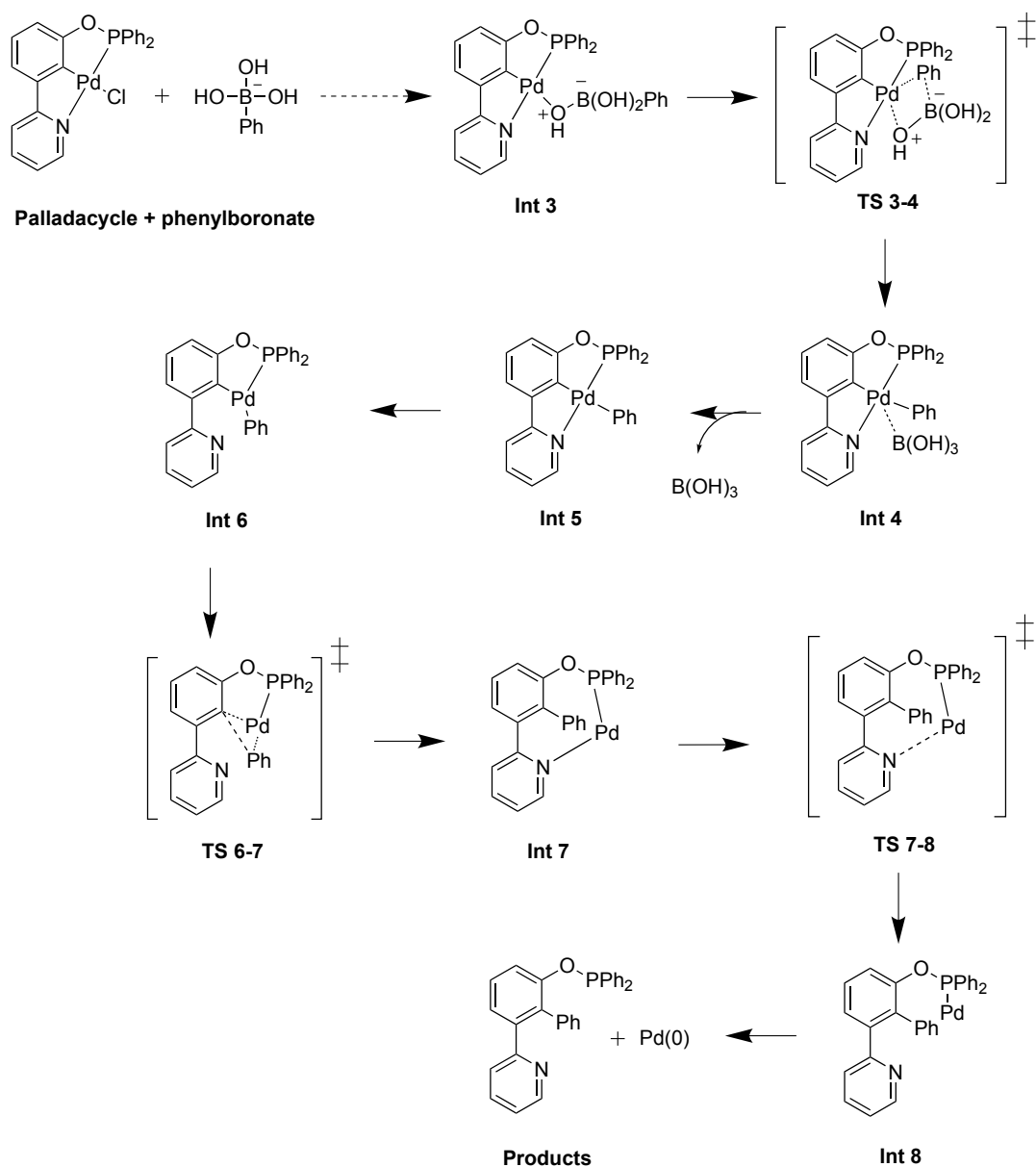
found for any of the 3 pathways. This is attributed to the computational demands, due to the significantly increased steric bulk of the phosphine ligands compared to the groups bonded to the N- or S- donor atoms calculated in previous chapters. With the phenylboronate group approaching the PCN or PCS palladacycle, the palladium atom is buried in the bulk of the phosphine ligand, and the phenyl group causes significant steric clash between the Ph and PPh₂ groups. However, the two key steps in the reaction mechanism are the transmetallation and reductive elimination steps, which have successfully been calculated for the PCN pincer palladacycles.

The ligand decoordination step following reductive elimination was also calculated for **17b** (Scheme 6.23) in order to confirm that this barrier is significantly smaller than the transmetallation and reductive elimination barriers.



Scheme 6.23 Ligand decooordination step post reductive elimination for **17b** palladacycle.

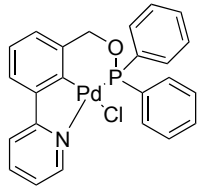
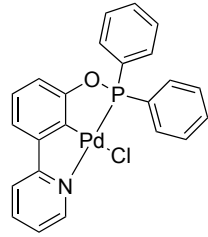
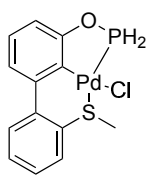
Therefore the pathway studied for **17b** is shown in Scheme 6.24. The pathway has also been calculated for **17a**, however **TS 7-8** could not be found in this pathway, however the barrier is expected to be insignificant, as in the **17b** the energy barrier is only 3.3 kJ mol^{-1} . For the PCS pincer palladacycle, **21**, the pathway has been established with the $i\text{Pr}$ groups replaced with H atoms, however despite extensive efforts, the key transmetallation and reductive elimination transition states could not be found with the $i\text{Pr}$ groups due to the computational demands, palladacycle with H atom replacement are denoted by **21**^{*}. The energies are presented in Table 6.12.



Scheme 6.24 Suzuki-Miyaura catalyst activation pathway for **17b**.

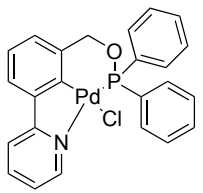
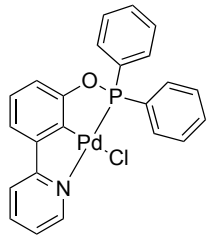
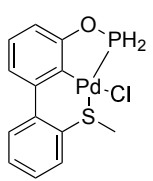
The key energies, such as the transmetalation and reductive elimination barriers, and the overall reaction energies are tabulated in Table 6.13, revealing that the overall reaction energies are very endergonic for the PCN pincer palladacycles ($>200 \text{ kJ mol}^{-1}$), however there are differences between the transmetalation barrier for the PCN pincer palladacycles of 21.7 kJ mol^{-1} . However, the fact that the overall reaction energy is significantly higher than the transmetalation step, and that the experimental catalytic activity is identical for the two PCN pincer palladacycles suggest that the overall reaction energy is the dominant factor in the palladacycle's

Table 6.12 Solvent corrected gibbs free energies (ΔG_S) for the Suzuki-Miyaura coupling reaction catalyst activation pathway for PCN and PCS pincer palladacycles.

Structure	Energy / kJ mol ⁻¹		
	17a 	17b 	21* 
Reactants	0.0	0.0	0.0
Int 3	59.5	63.3	62.7
TS 3-4	176.9	159.0	161.9
Int 4	10.0	11.9	18.5
Int 5	8.7	13.1	-5.3
Int 6	108.2	132.3	73.0
TS 6-7	174.5	205.3	128.5
Int 7	11.8	64.2	-52.3
TS 7-8		67.4	
Int 8		28.5	
Ligand + Pd(0)	208.4	204.7	129.6

catalytic activity. The transmetallation barrier for the PCS pincer palladacycle is intermediate between the two PCN pincer palladacycles, and the overall reaction energy barrier is significantly lower, at 129.6 kJ mol⁻¹ (albeit with ⁱPr substitution).

Table 6.13 Key energetic parameters in the Suzuki-Miyaura coupling catalyst activation pathway for PCN and PCS pincer palladacycles.

Structure	Energy / kJ mol ⁻¹		
	17a 	17b 	21* 
ΔG_S^\ddagger TS 3-4	117.4	95.7	99.2
ΔG_S^\ddagger TS 6-7	66.3	73.0	55.4
ΔG_S Overall reaction energy	208.4	204.7	129.6

The very high overall reaction energy can be rationalised due to the very strong Pd-P bond which is present in these PCN pincer palladacycles. In order to test this, the Atoms in Molecules $\rho(\mathbf{r})$ parameters for the Pd-P bonds for **17a**, **17b** and **21**

are presented in Table 6.14, along with the Pd-N_{amine} and Pd-S bonds for the SCN and N'CN pincer palladacycles presented in earlier chapters.

It can be seen in Table 6.14 that the Pd-P bonds are the strongest with the largest $\rho(\mathbf{r})$ values (>0.1). These stronger Pd-P bonds require greater energy to cleave, resulting in the higher overall reaction energies for the PCN palladacycles. For the PCS palladacycle, the overall reaction energy is significantly smaller, which can be attributed to the much weaker Pd-S bond, and the ⁱPr substitution may have an influence.

The catalytic activity of the PCN palladacycles Table 6.10 can be attributed to the highly endergonic overall reaction energy, meaning more controlled release of the catalytically active Pd(0) species, as discussed in Section 4.4.

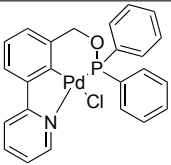
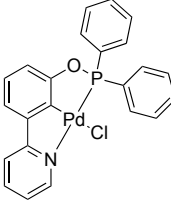
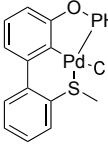
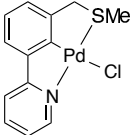
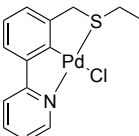
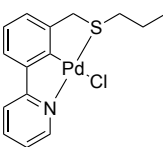
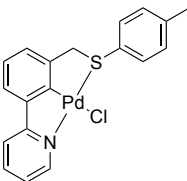
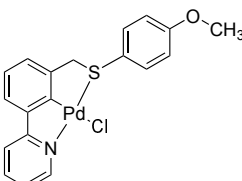
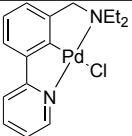
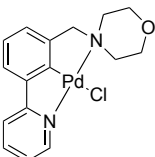
6.3 Conclusion

This chapter has summarised the synthesis of novel PCN and PCS pincer palladacycles, achieved from biaryl alcohol/phenol substrates. X-ray crystallography was performed on the three palladacycles presented.

The PCN and PCS palladacycles, along with two SCN, an N'CN, and several literature palladium catalysts were utilised in a catalytic aldol condensation, and vinyl epoxide coupling revealing differences in the ratio of structural isomers, demonstrating the ability to alter the outcome of reactions by varying the palladacycle donor atoms and groups. The PCN and PCS pincer palladacycles were also tested in the Suzuki-Miyaura coupling reaction, revealing excellent activity in the coupling of the sterically demanding and electronically deactivated aryl bromide. It was found that the two PCN pincer palladacycles exhibited slightly higher catalytic activity than the PCS pincer palladacycle tested.

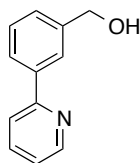
The Suzuki-Miyaura coupling catalyst activation pathway was studied using DFT, revealing high barriers for the transmetallation step, and very high overall reaction energies for the PCN pincer palladacycles, which likely is the reasoning behind their high catalytic activity.

Table 6.14 Bond strength $\rho(\mathbf{r})$ values for Pd-P, Pd-N_{amine} and Pd-S bonds in PCN, PCS, N'CN and SCN pincer palladacycles.

	Palladacycle	$\rho(\mathbf{r})$ / a.u.			
		Pd-P	Pd-N _{amine}	Pd-S	Pd-N _{pyr}
PCN/PCS	17a 	0.113			0.089
	17b 	0.114			0.087
	21* 	0.113		0.080	
SCN	2a 			0.097	0.096
	2b 			0.095	0.098
	2c 			0.095	0.098
	2e 			0.092	0.098
	2f 			0.092	0.098
N'CN	15b 		0.085		0.101
	15c 		0.084		0.102

6.4 Experimental Details

3-(Pyridin-2-yl)phenyl]methanol, **5**



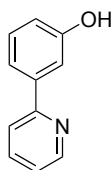
3-[(Hydroxymethyl)phenyl]boronic acid (4.04 mmol, 614 mg), 2-bromopyridine (4.04 mmol, 0.393 mL), $\text{Pd}(\text{PPh}_3)_4$ (0.16 mmol, 182 mg), 0.5 M K_3PO_4 (10 ml), toluene (7.5 ml), EtOH (5 ml) were added to a sealed 35 ml microwave vial and stirred under microwave irradiation (maximum power 300 W, using dynamic heating) at 150 °C for 20 minutes. The reaction was cooled, and the volatiles removed *in vacuo*. The mixture was diluted with H_2O (25 ml) and EtOAc (25 ml), washed with H_2O (2 x 25 ml) and brine (25 ml). The combined organic layers were dried over anhydrous MgSO_4 , filtered, and concentrated *in vacuo*. The crude material was purified using flash column chromatography (7:3 DCM:EtOAc) yielding 694 mg of the expected product **5** as a yellow solid in 93 % yield.

^1H NMR (500 MHz, Chloroform-*d*) δ (ppm): 8.70 (d, $J = 4.9$ Hz, 1H), 8.02 (s, 1H), 7.90 (d, $J = 7.6$ Hz, 1H), 7.78 - 7.74 (m, 2H), 7.48 (dd, $J = 7.6, 7.6$ Hz, 1H), 7.44 (d, $J = 7.6$ Hz, 1H), 7.24 (ddd, $J = 7.3, 4.9, 2.7$ Hz, 1H), 4.80 (d, $J = 6.0$ Hz, 2H), 1.79 (t, $J = 6.0$ Hz, 1H).

$^{13}\text{C}\{^1\text{H}\}$ NMR (126 MHz, Chloroform-*d*) δ (ppm): 157.3, 149.7, 141.5, 139.7, 136.8, 129.0, 127.5, 126.2, 125.5, 122.2, 120.6, 65.4.

HRMS (m/z). Calc. for $[\text{C}_{12}\text{H}_{11}\text{NO} + \text{Na}]^+$ 208.0733. Found 208.0731.

3-(Pyridin-2-yl)phenol, **18**.



3-[Hydroxyphenyl]boronic acid (3.59 mmol, 496 mg), 2-bromopyridine (3.59 mmol, 0.342 mL), $\text{Pd}(\text{PPh}_3)_4$ (0.14 mmol, 164 mg), K_3PO_4 (7.16 mmol, 1.52 g), H_2O (10 ml),

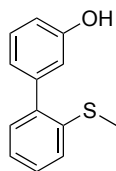
toluene (7.5 ml), EtOH (5 ml) were added to a sealed 35 ml microwave vial and stirred under microwave irradiation (maximum power 300 W, using dynamic heating) at 150 °C for 20 minutes. The reaction was cooled, and the volatiles were removed *in vacuo*. The mixture was diluted with H₂O (25 ml) and Et₂O (25 ml), washed with H₂O (2 x 25 ml) and brine (25 ml). The combined organic layers were dried over anhydrous MgSO₄, filtered, and concentrated *in vacuo*. The crude material was purified using flash column chromatography (8:2 DCM:EtOAc) yielding 450 mg of the expected product **18** as a clear liquid in 73 % yield.

¹H NMR (500 MHz, Dimethylsulfoxide-*d*6) δ (ppm): 9.51 (s, 1H), 8.63 (d, *J* = 4.4 Hz, 1H), 7.86 - 7.83 (m, 2H), 7.51 (s, 1H), 7.47 (d, *J* = 7.9 Hz, 1H), 7.34 - 7.32 (m, 1H), 7.24 (dd, 7.9, 7.9 Hz, 1H), 6.83 (d, *J* = 7.9 Hz, 1H).

¹³C{¹H}NMR (126 MHz, Dimethylsulfoxide-*d*6) δ (ppm): 158.2, 156.5, 149.9, 140.5, 137.6, 130.2, 123.0, 120.6, 117.7, 116.5, 113.8.

HRMS (*m/z*). Calc. for [C₁₁H₉NO + H]⁺ 172.0757. Found 172.0755.

2'-(Methylsulfanyl)[1,1'-biphenyl]-3-ol, **19**.



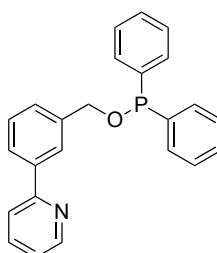
3-[Hydroxyphenyl]boronic acid (6.16 mmol, 850 mg), 2-bromothioanisole (6.16 mmol, 0.822 mL), Pd(PPh₃)₄ (0.25 mmol, 286 mg), K₃PO₄ (10.2 mmol, 2.61 g), H₂O (10 ml), toluene (7.5 ml), EtOH (5 ml) were added to a sealed 35 ml microwave vial and stirred under microwave irradiation (maximum power 300 W, using dynamic heating) at 150 °C for 30 minutes. The reaction was cooled, and the volatiles were removed *in vacuo*. The mixture was diluted with H₂O (25 ml) and EtOAc (25 ml), washed with H₂O (2 x 25 ml) and brine (25 ml). The combined organic layers were dried over anhydrous MgSO₄, filtered, and concentrated *in vacuo*. The crude material was purified using flash column chromatography (8:2 hexane:EtOAc) yielding 738 mg of the expected product **19** as a brown liquid in 55 % yield.

^1H NMR (500 MHz, Chloroform-*d*) δ (ppm): 7.35 - 7.27 (m, 3H), 7.22 - 7.18 (m, 2H), 6.99 (d, $J = 7.6$ Hz, 1H), 6.89 (s, 1H), 6.86 (d, $J = 8.1$ Hz, 1H), 4.75 (s, 1H), 2.37 (s, 3H).

$^{13}\text{C}\{^1\text{H}\}$ NMR (126 MHz, Chloroform-*d*) δ (ppm): 155.2, 142.1, 140.4, 137.0, 129.8, 129.4, 128.0, 125.3, 124.7, 122.0, 116.3, 114.5, 16.0.

HRMS (m/z). Calc. for $[\text{C}_{13}\text{H}_{12}\text{OS} + \text{H}]^+$ 217.0682. Found 217.0681.

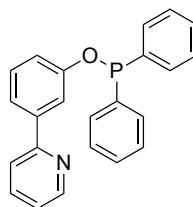
3-(Pyridin-2-yl)phenyl]methyl diphenylphosphinite, 16a.



Under an argon atmosphere, 3-(pyridin-2-yl)phenyl]methanol, **5** (418 mg, 2.26 mmol), NEt_3 (0.63 ml, 4.52 mmol) and DMAP (spatula tip) were dissolved in Et_2O (5 ml) and cooled to 0°C . ClPPh_2 (0.41 ml, 2.22 mmol) was added dropwise to the solution forming a white precipitate. The reaction was warmed to room temperature and stirred for 3 h.

The solution was filtered under an argon atmosphere using a filter cannula, and carried onto the next reaction crude due to air sensitivity.

3-(Pyridin-2-yl)phenyl diphenylphosphinite, 16b.

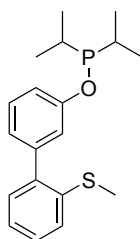


Under an argon atmosphere, 3-(pyridin-2-yl)phenol, **18** (644 mg, 3.76 mmol), NEt_3 (1.05 ml, 7.57 mmol) and DMAP (spatula tip) were dissolved in Et_2O (8 ml) and cooled to 0°C . ClPPh_2 (0.67 ml, 3.74 mmol) was added dropwise to the solution

forming a white precipitate. The reaction was warmed to room temperature and stirred for 3 h.

The solution was filtered under an argon atmosphere using a filter cannula, and carried onto the next reaction crude due to air sensitivity.

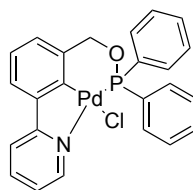
2'-(Methylsulfanyl)[1,1'-biphenyl]-3-yl dipropan-2-ylphosphinite, 20.



Under an argon atmosphere, 2'-(methylsulfanyl)[1,1'-biphenyl]-3-ol, **19** (496 mg, 2.17 mmol), NEt₃ (0.68 ml, 4.87 mmol) and DMAP (spatula tip) were dissolved in Et₂O (4 ml) and cooled to 0 °C. ClPiPr₂ (0.39 ml, 2.45 mmol) was added dropwise to the solution forming a white precipitate. The reaction was warmed to room temperature and stirred overnight.

The solution was filtered under an argon atmosphere using a filter cannula, and carried onto the next reaction crude due to air sensitivity.

3-(Pyridin-2-yl)phenyl]methyl diphenylphosphinite chloro palladacycle, 17a.



Under an argon atmosphere, carried on from the previous reaction without purification, 3-(pyridin-2-yl)phenyl]methyl diphenylphosphinite, **16a** (960 mg, 2.60 mmol) and Pd(OAc)₂ (687 mg, 3.06 mmol) were dissolved in AcOH (5 ml) and heated at 130 °C overnight. After cooling, the solvent was removed *in vacuo*, and reconcentrated with DCM to remove any residual AcOH.

NaCl (1.16 g, 19.9 mmol) was added to the crude mixture, which was dissolved in MeCN (10 ml) and H₂O (10 ml) and stirred at room temperature overnight. The

volatiles were removed *in vacuo*, and the crude mixture dissolved in DCM, and separated using a hydrophobic frit. The crude product was purified using flash column chromatography (7:3 DCM:EtOAc) yielding 383 mg of the expected product **17a** as a yellow solid in 29% yield.

^1H NMR (500 MHz, Chloroform-*d*) δ (ppm): 9.38 (s, 1H), 8.08 - 8.03 (m, 4H), 7.88 - 7.79 (m, 2H), 7.63 (d, $J = 7.6$ Hz, 1H), 7.52 - 7.44 (m, 6H), 7.30 (d, $J = 6.6$ Hz, 1H), 7.19 (dd, $J = 7.6, 7.6$ Hz, 1H), 7.03 (d, $J = 6.6$ Hz, 1H), 4.83 (d, $J = 19.5$ Hz, 2H).

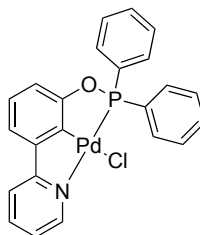
$^{13}\text{C}\{^1\text{H}\}$ NMR (126 MHz, Chloroform-*d*) δ (ppm): 163.3, 151.9, 149.4, 148.2, 139.2 (2C), 136.5, 133.2 (d, $^2J_{\text{PC}} = 13.4$ Hz), 133.0 (d, $^1J_{\text{PC}} = 59.8$ Hz, 2C), 131.7 (d, $^3J_{\text{PC}} = 2.4$ Hz), 128.4 (d, $^3J_{\text{PC}} = 2.0$ Hz, 4C), 128.3 (d, $^2J_{\text{PC}} = 11.6$ Hz, 4C), 125.4, 124.1, 122.5 (d, $^3J_{\text{PC}} = 3.4$ Hz), 118.5 (d, $^3J_{\text{PC}} = 1.9$ Hz), 72.1 (d, $^2J_{\text{PC}} = 2.8$ Hz).

^{31}P NMR (162 MHz, Chloroform-*d*) δ (ppm): 123.27.

HRMS (*m/z*). Calc. for $[\text{C}_{24}\text{H}_{19}\text{NOPd}]^+$ 474.0239. Found 474.0239.

Elemental Analysis. Calc. (%) for $\text{C}_{24}\text{H}_{19}\text{NOPdCl}$: C 56.49, H 3.75, N 2.75; found C 56.48, H 3.82, N 2.83.

3-(Pyridin-2-yl)phenyl diphenylphosphinite chloro palladacycle, **17b**



Under an argon atmosphere, carried on from the previous reaction without purification, 3-(pyridin-2-yl)phenyl diphenylphosphinite, **16b** (1.34 g, 3.76 mmol) and $\text{Pd}(\text{OAc})_2$ (920 mg, 4.10 mmol) were dissolved in AcOH (10 ml) and heated at 130 °C overnight. After cooling, the solvent was removed *in vacuo*, and the mixture was reconcentrated with DCM to remove any residual AcOH.

NaCl (2.35 g, 40.3 mmol) was added to the crude mixture, and dissolved in MeCN (10 ml) and H_2O (10 ml) and stirred at room temperature overnight. The

volatiles were removed *in vacuo*, and the crude mixture dissolved in DCM, and separated using a hydrophobic frit. The crude product was purified using flash column chromatography (7:3 DCM:EtOAc) yielding 409 mg of the expected product **17b** as a yellow solid in 22 % yield.

^1H NMR (500 MHz, Chloroform-*d*) δ (ppm): 9.16 (s, 1H), 8.06 - 8.02 (m, 4H), 7.88 (dd, 7.8, 7.8 Hz, 1H), 7.72 (d, 7.8 Hz, 1H), 7.54 - 7.46 (m, 5H), 7.34 (s, 1H), 7.29 - 7.26 (m, 2H), 7.15 (dd, 7.8, 7.8 Hz, 1H), 6.96 (d, 7.8 Hz, 1H). (>90 % purity)

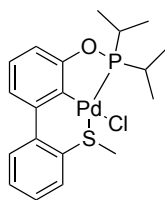
$^{13}\text{C}\{^1\text{H}\}$ NMR (126 MHz, Chloroform-*d*) δ (ppm): 164.5 (d, $^2J_{\text{PC}}$, $J = 3.0$ Hz) 162.6 (d, $^3J_{\text{PC}}$, 10.0 Hz), 149.5, 145.8, 139.3, 133.2 (d, $^1J_{\text{PC}}$, 55.2 Hz), 132.1 (d, $^3J_{\text{PC}}$, 2.5 Hz), 131.6 (d, $^2J_{\text{PC}}$, 14.8 Hz, 2C), 128.9 (d, $^3J_{\text{PC}}$, 11.9 Hz, 2C), 126.9, 123.1 (d, $^3J_{\text{PC}}$, 3.4 Hz), 119.0, 118.0, 113.5 (d, $^2J_{\text{PC}}$, 17.2 Hz). (>90 % purity)

^{31}P NMR (162 MHz, Chloroform-*d*) δ (ppm): 155.3.

HRMS (m/z). Calc. for $[\text{C}_{23}\text{H}_{17}\text{ClNOPdCl}]^+$ 460.0083 . Found 460.0080.

Elemental Analysis. Calc. (%) for $\text{C}_{23}\text{H}_{17}\text{ClNOPd}$: C 55.67, H 3.45, N 2.82; found C 55.76, H 3.58, N 2.84.

2'-(Methylsulfanyl)[1,1'-biphenyl]-3-yl dipropan-2-ylphosphinite chloro palladacycle, **21**.



Under an argon atmosphere, PdCl_2 (2.39 mmol, 424 mg) was dissolved in dry MeCN (15 ml) and heated under reflux until a red solution had formed. AgBF_4 (4.99 mmol, 972 mg), in dry MeCN (5 ml), was added to the PdCl_2 solution and heated under reflux for 2 h, forming a white precipitate. The precipitate was then removed by filtration.

Under an argon atmosphere the filtered solution was added to 2'-(methylsulfanyl)[1,1'-biphenyl]-3-yl dipropan-2-ylphosphinite, **21** (721 mg, 2.17 mmol), carried on from the previous reaction without purification. The reaction was heated at 85 °C overnight.

After cooling, the solvent was removed *in vacuo*.

NaCl (1.28 g, 21.9 mmol) was added to the crude mixture, and dissolved in MeCN (10 ml) and H₂O (10 ml) and stirred at room temperature for 3 h. The volatiles were moved *in vacuo*, and the crude mixture dissolved in DCM, and separated using a hydrophobic frit. The crude product was purified using flash column chromatography (4:1 hexane:EtOAc) yielding 750 mg of the expected product **21** as a yellow solid in 73 % yield.

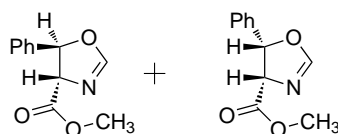
¹H NMR (500 MHz, Chloroform-*d*) δ (ppm): 7.46 - 7.43 (m, 2H), 7.35-7.27 (m, 2H), 7.20 (d, 7.7 Hz, 1H), 7.14 (ddd, 7.0, 7.0, 1.7 Hz, 1H), 6.81 (d, J = 7.7 Hz, 1H), 2.82 (d, 3.1 Hz, 3H), 2.53 (h, 7.1 Hz, 2H), 1.43 (d, 7.1 Hz, 3H), 1.40 (d, 7.1 Hz, 3H), 1.27 (d, 7.1 Hz, 3H), 1.23 (d, 7.1 Hz, 3H). (>90 % purity)

¹³C{¹H}NMR (126 MHz, Chloroform-*d*) δ (ppm): 164.3 (d, $^2J_{PC}$ = 7.7 Hz), 145.2, 141.5 (d, $^3J_{PC}$ = 2.3 Hz), 138.4 (d, $^3J_{PC}$ = 3.9 Hz), 132.2, 128.3, 127.7, 127.4, 126.8 (d, $^3J_{PC}$ = 2.8 Hz), 126.4 (d, 2.3 Hz), 122.9 (d, $^3J_{PC}$ = 1.2 Hz), 111.3 ($^2J_{PC}$ = 15.4 Hz), 29.0 (d, $^1J_{PC}$ = 25.4 Hz, 2C), 17.3 (d, $^2J_{PC}$ = 5.3 Hz, 4C), 16.7 (d, $^3J_{PC}$ = 1.5 Hz).

³¹P NMR (162 MHz, Chloroform-*d*) δ (ppm): 197.0

HRMS (m/z). Calc. for [C₁₉H₂₄OPPdS]⁺ 437.0320. Found 437.0319.

6.4.1 General procedure for aldol condensation



Under an argon atmosphere, the palladium catalyst (0.01 eq.) was dissolved in DCM (5 ml), then methylisocyanoacetate (1 eq.), benzaldehyde (1 eq.) and DIPEA (0.1 eq.) added to the reaction vessel. The reaction was stirred at rt for 24 h, then the reaction was diluted with H₂O and DCM and separated using a hydrophobic frit. A crude ¹H NMR was then taken.

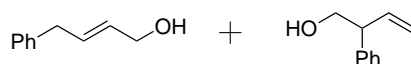
¹H NMR (500 MHz, Chloroform-*d*) δ (ppm): 7.47 - 7.27 (m, 12H), 5.75 (d, J =

11.1 Hz, 1H, *cis*), 5.70 (d, $J = 7.8$ Hz, 1H, *trans*), 5.10 (dd, 11.1, 2.0 Hz, 1H, *cis*), 4.65 (dd, 7.8, 2.2 Hz, 1H, *trans*), 3.85 (s, 3H, *trans*), 3.21 (s, 3H, *cis*).

Trans $^{13}\text{C}\{^1\text{H}\}$ NMR (126 MHz, Chloroform-*d*) δ (ppm): 170.7, 156.4, 138.9, 128.9 (2C), 125.5 (2C), 82.1, 75.2, 52.6.

MS (m/z). Calc. for $[\text{C}_{11}\text{H}_{11}\text{NO}_3]^+$ 205. Found 205.

6.4.2 General procedure for vinyl epoxide coupling



The palladium catalyst (0.04 eq.), phenylboronic acid (1.2 eq.) and Cs_2CO_3 (2 eq.) were dissolved in 10:1 THF: H_2O (3 ml). 2-Vinyloxirane was then added (1 eq.) and the reaction was stirred at room temperature for 24 h. The solvent was removed *in vacuo*, dissolved in DCM (5 ml), washed with H_2O (5 ml) and separated using a hydrophobic frit. The solvent was then removed *in vacuo*. A crude ^1H NMR was then taken to determine the linear/branched ratio.

A pure sample of the mixed branched/linear mixture was obtained by purification with flash column chromatography (6:4 Hexane: Et_2O).

^1H NMR (500 MHz, Chloroform-*d*) δ (ppm): 7.40 - 7.20 (m, 10H), 6.03 (ddd, $J = 18.0, 10.7, 7.3$ Hz, 1H, branched), 5.91 - 5.85 (m, 1H, linear), 5.77 - 5.69 (m, 1H, linear), 5.24 - 5.19 (m, 2H, branched), 4.13 (s, 2H, linear), 3.88 - 3.81 (m, 2H, branched), 3.55 (dt, $J = 7.3, 7.3$ Hz, 1H, branched), 3.40 (d, 6.7 Hz, 2H, linear), 1.66 (s, 1H, branched), 1.45 (s, 1H, linear).

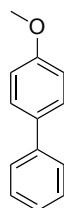
$^{13}\text{C}\{^1\text{H}\}$ NMR (126 MHz, Chloroform-*d*) δ (ppm): 140.7 (branched), 140.0 (linear), 138.3 (branched), 131.5 (linear), 130.3 (linear), 128.7 (branched), 128.5 (linear), 128.4 (linear), 126.9 (branched), 126.1 (linear), 117.0 (branched), 66.1 (branched), 63.5 (linear), 52.5 (branched), 38.6 (linear).

MS (m/z). Calc. for $[\text{C}_{10}\text{H}_{12}\text{O}]^+$ 148. Found 148.

6.4.3 General Procedure for Suzuki-Miyaura catalysis

Arylbromide (1 mmol), arylboronic acid (1.5 mmol) and K_2CO_3 (2 mmol) were added to a reaction vial. *o*-Xylene (3 ml) was added, and the catalyst in DCM solution of varying concentrations for different catalyst loadings were added. The reaction was heated at 130 °C for 6 hours, and aliquots taken at intervals, diluted in Et_2O , washed with H_2O , and the organic layer used for GC analysis.

4-Methoxy-1,1'-biphenyl, 10a



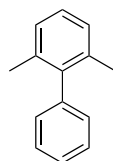
Values for 1H and $^{13}C\{^1H\}$ NMR are in agreement with values by Gopidas and co-workers.²⁸¹

1H NMR (500 MHz, Chloroform-*d*) δ (ppm): 7.56 - 7.52 (m, 4H), 7.42 (dd, 7.4, 7.45 Hz, 2H), 7.30 (ddd, 7.4, 7.4, 1.2 Hz, 1H), 6.98 (d, 8.8 Hz, 2H), 3.86 (s, 3H).

$^{13}C\{^1H\}$ NMR (126 MHz, Chloroform-*d*) δ (ppm): 159.2, 140.8, 133.8, 128.7 (2C), 128.1 (2C), 126.7 (2C), 126.6, 114.2 (2C), 55.3.

MS (m/z). Calc. for $[C_{13}H_{12}O]^+$ 184.1. Found 184.1.

2,6-Dimethyl-1,1'-biphenyl, 10c



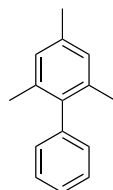
Values for 1H and $^{13}C\{^1H\}$ NMR are in agreement with values by Becht and co-workers.²⁸²

1H NMR (500 MHz, Chloroform-*d*) δ (ppm): 7.46 (dd, 7.6, 7.6 Hz, 2H), 7.38 - 7.35 (m, 1H), 7.20 - 7.18 (m, 3H), 7.15 (d, 7.6 Hz, 2H), 2.07 (s, 6H).

$^{13}C\{^1H\}$ NMR (126 MHz, Chloroform-*d*) δ (ppm): 141.8, 141.1, 136.0 (2C), 129.0 (2C), 128.4 (2C), 127.2 (2C), 127.0, 126.6, 20.8 (2C).

HRMS (m/z). Calc. for $[\text{C}_{14}\text{H}_{14}]^+$ 182.1095. Found 182.1100.

2,4,6-Trimethyl-1,1'-biphenyl, 10d



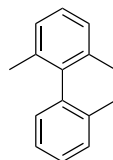
Values for ^1H and $^{13}\text{C}\{^1\text{H}\}$ NMR are in agreement with values by Shaughnessy and co-workers.²⁸³

^1H NMR (500 MHz, Chloroform-*d*) δ (ppm): 7.50 (dd, $J = 7.3, 7.3$ Hz, 2H), 7.41 (dd, $J = 7.3, 7.3$ Hz, 2H), 7.24 - 7.23 (m, 2H), 7.04 (s, 2H), 2.43 (2, 3H), 2.10 (s, 6H).

$^{13}\text{C}\{^1\text{H}\}$ NMR (126 MHz, Chloroform-*d*) δ (ppm): 141.4, 139.4, 136.8, 136.2, 129.6 (2C), 128.6 (2C), 128.4 (2C), 126.8 (2C), 21.3, 21.1 (2C).

HRMS (m/z). Calc. for $[\text{C}_{15}\text{H}_{16}]^+$ 196.1252. Found 129.1256.

2,2',6-Trimethyl-1,1'-biphenyl, 10e



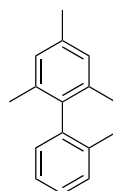
Values for ^1H and $^{13}\text{C}\{^1\text{H}\}$ NMR are in agreement with values by Doherty *et al.*²⁸⁴

^1H NMR (500 MHz, Chloroform-*d*) δ (ppm): 7.33 - 7.25 (m, 3H), 7.20 - 7.17 (m, 1H), 7.13 (d, 7.3 Hz, 2H), 7.05 - 7.03 (m, 1H), 2.00 (s, 3H), 1.97 (s, 6H).

$^{13}\text{C}\{^1\text{H}\}$ NMR (126 MHz, Chloroform-*d*) δ (ppm): 141.1, 140.5, 135.8, 135.6, 129.9, 128.8, 127.2 (2C), 127.0, 126.9, 126.0 (2C), 20.3 (2C), 19.3.

HRMS (m/z). Calc. for $[\text{C}_{15}\text{H}_{16}]^+$ 129.1252. Found 196.1243.

2,2',4,6-Tetramethyl-1,1'-biphenyl, 10f



Values for ^1H and $^{13}\text{C}\{^1\text{H}\}$ NMR are in agreement with values by Shaughnessy and co-workers.²⁸³

^1H NMR (500 MHz, Chloroform-*d*) δ (ppm): 7.33 - 7.25 (m, 3H), 7.07 - 7.05 (m, 1H), 6.99 (s, 2H), 2.38 (s, 3H), 2.03 (s, 3H), 1.97 (s, 6H).

$^{13}\text{C}\{^1\text{H}\}$ NMR (126 MHz, Chloroform-*d*) δ (ppm): 140.6, 138.2, 136.3, 135.9, 135.7, 129.9, 129.2 (2C), 128.0 (2C), 126.9, 126.0, 21.1, 20.2 (2C) 19.5.

HRMS (m/z). Calc. for $[\text{C}_{16}\text{H}_{18}]^+$ 210.1409. Found 210.1416.

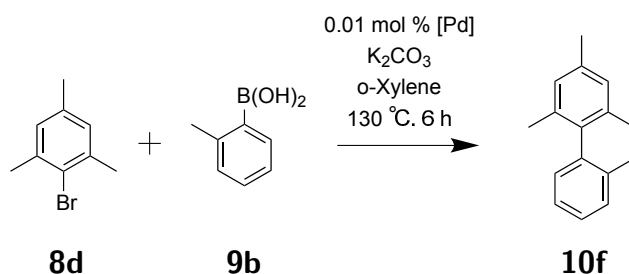
Chapter 7

Pincer palladacycle catalytic activity: an analysis and comparison

This final chapter summarises the varying catalytic activity in the Suzuki-Miyaura catalysis presented in this thesis, along with rationalisation of the activity provided by DFT calculations.

7.1 Suzuki-Miyaura catalysis

Throughout this thesis, Suzuki-Miyaura catalysis has been performed with a range of SCN (Chapter 4), N'CN (Chapter 5), PCN and PCS (Chapter 6) pincer palladacycles for the reaction shown in Scheme 7.1. The reaction is an example of a sterically demanding and electronically deactivated aryl bromide being coupling with 2-tolylboronic acid.



Scheme 7.1 Suzuki-Miyaura coupling reaction used to compare SCN, N'CN, PCN and PCS pincer palladacycles.

A summary of the catalysis results is shown in Table 7.1, which also include comparisons with the Herrmann-Beller palladacycle,³² a symmetrical NCN pincer palladacycle by van Koten and co-workers,²⁵³ and a symmetrical SCS pincer palladacycle by Dupont *et al.*^{245,246} The results show that the N'CN and PCN pincer palladacycles achieve the highest, and the SCN pincer palladacycles achieving the lowest GC conversions. The single PCS pincer palladacycle had intermediate catalytic activity. As discussed in Chapter 4 varying the substituents on the thioether donor group has influence on the conversions for this sterically demanding coupling reaction. For the PCN and N'CN pincer palladacycles, the different palladacycles tested do not reveal any significant differences in their catalytic activity.

The differences in catalytic activity of the various substituents on the thioether donor group for the SCN pincer palladacycles were attributed to the variations in the overall reaction energy (ΔG_S), calculated by studying the catalyst activation pathway using DFT, with a more endergonic energy yielding greater GC conversion (Section 4.4). In order to compare between the SCN, N'CN, PCN and PCS palladacycles, 6 h GC conversion, the overall reaction energy, and the transmetallation energy barrier for each palladacycle are tabulated in Table 7.2. The data show that transmetallation barriers ($\Delta G_S^{\ddagger TM}$) for the N'CN pincer palladacycles are larger than that of the SCN pincer palladacycles, resulting in the much higher catalytic activity, due to slower, more controlled Pd(0) generation.

A striking feature of the data presented in Table 7.2 is the significantly higher overall reaction energy (ΔG_S) for the PCN pincer palladacycles. It is likely that this is a significant factor in the high catalytic activity exhibited by the PCN pincer

Table 7.1 Summary of Suzuki-Miyaura catalysis reaction results for that shown in Scheme 7.1 for SCN, N'CN, PCN and PCS pincer palladacycles.

Entry	Palladacycle	GC conversion / %		
		2 h	4 h	6 h
1		69	76	79
2		-	62	64
3		76	77	79
4		24	34	39
5		-	32	37
6		95	96	98
7		97	98	99
8		92	95	97
9		90	93	94
10		83	84	85
11		50	50	57
12		37	43	47
13		96	97	98

palladacycles. The transmetallation barriers for the PCN pincer palladacycles are similar to the other palladacycles tested in this study. The PCS pincer palladacycle (however with the ⁱPr groups replace with H) has a larger overall reaction energy than the SCN and N'CN pincer palladacycles, but a lower transmetallation energy barrier than the N'CN pincer palladacycles, resulting in intermediate catalytic activity.

All of the data presented here provide a picture that suggests that for the palladacycles tested, greater catalytic activity can be attributed to slow, controlled release of catalytically active Pd(0), caused by large energy barriers, and/or large overall endergonic reaction energies. As discussed in Chapter 4, palladacycles likely act as a source of Pd(0) in Suzuki-Miyaura catalysis,^{45,249} and a route to catalyst deactivation is agglomeration of Pd(0) species into Pd black.^{250,251} Therefore the results presented here fit perfectly into this previous analysis, in that the key to designing palladacycles for Suzuki-Miyaura catalysis is to maximise the stability of the palladacycle, and inhibit the formation of Pd black.

Despite the previous reports that unsymmetrical pincer palladacycles often exhibit greater catalytic activity,^{23,172} this work has shown that in the Suzuki-Miyaura coupling reactions, minimal difference is found between the symmetrical and unsymmetrical pincer palladacycles. However more significant differences in the study into the Pd(II) catalytic applications (Chapter 6) suggesting that whilst not a general feature in all applications, the use of unsymmetrical pincer palladacycles can show enhanced catalytic properties as opposed to their symmetrical analogues, providing the opportunity to fine-tune catalytic activity.

Table 7.2 GC conversion for reaction shown in Scheme 7.1, overall reaction energies (ΔG_s), and transmetallation barriers ($\Delta G_s^{\ddagger TM}$) for SCN, N'CN, PCN and PCS pincer palladacycles.

Entry	Palladacycle	6 h GC conversion / %	Energy / kJ mol^{-1}	
			ΔG_s	$\Delta G_s^{\ddagger TM}$
1		79	72.4	99.7
2		64	83.0	97.4
3		79	84.1	101.3
4		39	59.9	104.2
5		37	61.6	98.1
6		98	88.3	129.1
7		99	71.5	127.0
8		97	208.4	117.4
9		94	204.7	95.7
10 ^a		85	129.6	99.2
11		57	-	-
12		47	-	-
13		98	-	-

^a = For DFT calculations, ⁱPr groups replaced with H.

Chapter 8

Concluding remarks, and future directions

8.1 Concluding remarks

An analysis of all bonded and interatomic bond distances obtained from geometry optimisation using several DFT functionals and basis sets was used to test their ability to predict experimental X-ray crystallographic structures was presented in Chapter 2. The analysis showed that the ω B97XD functional, incorporating non-covalent interactions, provides the most accurate structures in geometry optimisation. It was also found that the SDD effective core potential was more effective than the LanL2DZ effective core potential for palladium. Therefore the ω B97XD/6-311++G(2df,2p)[SDD]/ ω B97XD/6-31++G(d,p)[SDD] methodology was applied to DFT studies in the DFT calculations presented in this thesis. This work was published in Dalton Transactions.⁹⁶

A new and amenable experimental synthesis to unsymmetrical SCN pincer ligands, and the resulting C-H bond activation yielding a novel SCN pincer palladacycle was presented in Chapter 3. A model formation reaction pathway was studied using DFT, and Bader's Atoms in Molecules analysis was used to characterise the stationary points along the pathway. This analysis revealed differences in the various Pd-L

bond strengths and natures, influencing the key C-H bond activation step. The calculations showed that the model synthetic pathway was energetically feasible, and spontaneous. This work has been published in Royal Society Open Science.⁹⁷

The new experimental synthetic route devised in Chapter 3 was used in Chapter 4 in order to synthesise a library of novel SCN pincer ligands, and the resulting C-H bond activation was reported, providing a family of new SCN pincer palladacycles. These palladacycles were tested in Suzuki-Miyaura catalysis of aryl bromide coupling partners, which revealed differences in catalytic activity depending on the substituents found on the sulphur donor atom. In order to understand the varying catalytic activities, a catalyst activation pathway was studied using DFT and Bader charge analysis, showing that the overall reaction energy was likely responsible for the differing catalytic activities, as SCN pincer palladacycles that are most endergonic exhibit the greatest catalytic activity, attributed to the more controlled release of catalytically active Pd(0).

The novel route to unsymmetrical SCN pincer ligands was adapted to provide a route to unsymmetrical N'CN pincer ligands in Chapter 5. These unsymmetrical pincer ligands underwent C-H bond activation yielding a series of novel unsymmetrical N'CN pincer palladacycles. Two of these palladacycles were then tested in a Suzuki-Miyaura coupling, revealing no difference in the catalytic activity of the palladacycles studied. The DFT study of the catalyst activation pathway showed that the overall reaction energies were slightly different between the two palladacycles, however the transmetallation energy barriers were identical for both pathways for which experimental data was obtained.

The synthesis of a series of novel PCN and PCS pincer palladacycles were described in Chapter 6, including mixed 5-,6-ring systems. The PCN and PCS palladacycles, along with several SCN and N'CN pincer palladacycles were tested in two catalytic applications, including an aldol condensation, and a vinyl epoxide coupling reaction revealing differences dependent on the donor atom, and groups upon those donor atoms. In the aldol condensation reaction, it appears that phosphorus donor atoms

favour *trans* product formation, with other donor atoms providing a higher proportion of *cis* products. In the vinyl epoxide coupling, varying degrees of linear and branched products can be obtained again by varying the donor atoms or groups. These reactions show the potential for use of the unsymmetrical pincer palladacycles in future catalytic applications, with an easy and modular approach to altering the donor atoms and groups in the final resulting palladacycle. Finally the PCN and PCS pincer palladacycles were tested in the Suzuki-Miyaura coupling studied in other chapters, again providing excellent results for the sterically demanding and electronically deactivated coupling reaction studied. The catalyst activation pathway studied using DFT showed significant differences in the overall reaction energy between the PCN and PCS pincer palladacycles.

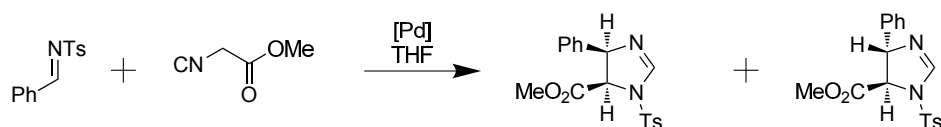
Finally, in Chapter 7 the results from the Suzuki-Miyaura coupling reaction were compared for each of the SCN, N'CN, PCN and PCS pincer palladacycles, along with rationalisation of the catalytic activity by the DFT results presented in each of the preceding chapters. The results show that for the varying thioether substituents in the SCN pincer palladacycles, the overall reaction energy influences the catalytic activity. It was shown that the transmetallation barriers for the N'CN pincer palladacycles were higher than that for the SCN pincer palladacycles, with similar overall reaction energies. The PCN pincer palladacycles have the highest overall reaction energy when compared to the N'CN and SCN pincer palladacycles, with the PCS palladacycle intermediate. These data show that enhanced catalytic activity in the Suzuki-Miyaura coupling reaction is dependent on slowing the release of catalytically active Pd(0), and the design of new catalysts should aim to maximise the transmetallation barriers and overall reaction energy to increase their catalytic activity where the palladacycle acts as a Pd(0) reservoir.

8.2 Future directions

This thesis has described the design of a new synthetic route to unsymmetrical pincer palladacycles, allowing late stage diversification, and synthesis of a diverse range

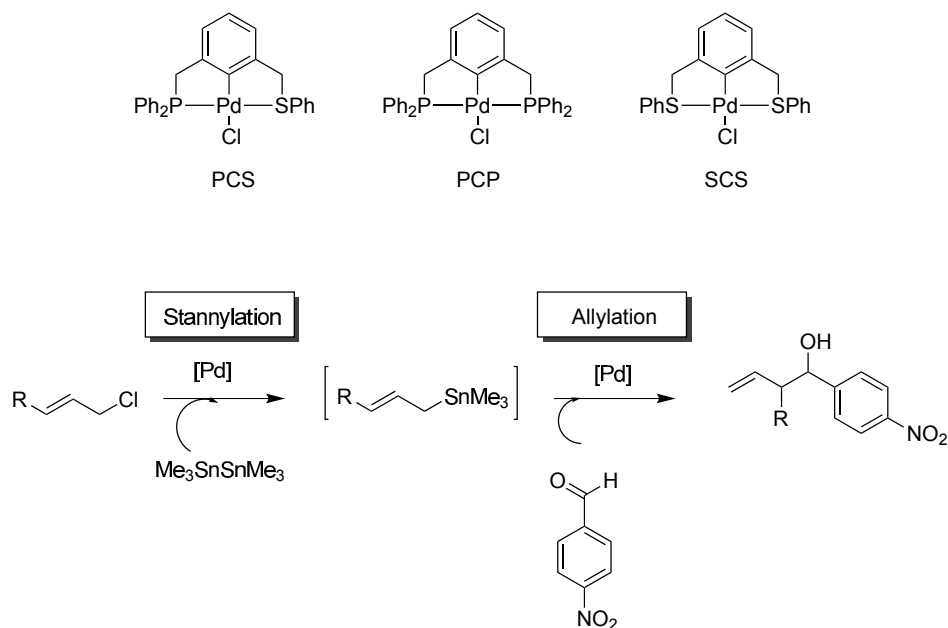
of novel unsymmetrical pincer palladacycles. These palladacycles were tested as catalysts in several reactions, and a model formation reaction, and catalyst activation pathway studied using Density Functional Theory.

Future directions for this project should encompass an investigation of the application of the novel palladacycles in a number of other catalytic applications. Palladacycles have found application in a plethora of catalytic applications, and the examples presented in this thesis are a small selection of interesting examples, this would benefit from being extended. Due to the interesting stereochemical outcomes presented in this thesis for the aldol condensation and vinyl epoxide couplings, future work could be to extend this to the coupling of sulfonimines and isocyanoacetate, in order to obtain different *syn/anti* ratios, as shown in (Scheme 8.1) performed by Szabó and co-workers.²⁸⁵



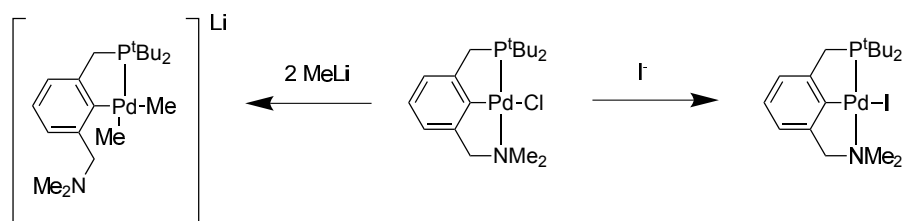
Scheme 8.1 Sulfonimine and isocyanoacetate condensation by Szabó and co-workers.

It would also be interesting to study whether the unsymmetrical pincer palladacycles in this thesis could provide the desired combination of ligand effects to successfully catalyse the tandem stannylation and allylation shown in Scheme 8.2 by Szabó and co-workers discussed in Chapter 1.¹³



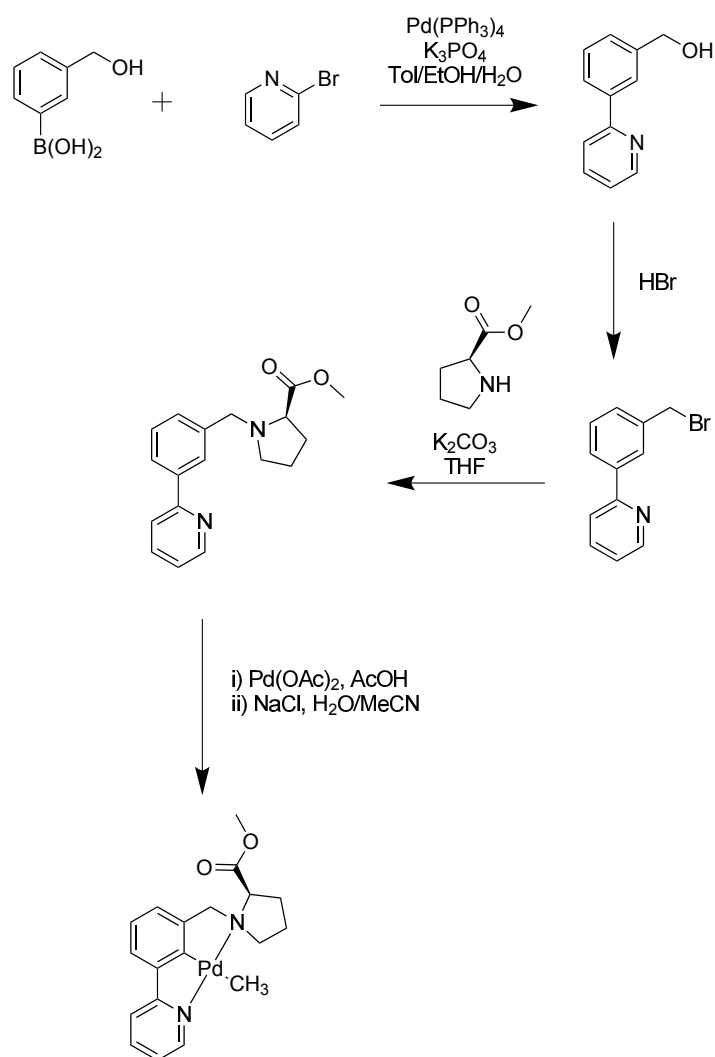
Scheme 8.2 Tandem stannylation and allylation by Szabó and co-workers.

In order to experimentally investigate potential hemilability in the unsymmetrical pincer palladacycles, an investigation analogous to that of Wendt and co-workers could be performed,¹⁴ by reacting the palladacycles with nucleophiles to probe the strength of the Pd-L bonds, demonstrating the stronger Pd-P bond, as compared to the weaker Pd-N bond, as shown in Scheme 8.3. This could also feed into further DFT calculations, to compare to Atoms in Molecules analysis of the palladacycles on their bond strengths.



Scheme 8.3 Experimental hemilability probe of unsymmetrical pincer palladacycles by Wendt and co-workers.

The use of palladacycles as chiral catalysts are also becoming increasingly common, and therefore the novel synthetic route presented in this thesis provide a potentially simple route to chiral unsymmetrical pincer palladacycles, for example a synthesis as shown in Scheme 8.4 is potentially possible.



Scheme 8.4 Potential route to a chiral unsymmetrical N'CN pincer palladacycle.

Finally, for the vinyl epoxide coupling presented in this thesis, a key step in this reaction is transmetallation, which also appears in the catalyst activation pathway studied using DFT presented in this thesis. This provides the opportunity to modify the catalyst activation pathway to study the reaction mechanism of the vinyl epoxide coupling reaction, in order to rationalise the different ratios of linear and branched product depending on the palladacycle.

References

- [1] A. C. Cope and R. W. Siekman, *J. Am. Chem. Soc.*, 1965, **87**, 3272–3273.
- [2] A. C. Cope and E. C. Friedrich, *J. Am. Chem. Soc.*, 1968, **90**, 909–913.
- [3] M. I. Bruce, *Angew. Chemie, Int. Ed. English*, 1977, **16**, 73–86.
- [4] I. Omae, *Chem. Rev. (Washington, DC, United States)*, 1979, **79**, 287–321.
- [5] A. Bahsoun, J. Dehand, M. Pfeffer, M. Zinsius, S.-E. Bouaoud and G. Le Borgne, *J. Chem. Soc. Dalt. Trans.*, 1979, 547–556.
- [6] C. J. Moulton and B. L. Shaw, *J. Chem. Soc. Dalt. Trans.*, 1976, 1020–1024.
- [7] J. Dupont, C. S. Consorti and J. Spencer, *Chem. Rev.*, 2005, **105**, 2527–2572.
- [8] C. A. Kruithof, H. P. Dijkstra, M. Lutz, A. L. Spek, R. J. M. Klein Gebbink and G. van Koten, *Organometallics*, 2008, **27**, 4928–4937.
- [9] B.-B. Liu, X.-R. Wang, Z.-F. Guo and Z.-L. Lu, *Inorg. Chem. Commun.*, 2010, **13**, 814–817.
- [10] O. A. Wallner and K. J. Szabó, *Chem. Eur. J.*, 2006, **12**, 6976–6983.
- [11] J. Aydin, N. Selander and K. J. Szabó, *Tetrahedron Lett.*, 2006, **47**, 8999–9001.
- [12] Q. W. Yao, E. P. Kinney and C. Zheng, *Org. Lett.*, 2004, **6**, 2997–2999.
- [13] M. Gagliardo, N. Selander, N. C. Mehendale, G. van Koten, R. J. M. Klein Gebbink and K. J. Szabó, *Chem. - A Eur. J.*, 2008, **14**, 4800–4809.

-
- [14] A. Fleckhaus, A. H. Mousa, N. S. Lawal, N. K. Kazemifar and O. F. Wendt, *Organometallics*, 2015, **34**, 1627–1634.
- [15] X.-Q. Hao, Y.-N. Wang, J.-R. Liu, K.-L. Wang, J.-F. Gong and M.-P. Song, *J. Organomet. Chem.*, 2010, **695**, 82–89.
- [16] D. V. Aleksanyan, V. A. Kozlov, N. E. Shevchenko, V. G. Nenajdenko, A. A. Vasil'ev, Y. V. Nelyubina, I. V. Ananyev, P. V. Petrovskii and I. L. Odinets, *J. Organomet. Chem.*, 2012, **711**, 52–61.
- [17] G. Ebeling, M. R. Meneghetti, F. Rominger and J. Dupont, *Organometallics*, 2002, **21**, 3221–3227.
- [18] S. K. Callear, J. Spencer, H. Patel, J. J. Deadman and M. B. Hursthouse, *J. Chem. Crystallogr.*, 2011, **41**, 523–527.
- [19] C. S. Consorti, G. Ebeling, F. Rodembusch, V. Stefani, P. R. Livotto, F. Rominger, F. H. Quina, C. Yihwa and J. Dupont, *Inorg. Chem.*, 2004, **43**, 530–536.
- [20] B. Riffade, J. Oble, L. Chenneberg, E. Derat, B. Hasenknopf, E. Lacôte and S. Thorimbert, *Tetrahedron*, 2013, **69**, 5772–5779.
- [21] W. B. Cross, E. G. Hope, Y.-H. H. Lin, S. A. Macgregor, K. Singh, G. A. Solan and N. Yahya, *Chem. Commun. (Camb.)*, 2013, **49**, 1918–1920.
- [22] D. J. Cardenas, A. M. Echavarren and M. C. R. de Arellano, *Organometallics*, 1999, **18**, 3337–3341.
- [23] I. Moreno, R. SanMartin, B. Ines, M. T. Herrero and E. Domínguez, *Curr. Org. Chem.*, 2009, **13**, 878–895.
- [24] P. Braunstein and F. Naud, *Angew. Chemie Int. Ed.*, 2001, **40**, 680–699.
- [25] J. R. Khusnutdinova and D. Milstein, *Angew. Chemie Int. Ed.*, 2015, **54**, 12236–12273.

-
- [26] W.-H. Zhang, S. W. Chien and T. A. Hor, *Coord. Chem. Rev.*, 2011, **255**, 1991–2024.
- [27] S. Ramírez-Rave, F. Estudiante-Negrete, R. A. Toscano, S. Hernández-Ortega, D. Morales-Morales and J.-M. Grévy, *J. Organomet. Chem.*, 2014, **749**, 287–295.
- [28] D. Saha, R. Verma, D. Kumar, S. Pathak, S. Bhunya and A. Sarkar, *Organometallics*, 2014, **33**, 3243–3246.
- [29] E. Poverenov, M. Gandelman, L. J. W. Shimon, H. Rozenberg, Y. Ben-David and D. Milstein, *Organometallics*, 2005, **24**, 1082–1090.
- [30] M. Gargir, Y. Ben-David, G. Leitun, Y. Diskin-Posner, L. J. W. Shimon and D. Milstein, *Organometallics*, 2012, **31**, 6207–6214.
- [31] *Palladacycles*, ed. J. Dupont and M. Pfeffer, Wiley-VCH Verlag GmbH & Co. KGaA, Weinheim, Germany, 2008.
- [32] M. Beller, H. Fischer, W. A. Herrmann, K. Öfele and C. Brossmer, *Angew. Chemie Int. Ed. English*, 1995, **34**, 1848–1849.
- [33] W. A. Herrmann, V. P. W. Böhm, C.-P. Reisinger and V. P. W. Böhm, *J. Organomet. Chem.*, 1999, **576**, 23–41.
- [34] V. A. Kozlov, D. V. Aleksanyan, Y. V. Nelyubina, K. A. Lyssenko, E. I. Gutsul, L. N. Puntus, A. A. Vasil'ev, P. V. Petrovskii and I. L. Odinet, *Organometallics*, 2008, **27**, 4062–4070.
- [35] V. A. Kozlov, D. V. Aleksanyan, Y. V. Nelyubina, K. A. Lyssenko, A. A. Vasil'ev, P. V. Petrovskii and I. L. Odinet, *Organometallics*, 2010, **29**, 2054–2062.
- [36] K. Karami, S. Esfarjani, S. Abedanzadeh and J. Lipkowski, *Polyhedron*, 2014, **68**, 249–257.

-
- [37] R. B. Bedford, L. Hazelwood, N. Horton and M. B. Hursthouse, *Dalt. Trans.*, 2003, 4164–4174.
- [38] D. A. Albisson, R. B. Bedford, S. E. Lawrence and P. N. Scully, *Chem. Commun.*, 1998, 2095–2096.
- [39] R. B. Bedford, S. M. Draper, S. L. Welch and P. N. Scully, *New J. Chem.*, 2000, **24**, 745–747.
- [40] Q. Luo, S. Eibauer and O. Reiser, *J. Mol. Catal. A Chem.*, 2007, **268**, 65–69.
- [41] G. K. Rao, A. Kumar, S. Kumar, U. B. Dupare and A. K. Singh, *Organometallics*, 2013, **32**, 2452–2458.
- [42] D. Olsson and O. F. Wendt, *J. Organomet. Chem.*, 2009, **694**, 3112–3115.
- [43] E. Alacid and C. Nájera, *Adv. Synth. Catal.*, 2007, **349**, 2572–2584.
- [44] J. Spencer, D. P. Sharratt, J. Dupont, A. L. Monteiro, V. I. Reis, M. P. Stracke, F. Rominger and I. M. McDonald, *Organometallics*, 2005, **24**, 5665–5672.
- [45] A. H. M. de Vries, J. M. C. A. Mulders, J. H. M. Mommers, H. J. W. Henderickx and J. G. de Vries, *Org. Lett.*, 2003, **5**, 3285–8.
- [46] S. Sabounchei, M. Ahmadi, T. Azizi and M. Panahimehr, *Synlett*, 2013, **25**, 336–342.
- [47] R. SanMartin, B. Ines, M. Jesus Moure, M. Teresa Herrero, E. Dominguez, M. J. Moure and M. T. Herrero, *Helvetica Chim. Acta*, 2012, **95**, 955–962.
- [48] D. S. Rosa, F. Antelo, T. J. Lopes, N. F. de Moura and G. R. Rosa, *Quim. Nova*, 2015, **38**, 605–608.
- [49] B. Inés, R. SanMartin, F. Churruca, E. Domínguez, M. K. Urtiaga and M. I. Arriortua, *Organometallics*, 2008, **27**, 2833–2839.
- [50] D. A. Alonso, C. Nájera and M. C. Pacheco, *Org. Lett.*, 2000, **2**, 1823–1826.

-
- [51] W. Susanto, C.-Y. Chu, W. J. Ang, T.-C. Chou, L.-C. Lo and Y. Lam, *J. Org. Chem.*, 2012, **77**, 2729–2742.
- [52] J. Louie and J. F. Hartwig, *Angew. Chemie Int. Ed. English*, 1996, **35**, 2359–2361.
- [53] Y. Yang, N. J. Oldenhuis and S. L. Buchwald, *Angew. Chem. Int. Ed. Engl.*, 2013, **52**, 615–619.
- [54] D. A. Alonso, C. Nájera and M. C. Pacheco, *J. Org. Chem.*, 2002, **67**, 5588–5594.
- [55] N. Selander and K. J. Szabó, *Chem. Rev.*, 2011, **111**, 2048–2076.
- [56] S. Chakrabarty, S. Choudhary, A. Doshi, F. Q. Liu, R. Mohan, M. P. Ravindra, D. Shah, X. Yang and F. F. Fleming, *Adv. Synth. Catal.*, 2014, **356**, 2135–2196.
- [57] M. A. Stark and C. J. Richards, *Tetrahedron Lett.*, 1997, **38**, 5881–5884.
- [58] J. M. Longmire and X. Zhang, *Organometallics*, 1998, **7333**, 4374–4379.
- [59] R. van de Coevering, A. P. Alferys, J. D. Meeldijk, E. Martínez-Viviente, P. S. Pregosin, R. J. M. K. Gebbink and G. van Koten, *J. Am. Chem. Soc.*, 2006, **128**, 12700–12713.
- [60] M. A. Stark, G. Jones and C. J. Richards, *Organometallics*, 2000, **19**, 1282–1291.
- [61] Y. Motoyama, H. Kawakami, K. Shimosono, K. Aoki and H. Nishiyama, *Organometallics*, 2002, **21**, 3408–3416.
- [62] S. Gosiewska, S. M. Herreras, M. Lutz, A. L. Spek, R. W. A. Havenith, G. P. M. van Klink, G. van Koten and R. J. M. Klein Gebbink, *Organometallics*, 2008, **27**, 2549–2559.
- [63] Q. Yao and M. Sheets, *J. Org. Chem.*, 2006, **71**, 5384–5387.

-
- [64] R. A. Baber, R. B. Bedford, M. Betham, M. E. Blake, S. J. Coles, M. F. Haddow, M. B. Hursthouse, a. G. Orpen, L. T. Pilarski, P. G. Pringle and R. L. Wingad, *Chem. Commun.*, 2006, **2**, 3880–3882.
- [65] O. Piechaczyk, T. Cantat, N. Mezailles, P. L. Floch and N. Mézailles, *J. Org. Chem.*, 2007, **72**, 4228–4237.
- [66] S. H. Eitel, S. Jautze, W. Frey and R. Peters, *Chem. Sci.*, 2013, **4**, 2218–2233.
- [67] H. P. Dijkstra, M. Q. Slagt, A. McDonald, C. A. Kruithof, R. Kreiter, A. M. Mills, M. Lutz, A. L. Spek, W. Klopper, G. P. M. van Klink and G. van Koten, *Eur. J. Inorg. Chem.*, 2003, 830–838.
- [68] A. R. Mcdonald, H. P. Dijkstra, B. M. J. M. Suijkerbuijk, G. P. M. van Klink and G. van Koten, *Organometallics*, 2009, **28**, 4689–4699.
- [69] J. Spencer, B. Z. Chowdhry, A. I. Mallet, R. P. Rathnam, T. Adatia, A. Bashall and F. Rominger, *Tetrahedron*, 2008, **64**, 6082–6089.
- [70] R. Khan, R. Felix, P. D. Kemmitt, S. J. Coles, I. J. Day, G. J. Tizzard and J. Spencer, *Adv. Synth. Catal.*, 2016, **358**, 98–109.
- [71] J. Kjellgren, J. Aydin, O. A. Wallner, I. V. Saltanova and K. J. Szabó, *Chem. - A Eur. J.*, 2005, **11**, 5260–5268.
- [72] T.-K. Zhang, K. Yuan and X.-L. Hou, *J. Organomet. Chem.*, 2007, **692**, 1912–1919.
- [73] *Pincer and Pincer-Type Complexes*, ed. K. J. Szabó and O. F. Wendt, Wiley-VCH Verlag GmbH & Co. KGaA, Weinheim, Germany, 2014.
- [74] M. Feller, A. Karton, G. Leitus, J. M. L. Martin, D. Milstein and V. Reho, *J. Am. Chem. Soc.*, 2006, **128**, 12400–12401.
- [75] G. Zeng, Y. Guo and S. Li, *Inorg. Chem.*, 2009, **48**, 10257–10263.

-
- [76] K. Krogh-jespersen, M. Czerw, K. Zhu, B. Singh, M. Kanzelberger, N. Darji, P. D. Achord, K. B. Renkema and A. S. Goldman, *J. Am. Chem. Soc.*, 2002, **124**, 10797–10809.
- [77] E. Balaraman, C. Gunanathan, J. Zhang, L. J. W. Shimon and D. Milstein, *Nat. Chem.*, 2011, **3**, 609–614.
- [78] D. M. Grove, G. van Koten and A. H. Verschuuren, *J. Mol. Catal.*, 1988, **45**, 169–174.
- [79] G. van Koten, J. T. Jastrzebski, J. G. Noltes, A. L. Spek and J. C. Schoone, *J. Organomet. Chem.*, 1978, **148**, 233–245.
- [80] E. Poverenov, I. Efremenko, A. I. Frenkel, Y. Ben-David, L. J. W. Shimon, G. Leitun, L. Konstantinovski, J. M. L. Martin and D. Milstein, *Nature*, 2008, **455**, 1093–1096.
- [81] S. Bonnet, J. Li, M. A. Siegler, L. S. von Chrzanowski, A. L. Spek, G. van Koten and R. J. M. Klein Gebbink, *Chem. A Eur. J.*, 2009, **15**, 3340–3343.
- [82] S. Bonnet, M. Lutz, A. L. Spek, G. van Koten and R. J. M. Klein Gebbink, *Organometallics*, 2010, **29**, 1157–1167.
- [83] M. E. O. Reilly and A. S. Veige, *Chem. Soc. Rev.*, 2014, **43**, 6325–6369.
- [84] J. Koller, S. Sarkar, K. A. Abboud and A. S. Veige, *Organometallics*, 2007, **26**, 5438–5441.
- [85] K. P. McGowan, K. A. Abboud and A. S. Veige, *Organometallics*, 2011, **30**, 4949–4957.
- [86] I. Korobkov, S. Gorelsky and S. Gambarotta, *J. Am. Chem. Soc.*, 2009, **131**, 10406–10420.
- [87] R. Gedye, F. Smith, K. Westaway, H. Ali, L. Baldisera, L. Laberge and J. Rousell, *Tetrahedron Lett.*, 1986, **27**, 279–282.

-
- [88] R. J. Giguere, T. L. Bray, S. M. Duncan and G. Majetich, *Tetrahedron Lett.*, 1986, **27**, 4945–4948.
- [89] C. O. Kappe and D. Dallinger, *Mol. Divers.*, 2009, **13**, 71–193.
- [90] C. O. Kappe, *Chem. Soc. Rev.*, 2008, **37**, 1127–1139.
- [91] S. Caddick and R. Fitzmaurice, *Tetrahedron*, 2009, **65**, 3325–3355.
- [92] C. O. Kappe, A. Stadler and D. Dallinger, *Microwaves in Organic and Medicinal Chemistry*, Wiley-VCH Verlag GmbH & Co. KGaA, Weinheim, Germany, 2nd edn., 2012, pp. 9–36.
- [93] L. Perreux and A. Loupy, *Tetrahedron*, 2001, **57**, 9199–9223.
- [94] D. M. P. Mingos and D. R. Baghurst, *Chem. Soc. Rev.*, 1991, **20**, 1–47.
- [95] C. Gabriel, S. Gabriel, E. H. Grant, E. H. Grant, B. S. J. Halstead and D. Michael P. Mingos, *Chem. Soc. Rev.*, 1998, **27**, 213–223.
- [96] S. Boonseng, G. W. Roffe, J. Spencer and H. Cox, *Dalt. Trans.*, 2015, **44**, 7570–7577.
- [97] G. W. Roffe, S. Boonseng, C. B. Baltus, S. J. Coles, I. J. Day, R. N. Jones, N. J. Press, M. Ruiz, G. J. Tizzard, H. Cox and J. Spencer, *R. Soc. Open Sci.*, 2016, **3**, 150656.
- [98] P. Hohenberg and W. Kohn, *Phys. Rev.*, 1964, **136**, B864–B871.
- [99] P. Atkins and J. de Paula, in *Atkins Phys. Chem.*, Oxford University Press, Oxford, UK, 8th edn., 2006, pp. 395–396.
- [100] E. Lewars, in *Comput. Chem. Introd. to Theory Appl. Mol. Quantum Mech.*, Kluwer Academic Publishers, Dordrecht, The Netherlands, 2003, pp. 385–446.
- [101] L. J. Sham and W. Kohm, *Phys. Rev.*, 1965, **140**, A1133–A1138.

-
- [102] W. Koch and M. C. Holthausen, *A Chemist's Guide to Density Functional Theory*, Wiley-VCH Verlag GmbH & Co. KGaA, Weinheim, Germany, 2nd edn., 2002, pp. 65–89.
- [103] J. B. Foresman and A. Frisch, in *Explor. Chem. with Electron. Struct. Methods*, Gaussian, Inc., Pittsburgh, USA, Second Edi edn., 1996, pp. 272–275.
- [104] S. F. Sousa, P. A. Fernandes and M. J. Ramos, *J. Phys. Chem. A*, 2007, **111**, 10439–10452.
- [105] A. D. Becke, *Phys. Rev. A*, 1988, **38**, 3098–3100.
- [106] J. P. Perdew, *Phys. Rev. B*, 1986, **33**, 8822–8824.
- [107] A. D. Becke, *Phys. Rev. A*, 1988, **38**, 3098–3100.
- [108] M. J. Frisch, G. W. Trucks, H. B. Schlegel, G. E. Scuseria, M. A. Robb, J. R. Cheeseman, G. Scalmani, V. Barone, B. Mennucci, G. A. Petersson, H. Nakatsuji, M. Caricato, X. Li, H. P. Hratchian, A. F. Izmaylov, J. Bloino, G. Zheng, J. L. Sonnenberg, M. Hada, M. Ehara, K. Toyota, R. Fukuda, J. Hasegawa, M. Ishida, T. Nakajima, Y. Honda, O. Kitao, H. Nakai, T. Vreven, J. A. Montgomery, J. E. Peralta, F. Ogliaro, M. Bearpark, J. J. Heyd, E. Brothers, K. N. Kudin, V. N. Staroverov, R. Kobayashi, J. Normand, K. Raghavachari, A. Rendell, J. C. Burant, S. S. Iyengar, J. Tomasi, M. Cossi, N. Rega, J. M. Millam, M. Klene, J. E. Knox, J. B. Cross, V. Bakken, C. Adamo, J. Jaramillo, R. Gomperts, R. E. Stratmann, O. Yazyev, A. J. Austin, R. Cammi, C. Pomelli, J. W. Ochterski, R. L. Martin, K. Morokuma, V. G. Zakrzewski, G. A. Voth, P. Salvador, J. J. Dannenberg, S. Dapprich, A. D. Daniels, Ö. Farkas, J. B. Foresman, J. V. Ortiz, J. Cioslowski and D. J. Fox, *Gaussian 09, Revision D.01*. Wallingford CT, 2009.
- [109] E. G. Lewars, in *Comput. Chem. Introd. to Theory Appl. Mol. Quantum Mech.*, Springer, London, UK, 2nd edn., 2011, p. 464.

- [110] J. Tao, J. Perdew, V. Staroverov and G. Scuseria, *Phys. Rev. Lett.*, 2003, **91**, 146401.
- [111] Y. Zhao and D. G. Truhlar, *J. Chem. Phys.*, 2006, **125**, 194101.
- [112] J. B. Foresman and A. Frisch, in *Explor. Chem. with Electron. Struct. Methods*, Gaussian, Inc., Pittsburgh, USA, 1996, p. 275.
- [113] A. D. Becke, *J. Chem. Phys.*, 1996, **104**, 1040–1046.
- [114] J.-D. Chai and M. Head-Gordon, *Phys. Chem. Chem. Phys.*, 2008, **10**, 6615–6620.
- [115] Y. Zhao and D. G. Truhlar, *Theor. Chem. Acc.*, 2007, **120**, 215–241.
- [116] S. Grimme, *J. Comput. Chem.*, 2006, **27**, 1787–1799.
- [117] A. Tkatchenko, R. A. DiStasio, M. Head-Gordon and M. Scheffler, *J. Chem. Phys.*, 2009, **131**, 094106.
- [118] J. M. Pérez-Jordá and A. D. Becke, *Chem. Phys. Lett.*, 1995, **233**, 134–137.
- [119] S. Kristyán and P. Pulay, *Chem. Phys. Lett.*, 1994, **229**, 175–180.
- [120] S. Grimme, J. Antony, T. Schwabe and C. Muck-Lichtenfeld, *Org. Biomol. Chem.*, 2007, **5**, 741–758.
- [121] S. Grimme, J. Antony, S. Ehrlich and H. Krieg, *J. Chem. Phys.*, 2010, **132**, 154104.
- [122] M. P. Waller, A. Robertazzi, J. A. Platts, D. E. Hibbs and P. A. Williams, *J. Comput. Chem.*, 2006, **27**, 491–504.
- [123] P. J. Hay and W. R. Wadt, *J. Chem. Phys.*, 1985, **82**, 299–310.
- [124] P. J. Hay and W. R. Wadt, *J. Chem. Phys.*, 1985, **82**, 270–283.
- [125] D. Andrae, U. Haubermann, M. Dolg, H. Stoll and H. Preub, *Theor. Chim. Acta*, 1990, **77**, 123–141.

-
- [126] J. Tomasi, B. Mennucci and R. Cammi, *Chem. Rev.*, 2005, **105**, 2999–3093.
- [127] Y. Wang, X. Cheng, X. Yang and X. Yang, *J. Solution Chem.*, 2006, **35**, 869–878.
- [128] D. L. Davies, C. E. Ellul, S. A. Macgregor, C. L. McMullin and K. Singh, *J. Am. Chem. Soc.*, 2015, **137**, 9569–9669.
- [129] D. Tang, L. Zhu and C. Hu, *RSC Adv.*, 2012, **2**, 2329–2333.
- [130] M. E. Evans and W. D. Jones, *Organometallics*, 2011, **30**, 3371–3377.
- [131] M. Viciano, M. Feliz, R. Corberán, J. A. Mata, E. Clot and E. Peris, *Organometallics*, 2007, **26**, 5304–5314.
- [132] H. Eshtiagh-Hosseini, S. A. Beyramabadi, A. Morsali and M. R. Housaindokht, *J. Mol. Struct. THEOCHEM*, 2010, **941**, 138–143.
- [133] R. F. W. Bader, *Atoms in Molecules: A Quantum Theory*, Oxford University Press, Oxford, UK, 1990.
- [134] R. F. W. Bader, *Acc. Chem. Res.*, 1985, **18**, 9–15.
- [135] M. Ziolkowski, S. Grabowski and J. Leszczynski, *J. Phys. Chem. A*, 2006, **110**, 6514–6521.
- [136] R. N. Behera and A. Panda, *Comput. Theor. Chem.*, 2012, **999**, 215–224.
- [137] M. Palusiak, B. Rudolf, J. Zakrzewski, A. Pfitzner, M. Zabel and S. J. Grabowski, *J. Organomet. Chem.*, 2006, **691**, 3232–3238.
- [138] *Quantum Theory Atoms Mol.*, ed. C. F. Matta and R. J. Boyd, Wiley-VCH Verlag GmbH & Co. KGaA, Weinheim, Germany, 2007, pp. 1–34.
- [139] R. Cammi, M. Lanfranchi, L. Marchiò, C. Mora, C. Paiola and M. A. Pellinghelli, *Inorg. Chem.*, 2003, **42**, 1769–1778.

-
- [140] R. Shankar, P. Kolandaivel and L. Senthilkumar, *J. Phys. Org. Chem.*, 2011, **24**, 553–567.
- [141] S. Boonseng, *PhD Thesis. Prep.*
- [142] J. P. Perdew, K. Burke and M. Ernzerhof, *Phys. Rev. Lett.*, 1996, **77**, 3865–3868.
- [143] J. P. Perdew, K. Burke and M. Ernzerhof, *Phys. Rev. Lett.*, 1997, **78**, 1396.
- [144] J. P. Perdew and K. Schmidt, *AIP Conf. Proc.*, 2001, **577**, 1–20.
- [145] D.J. Heisterberg, *The Quatfit Program, the CCL archive. 1990.*, p. <http://www.ccl.net/cca/software/SOURCES/C/quaterni>.
- [146] Y. Minenkov, Å. Singstad, G. Occhipinti and V. R. Jensen, *Dalt. Trans.*, 2012, **41**, 5526–5541.
- [147] A. King, *Private communication*, Member of the Cox group wrote a program to obtain interactomic distances.
- [148] M. P. Waller, H. Braun, N. Hojdis and M. Bühl, *J. Chem. Theory Comput.*, 2007, **3**, 2234–2242.
- [149] M. L. Laury and A. K. Wilson, *J. Chem. Theory Comput.*, 2013, **9**, 3939–3946.
- [150] Y. Zhao and D. G. Truhlar, *J. Chem. Theory Comput.*, 2011, **7**, 669–676.
- [151] T. Lu and F. Chen, *J. Comput. Chem.*, 2012, **33**, 580–592.
- [152] P. K. Sajith and C. H. Suresh, *Inorg. Chem.*, 2011, **50**, 8085–8093.
- [153] R. A. Holton, M. P. Sibi and W. S. Murphy, *J. Am. Chem. Soc.*, 1988, **110**, 314–316.
- [154] V. A. Kozlov, D. V. Aleksanyan, Y. V. Nelyubina, K. A. Lyssenko, P. V. Petrovskii, A. A. Vasil’ev and I. L. Odinet, *Organometallics*, 2011, **30**, 2920–2932.

-
- [155] C. B. Baltus, *PhD Thesis*, University of Greenwich, 2011.
- [156] N. Miyaura, T. Yanagi and A. Suzuki, *Synth. Commun.*, 1981, **11**, 513–519.
- [157] N. Miyaura and A. Suzuki, *Chem. Rev. (Washington, DC, United States)*, 1995, **95**, 2457–2483.
- [158] A. Suzuki, *J. Organomet. Chem.*, 1999, **576**, 147–168.
- [159] I. Maluenda and O. Navarro, *Molecules*, 2015, **20**, 7528–7557.
- [160] J. Schwarz, E. Herdtweck and W. Herrmann, *Organometallics*, 2000, **19**, 3154–3160.
- [161] P. Saxena, N. Thirupathi and M. Nethaji, *Organometallics*, 2014, **33**, 5554–5565.
- [162] R. B. Bedford and C. S. J. Cazin, *Chem. Commun.*, 2001, 1540–1541.
- [163] R. B. Bedford and S. L. Welch, *Chem. Commun.*, 2001, 129–130.
- [164] I. Blaszczyk, A. Gniewek and A. M. Trzeciak, *J. Organomet. Chem.*, 2011, **696**, 3601–3607.
- [165] M. C. Lipke, R. A. Woloszynek, L. Ma and J. D. Protasiewicz, *Organometallics*, 2009, **28**, 188–196.
- [166] J. Aydin, C. S. Conrad and K. J. Szabó, *Org. Lett.*, 2008, **10**, 5175–5178.
- [167] J. Aydin and K. J. Szabó, *Org. Lett.*, 2008, **10**, 2881–2884.
- [168] G. Dutheuil, N. Selander, K. J. Szabó and V. K. Aggarwal, *Synthesis (Stuttg.)*, 2008, **14**, 2293–2297.
- [169] J. K.-P. Ng, S. Chen, G.-K. Tan and P.-H. Leung, *Eur. J. Inorg. Chem.*, 2007, 3124–3134.
- [170] A. D. Ryabov, *Chem. Rev.*, 1990, **90**, 403–424.

- [171] A. D. Ryabov, *Synthesis (Stuttg.)*, 1985, 233–252.
- [172] J.-L. Niu, X.-Q. Hao, J.-F. Gong and M.-P. Song, *Dalt. Trans.*, 2011, **40**, 5135–5150.
- [173] D. L. Davies, S. M. A. Donald and S. A. Macgregor, *J. Am. Chem. Soc.*, 2005, **127**, 13754–13755.
- [174] Y. Boutadla, D. L. Davies, S. A. Macgregor and A. I. Poblador-Bahamonde, *Dalt. Trans.*, 2009, 5820–5831.
- [175] M. Lafrance and K. Fagnou, *J. Am. Chem. Soc.*, 2006, **128**, 16496–16497.
- [176] D. García-Cuadrado, P. de Mendoza, A. A. C. Braga, F. Maseras and A. M. Echavarren, *J. Am. Chem. Soc.*, 2007, **129**, 6880–6886.
- [177] S. Pascual, P. de Mendoza, A. A. Braga, F. Maseras and A. M. Echavarren, *Tetrahedron*, 2008, **64**, 6021–6029.
- [178] C. B. Baltus, N. J. Press and J. Spencer, *Synlett*, 2012, **23**, 2477–2480.
- [179] M. R. Sorube, *BSc Dissertation*.
- [180] T. Kinzel, Y. Zhang and S. L. Buchwald, *J. Am. Chem. Soc.*, 2010, **132**, 14073–14075.
- [181] G. A. Olah, B. G. B. Gupta, R. Malhotra and S. C. Narang, *J. Org. Chem.*, 1980, **45**, 1638–1639.
- [182] L. Feng, K. Lv, M. Liu, S. Wang, J. Zhao, X. You, S. Li, J. Cao and H. Guo, *Eur. J. Med. Chem.*, 2012, **55**, 125–136.
- [183] S. M. Klein, C. Zhang and Y. L. Jiang, *Tetrahedron Lett.*, 2008, **49**, 2638–2641.
- [184] W. Mathes and H. Schuly, *Angew. Chemie, Int. Ed.*, 1963, **2**, 144–149.
- [185] H. L. Holland, F. M. Brown and B. G. Larsen, *Tetrahedron: Asymmetry*, 1995, **6**, 1561–1567.

-
- [186] P. A. Chase, M. Gagliardo, M. Lutz, A. L. Spek, G. P. M. van Klink and G. van Koten, *Organometallics*, 2005, **24**, 2016–2019.
- [187] B. D. Steffey, A. Miedaner, M. L. Maciejewski-Farmer, P. R. Bernatis, A. M. Herring, V. S. Allured, V. Carperos and D. L. DuBois, *Organometallics*, 1994, **13**, 4844–4855.
- [188] A. Sen and T.-W. Lai, *J. Am. Chem. Soc.*, 1981, **103**, 4627–4629.
- [189] W. Nakanishi and S. Hayashi, *Curr. Org. Chem.*, 2010, **14**, 181–197.
- [190] M. Montag, I. Efremenko, G. Leitus, Y. Ben-David, J. M. L. Martin and D. Milstein, *Organometallics*, 2013, **32**, 7163–7180.
- [191] S. K. Brayshaw, J. C. Green, G. Kociok-Köhn, E. L. Sceats and A. S. Weller, *Angew. Chemie Int. Ed.*, 2006, **45**, 452–456.
- [192] X. Li, J. Sun, Z. Sun, Y. Zeng, S. Zheng and L. Meng, *Organometallics*, 2012, **31**, 6582–6588.
- [193] J. A. Cabeza, J. F. Van der Maelen and S. Garcia-Granda, *Organometallics*, 2009, **28**, 3666–3672.
- [194] M. Niskanen, P. Hirva and M. Haukka, *J. Chem. Theory Comput.*, 2009, **5**, 1084–1090.
- [195] S. J. Coles and P. A. Gale, *Chem. Sci.*, 2012, **3**, 683–689.
- [196] K. Zhu, P. D. Achord, X. Zhang, K. Krogh-Jespersen and A. S. Goldman, *J. Am. Chem. Soc.*, 2004, **817**, 13044–13053.
- [197] K. van Gerard., *Pure Appl. Chem.*, 1989, **61**, 1681–1694.
- [198] K. Gopi, P. Saxena, M. Nethaji and N. Thirupathi, *Polyhedron*, 2013, **52**, 1041–1052.
- [199] G. Maestri, E. Motti, N. Della Ca', M. Malacria, E. Derat and M. Catellani, *J. Am. Chem. Soc.*, 2011, **133**, 8574–8585.

-
- [200] F. Amoroso, E. Zangrando, C. Carfagna, C. Müller, D. Vogt, M. Hagar, F. Ragaini and B. Milani, *Dalton Trans.*, 2013, **42**, 14583–14602.
- [201] A. O. Eseola, H. Görls, J. A. Woods and W. Plass, *J. Mol. Catal. A Chem.*, 2015, **406**, 224–237.
- [202] *The Chemistry of Pincer Compounds*, ed. D. Morales-Morales and C. M. Jensen, Elsevier, Amsterdam, 2007.
- [203] N. Miyaura, K. Yamada and A. Suzuki, *Tetrahedron Lett.*, 1979, **20**, 3437–3440.
- [204] S. D. Roughley and A. M. Jordan, *J. Med. Chem.*, 2011, **54**, 3451–3479.
- [205] R. B. Bedford, C. S. Cazin and D. Holder, *Coord. Chem. Rev.*, 2004, **248**, 2283–2321.
- [206] V. V. Grushin and H. Alper, *Chem. Rev.*, 1994, **94**, 1047–1062.
- [207] M. A. Düfert, K. L. Billingsley and S. L. Buchwald, *J. Am. Chem. Soc.*, 2013, **135**, 12877–12885.
- [208] H. Weissman and D. Milstein, *Chem. Commun.*, 1999, 1901–1902.
- [209] E. Alacid, D. A. Alonso, L. Botella, C. Nájera and M. C. Pacheco, *Chem. Rec.*, 2006, **6**, 117–132.
- [210] A. N. Marziale, D. Jantke, S. H. Faul, T. Reiner, E. Herdtweck and J. Eppinger, *Green Chem.*, 2011, **13**, 169–177.
- [211] J. L. Bolliger, O. Blacque and C. M. Frech, *Angew. Chemie Int. Ed.*, 2007, **46**, 6514–6517.
- [212] B. Ines, I. Moreno, R. SanMartin and E. Dominguez, *J. Org. Chem.*, 2008, **73**, 8448–8451.
- [213] W. A. Herrmann, C. Brossmer, K. Öfele, C.-P. Reisinger, T. Priermeier, M. Beller and H. Fischer, *Angew. Chemie Int. Ed. English*, 1995, **34**, 1844–1848.

-
- [214] A. Kumar, G. K. Rao, S. Kumar and A. K. Singh, *Dalton Trans.*, 2013, **42**, 5200–23.
- [215] N. T. S. Phan, M. Van Der Sluys and C. W. Jones, *Adv. Synth. Catal.*, 2006, **348**, 609–679.
- [216] A. A. Kurokhtina and A. F. Schmidt, *ARKIVOC*, 2009, 185–203.
- [217] C.-A. Lin and F.-T. Luo, *Tetrahedron Lett.*, 2003, **44**, 7565–7568.
- [218] R. B. Bedford, C. S. Cazin, M. B. Hursthouse, M. E. Light, K. J. Pike and S. Wimperis, *J. Organomet. Chem.*, 2001, **633**, 173–181.
- [219] K. Karami, Z. K. Moghadam and M. Hosseini-Kharat, *Catal. Commun.*, 2014, **43**, 25–28.
- [220] I. D. Kostas, A.-C. Tenchiu, C. Arbez-Gindre, V. Psycharis and C. P. Raptopoulou, *Catal. Commun.*, 2014, **51**, 15–18.
- [221] D. Astruc, *Inorg. Chem.*, 2007, **46**, 1884–94.
- [222] A. R. Kapdi, G. Dhangar, J. L. Serrano, J. Pérez, L. García and I. J. S. Fairlamb, *Chem. Commun.*, 2014, **50**, 9859–9861.
- [223] F. D’Orlyé and A. Jutand, *Tetrahedron*, 2005, **61**, 9670–9678.
- [224] A. J. J. Lennox and G. C. Lloyd-Jones, *Angew. Chemie - Int. Ed.*, 2013, **52**, 7362–7370.
- [225] M. García-Melchor, A. A. C. Braga, A. Lledós, G. Ujaque and F. Maseras, *Acc. Chem. Res.*, 2013, **46**, 2626–2634.
- [226] A. A. C. Braga, N. H. Morgon, G. Ujaque, A. Lledós and F. Maseras, *J. Organomet. Chem.*, 2006, **691**, 4459–4466.
- [227] C.-M. Weng and F.-E. Hong, *Dalton Trans.*, 2011, **40**, 6458–6468.

-
- [228] J. Jover, N. Fey, M. Purdie, G. C. Lloyd-Jones and J. N. Harvey, *J. Mol. Catal. A Chem.*, 2010, **324**, 39–47.
- [229] Y. L. Huang, C. M. Weng and F. E. Hong, *Chem. - A Eur. J.*, 2008, **14**, 4426–4434.
- [230] C. Amatore, A. Jutand and G. Le Duc, *Chem. - A Eur. J.*, 2011, **17**, 2492–2503.
- [231] B. P. Carrow and J. F. Hartwig, *J. Am. Chem. Soc.*, 2011, **133**, 2116–2119.
- [232] A. A. C. Braga, G. Ujaque and F. Maseras, *Organometallics*, 2006, **25**, 3647–3658.
- [233] C. F. R. A. C. Lima, A. S. M. C. Rodrigues, V. L. M. Silva, A. M. S. Silva and L. M. N. B. F. Santos, *ChemCatChem*, 2014, **6**, 1291–1302.
- [234] M. A. Ortuno, A. Lledos, F. Maseras and G. Ujaque, *ChemCatChem*, 2014, **6**, 3132–3138.
- [235] V. P. Ananikov, D. G. Musaev and K. Morokuma, *Organometallics*, 2005, **24**, 715–723.
- [236] M. Perez-Rodriguez, A. A. C. Braga, M. Garcia-Melchor, M. H. Perez-Temprano, J. A. Casares, G. Ujaque, A. R. de Lera, R. Alvarex, F. Maseras and P. Espinet, *J. Am. Chem. Soc.*, 2009, **131**, 3650–3657.
- [237] V. P. Ananikov, D. G. Musaev and K. Morokuma, *Eur. J. Inorg. Chem.*, 2007, 5390–5399.
- [238] R. Ghosh, T. J. Emge, K. Krogh-Jespersen and A. S. Goldman, *J. Am. Chem. Soc.*, 2008, **130**, 11317–11327.
- [239] C. Ryan, A. K. K. de Lewis, S. Caddick and N. Kaltsoyannis, *Theor. Chem. Acc.*, 2011, **129**, 303–312.
- [240] R. Cohen, D. Milstein and J. M. L. Martin, *Organometallics*, 2004, **23**, 2336–2342.

-
- [241] M. Perez-Rodriguez, A. A. C. Braga, A. R. de Lera, F. Maseras, R. Alvarez and P. Espinet, *Organometallics*, 2010, **29**, 4983–4991.
- [242] J. Spencer and R. Jones, *MChem Diss. Univ. Sussex*, 2013.
- [243] L. Bretherick, *J. Chem. Educ.*, 1989, **66**, A220–A224.
- [244] L. J. Farrugia, *J. Appl. Crystallogr.*, 2012, **45**, 849–854.
- [245] J. Dupont and M. Pfeffer, *J. Chem. Soc. Dalt. Trans.*, 1990, 3193–3198.
- [246] J. Dupont, M. Pfeffer, J. C. Daran and Y. Jeannin, *Organometallics*, 1987, **6**, 899–901.
- [247] A. A. C. Braga, N. H. Morgon, G. Ujaque and F. Maseras, *J. Am. Chem. Soc.*, 2005, **127**, 9298–9307.
- [248] T.-X. X. Zhang and Z. Li, *Comput. Theor. Chem.*, 2013, **1016**, 28–35.
- [249] M. T. Reetz and J. G. de Vries, *Chem. Commun. (Camb)*., 2004, 1559–1563.
- [250] C. S. Consorti, R. Flores, J. Dupont, P. Alegre and R. S. Brazil, *J. Am. Chem. Soc.*, 2005, **127**, 12054–12065.
- [251] J. G. de Vries, *Dalt. Trans.*, 2006, 421–429.
- [252] R. B. Bedford, S. M. Draper, P. Noelle Scully and S. L. Welch, *New J. Chem.*, 2000, **24**, 745–747.
- [253] D. M. Grove, G. van Koten, J. N. Louwen, J. G. Noites, A. L. Spek and H. J. C. Ubbels, *J. Am. Chem. Soc.*, 1982, **104**, 6609–6616.
- [254] Q.-L. Luo, J.-P. Tan, Z.-F. Li, W.-H. Nan and D.-R. Xiao, *J. Org. Chem.*, 2012, **77**, 8332–8337.
- [255] S. E. Denmark, R. A. Stavenger, A.-m. Faucher and J. P. Edwards, *Organometallics*, 1997, **3263**, 3375–3389.

-
- [256] Y. Motoyama, H. Narusawa and H. Nishiyama, *Chem. Commun.*, 1999, 131–132.
- [257] P. Steenwinkel, R. A. Gossage, T. Maunula, D. M. Grove and G. van Koten, *Chem. Eur. J.*, 1998, **4**, 763–768.
- [258] A. F. Abdel-Magid, K. G. Carson, B. D. Harris, C. A. Maryanoff, R. D. Shah and A. F. Abdel-Magid, *J. Org. Chem.*, 1996, **61**, 3849–3862.
- [259] R. J. Mattson, K. M. Pham, D. J. Leuck and K. A. Cowen, *J. Org. Chem.*, 1990, **55**, 2552–2554.
- [260] J. Singh, D. Kumar, N. Singh and A. J. Elias, *Organometallics*, 2014, **33**, 1044–1052.
- [261] S. J. Loeb, G. K. H. Shimizu and J. A. Wisner, *Organometallics*, 1998, **17**, 2324–2327.
- [262] L.-Y. Wu, X.-Q. Hao, Y.-X. Xu, M.-Q. Jia, Y.-N. Wang, J.-F. Gong and M.-P. Song, *Organometallics*, 2009, **28**, 3369–3380.
- [263] J. S. Fossey and C. J. Richards, *Organometallics*, 2004, **23**, 367–373.
- [264] R. B. Bedford, M. F. Haddow, C. J. Mitchell and R. L. Webster, *Angew. Chem. Int. Ed. Engl.*, 2011, **50**, 5524–5527.
- [265] J. J. Li, C. Limberakis and D. A. Pflum, *Modern Organic Synthesis in the Laboratory*, Oxford University Press, Oxford, UK, 2007, p. 144.
- [266] X. Huang, K. W. Anderson, D. Zim, L. Jiang, A. Klapars and S. L. Buchwald, *J. Am. Chem. Soc.*, 2003, **125**, 6653–6655.
- [267] K. Karami, C. Rizzoli and M. M. Salah, *J. Organomet. Chem.*, 2011, **696**, 940–945.
- [268] S. A. Burgess, A. Kassie, S. A. Baranowski, K. J. Fritzsche, K. Schmidt-Rohr, C. M. Brown and C. R. Wade, *J. Am. Chem. Soc.*, 2016, **138**, 1780–1783.

-
- [269] N. Solin, O. A. Wallner and K. J. Szabó, *Org. Lett.*, 2005, **7**, 689–691.
- [270] O. A. Wallner, V. J. Olsson, L. Eriksson and K. J. Szabó, *Inorganica Chim. Acta*, 2006, **359**, 1767–1772.
- [271] R. B. Bedford and L. T. Pilarski, *Tetrahedron Lett.*, 2008, **49**, 4216–4219.
- [272] A. G. Orpen and N. G. Connelly, *Organometallics*, 1990, **9**, 1206–1210.
- [273] S. M. Khake, V. Soni, R. G. Gonnade and B. Punji, *Dalt. Trans.*, 2014, **43**, 16084–16096.
- [274] M. R. Eberhard, S. Matsukawa, Y. Yamamoto and C. M. Jensen, *J. Organomet. Chem.*, 2003, **687**, 185–189.
- [275] M. R. Eberhard, S. Matsukawa, Y. Yamamoto and C. M. Jensen, *J. Organomet. Chem.*, 2003, **687**, 185–189.
- [276] P. K. Sajith and C. H. Suresh, *Dalton Trans.*, 2010, **39**, 815–822.
- [277] P. K. Sajith and C. H. Suresh, *J. Organomet. Chem.*, 2011, **696**, 2086–2092.
- [278] N. C. Mehendale, J. R. A. Sietsma, K. P. De Jong, C. A. Van Walree, R. J. M. K. Gebbink and G. van Koten, *Adv. Synth. Catal.*, 2007, **349**, 2619–2630.
- [279] G. Hamasaka, T. Muto and Y. Uozumi, *Angew. Chemie - Int. Ed.*, 2011, **50**, 4876–4878.
- [280] M. H. Shaw, N. G. McCreanor, W. G. Whittingham and J. F. Bower, *J. Am. Chem. Soc.*, 2015, **137**, 463–468.
- [281] V. K. R. Kumar, S. Krishnakumar and K. R. Gopidas, *European J. Org. Chem.*, 2012, **2012**, 3447–3458.
- [282] C. Diebold, A. Derible, J. M. Becht and C. Le Drian, *Tetrahedron*, 2013, **69**, 264–267.

- [283] S. M. Raders, J. N. Moore, J. K. Parks, A. D. Miller, T. M. Leibing, S. P. Kelley, R. D. Rogers and K. H. Shaughnessy, *J. Org. Chem.*, 2013, **78**, 4649–4664.
- [284] S. Doherty, J. G. Knight, N. A. B. Ward, D. M. Bittner, C. Wills, W. McFarlane, W. Clegg and R. W. Harrington, *Organometallics*, 2013, **32**, 1773–1788.
- [285] J. Aydin, K. S. Kumar, L. Eriksson and K. J. Szabó, *Adv. Synth. Catal.*, 2007, **349**, 2585–2594.